Site and Basin Effects on Seismic Hazard in Indonesia:

Sulawesi and Jakarta Case Studies

Athanasius Cipta

A thesis submitted for the degree of
Doctor of Philosophy at
Research School of Earth Sciences
The Australian National University

8 May 2019

Declaration

This dissertation is the complete account of the research undertaken from November 2013 to November 2017 at the Research School of Earth Sciences, Australian National University in Canberra, Australia. Unless otherwise indicated and to the best of my knowledge, the research described in this dissertation is my own original work and has not been submitted in whole or part for a degree in any university.

Athanasius Cipta
8 May 2019

to my super Mom at home

Acknowledgements

Foremost, I would like to express my sincere gratitude to my supervisor, Prof. Phil Cummins, for the continuous support of my research, for his patience, motivation, enthusiasm, and immense knowledge. His guidance helped me in all the time of research and writing of this thesis. I could not have imagined having a better advisor and mentor for my Ph.D study.

My utmost appreciation to my thesis committee: Dr. Erdinc Saygin, Dr. Hadi Ghasemi, and Prof. Masyhur Irsyam for their encouragement, insightful comments, and hard questions.

My sincere thanks also goes to Jan Dettmer for inundating me with a bunch of inversion materials, Jonathan Griffin, Nick Horspool, Annie (Ngoc Nguyen), R. Robiana and Sri Hidayati, for our collaborative works.

My heartfelt thanks to my colleagues at RSES for the motivation, positive vibes and sincere friendships. Many thanks to the Earth Physics group where I have enjoyed the company of amazing and lovely people.

Special thanks to my nephews Mikael and Raphael who have been great sources of laughter and headache :) during my coming home. Many thanks also go to 理恵 for providing me a great Tsukuba nights here in Australia. This material is dedicated to Mom and our family, many thanks for the pure love, morale booster and impeccable support which drive me to reach higher goals.

I also have to thaks 村上 春樹 and 新垣 結衣 for the Norwegian Wood and Umberto Eco for your Rose that company me during the boring nights.

Finally, I have to give thanks to Persib, my Maung Bandung. No reason is needed.

Abstract

Earthquakes are among the most costly, devastating and deadly natural hazards. The extent of the seismic hazard is often influenced by factors like the source location and site characteristics, while the susceptibility of assets is influenced by the population density, building design, infrastructure and urban planning. A comprehensive knowledge of the nature of source and local geology enables the establishment of an effective urban planning that takes into account the potential seismic hazard, which in turn may reduce the degree of vulnerability.

The first probabilistic seismic hazard assessment (PSHA) incorporating the effects of local site characteristic for the island of Sulawesi in Indonesia has been conducted. Most of the island, with the exception of South Sulawesi, is undergoing rapid deformation. This leads to high hazard in most regions (such that PGA $>$ 0.4g at 500 year return period including site effects) and extremely high hazard (like PGA $>$ 0.8 g at 500 year return period) along fast-slipping crustal fault. On the other hand, a distant site relative to fault might suffer higher ground motion if that site is composed of soft soil. This research has proven that incorporating near-surface physical properties, in this case is represented by V_S30, surface geology contribute significantly to ground motions, consequently, responsible for potential building damage.

The PSHA study that took place in Sulawesi took us move further, investigate the effect of deep structure on seismic waves. Jakarta was chosen for its location sitting on less known deep sediment basin and economic and political importances. A dense portable-seismic-broadband network, comprising 96 stations, has been operated within four months covering the Jakarta. The seismic network sampled broadband seismic-noise mostly originating from ocean waves and anthropogenic activity. We used Horizontal-to-Vertical Spectral Ratio (HVSR) measurements of the ambient seismic noise to estimate the fundamental-mode Rayleigh wave ellipticity curves, which were used to infer the seismic velocity structure of the Jakarta Basin. By mapping and modeling the spatial variation of low-frequency (0.124–0.249 Hz) HVSR peaks, this study reveals variations in the depth to the Miocene basement. To map these velocity profiles of unknown complexity, we employ a Transdimensional-Bayesian framework for the inversion of HVSR curves for 1D profiles of velocity and density beneath each station. The inverted velocity profiles show a sudden change of basement depth from 400 to 1350 m along N-S profile through the center of the city, with an otherwise gentle increase in basin depth from south to north.

Seismic wave modelings are conducted afterward and shows that for very deep basin of Jakarta, available ground motion prediction equation (GMPE) is less sufficient in capturing the effect of basin geometry on seismic waves. Earrthquake scenario modeling using SPECFEM2D is performed to comprehend the effect of deep basin on ground motions. This modeling reveals that the city may experience high peak ground velocity (PGV) during large megathrust earthquake. The complexity of the basin is responsible for magnifying ground motions observed in the basin.

Contents

Declaration iii

Acknowledgements v

Abstract vii

1 Introduction 3
- 1.1 Objectives . . . 4
- 1.2 Organization of the Dissertation . . . 5
- 1.3 Original Contributions of the Thesis . . . 6
- 1.4 Regional Tectonic Setting and Seismicity . . . 7

2 PSHA Sulawesi 11
- 2.1 Introduction . . . 11
- 2.2 Geological and seismotectonic setting . . . 12
- 2.3 Methods . . . 13
  - 2.3.1 Earthquake Hazard Modeling . . . 13
  - 2.3.2 Input Parameters . . . 15
- 2.4 Hazard modeling results . . . 24
- 2.5 Discussion . . . 30
- 2.6 Conclusions . . . 35

3 Jakarta's Earthquake 37
- 3.1 Introduction . . . 37
- 3.2 Seismic Hazard of Jakarta . . . 38
- 3.3 DSHA of the 5 January 1699 event . . . 41
- 3.4 DSHA of the 22 January 1780 event . . . 44
- 3.5 DSHA of the 10 October 1834 event . . . 47
- 3.6 Conclusion . . . 49

4 HVSR–Seismic Velocity Structure of the Jakarta Basin 51
- 4.1 Introduction . . . 52
- 4.2 Geotectonic Setting and Historical Earthquakes . . . 53
- 4.3 HVSR Measurements . . . 54
  - 4.3.1 Assumptions . . . 57
  - 4.3.2 Data . . . 58
- 4.4 HVSR Curves . . . 59
  - 4.4.1 Sharp f_0^l peaks . . . 59
  - 4.4.2 Broad f_0^l peaks . . . 60
- 4.5 HVSR peak frequencies and amplitudes . . . 60
- 4.6 Inversion of HVSR curve . . . 63
  - 4.6.1 Synthetic tests . . . 67

4.6.2 Inversion of Jakarta's HVSR curves . . . 68
4.7 Shallow-depth velocity profile . . . 72
4.8 Discussion . . . 72
4.9 Conclusion . . . 77

5 Basin Resonance and Seismic Hazard in Jakarta, Indonesia 81
5.1 Introduction . . . 81
5.2 Tectonic Setting of Jakarta and Surroundings . . . 83
5.3 The Jakarta Basin . . . 84
5.4 Ground Motion Prediction Equations (GMPEs) . . . 88
5.5 Numerical Simulation of Seismic Waves . . . 92
5.5.1 2D fault in Cartesian coordinate system . . . 93
5.5.2 Domain area and source parameters . . . 94
5.6 Results . . . 97
5.6.1 GMPE Modeling Results . . . 97
5.6.2 Numerical Simulation Results . . . 99
5.7 Discussion . . . 103
5.7.1 GMPE-Seismic Hazard . . . 103
5.7.2 Numerical Simulations–Peak Ground Velocity (PGV) . . . 104
5.7.3 Numerical Simulation-Response Spectral Acceleration . . . 104
5.8 Conclusion . . . 111

6 Summary and Future Works 113
6.1 Summary . . . 113
6.1.1 Historical Earthquakes Impacting the Jakarta Area . . . 113
6.1.2 PSHA with Site Response: Sulawesi Case Study . . . 114
6.1.3 HVSR Analysis for Jakarta Basin Structure . . . 115
6.1.4 Earthquake Scenario Ground Motions for Jakarta . . . 116
6.2 Future Work . . . 116

List of Figures

1.1 Map of V_{S30} of Indonesian Region 7
1.2 Tectonic setting and volcanic activity of Indonesian region 9
1.3 Seismicity of Indonesian Region in 1900-2014. 10

2.1 Sulawesi's active faults 14
2.2 Earthquake distributions 15
2.3 Earthquake source zone 20
2.4 Earthquake source zone 21
2.5 V_{S30} Map of Sulawesi 24
2.6 V_{S30} histogram 25
2.7 Site-class histogram 27
2.8 PGA and RSA of Sulawesi 29
2.9 MMI of Sulawesi 31
2.10 PGA and RSA of Sulawesi 33
2.11 PGA and RSA of Sulawesi 34

3.1 PGA at bedrock of Jakarta 39
3.2 PGA at bedrock of Jakarta 42
3.3 Intensity model of 5 January 1699 event 43
3.4 Intensity model of 22 January 1780 event 46
3.5 Intensity model of 10 October 1834 event 48

4.1 Simplified tectonic setting of Indonesia and surrounding regions 53
4.2 Influence of window-length 56
4.3 Typical ellipticity curves 61
4.4 Broad ellipticity curves 62
4.5 Peak and amplitude HVSR map 63
4.6 SN and WE transects 64
4.7 Synthetic TransD 69
4.8 Synthetic 3 layers non-transD 70
4.9 Synthetic 20 layers non-transD 71
4.10 JKB18 transD 73
4.11 ellipticity curves fitting 74
4.12 Jakarta Basin depth 75
4.13 HVSR vs ANT results, inverted velocity pofile along SN cross-section 76
4.14 HVSR vs ANT results, inverted velocity pofile along SN cross-section 78

5.1 Effect of distance to spectral accelereation 83
5.2 Simplified tectonic setting of Indonesia and surrounding regions 84
5.3 Jakarta basin depth 86
5.4 Contour lines and drainage pattern overlaid on a geological map 86

5.5 Jakarta basin WE transection 87
5.6 Fold reconstruction 88
5.7 Extended Jakarta basin depth 89
5.8 V_{S30} against basin depth 91
5.9 Fault in Cartesian coordinate system 93
5.10 Domain area 95
5.11 V_{S30} against basin depth 98
5.12 Snapshots of waves propagation 100
5.13 Horizontal direction seismogram 101
5.14 Seismograms at stations S2169, both for vertical (**a**) and horizontal (**b**) components. 102
5.15 Design response spectra 103
5.16 PGVs amplification 105
5.17 PGVs amplification resulted from crustal earthquake 106
5.18 PGVs amplification resulted from megathrust earthquake 106
5.19 PGVs amplification resulted from intraslab earthquake 108
5.20 Spectral acceleration at S2169 and S2173 (Megathrust) 109
5.21 Spectral acceleration at S2131 and S2165 (Intraslab) 110

List of Tables

2.1 Sources parameters 18
2.2 GMPEs and logic tree 22
2.3 Geomorphic units 22

3.1 GMPEs and sources parameters 41

5.1 Layer parameters used in simulation of seismic waves propagation 96
5.2 Layer parameters used in simulation 96
5.3 Peak velocity 107

Chapter 1

Introduction

Earthquakes are among the most costly, devastating and deadly natural hazards. The extent of the seismic hazard is often influenced by factors like the source location and site characteristics, while the susceptibility of assets is influenced by the population density, building design, infrastructure and urban planning. A comprehensive knowledge of the nature of source and local geology enables the establishment of an effective urban planning that takes into account the potential seismic hazard, which in turn may reduce the degree of vulnerability.

From the earthquake source point of view, many large historical earthquakes have occurred along subduction interface such as the 1960 Great Chilean, the 1964 Alaska, the 1985 Michoacán, the 2004 Sumatra-Andaman and the 2011 Tohōku earthquakes, which caused major impact to structures and society, and triggered tsunami resulting in even higher collateral damage. Another seismic event that caused devastation is the M 7.6 Padang Indonesia earthquake which was an intraslab event that took place on 30 September 2009. Nonetheless, it should be noted that low magnitude shallow crustal earthquakes are also capable of inducing building damage owing to their proximity to the residential areas. The 1995 Kobe, the 2006 Yogyakarta, the 2009 L'Aquila and the 2016 Kumamoto earthquakes are few of the numerous destructive crustal earthquakes. The 1995 Kobe, the 2006 Yogyakarta, the 2009 L'Aquila and the 2016 Kumamoto earthquakes are a few of numerous destructive crustal earthquakes that have occured recently. Amongst these destructive earthquakes, the 1985 Michoacán [*Cruz-Atienza et al.*, 2016; *Padilla y Sanchez*, 1989] and the 1995 Kobe earthquakes [*Kawase*, 1996] events have had immense impacts.

The occurrence of the 1985 Michoacán Earthquake prompted many researchers to improve the understanding of seismic site response. This M 8.0 event was associated with 15,000 fatalities. Though the epicenter was more than 450 km away from Mexico City, it produced extremely long duration of ground motions aswell as amplification of seismic waves. Spectral amplification for subduction earthquakes at these lake-bed sites (with average thickness of 50 m) ranges from 10-50 at spectral periods between 1.4 to 5 seconds with respect to bedrock sites mostly made up of Oligocene volcanics. However, the bedrock sites also experienced 10 times amplification with respect to the older Transmexican Volcanic Belts. This made Mexico City the first city to experience an accumulation of 100 to 500 times spectral amplification [*Cruz-Atienza et al.*, 2016] in a major earthquake. Such an event highlighted the high probability of a similar scenario occurring in other cities built on similar soft sediment deposits.

The M 6.9 Kobe earthquake, known as the Hyogo-ken Nambu or the Great Hanshin earthquake, in 17 January 1995 claimed more than 5500 lives and destroyed almost 100,000 residential buildings. Despite its shallow epicenter and close proximity to the city, a constructive interference between the direct S-wave in the basin and edge-wave

amplified the ground motions [*Kawase*, 1996]. *Kawase & Hayashi* [1996] and *Motosaka & Nagano* [1996] have inferred that both deep basin structure and shallow sedimentary layers were responsible for the exceptionally strong ground shaking in the city of Kobe. Deep sedimentary structure contributed to high amplitudes at dominant frequency of 0.25 Hz while near-surface sedimentary layers produced high amplification at frequencies of 1 Hz and higher [*Pitarka et al.*, 1996].

The difference in source mechanisms and tectonic setting related to these two events against the type building damaged and location of damage clearly demonstrated the importance of understanding the effects of local geology on the amplification of seismic waves. The effects of local site conditions pose a challenge to seismologists and earthquake engineers, especially when related to the dynamic response of building systems. Local site response is affected by topography, properties of near-surface sediments properties and deep basin structure at the site. Seismic amplification is generated due to conservation of energy. As seismic waves propagate from high to low impedance medium, the resistance to motion decreases. Hence, the particle velocity and the amplitude of the seismic waves increase. The impedance contrast, which determines the extent of this increase in amplitude, depends on shear-wave velocity (V_S) and density as a function of depth, wherein the former changes more rapidly with depth. V_S as a function of depth is therefore the most important criterion defining the seismic site amplification. The US Federal Emergency Management Agency [*FEMA*, 2003] and Building Seismic Safety Council [*BSSC*, 2003] recommended the average V_S measured in the upper 30 m of the soil profile (V_S30) as the parameter used to classify site condition.

A variety of methodologies have been developed to resolve the V_S profile at a site, both in invasive and non-invasive ways. Among the available invasive techniques, borehole and Seismic Cone Penetration Test (SCPT) are the widely used in geotechnical studies, which are both capable of providing accurate estimates of V_S and in detecting deep low velocity layers as well as thin high velocity layers overlying low velocity layers. However, these methods are costly, time consuming and often impractical to apply in urban areas. On the other hand, the combination of passive, array spatial autocorrelation(SPAC) processing and the horizontal-to-vertical spectral ratio (HVSR) measurements offer an alternative in resolving the basement boundary up to a depth of 1000 m. Introducing geological information into single-station HVSR analysis produces consistent V_S profiles up to a depth of 1000 m [*Asten & Boore*, 2005].

In this thesis, ambient noise recordings from 96 seismic stations covering the city of Jakarta are utilized to obtain HVSR curves. To retrieve a robust 1D velocity profiles at each station, a priori information on the geological setting is incorporated in the inversion process. Through these 1D velocity profiles, a 3D image of Jakarta basin is constructed. Furthermore, the geometry of the basin and the physical properties of the potential earthquake sources were used to simulate seismic wave propagation from source through a multi-layer medium to recording stations on the surface. The methodologies used for the HVSR computation, basin model construction and the spectral amplification estimation are presented in the chapter on **Methodology**.

1.1 Objectives

The main objective of this research is to verify and establish the single-station seismic noise HVSR method in constructing basin geometry and velocity structure. By incorporating the constructed basin geometry and other elastodynamic properties into wave propagation

simulations, the effect of the thick sedimentary basin on seismic waves can be analysed.

Looking through the many published studies on the HVSR technique, it appears that no study as yet has relied solely on HVSR to image the 3D interior of a deep basin filled with highly saturated sediments (> 100 m). It would therefore appear that this is the first time ambient noise recordings are applied in estimating HVSRs over a wide area, which are then inverted to retrieve local V_S profile used to construct a deep, 3D basin model. We demonstrated that inversion of HVSRs provide the adequate resolution required for development of 3D basin models, although for retrieving V_S on the near surface layer, dispersion (e.g. SPAC, MASW) data and/or invasive V_S measurements are highly required (e.g. borehole, NSPT, CPT). Perhaps more significantly, a Trans-dimensional Bayesian approach is used to invert the HVSR (interpreted as Rayliegh wave ellipticity) curves. This approach allowed the exploration of the a priori unknown number of layers required to fit each HVSR curve, as well as its effect on the model uncertainty (i.e., posterior probability density function). Trans-dimensional Bayesian inversion accounting for unknown data error and model parametrizations allows us to estimate the most-probable model of the subsurface V_S profile together with quantitative assessments of uncertainty.

1.2 Organization of the Dissertation

Chapter 1: Introduction – This first chapter highlights the significance of this research, especially its application on seismic hazard assessment assessment. This chapter also provides an overview of the methods implemented to meet the research objectives and to also emphasize its applicability to building code development in deep basin areas. A general description of the study area is presented which covers the demographics, economic and political importance, and geological setting and seismicity.

Chapter 2: A Probabilistic Seismic Hazard Assesment for Sulawesi, Indonesia – One of the most popular proxies in estimating seismic amplification is V_{S30} , the average shear-velocity at the top 30 m of soil. A regional study in Sulawesi used V_S30 in estimating ground motions. This is a probabilistic seismic hazard assessment taking into account megathrust, intraslab, crustal fault and background seismicity to producing the corresponding exceedance levels spectral accelerations at different periods. This study enables the assessment of V_S30 in quantifying the seismic amplification both for short and long spectral periods. It also shows that methods for estimating V_{S30} using topography and geomorphology often yield results that are inconsistent with ach the and with in situ measurements of V_{S30} .

Chapter 3: Historical and Hypothetical Future Earthquake Affecting Jakarta – Jakarta city has been growing fast since the late 1960s and has become one of the most populous citis in Asia with the highest economic growth. For more than a century, large ground shaking has yet to strike the city, owing to its long distance from the Java Trench subduction zone. Destructive earthquakes have hit Jakarta in the historic as but were not well document. By considering the intensity data, these historical events have been simulated in an effort to verify potential sources and check plausible ground motion estimates that may seriously impact the city.

Chapter 4: Seismic Velocity Structure of the Jakarta Basin, Indonesia, using Trans-dimensional Bayesian Inversion of Horizontal-to-Vertical Spectral

Ratios – Horizontal-to-vertical-spectral ratio (HVSR) are estimated based on records from 96 seismic stations deployed in Jakarta. The fundamental period in these curves is thought to be indicative of the relative sediment thickness overlying bedrock. In this way HVSR curves along SN and EW lines can be used to identify apparent changes in bedrock depth and stratigraphy. A more quantitative approach can be taken by interpreting the HVSR curves in terms of fundamental mode Rayleigh wave ellipticity, and inverting them to obtain estimated profiles of V_S, density and V_P/V_S ratios. Using a Trans-dimensional Bayesian framework, these curves are inverted to obtain the velocity profile for profiles of unknown complexity, where both the level of noise and model complexity (i.e., the number of layers) can adapt to fit the data. The 1D velocity profiles are then interpolated to create the 3D basin structure.

Chapter 5: Basin Resonance and Seismic Hazard in Jakarta, Indonesia – Characterization of Seismic Amplification in Jakarta – Earthquake scenario modelling is performed to characterize the seismic wave propagation through the basin model created in Chapter 4. Three earthquake scenarios are investigated: a crustal, an intraslab and a megathrust earthquake. A simplified model of the basin, in which it is characterized by a uniform, average V_S, is used with the spectral element seiscmic waveform modeling software SPECFEM2D [*Komatitsch et al.*, 2004].

Chapter 6 : Summary – This dissertation is finalized with a set of summary and future works. In this chapter, the primary results of the study are highlighted. Recommendations for future studies are also proposed.

1.3 Original Contributions of the Thesis

The first attempt to apply geomorphic approach to estimate average shear-wave velocity at top 30 m of soil (V_{S30}) introduced by *Matsuoka et al.* [2006] has been implemented for most of Indonesian Archipelago. This calculation is made in spatial grid 1 km using digitized geological map produced by Geological Agency of Indonesia and SRTM topographic dataset (http://www.cgiar-csi.org/data/srtm-90m-digital-elevation-database-v4-1) as main sources and hydrogeological as supporting data especially in a basinal area.

Study of probabilistic seismic hazard asessment (PSHA) in Sulawesi, that incorporate site classes, represented by V_{S30} , became the first work dedicated to investigate seismic hazard at site specific to a part of Indonesian region. PSHA study is intended to quantify the level of seismic hazard, in term of ground motion, at particular point during particular period of time. The inclusion of site class is to show how nonlinear is the effect of local geology on ground motion, hence, disclose the importance of introducing reliable site class into seismic hazard calculation. This study also shows that proximity to earthquake source in only one aspect contribute to ground motions, thick soft sediment is also responsible to amplify earthquake shaking.

The Horizontal-to-Vertical Spectral Ratio (HVSR) is a passive seismic method widely used for site characterization [*Nakamura*, 1997], 1D velocity profile imaging [*Lontsi et al.*, 2015], geothermal field exploration [*Wardhani et al.*, 2013; *Galgaro et al.*, 2014; *Agostini et al.*, 2015], structural geology surveys [*Tarabusi & Caputo*, 2016], basin modeling [*Guéguen*, 2007; *Borges et al.*, 2016], liquefaction vulnerability [*Beroya & Aydin*, 2010; *Prabowo et al.*, 2016; *Fergany & Omar*, 2017; *Singh et al.* , 2017], landslide characterization [*Panzera et al.*, 2012; *Pilz et al.*, 2013; *Pazzi et al.*, 2017] and paleosoil maping [*Zeid et al.*,

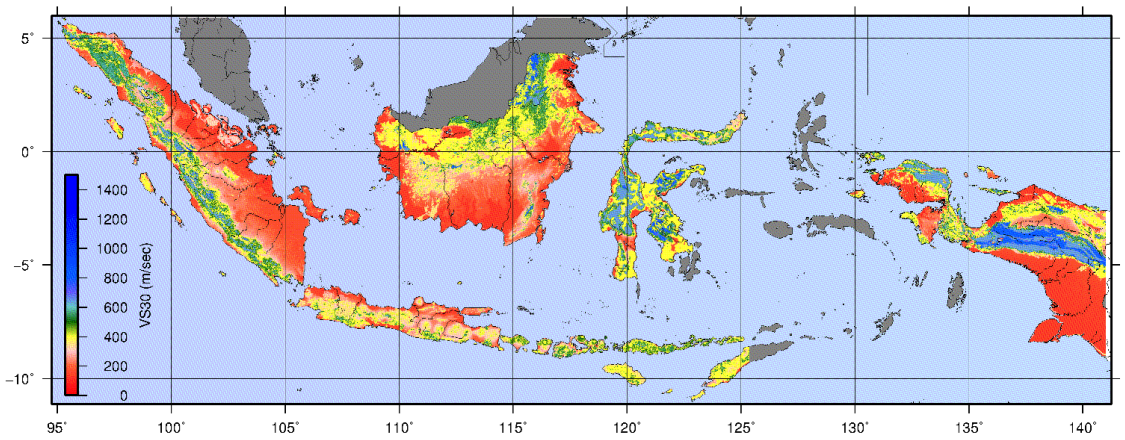

Figure 1.1: Map showing V_{S30} of Indonesian region, V_{S30} is the most widely used parameter to determine soil class. The higher the V_{S30} , the hardest the soil and vise versa. Engineering bedrock is defined as the medium having $V_{S30} \geq 760$ m/s.

2017]. In these studies, researchers often utilize the HVSR method with other techniques such as SPAC, borehole measurements, etc., or use *ad hoc* constraints on model complexity to constrain the range of models searched in the nonlinear inversion of HVSR curves. In this study, we used a Trans-dimensional Bayesian framework that allows model complexity to adapt to the data, while ascribing low posterior probability to complexity that is not required by the data (e.g., low velocity zones – see "Bayesian Parsimony" in *Malinverno* [2002]. We believe this property is important for HVSR inversion in deep basins like Jakarta, where shallow layering is required to account for compaction but deeper layering must be included to account for the basement.

The biggest contribution of this research is that the first ever geological model of Jakarta basin successfully constructed.

1.4 Regional Tectonic Setting and Seismicity

The geologically complex region of Indonesia is situated on the southern tip of the Eurasian continental plate. The archipelago comprised of 13,466 islands –officially enlisted in and recognized by the UN– [*BIG*, 2015] and extends more than 5000 km from west to east between 95°E and 141°E and spans the equator region from 6°N to 11°S. On the other hand, the Ministry of Marine and Fisheries [*KKP*, 2017] indicated that as per 2017, 14,572 island have been verified. The region is located at a confluence of five major plates: Eurasian, Indian, Australian, Pacific and Phillippine Sea plates [*DeMets et al.*, 2010]. The Indian and Australian plates are moving northeastward and converging with the western part of Sunda Block of the Eurasian plate at a rate of about 10 cm/yr [*Bock et al.*, 2003].

As shown in Fig. 1.2, the Indo-Australian plate collides beneath eastern part of Sunda Block at a rate of 7 cm/yr. The Australian plate also moves east-northeastward relative to the Pacific plate at a rate of 11 cm/yr while the Pacific-Philippine Sea plate moves westward relative to Eurasian plate at a rate of 10 cm/yr [*Hall*, 2009].

The interaction between plates manifests as earthquakes, volcanism, folding and faulting activity. These active tectonic plate margins and geological structures are well defined by seismicity. The subduction zone that forms when an oceanic plate is colliding

and sinking beneath a continental plate is clearly illustrated by the seismicity and the presence of volcanic activity. Shallow earthquakes dominate the Sunda Megathrust from west of Sumatra Island to South of Java and continue to the south of the Nusa Tenggara islands arc, then extend northward to South Moluccas, and bend to the north of the Ceram Island. Focal depths of intraslab earthquakes deepen as they occur further from the subduction margin.

The seismicity maps in (Fig. 1.3) illustrate that the subducting slab in Sumatra can be observed down to 300 km depth, whereas in Java, the subducting plane can be estimated down to 500 km depth. The Sangir subduction zone in the east of Sulawesi produces deep earthquakes up to 500 km in depth. The Halmahera subduction zone produces much shallower earthquakes down to a depth of only 200 km. The upper part of the subduction zone, from trench to a depth of around 40 km is usually elastic and the contact plane between subducted and underlying plates is locked. Movement of the subducted plate accumulates strain at this locked interface, which is capable of generating megathrust earthquakes.

At a depth greater than 40 km, temperature along the megathrust ranges from 300 to 400°C, a condition that does not support strain accumulation. In other words, locking does not happen at the interface at this depth. Small earthquakes commonly occur in the subducting slab as it releases volatiles in the temperature range 450-600°C, usually when the subducted slab reaches an approximate depth of 150-200 km. The volatiles migrate upward and can cause partial melting in the mantle forearc wedge and thus volcanoes appear on the surface [*McCaffrey*, 2009].

The oblique movement along the Indian and Australian plates in the west coast of Sumatra is accommodated by the Great Sumatran Fault (GSF). This right lateral fault stretches from Aceh in the north to Lampung in the south and produces medium magnitude and shallow depth earthquakes. This fault can be divided into 20 segments with 35-200 km lengths and separated from each other by gaps of 4-12 km. These gaps confine the maximum earthquake produced by a particular segment. Each segment has a different slip-rate that limits the recurrence period of earthquakes. More than half of the 1900 km GSF has the potential to produce earthquakes larger than M 6.5 [*Natawidjaja & Triyoso*, 2007].

The 26 December 2004 Mw 9.1 earthquake was the most prominent megathrust earthquake to hit Sumatra. This earthquake triggered a tsunami causing more than 200,000 casualties along the coasts of the Indian Ocean. The Mw 7.6 Padang earthquake on 30 September 2009 is one example of an intraslab event that resulted to 1,193 fatalities and about 250 thousand buildings damage in West Sumatra Provinces and triggered mega landslide that buried 3 villages. The Gunung Tigo, Sumani and Sianok segments of the GSF were associated with the Mw 6.4 Sumani and Mw 6.3 Sianok earthquakes on 6 March 2007. These doublet earthquakes caused 68 casualties and damaged around 800 buildings in Sumatra Barat Provinces.

In and around Java, megathrust and crustal earthquakes have dominated the seismicity since 1900 and some earthquakes have caused heavy damage and large casualties. The 2 September 2009 Mw 7.5 Tasikmalaya earthquake killed at least 80 people and caused hundreds of injuries. The earthquake induced a rockfall at Cikangkareng Cianjur Regency which killed 12 people, with 45 people missing and hundreds damaged houses [*Geological Agency*, 2009].

In Yogyakarta, a Mw 6.3 earthquake on 27 May 2006 caused more than 3000 fatalities. More than 6000 buildings were damaged in Yogyakarta and the Central Java

provinces. This earthquake is a crustal earthquake associated with the Opak Fault, a rather poorly understood right lateral fault crossing the Yogyakarta Province from southwest to northeast.

The number of earthquakes and the maximum earthquake size in Java appears to be less than in Sumatra. This difference in seismicity may be attributed to variation in nature and age of the subducting plates [*Newcomb & McCann*, 2007]. The age of the subducting plate varies from 50 to 90 million years along the west coast of Sumatra to 100 to 135 ma and 140 to 160 ma to the south of Java and Flores respectively. While earthquakes with focal depths up to 670 km occur in the seismic zone beneath Java with a slab dip of $\sim 60°$, earthquakes with focal depths deeper than 300 km are nonexistent beneath Sumatra where the lithosphere is subducting at dip angles of $\sim 30°$ to $45°$ [*Widiyantoro & van der Hilst*, 1996].

In central and east Indonesia, movement along the Philippine Sea and Pacific Plates becomes the primary cause of earthquakes. The North Sulawesi Subduction Zone, New Guinea Subduction Zone and the subduction zone in Moluccas Sea are marked by high rates of seismicity especially at shallow depth. From subduction zones previously mentioned, the double subductions of Sangir and Halmahera have different characteristics. Due to the steep dip of the slabs, these produce medium and deep earthquakes more frequent than shallow earthquakes as shown in Fig. 1.3. The earthquake events including the 30 September 1899 Mw7.5 Seram-Moluccas, the 13 April 1924 Tarakan-East Kalimantan (MMI VII), the 17 February 1996 Mw8.2 Biak Papua, the 1 January 1996 Mw 7.8 Donggala, the 24 January 2005 M6.2 Bora-Central Sulawesi and the 4 January 2009 Mw7.6 Manokwari-West Papua demonstrated how seismically active these regions are. Eventhough the Central and West Kalimantan have relatively low seismicity, felt earthquakes also hit these areas. Singkawang in West Kalimantan experienced 3 felt earthquakes in 2 consecutive days on August 2011 as well as the Muara Teweh in Central Kalimantan for an earthquake that happened in 1996. A number of historical and recent earthquakes presented above show that there is no place in Indonesia can be claimed as seismically not

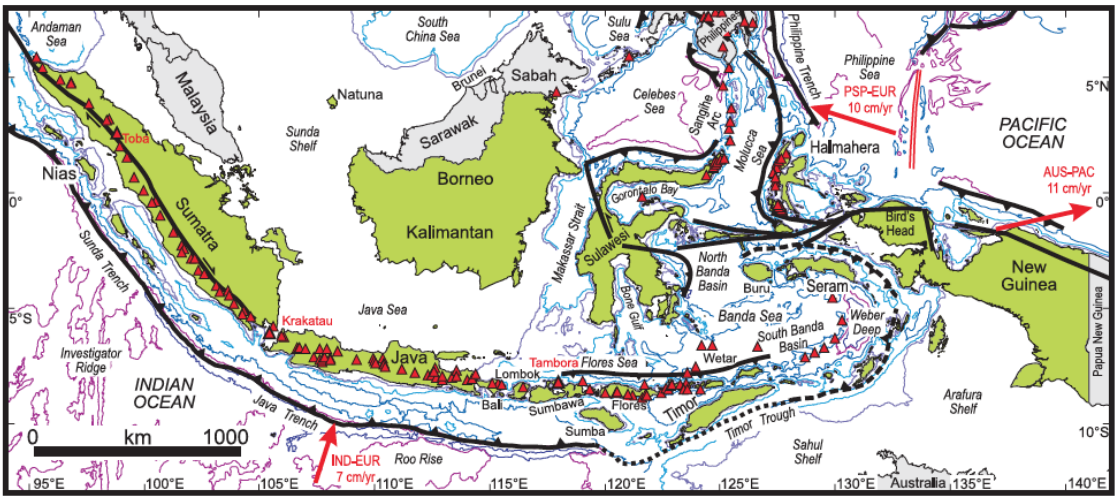

Figure 1.2: Tectonic setting and volcanic activity of Indonesian region. Red triangle indicates active volcano, while purple, light blue, dark blue, and red contour indicated bathymetric contour at 200 m, 1000 m, 3000 m, and 5000 m. Toothed, solid and dashed lines are subduction, strike-slip fault and through traces (Hall, 2009).

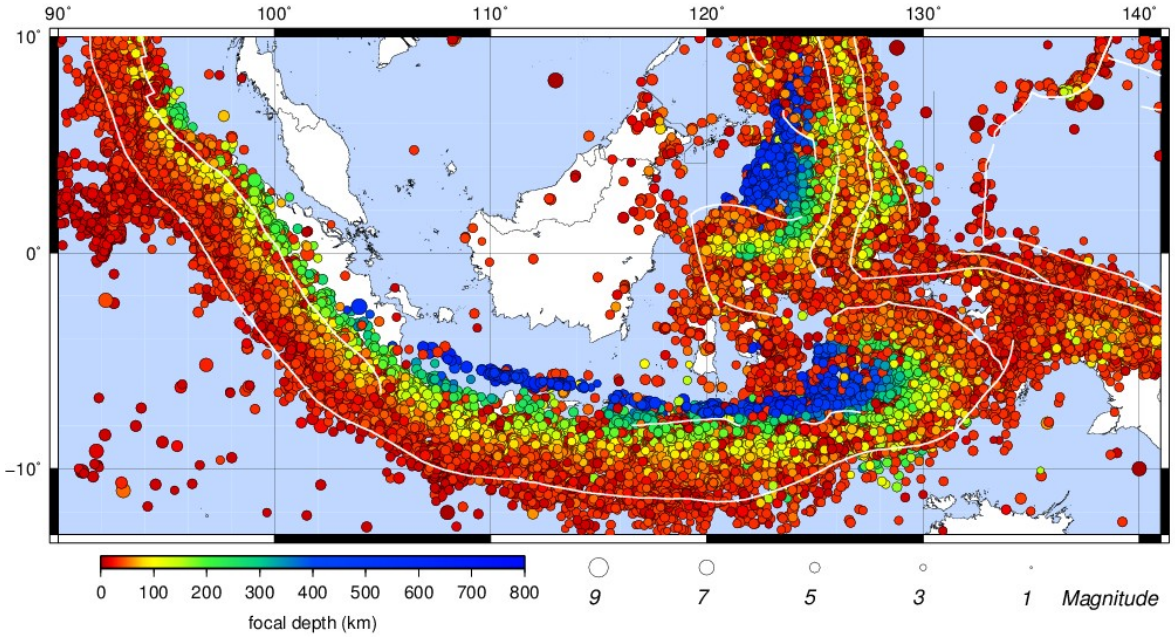

Figure 1.3: Seismicity of Indonesian Region in 1900-2014. Data taken from USGS (1900-2008). Focal depth and magnitude are indicated by color and size of circle while white lines indicate subduction margins and main active faults.

active.

Chapter 2

A Probabilistic Seismic Hazard Assessment for Sulawesi, Indonesia

Abstract: Quantifying the effects of site amplification is an essential component of probabilistic seismic hazard assessment. The average shear wave velocity in the topmost 30 m of soil, based on travel time from surface to the 30 m of depth (V_{S30}) is a parameter widely used in determining seismic site response. In this study, a V_{S30} dataset considering the geological condition of Sulawesi Island in Indonesia, is utilized to compute seismic ground motion. The high seismic activity rates observed from the Palu-Koro-Matano Fault System and in regions of distributed deformation contribute to the earthquake hazard along the south-west part of the island. Of particular concern is the seismic risk imposed on numerous cities including the provincial capitals of Palu and Goronalo, which sit on top of soft sedimentary basins where amplification of earthquake ground motions is imminent.

2.1 Introduction

The island of Sulawesi in central Indonesia (Fig. 2.1) is subjected to active deformation as it experiences recurring seismicity. To better understand the threat due to earthquakes faced by more than 17 million inhabitants of the island[*BPS*, 2010], characterizing the earthquake sources is an important step. The Ms7.4 Toli-toli earthquake in 1968 [*Pelinovsky et al.*, 1997] killed at least 200 people [*BNPB*, 2010] was the deadliest earthquake known to have occurred in this region. Although high-magnitude earthquakes have not occurred recently, the frequency of small magnitude events has contributed to an increasing number of fatalities and economic losses. In some area, local site effect significantly contribute to amplify seismic ground shaking that leads to increasing the scale of building damages and/or fatalities. The extension of faults offshore also opens the potential for earthquake and mass-movement generated tsunami.

Seismic hazard maps for the six provinces comprising the island of Sulawesi are published by the Geological Agency of Indonesia (Badan Geologi). These maps can be further improved by incorporating the effects of local site conditions. The correlation of geological and morphological data to site amplification produces the amplification needed for accurate estimates of ground motions. This, in turn would translate to better hazard maps for more effective disaster management plans, local spatial planning and seismic

resilient building design.

This chapter provides a brief review of the geology and seismotectonics of Sulawesi Island and its implications for seismic hazard assessment. The hazard assessment methodology and the input parameters used in the model are presented, and the the applicability of the Earthquake Risk Model (EQRM) software package is demonstrated. A key component in the modeling is the implementation of site class proxy methods proposed by *Matsuoka et al.* [2006] and *Wald & Allen* [2007] in estimating the amplification due to local site effects.

2.2 Geological and seismotectonic setting

Sulawesi consists of fragments of lithosphere that display a complex geological history of subduction, collision and local extension as shown in Fig. 2.1. The western and southern portions of Sulawesi are underlain by relatively strong, thick and cool lithosphere that was rifted from Australia and accreted to Sundaland in the Cretaceous period [*Hall*, 2011]. The southeast and eastern arms are derived from fragments of continental Australia, called the Sula Spur, which coalesced during the Miocene. The northern arm is a volcanic arc formed by subduction of the Sulawesi Sea since the early Miocene, along with thrusting of ophiolites onto the Sula Spur during collision [*Silver et al.*, 1983b; *Hall*, 2011]. The subduction polarity of the northern arm has reversed and at present, the Sulawesi Basin subducts southward beneath the north arm along the North Sulawesi Trench. A north-dipping slab east is reported along 122.6° [*McCaffrey & Sutardjo*, 1982]while the south-dipping slab extends deeper west of this coordinate.

The double-subduction zone situated to the east of the North Sulawesi Trench marks where the Molucca Sea Plate has sunk beneath the collision zone where continental lithosphere of the Phillipine Sea and Eurasian Plates meet [*Silver & Moore*, 1978]. Intense seismic activity is observed in this area, both within the slab and in the collision zone. Meanwhile, there are also deep earthquakes associated with the slab subducting beneath northern Sulawesi from the North Sulawesi Trench. There are also deep earthquakes observed in the vicinity of Una-una Volcano in the middle of the Gorontalo Basin (east of Gulf of Tomini depicted in Fig. 2.2, which *Simandjuntak* [1986] attributes to an westward extension of the subducted Molucca Sea Plate. This basin may represent an extensional zone as expressed in the sharp changes in topography from the mountains of Central Sulawesi, to the basin in the Gulf of Tomini, to the mountains of the North Arm [*Hall*, 2011]. Furthermore, low-angle detachment zones have been identified in the Tokorondo and Pompangeo Mountains in Central Sulawesi [*Spencer*, 2011]. Thrusting has also been observed along the SE section of the Tolo Thrust and western section of the Makassar Thrust. Based on seismic reflection proles of *Puspita et al.* [2005], the Makassar Thrust is a significant feature that extends up to the Palu-Koro Fault Zone located NW of Palu. This observation is consistent with the horizontal GPS velocities which are directed to the NW quadrant of the stable Sunda Block[*Sarsito et al.*, 2011].

Various studies have been conducted using blocks or micro-continents from GPS and gravity data to model the seismicity of Sulawesi [*Socquet et al.*, 2006; *Sarsito et al.*, 2011]. The number of blocks used was not clearly defined, however the availability of more data can lead to a more comprehensive seismic source zone model (*Sarsito*, 2011, pers. comm.). Block boundaries interpreted from GPS measurements match the location of major mapped faults including the Palu-Koro Fault Zone and the North Sulawesi Trench, while others are more speculative like the extension of the Poso Fault through the

Gorontalo Basin towards the West Molucca Sea Thrust *Socquet et al.* [2006]) suggested four strands of the Palu-Koro Fault covering a width of 50 km near Palu. Meanwhile, geological maps from Badan Geologi featured a highly faulted landscape, with numerous active seismic faults. Most of these structures however, have no information on activity rates or were not correlated with the GPS block models of *Sarsito et al.* [2011]. Such a scenario makes it challenging to include individual faults in the seismic hazard model. *Hall* [2011] suggested that the region is better interpreted as a continuum of weak lithosphere overlying a heterogeneous basement including areas of old and strong crust like West Sulawesi. The following are the challenges posed by this interpretation in the development of an earthquake hazard model for the region:

1. *Developing a source model that incorporates specific faults and background source zones.* IIncluding only the fault sources that accommodate the GPS velocities may lead to underestimation of hazard in areas with continuous and distributed deformation and overestimation along mapped faults if unmapped faults accommodate some of the relative motion. In the study, the model introduces active fault structures and distributed source zones in well-defined regions, backed up with sufficient information. This balances the seismic moment between fault and background sources based on recorded seismicity.

2. *Application of ground motion prediction equations (GMPEs) for different source regions.* The heterogeneous basement structure, including Sundaland and Australian continental crust, active island arc settings and subducted oceanic crust presents large differences in the ground motion propagation to be expected for regions of different geology. In addition, the paucity in data with which to constrain ground motion models makes the selection of the most suitable GMPE for each source region difficult.

2.3 Methods

2.3.1 Earthquake Hazard Modeling

The Earthquake Risk Model (EQRM), an open-source software developed by Geoscience Australia [*Robinson et.al.,*, 2006], is the application used for the seismic hazard modelling in this study. EQRM generates a synthetic earthquake catalogue based on input parameters defining the recurrence and geometry of earthquake sources. Earthquake recurrence is defined using the classic Guttenberg-Richter model [*Youngs & Coppersmith*, 1985; *Kramer*, 1996] or the characteristic earthquake model [*Schwartz & Coppersmith*, 1984]. The geometric representations often used to define a seismic sources include zone sources, faults or intraslab sources.

Zone sources are geographic polygons wherein the minimum and maximum depths are specified. Synthetic ruptures occur randomly within this zone with strike and dip values randomly sampled using a uniform distribution. Fault sources are rectangular planes described using information on up-dip surface projection of the fault trace. Synthetic rupture centroids are randomly distributed on the plane whereas its orientation is dictated by the fault geometry. Like fault sources, intraslab sources follow a planar geo-metry, however the individual synthetic events are allowed to rupture at out-of-plane angles. This allows a realistic simulation of focal mechanisms along subducting slabs wherein the uncertainty of out-of-dip rupture can be estimated.

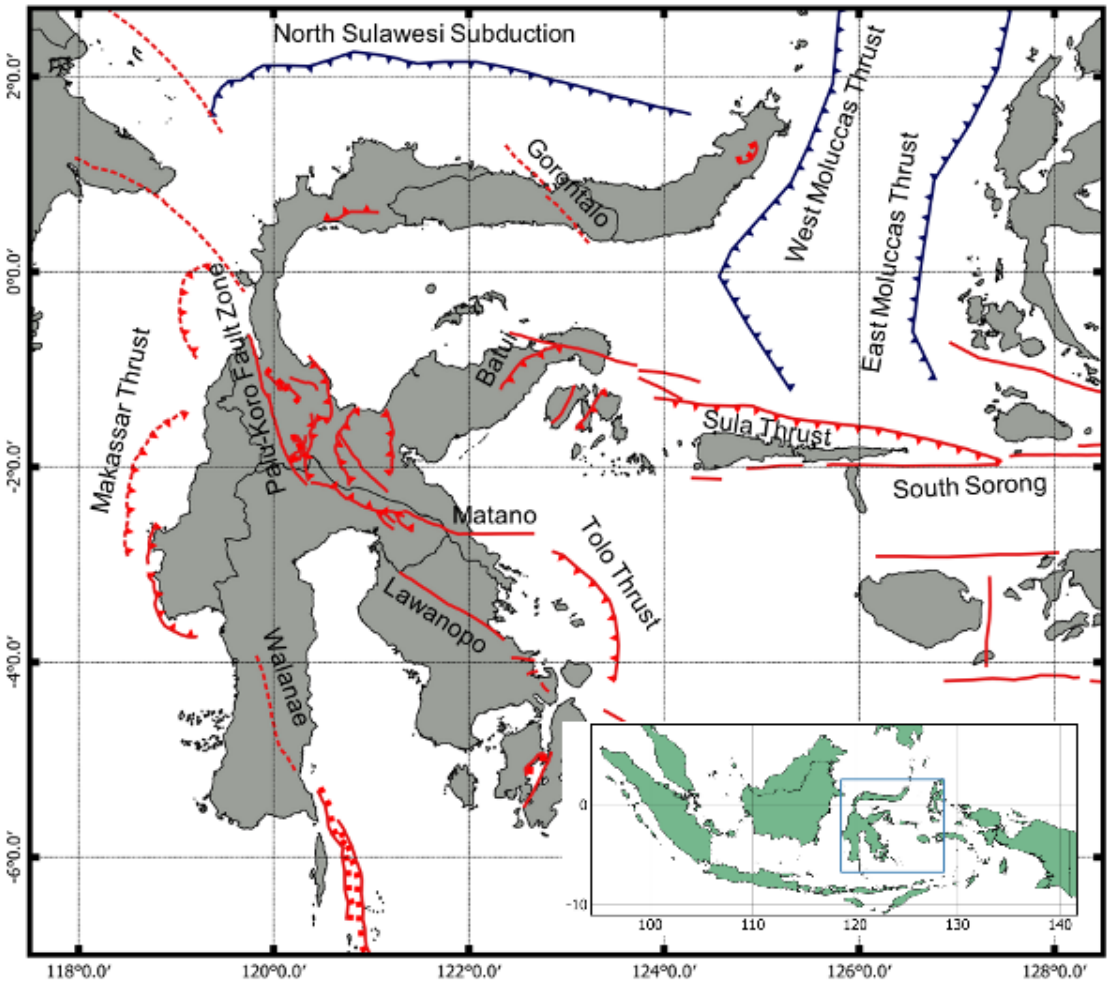

Figure 2.1: Map of the main active faults of the Sulawesi region. Inset map shows location of Sulawesi Island within Indonesian Archipelago.

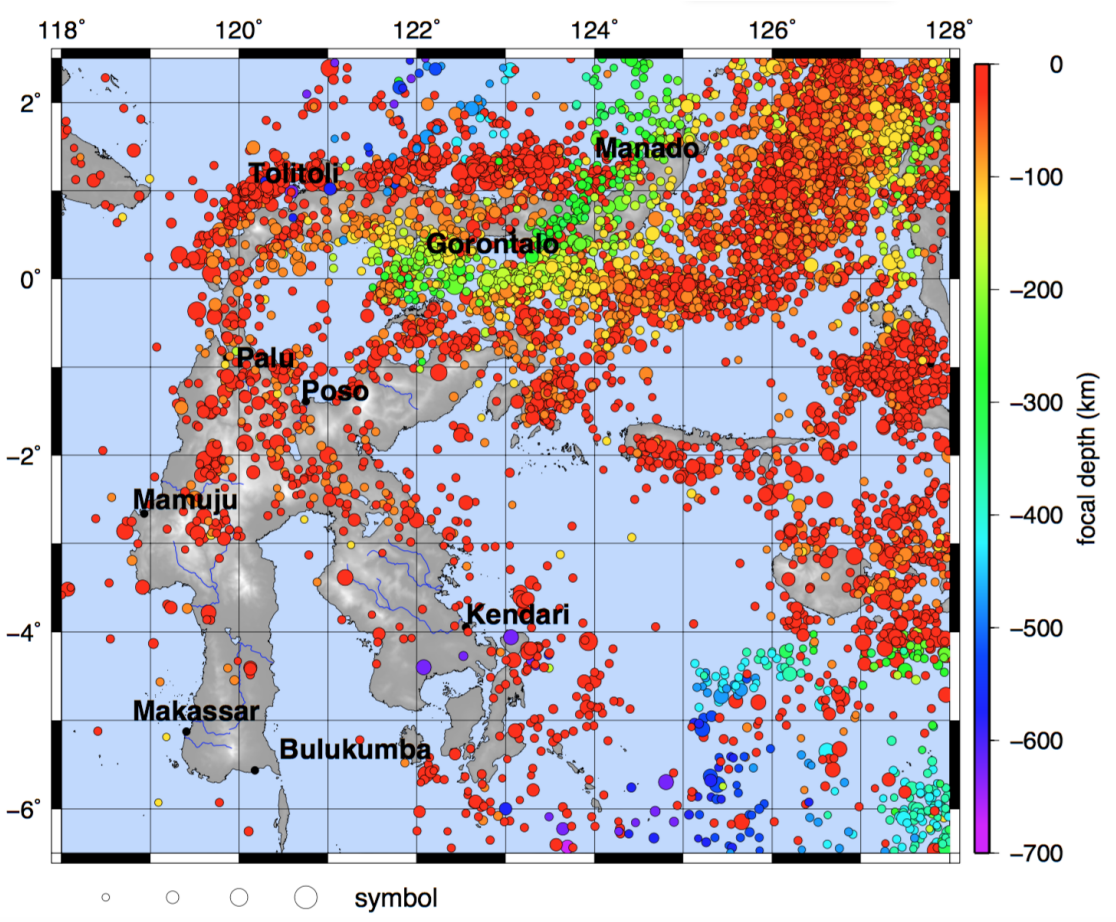

Figure 2.2: Map of the distribution of earthquake epicentres. Major cities are labelled

2.3.2 Input Parameters

Catalogue and background crustal source zones

The earthquake catalogue from the International Seismological Center (ISC) was used and de-clustered using the Seisan software package [*Ottemöller et al.*, 2011]. The events in this catalogue were categorized based on focal depth including shallow crustal events (depth $\leq$ 35 km), intraslab events (depth $>$ 35 km) and megathrust events. It was assumed that this catalogue is complete for crustal and intraslab events for magnitudes greater than M_w 4.8 and M_w 5.0, respectively. For these events, the b-values for the Gutenberg-Richter model were calculated using the maximum likelihood method [*Aki*, 1965]. Activity rates (λm_0) above the magnitude of catalogue completeness m_0 were calculated based on the average annual number of events above m_0 within each source zone. We used both approaches by giving 1/3 and 2/3 of weighing for the Gutenberg-Richter and characteristic, respecitively, for all source zones, except for background source zone. the Gutenberg-Richter model is used to estimate earthquake reccurence for background source zone.

Crustal earthquakes within 10 km of mapped active faults were assumed to occur on these faults, allowing for hypocentre location errors [*Husen & Hardebeck*, 2010]. These were excluded from the background zone analysis. Major crustal-scale faults were used as boundaries for the source zones, including the Palu-Koro and Matano faults. Maximum

magnitude (M_{max}) for background crustal source zones is set to 7.5 as it is likely that there are large seismic structures capable of producing earthquakes of this size which are not taken into account in the fault source model. Focal mechanisms from the Global Centroid Moment Tensor (GCMT) catalogue were used to determine faulting type and to infer the geometry of fault structures with background zones.

Four background zones were defined: the Sulawesi Zone, the Sulawesi Barat, the Sulawesi Selatan and the Sulawesi Baratdaya zones. The Northern Sulawesi Zone is bounded to the south and west by the Palu-Koro-Matano Fault, to the north by the North Sulawesi Trench and to the east by the West Moluccas Sea Thrust. It is characterized by the crust undergoing high shear strain resulting from the clockwise rotation of the Sula Block along the Palu-Koro-Matano fault system. A number of strike-slip faults are present within the zone, including the Poso and Gorontalo faults and the eastern strands of the Palu-Koro Fault zone [*Socquet et al.*, 2006]. Extension is probably occurring within the Gorontalo Bay [*Hall*, 2011] and this structure may connect the Poso Fault to the Gorontalo Fault and West Moluccas Thrust. In addition, this structure also defines a boundary in *Sarsito et al.* [2011]'s block model. There is also thrusting to the east along the Batui Thrust. The whole area is seismically active, making further delineation of specific structures difficult without more detailed fault studies. As shown in Fig. 2.3, the high background activity rate means lack of resolution of specific faults should not adversely affect the results of the seismic hazard assessment.

The West Sulawesi Zone encompasses the seismically active region west of the Palu-Koro Fault zone and east of the Makassar Thrust. As above-mentioned, many faults are delineated on geological maps but information on activity rates are not available. The Southwest Sulawesi Zone is a seismically quiet zone along the south-western arm of Sulawesi and is bounded on the east by the Bone Gulf. This area consists of continental crust which is not actively deforming. The Walanae Fault crosses this structure with low reported slip rates of approximately 2 mm/year [*Irsyam et al.*, 2010]. The Southeast Sulawesi Zone is bounded to the north by the Matano Fault, to the east by the Tolo Thrust, and to the west by the Bone Gulf. The Lawanopo Fault crosses this zone and the reported activity rates are lower than the North and West Sulawesi Zones.

Fault sources

We used a reference fault model based on the 2010 revision of Indonesia's national seismic hazard map [*Irsyam et al.*, 2010]. Several fault sources were modified to take into account new data regarding fault locations, geometry and earthquake recurrence. Furthermore, where fault sources were located within background source zones, fault-source slip rates were derived using geological or geodetic methods (S_g). (S_g) were reduced by the equivalent slip rate from the activity rate of the background source model. The seismic moment rate (M^T) is related to the shear modulus (μ), fault area (A_f) and slip rate (S) using the Eq. 3 in *Youngs & Coppersmith* [1985] as follow:

$$M^T = \mu A_f S \tag{2.1}$$

The Gutenberg-Richter magnitude distribution, which describes the rate of seismicity and hence the seismic moment rate, can be used to relate the slip rate to the seismic activity rate. The background seismicity rate is used to calculate an equivalent slip rate for the fault that lies within it by rearranging the *Youngs & Coppersmith* [1985] equation:

$$S_\lambda = \frac{b\lambda^f_{m_0} M_0^{max-\beta(m_{max}-m_0)}}{\mu A_f (c-b)(1-e^{-\beta(m_{max}-m_0)})} \tag{2.2}$$

Where S_λ is the estimated slip-rate for the fault derived from background seismicity only, M_0^{max} is the moment of the maximum magnitude earthquake (m_{max}) for the background zone, c = 1.5 from the moment magnitude definition of *Hanks & Kanamori* [1979] and $\beta = 2.303$, and $\lambda^f_{m_0}$ represents the activity rate of the source zone (λ_{m_0}) scaled using a 10 km buffer around the fault

$$\lambda^f_{m_0} = \frac{\lambda^f_{m_0} V_{buffer}}{V_{zone} - V_{buffer}} \tag{2.3}$$

Therefore the final input slip rate for the fault is indicated:

$$S = S_g - S_\lambda \tag{2.4}$$

For some seismic fault sources, the reported slip rates were lower than that the calculated value based on seismicity, yielding a negative slip rate value. This demonstrates the challenge in characterizing individual faults for seismic hazard assessment within a zone of high shear strain and seismicity. However, as these active faults exist, these sources with nominal slip rate of 2 mm/year, were included in the analysis which may result to overestimation of total seismic moment rate as compared with that derived purely from seismicity (though we cannot be sure due to incompleteness of the instrumental catalogue).

Fault input parameter

The fault parameters used in this study are shown in Table. 2.1. A brief summary of the key differences between this paper and the parameters used in *Irsyam et al.* [2010] is also given.

Minahasa (North Sulawesi) Trench: This fault is mapped at the trench axis as observed from the bathymetry data [*Silver et al.*, 1983a; *Irsyam et al.*, 2010]. Although a few thrust events have occurred on this fault, the majority of the thrust events are located 50-100 km to the south. Focal mechanisms as depicted in Fig. 2.4, show steeper thrusting in the east (with average dip 24°) than the west (average dip is 18°). This is consistent with *Silver et al.* [1983a] who observed a steeper frontal slope in the east using seismic reflection profiles. These data show a shallow dipping main thrust plane with steeper splay faults in the overriding wedge, including north-dipping structures in the eastern section of the fault [*Silver et al.*, 1983a].

It is unclear whether the lack of earthquakes near the trench is due to the strain not being accumulated within weak sediments *Wang & Hu* [2006] or these sediments are slowly accumulating strain and could potentially host a large earthquake as has been observed in the 2004 Great Sumatra-Andaman Earthquake (where there is a thick sedimentary wedge; *Gullick et al.* [2011]). If it is the latter, then this fault can also be treated as a tsunamigenic fault source. However, as short-period ground motions generated by subduction interface earthquakes decrease rapidly with distance (e.g. *Youngs et al.* [1997]), we place the source fault landward of the trench axis in order to reproduce as accurately as possible the observed seismicity on the main section of the subduction interface. The fault plane is modeled at a dip angle of 21° but the synthetic events were allowed to thrust out of this plane by randomly sampling a uniform distribution of dips between 11°–43°. Events rupturing out-of-plane were further constrained to extend a maximum of 5 km

Table 2.1: Summary of faults parameters used in this paper and *Irsyam et al.* [2010]

Fault	Slip rate (mm)		M_{max} (M_w)		Fault	A-, b-values
	Irsyam	this paper	Irsyam	this paper	type	
North Sulawesi			8.20	8.20	M	4.820, 0.914
Palu-Koro	30 (0.25)	35	7.94	7.90	SS	- , 0.950
	35 (0.50)				SS	
	45 (0.25)				SS	
Poso	2	2	6.93	6.90	SS	- , 0.950
Matano	37 (0.50)	41	7.90	7.90	SS	- , 0.950
	44 (0.50)				SS	- , 0.950
Lawanopo	25	20.3	7.59	7.00	SS	- , 0.950
Walanae	2		7.53	-	SS	- , 0.950
Walanae North		1.7		6.60	SS	- , 0.950
Walanae Middle		1.7		6.60	SS	- , 0.950
Walanae South		1.7		6.60	SS	- , 0.950
Gorontalo	11	5	7.06	7.60	SS	- , 0.950
Batui	2	2	7.06	7.30	R	- , 0.950
Tolo	9 (0.50)	14	7.94	7.50	R	- , 0.950
	19 (0.50)					- , 0.950
Makassar	4 (0.50)	9	7.46	7.50	R	- , 0.950
	13 (0.50)					- , 0.950
Sula	10	14	7.19	7.70	R	- , 0.950
W. Moluccas	13	13	8.47	7.90	R	- , 0.950
E. Moluccas	29	13	8.47	8.10	R	- , 0.950
Intraslab						
Intraslab 1	-	-	-	-	I	0.690, 1.210
Intraslab 2A	-	-	-	-	I	1.100, 1.210
Intraslab 2B	-	-	-	-	I	5.200, 1.210
Intraslab 3	-	-	-	-	I	1.900, 1.210
Intraslab 3A	-	-	-	-	I	6.080, 1.210
Intraslab 3B	-	-	-	-	I	6.675, 1.210
Intraslab 4A	-	-	-	-	I	8.125, 1.210
Intraslab 6	-	-	-	-	I	15.575, 1.210
Intraslab 6A	-	-	-	-	I	12.600, 1.210
Intraslab 6B	-	-	-	-	I	23.625, 1.210
Background Seismicty Zones						
Sulawesi	-	-	-	7.50	C	10.825, 0.950
Sulawesi T	-	-	-	7.50	C	2.925, 0.950
Sulawesi B	-	-	-	7.50	C	1.100, 0.950
Sulawesi BD	-	-	-	7.50	C	0.175, 0.950

Note: M, SS, R, and I are megathrust, strike-slip, reverse and intraslab, respectively. Values in the brackets are weighing value.

from the fault plane, whereas the fault width is approximated at 100 km with a maximum depth of 35 km.

Batui Thrust: Recent work using high resolution multi-beam bathymetric and seismic data enabled the re-assessment of the tectonics in the region [*Watkinson et al.*, 2011]. Although there was no evidence for the Batui Thrust as previously mapped to the north of Poh Head [*Silver et al.*, 1983a; *Irsyam et al.*, 2010], this fault is assumed to occur as a thrust zone to the south-west of the Poh Head Peninsula. We follow this new interpretation of the location of the Batui Thrust in this study. Slip rates of 2 mm/year based on I*rsyam et al.* [2010] are poorly constrained. However, in the absence of further information, this estimated rate is used in this study, which is lower than that calculated from background seismicity in the surrounding source zone.

Balantak Fault: This fault is a right lateral strike-slip structure that cuts Poh Head to the north of the Batui Thrust. It has a clear geomorphic expression and has been associated with recent seismicity [*Watkinson et al.*, 2011]. This fault is not included in *Irsyam et al.* [2010] and there are no available data on slip rates. Hence, this seismic fault is not included in our assessment.

Makassar Thrust: *Irsyam et al.* [2010] included this fault offshore of the western bulge of Sulawesi near the city of Majene. In this study, we extend this thrust fault to the north to meet the Palu-Koro Fault Zone, north-west of Palu as inferred from the seismic reflection profiles of *Puspita et al.* [2005]. These profiles suggest the thrusting offshore of West Sulawesi. However, it is not obvious if this is a continuous structure or a number of segmented thrust faults and fold zones.

Irsyam et al. [2010] also identified other active fault structures throughout Sulawesi that were not included in their hazard model due to lack of information on slip rates. In addition, the active fault database of the Geological Agency of Indonesia also contains numerous mapped structures, many of which are discernable as topographic lineaments using the Shuttle Radar Topography Mission (SRTM) Digital Elevation Model. In the absence of geological and geodetic data to constrain the slip rates and identify the seismically active faults, the source zones covering areas of distributed deformation are used instead.

Intraslab sources

Deep seismicity is visible throughout northern Sulawesi as a result of the complex system of active and inactive subduction systems previously defined. Although much of the deep seismicity can be explained through these systems, the catalogue also contains a number of enigmatic events which are difficult to assign to any structures and suggest a complex pattern of Cenozoic collision not fully understood. Identifying structures is further complicated by the hypocentre depth uncertainties of up to 25 km in the catalogue [*Husen & Hardebeck*, 2010]. In this instance, we define a number of intraslab sources that fit the geological interpretations of the area.

Ground motions models

At present, Indonesia is yet to develop a ground motion prediction equation (GMPE) based on local strong motion data, although recently, there have been initiatives in deriving a GMPE using the new strong motion accelerometer network deployed by the Indonesian Meteorology, Climatology and Geophysics Agency (BMKG). At present time, this undertaking is still in progress and results are not yet available [*Rudyanto*, 2013]. However, the author mention that out of 9 investigated GMPEs, *Youngs et al.* [1997] and

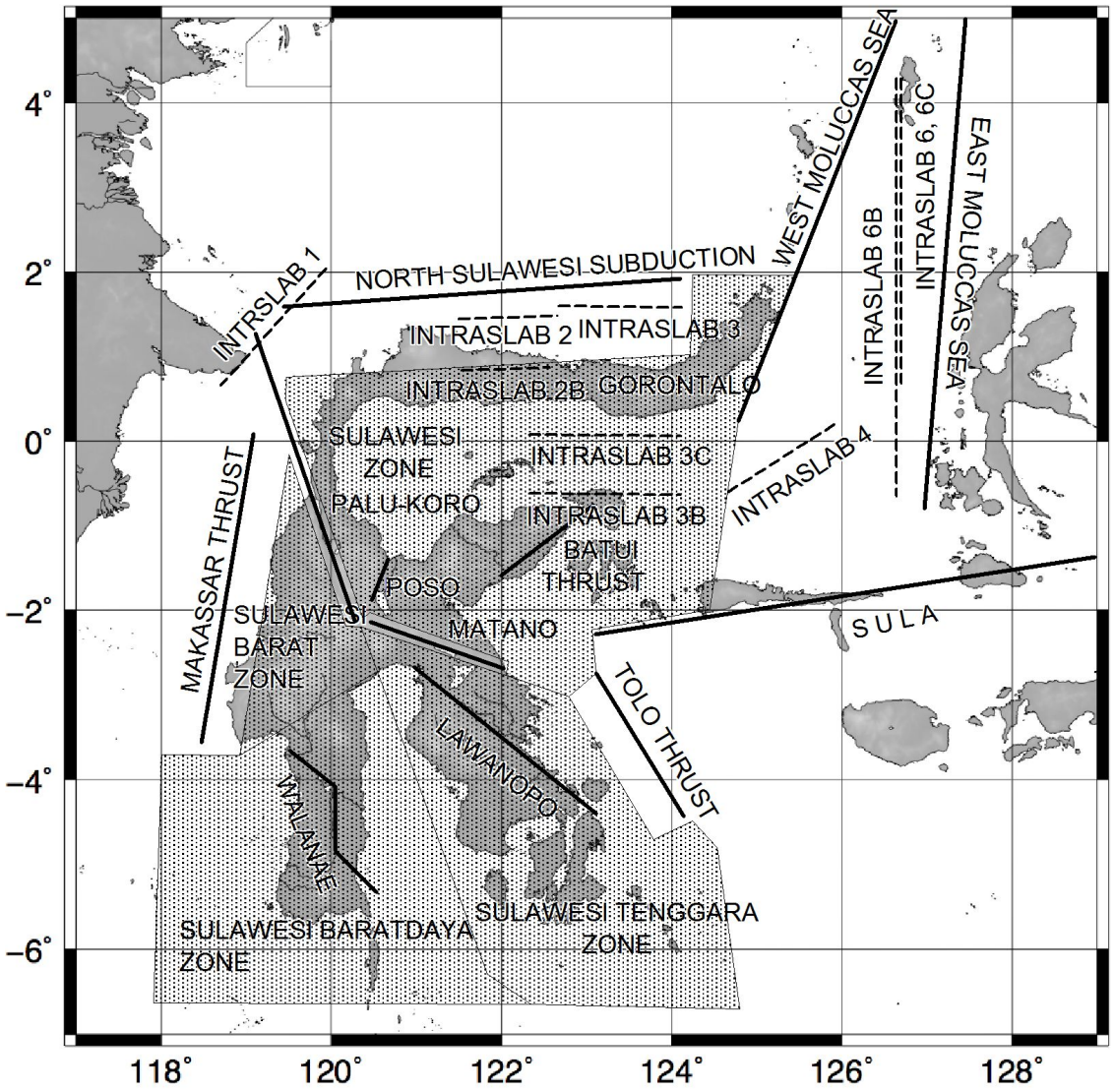

Figure 2.3: Fault sources, intraslab sources (updip surface projection of slab trace) and background source zones

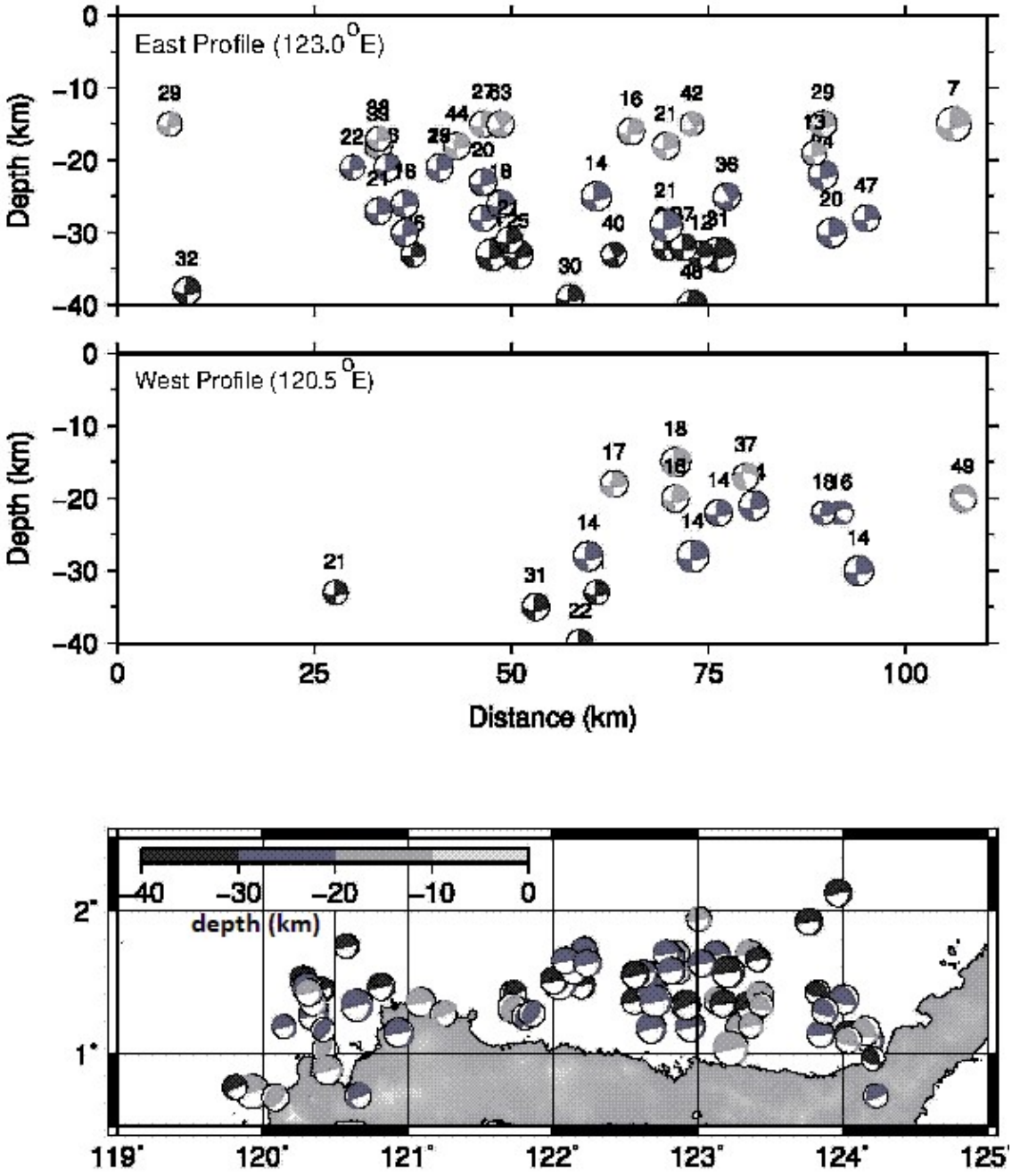

Figure 2.4: Focal mechanisms for the Minahasa Trench along north–south profiles showing steeper average dips in the west than in the east. Numbers over each beachball in the upper and middle panels indicate the dip.

Zhao et al. [2006] are the most capable for Indonesian setting. In this study, we used GMPE as summarized in Table. 2.2.

Table 2.2: GMPEs and logic tree used for seismic hazard simulations

Region	Ground-motion model	Weight
Crustal	*Boore & Atkinson* [2008]	0.33
	Campbell & Bozorgnia [2008]	0.34
	Chiou & Youngs [2008]	0.33
Subduction interface	*Youngs et al.* [1997]	0.25
	Atkinson & Boore [2003]	0.25
	Zhao et al. [2006]	0.50
Intra-slab	*Atkinson & Boore* [2003] - Cascadia seismicity	0.33
	Youngs et al. [1997]	0.34
	Atkinson & Boore [2003] - worldwide seismicity	0.33

Site amplification

Table 2.3: Geomorphological unit classification, simpilified from *Matsuoka et al.* [2006]

Slope (°)	Elevation (m)	Lithology	Geomorphological unit *Matsuoka et al.* [2006]	Notes
>15	> 700	Pre-Tertiary rocks	Pre-Tertiary mountain	
		Tertiary rocks	Tertiary mountain	
	< 700	Tertiary rocks	Hill	
		Volcanic	Volcanic hill	
5–15		Non-volcanic	Mountain footslope	
		Volcanic	Volcanicn footslope	
≤5		Alluvium, colluvium, fluvial and other terrestrial deposits	• valley bottom lowland • alluvial fan • back marsh • abandoned river channel • delta & coastal lowland • marine sand & gavel bars	
Active volcano		volcanic rocks	Volcano	Eruption centers
Terrace		• brecciated rocks	• Rocky strath terrace	geological structure
		• alluvium	• Gravelly terrace	geological structure
		• volcanic ash	• Terrace covered by volcanic ash soil	geological structure
5–15		Loose sand mud, sand, gravel, etc	Sand dune • reclamied land • fille+d land • natural leeve	

Amplification of seismic waves in shallow soil near the surface can contribute significantly to variations in seismic hazard in areas exposed to seismic sources. To apply site amplification to a regional scale hazard assessment in Sulawesi where field measurements are limited, proxy methods are used to estimate the average shear wave velocity in the upper 30 m of the earth (V_{S30}). Estimated V_{S30} values are either incorporated

into selected GMPEs or classified into the NEHRP site classes and amplification factors [*Borcherdt*, 1994]. These are used to scale ground motion estimates for each site.

Two proxy methods are used in estimating V_{S30} : (**a**) the *Wald & Allen* [2007] method and (**b**) the *Matsuoka et al.* [2006] method. Computation of V_{S30} based on *Wald & Allen* [2007] uses topographic slope using empirical relations derived using data from California and Taiwan. A global grid of V_{S30} is generated through the global SRTM topography, accessible online from the USGS Global V_{S30} server. The *Matsuoka et al.* [2006] method proposes an empirical function that relates geomorphology, elevation, slope and distance from hills and mountains in the computation of V_{S30} as mathematically describe:

$$logV_{S30} \;=\; a \;+\; b\, logEv \;+\; c\, logSp \;+\; d\, logDm \pm \delta \tag{2.5}$$

where $Ev, SpDm$ are elevation (m), 1000 × tangent of slope and distance from Pre- or Tertary mountain or hill. Value of a, b, c and d are presented in Table 3 of [*Matsuoka et al.*, 2006].

Empirical factors for this approach were derived from field measurements obtained in Japan. Table 2.3 provides the list of geomorphological unit classification for this method. Empirical estimates from these methods were compared against field measurements of the response spectral ratio from recorded ambient noise measurements corresponding to horizontal and vertical components of seismograms (HVSR).

Geomorphological and geological maps published by the Geological Agency of Indonesia from 1973 to 1998 were used along with the SRTM topography data to classify Sulawesi's geomorphology. Sulawesi is divided into 14 geomorphic units using the *Matsuoka et al.* [2006] scheme. Of these, the classes of pre-Tertiary mountain, tertiary mountain, hill, mountain footslope, volcanic footslope and volcano cover more than 75% of the island's area. These classes of geomorphic units are situated in steep and elevated areas subject to erosion, where the ground surface is assumed to be composed of hard and compacted material with high average V_{S30} values. On the other hand, the V_{S30} is lower for volcanic than non-volcanic mountains –this key distinction is useful for Indonesia. The remaining 25% of Sulawesi Island is characterized by undulating or flat morphology where sediments are accumulating.

Fig. 2.5 shows the geomorphological classification of Sulawesi using *Matsuoka et al.* [2006] and the corresponding V_{S30} values. High V_{S30} estimates (equivalent to NEHRP site class A and B) correspond to mountainous areas. Footslopes and volcanic areas have moderate V_{S30} (NEHRP site class C). Lowland areas including valleys, deltas and coastal areas have lower V_{S30} values (NEHRP site class D and E).

The V_{S30} estimated using the slope-topographic [*Wald & Allen*, 2007] and geomorphic [*Matsuoka et al.*, 2006] methods are compared with calculated V_{S30} from ambient noise field measurements in the cities of Gorontalo, Palu and Manado. Measurement locations were categorized based on *Matsuoka et al.* [2006] scheme, which include volcanic footslope, mountain footslope, valley bottom lowland and delta/coastal lowland.

HVSR curves were collected from a single three-component 1 Hz L4-3D seismometers deployed at each site. Noise was recorded for approximately 20 minutes and the spacing between measurements is around 1-2 km. The fundamental frequency of HVSR is determined using the Geopsy processing software. This is used in estimating the V_{S30}

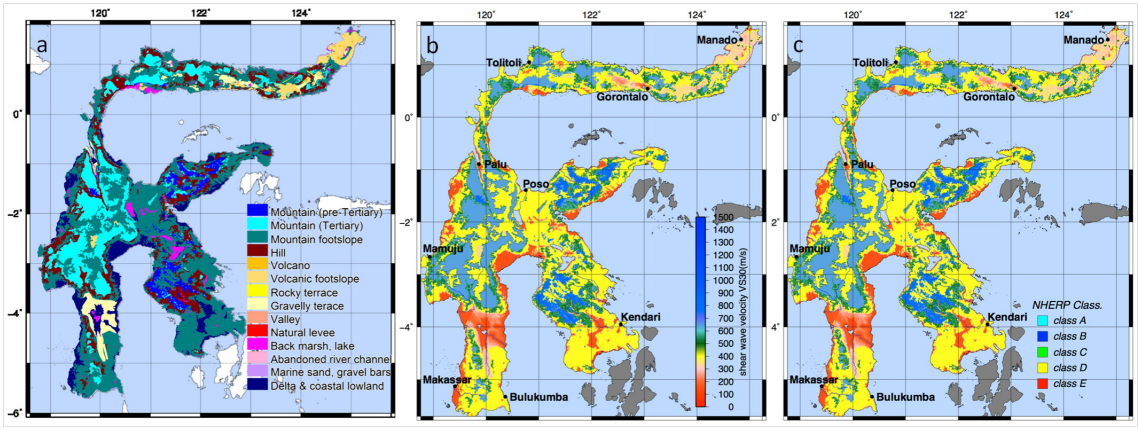

Figure 2.5: (a) Geomorphology of Sulawesi using the *Matsuoka et al.* [2006] classification, (b) V_{S30} values for Sulawesi derived from the Matsuoka et al. (2006) method (higher V_{S30} values are indicated in blue and lower V_{S30} values are indicated in red (right)) and (c) NEHRP's soil classification.

based on the empirical equation proposed by *Zhao* [2011]; *Zhao & Xu* [2013].

$$V_{S30} = T \times 120 \tag{2.6}$$

Such equation relates the site period (TV_{S30}) to V_{S30} , assuming bedrock is reached at 30 m depth. In the process, it was assumed that the site period and V_{S30} are correlated and that the fundamental period of the HVSR is equivalent to TV_{S30} . This however, introduced a large degree of uncertainty, aside from taking V_{S30} as the predictor variable for site effects. Nevertheless, the method is more robust for shorter site periods [*Zhao*, 2011]. Correspondingly, V_{S30} values are classified into NEHRP site classes from *BSSC* [2003].

Depicted in Fig. 2.6 are the histograms reflecting the comparison between V_{S30} values from proxy methods and field measurement. The proxy methods yield higher estimates than those computed from HVSR measurements. The V_{S30} estimated using the *Wald & Allen* [2007] method (222 ± 212 m/s) are about twice as much as the *Matsuoka et al.* [2006] method (102 ± 194 m/s).

In terms of site classification, the higher estimates of V_{S30} using the *Wald & Allen* [2007] method means that this method is more likely to correctly assign site class C while the *Matsuoka et al.* [2006]) method is more likely to correctly assign site class D as shown in Fig. 2.6. The latter yields the same site class compared with the V_{S30} from HVSR measurements [*Zhao*, 2011] at approximately 25% of the measured locations compared with the former which resulted in the same site class at 15% of the measured sites as shown in Fig. 2.7.

2.4 Hazard modeling results

Using the EQRM, the ground acceleration corresponding to every point on a 1×1 km grid is computed for all return periods and spectral periods. The results are useful in updating the seismic design code for seismically resilient buildings and infrastructure. For spatial planning purposes at the local scale and for construction of non-engineered buildings, the expected felt seismic intensity is a simpler and more easily communicated

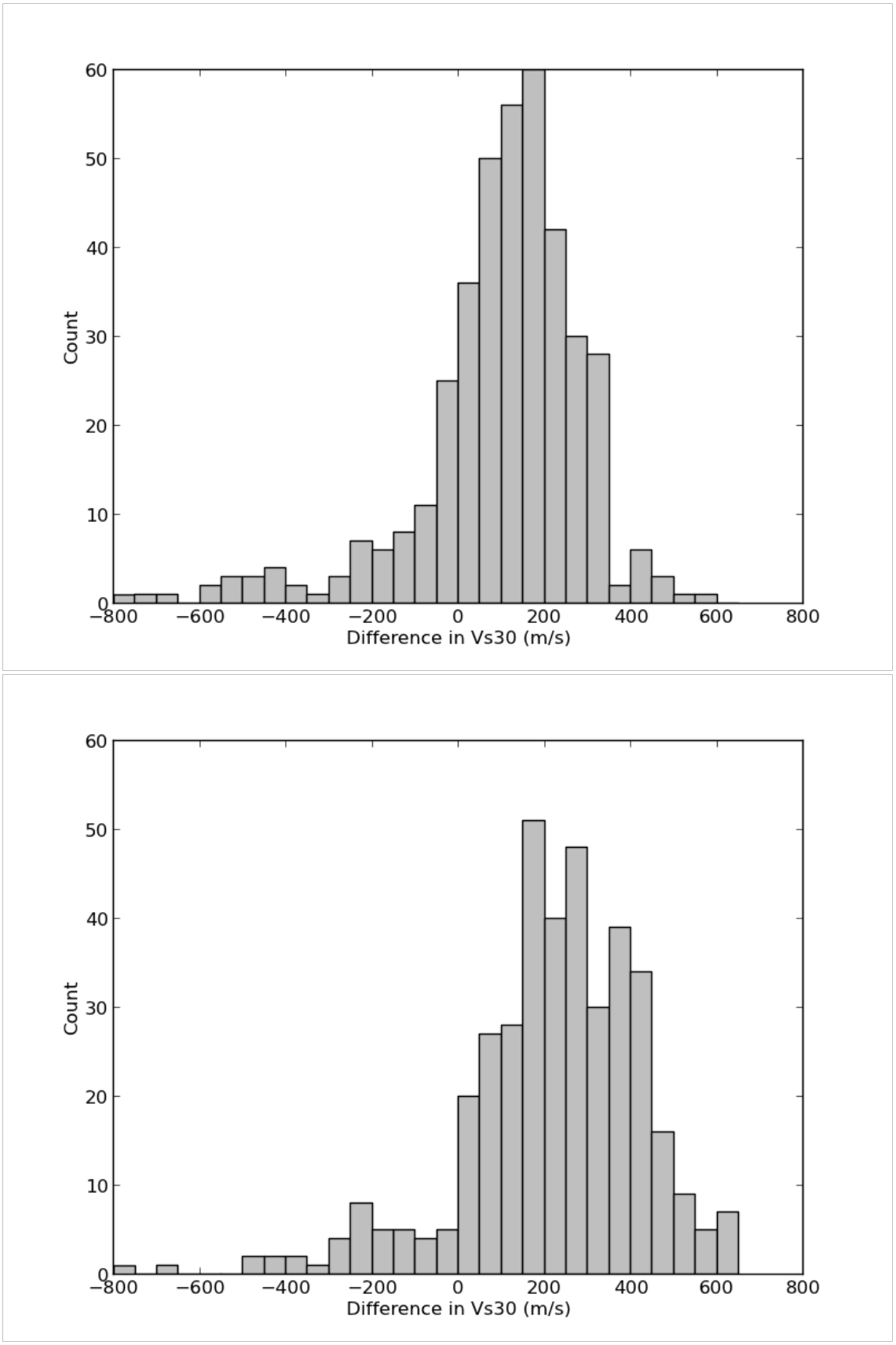

Figure 2.6: Histogram of differences in V_{S30} values for (a) the Matsuoka et al. (2006) method minus HVSR-derived measurements, and (b) the United States Geological Survey [*Wald & Allen*, 2007] method is subtracted by V_{S30} derived from measured HVSR.

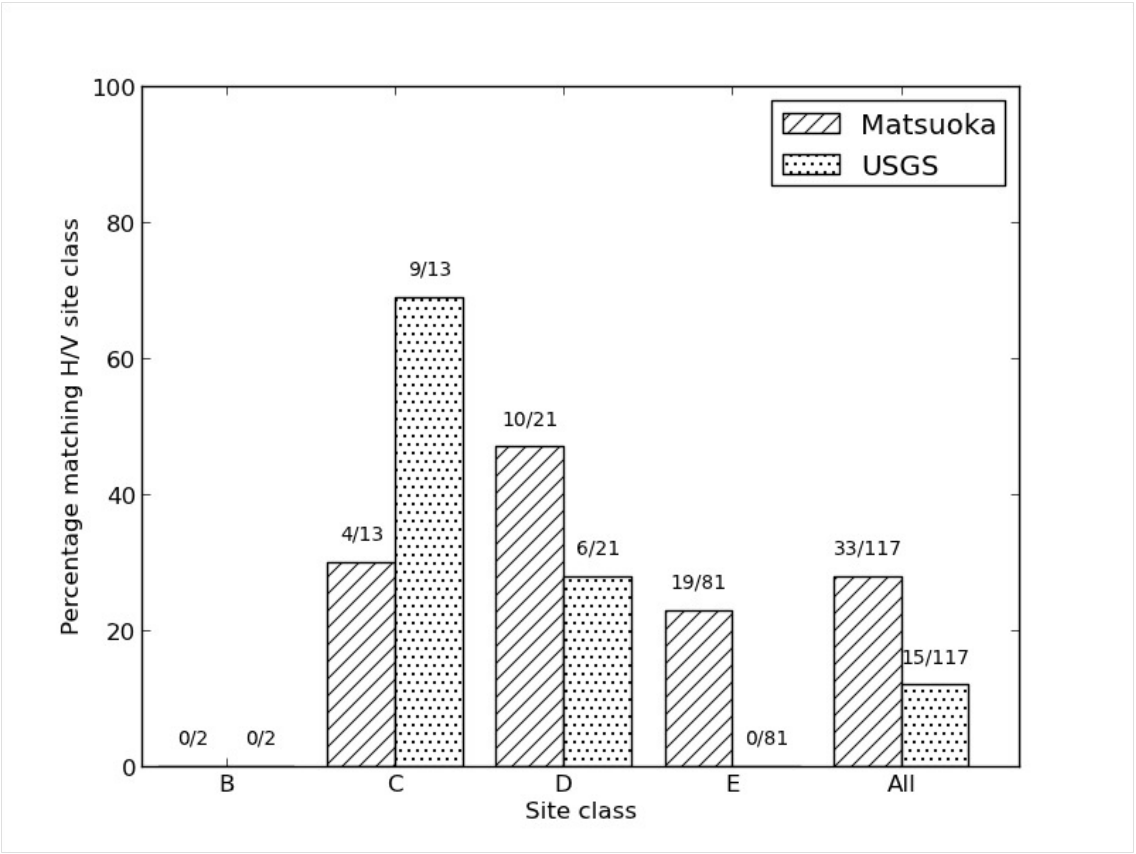
Matsuoka
USGS
Percentage matching H/V site class
Site class
B
C
D
E
All
0
20
40
60
80
100
0/2
0/2
4/13
9/13
10/21
6/21
19/81
0/81
33/117
15/117

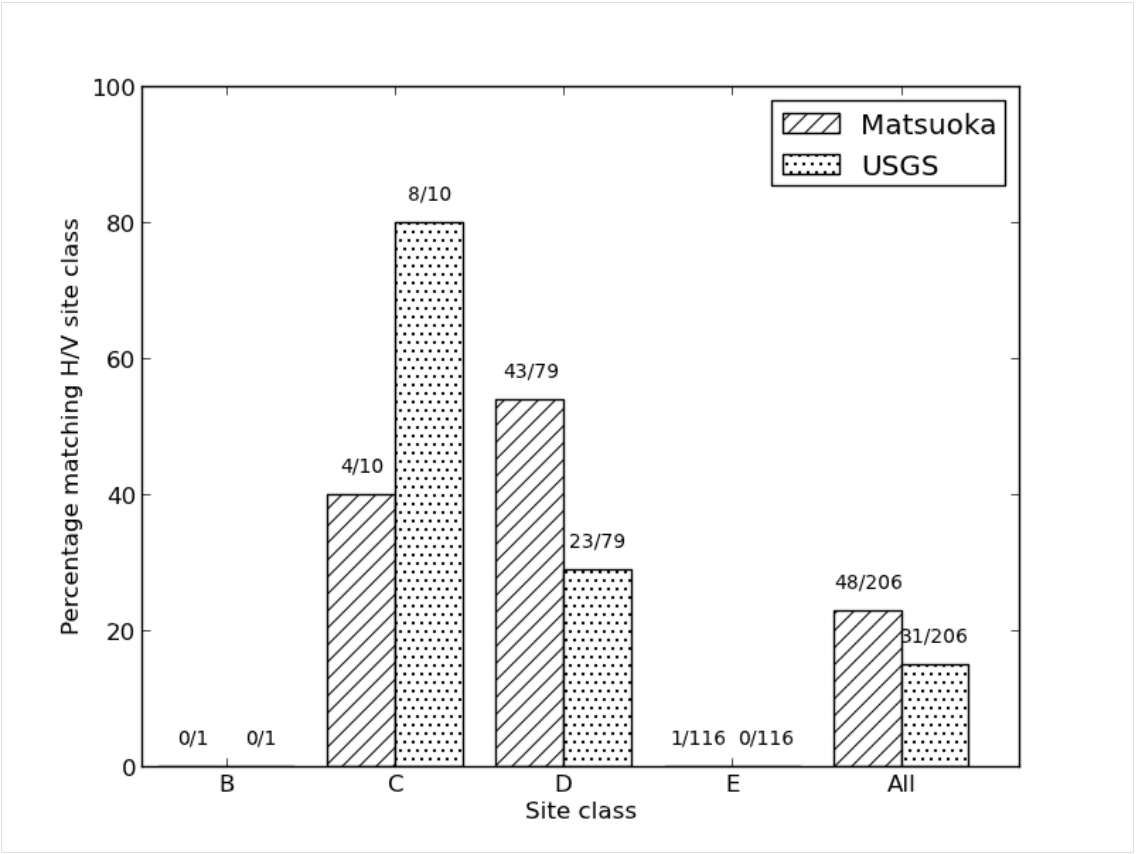
Matsuoka
USGS
Percentage matching H/V site class
Site class
B
C
D
E
All
0
20
40
60
80
100
0/1
0/1
4/10
8/10
43/79
23/79
1/116
0/116
48/206
31/206

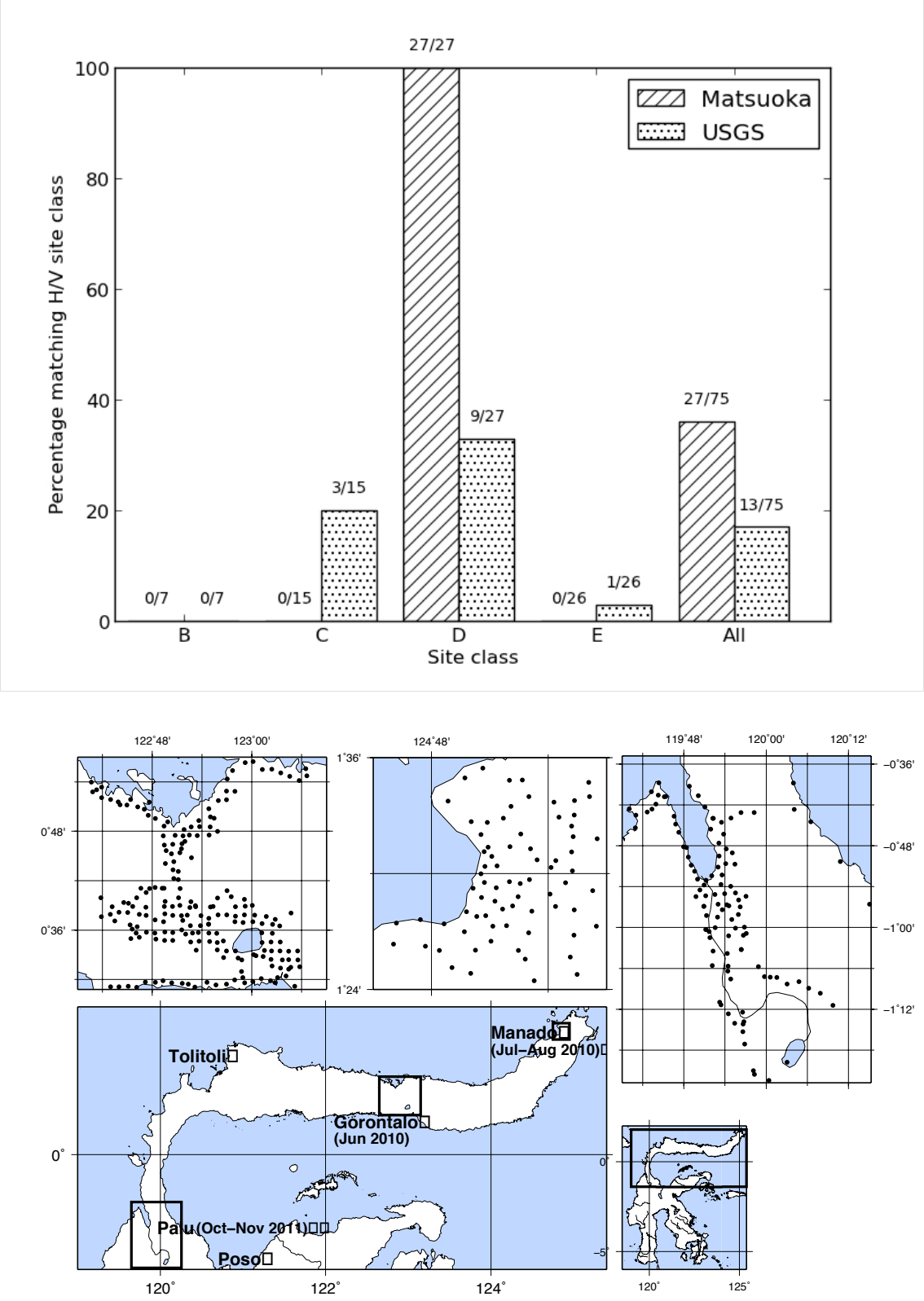

Figure 2.7: Comparison of Matsuoka et al. (2006) and United States Geological Survey [*Wald & Allen*, 2007] proxy estimates of site class with those derived from HVSR measurements using the Zhao (2011) method for (a) Palu, (b) Gorontalo and (c) Manado.Panel (d) shows measurement points, the year that the measurements were made is written in brackets

measure of hazard. For this reason, the ground acceleration is converted to MMI (Modified Mercalli Intensity) using the equation formulated by *Atkinson & Kaka* [2007] for spectral acceleration at 1.0 sec, including site effects. MMI is then classified into four classes: (**1**) high hazard zone MMI $\geq$ VIII, (**2**) medium hazard zone (MMI VII–VIII), (**3**) low hazard zone (MMI V–VII) and (**4**) very low hazard zone (MMI $<$ V) based on the 500 year return period. This classification is similar to that conducted by *Arya et al.* [2013].

Probabilistic seismic hazard results are presented for annual probabilities of exceedance corresponding to 0.002, 0.001 and 0.0004 (for return periods of 500, 1000 and 2500 years respectively), for response spectral acceleration (RSA) of 0.2 and 1.0 sec and peak ground acceleration (PGA). Shown in Fig. 2.8 are the hazard maps, including site amplification. Evident in these maps are the high seismic hazard in almost all areas except the south arm of Sulawesi. The hazard is at its peak along Palu-Koro, Matano and Lawanopo faults, where slip rates are greater than 30 mm per year.

North arm. Earthquake hazard in the northern arm of Sulawesi is controlled by the North Sulawesi Subduction Zone and the associated intraslab sources to the north and east arm. At longer return periods (e.g. 1000 and 2500 years), the Gorontalo Fault contributes significantly to the hazard level. Although the frequency of large earthquakes which occur along the Gorontalo Fault is lower than other source regions, these events can cause high levels of ground shaking if they occur because this is an inland shallow source. Earthquake hazard in this area is amplified by soft sediments along the depression created by the Gorontalo fault, most notably surrounding Lake Limboto between the populated cities of Limboto (with population estimated at 50,000) and Gorontalo (200,000 inhabitants). Earthquake hazard in the northern arm of Sulawesi is highest in Buol and Toli-toli districts.

Central and East Sulawesi. Earthquake hazard in central and east Sulawesi is very high, especially along fast-moving on-shore faults like the Palu-Koro-Matano Fault System and Balantak-Batui Faults. High background seismicity rates drive high hazard in area far from the major faults included in our model. This pattern is consistent in all return periods and spectral periods. Extremely high hazard (e.g. PGA $>$ 0.8 g at 500 year return period) occurs in the city of Palu (with a population of 335,000), located on a pull-apart basin created by strands of the Palu-Koro Fault zone.

West Sulawesi. Earthquake hazard is generally high in West Sulawesi due to the high background seismicity rate. Hazard is higher in the east, near the Palu-Koro Fault, and to the west, where the offshore Makassar Thrust is located.

South-east Sulawesi. Earthquake hazard in southeast Sulawesi is extremely high along the Matano and Lawanopo Faults. The Lawanopo Fault runs to the north of the city of Kendari which is sited on a delta and surrounding coastal lowlands near Kendari Bay. Background seismicity rates are lower to the south of the Matano Fault. To the south of the Matano and Lawanopo Faults, the earthquake hazard is high but relatively lower than in Central and East Sulawesi.

South Sulawesi. Earthquake hazard is high along the Walanae Fault, with lowlands along the depression created by the fault causing high amplification of ground motions. Background seismicity is low, with only a few historical earthquakes recorded in the background zone. Away from the Walanae Fault, hazard is much lower than the rest of Sulawesi. Makassar (with a population of 1.34 million), being the largest population centre in Sulawesi, is located in a region of lower hazard as compared to other areas.

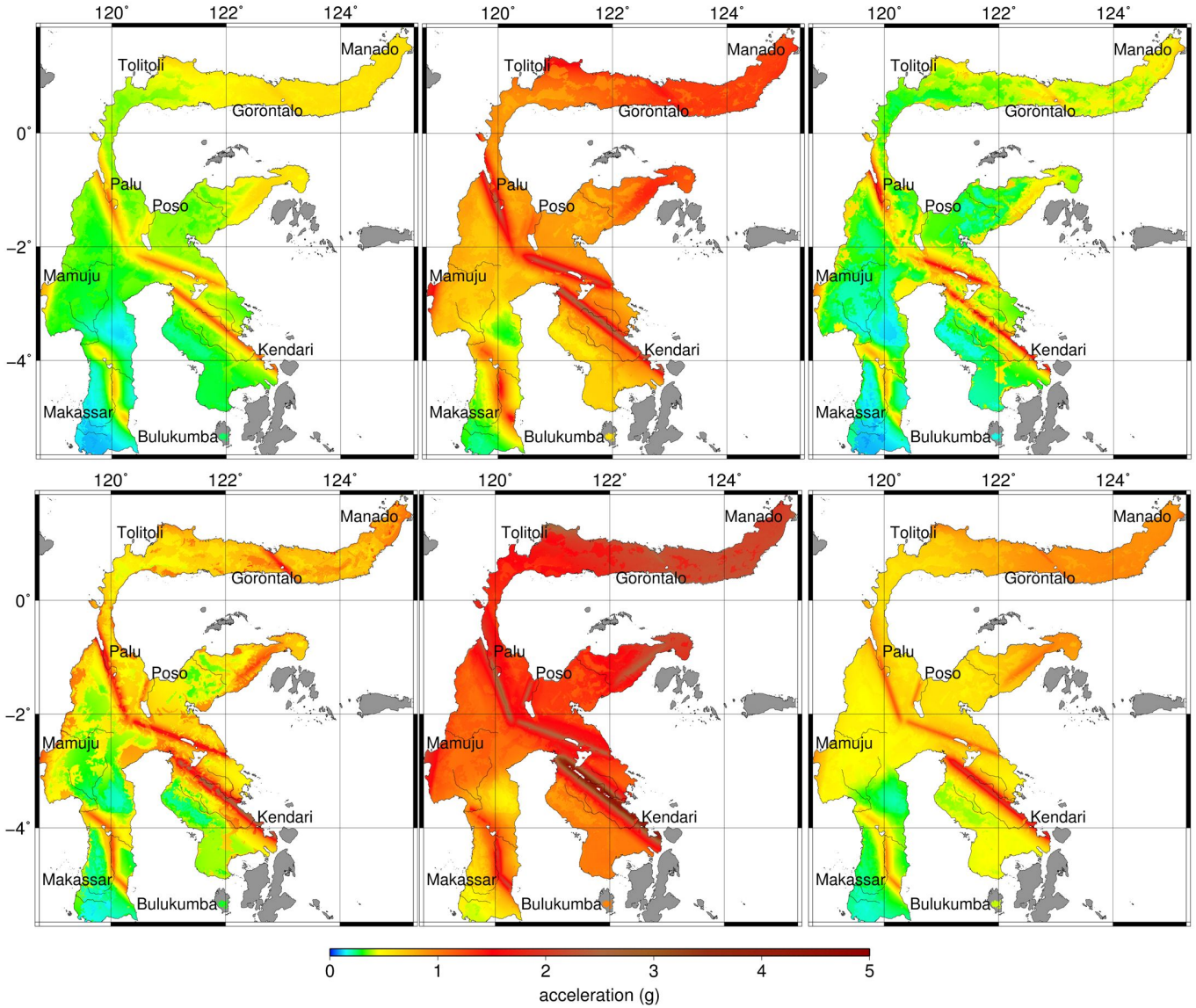

Figure 2.8: Peak ground acceleration (PGA) and response spectra (RSA) of 0.2 and 1.0 s for (top) a 500 year return period and (bottom) a 2500 year return period

Comparison against historical data.

The conversion of 500 years recurrence interval 1.0 s hazard to MMI is shown in Fig. 2.9. Also shown in this figure are the epicenters of historical damaging earthquakes *Supartoyo & Surono* [2008]. All historical destructive events occur in regions classified as moderate (4 events) or high (30 events) hazard, with the exception of the 1828 Bulukumba earthquake, which occurs in a low hazard region.

2.5 Discussion

Based on the probabilistic seismic hazard assessment conducted for the island of Sulawesi, a huge portion of the region is assessed at high hazard. This is due to fast-slipping crustal faults in the highly sheared region north of the Palu-Koro-Matano fault system and along Sulawesi's north arm. In the southwest, including the city of Makassar, a lower seismic hazard is assigned. It should be noted however that the whole island is subject to damaging events at longer return periods. The high hazard regions correlate well with the epicenters of historical earthquakes except for the 1828 Bulukumba earthquake which may be associated to Walanae Fault or an unmapped fault offshore.

A key challenge in developing the hazard map for Sulawesi is reconciling the abundant recent seismicity with the geological evidence of active structures. With the exception of the Palu-Koro Fault, available geologic and geodetic data provide weak evidence for activity rates whereas the uncertainties in earthquake locations [*Husen & Hardebeck*, 2010] make it difficult to associate the earthquakes to specific sources. In order to address these issues, large crustal scale faults that form the boundaries of different domains (e.g. the Palu-Koro-Matano Fault System) are included as fault sources which do not overlap background zone sources. The slip rates of smaller faults outside the zone sources were adjusted to avoid the overestimation of seismicity. This is done by assuming a volume around the fault (V_{buffer}) and using the data in the surrounding source zone (V_{zone}) to scale the seismicity with respect to this volume. Correspondingly, the equivalent slip rate for the fault is calculated, while taking into account the reported slip rate. In some cases, like for the Poso Fault in North Central Sulawesi, the activity rate estimated from seismicity in the surrounding zone is higher than the estimated slip rate from *Irsyam et al.* [2010]. For such cases, more detailed geodetic studies are needed to arrive at a good estimate.

Hazard results in the northern half of Sulawesi (e.g. north of the Palu-Koro-Matano Fault System) are generally high. The role of individual crustal faults in the seismic hazard is relatively minor. The subduction interface and intraslab sources in the northern arm contribute significantly to the hazard, with the effect of the onshore Gorontalo Fault only becoming significant at long return periods (e.g. $>$ 1000 years). South of this region, and most noticeably in South Sulawesi, background seismicity is lower and seismic activity is concentrated along individual faults like the Walanae Fault. Seismic hazard in the central part of Sulawesi is concentrated along the fast moving Palu-Koro-Matano Fault System and Lawanopo Fault. Several pull-apart basins are present along these fault systems, where sediments have accumulated resulting in high estimats of site amplifications. This is particularly evident near the city of Palu, which sits on a basin of alluvial and coastal sediments bounded to the east and west by two strands of the Palu-Koro Fault zone.

Palu and Gorontalo are the two most significant population centers located along coastal basins formed by active faulting, although other centers are also in similar situations, including Kendari. These centers are exposed to a combination of high earthquake

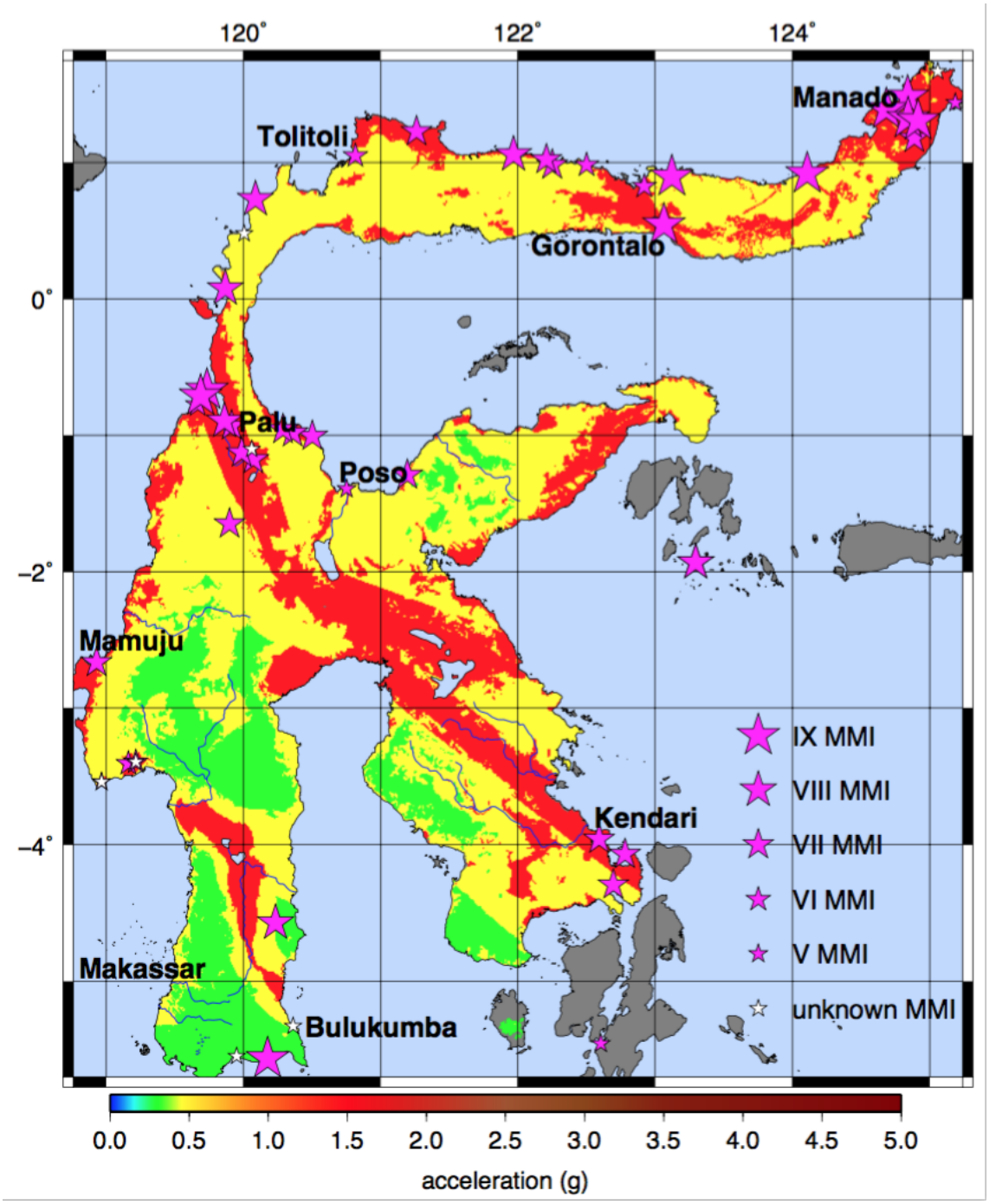

Figure 2.9: Intensity map of Sulawesi (500 year recurrence interval 1.0 s) and historical damage location (the size of the star indicates the MMI scale

activity from near field sources, amplified ground motions, liquefaction, landslide and localized tsunami, especially if the earthquake deformation extends offshore or triggers submarine landslides (e.g. tsunamis occured near Palu in 1927 and 1968; *Pelinovsky et al.* [1997]). Hence, priority should be given to these centers for more comprehensive site amplification studies, hazard assessment for secondary earthquake hazards and risk reduction activities.

The bedrock hazard results in this study have shown higher hazard in the northern part of the island as compared with the study conducted by Irsyam in 2010. This may be due to the delineation of the North Sulawesi Subduction Zone close to the island near the region of high seismicity, rather than at the trench. Also, intraslab sources were explicitly included using fault planes with out-of-plane ruptures, leading to a more realistic geometrical model. For *Irsyam et al.* [2010], a smoothed seismicity was utilized within stepped rectangular volumes to represent the slab leading to higher hazard along the major crustal faults, including the Palu-Koro-Matano Fault System as depicted in Fig. 2.10 and Fig. 2.11.

The assessment presented in this study uses the same ground motion prediction equations, and logic tree weights, as *Irsyam et al.* [2010]. None of these GMPEs have been developed using strong motion data from Indonesia. Therefore, there is considerable uncertainty in their application. It is assumed that the analysis of available data from the newly-established Indonesian strong motion network would reduce the uncertainty, although recent researches have focused on Java and Sumatra [*Rudyanto*, 2013]. Furthermore, the geological heterogeneity of Sulawesi, including thick continental crust from the Sundaland and Australian continents, overthrust ophiolites and melange complexes, actively deforming crustal regions and active and inactive arc systems, mean that a high degree of heterogeneity in ground motions is to be expected within Sulawesi.

Proxy methods used to estimate site amplification are subject to considerable uncertainty. The *Matsuoka et al.* [2006] method based on geomorphology is slightly more accurate, correctly classifying site class at approximately 25% of the measured locations compared with the *Wald & Allen* [2007] topographic slope method which is correct for approximately 15% of the measured sites. *Wald & Allen* [2007]) method more accurately assigns site class C while *Matsuoka et al.* [2006] method more accurately predicts site class D. Noting the considerable uncertainty in the use of HVSR measurements as a basis for estimating site effects [*Zhao*, 2011; *Ghasemi et al.*, 2009] the main conclusion that can be drawn is that *Matsuoka et al.* [2006] proxy method is probably more suitable for Sulawesi, but that site amplification remains a major source of uncertainty in the hazard results.

By discriminating between volcanic and non-volcanic mountains, the *Matsuoka et al.* [2006] method is expected to have a distinct advantage over slope-based approaches as there are both active volcanoes and non-volcanic mountain regions in Sulawesi. Unfortunately, at present, there are no available field data with which to test these regions against the *Matsuoka et al.* [2006] classification. Furthermore, many of the major cities are situated in valleys, coastal lowlands and delta. In many cases these geomorphic environment are a direct result of active faulting in the area. Hence, quantification of site amplification at the local scale is essential in building and infrastructure design as well as in the spatial planning. This will potentially reduce the exposure to areas of large amplification. Future field measurements to better understand site amplification should use more robust techniques for calculating site amplification such as multichannel analysis of surface waves (MASW) or borehole measurements.

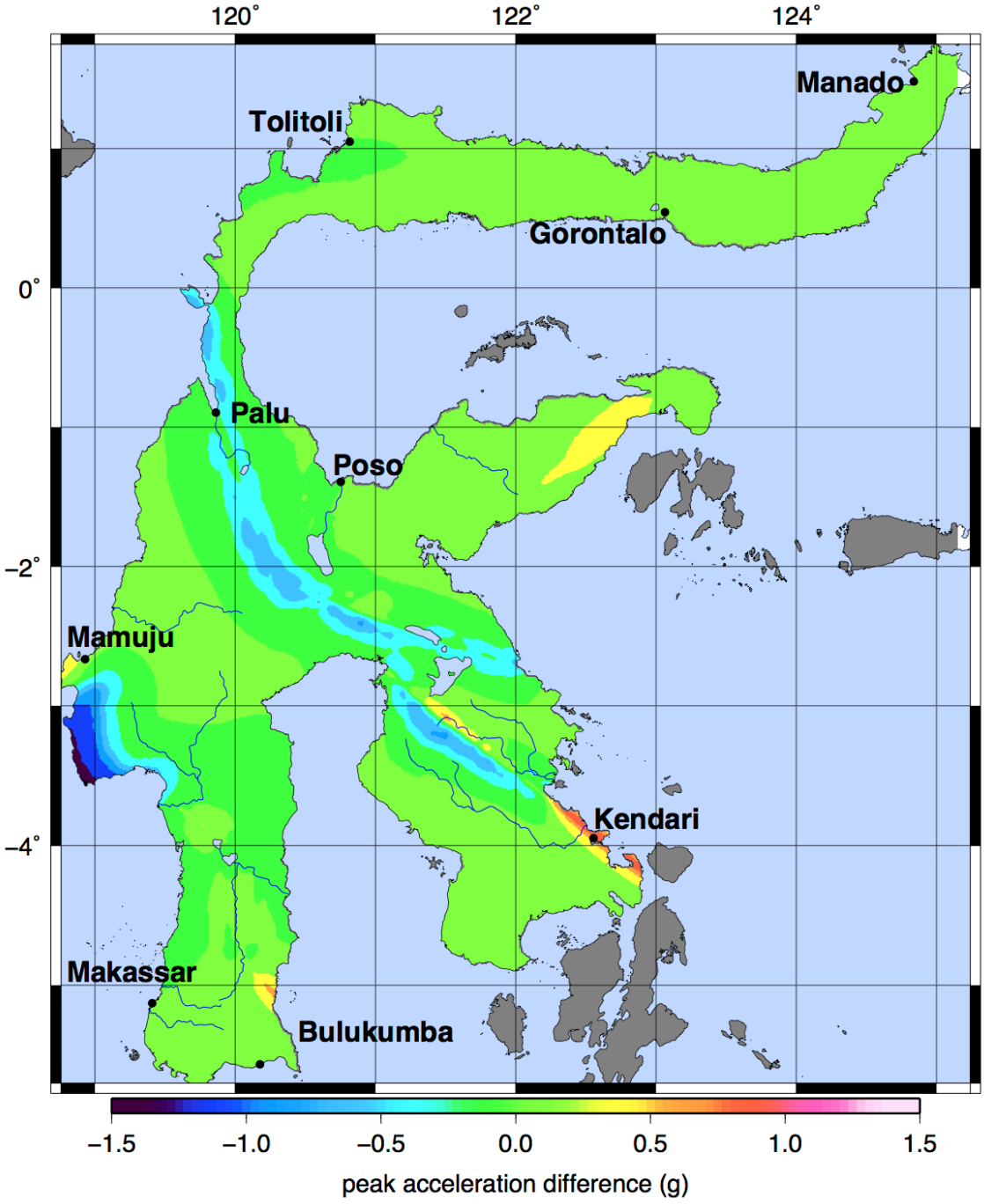

Figure 2.10: Peak response spectra (RSA) of 1.0 s for 500 year return period

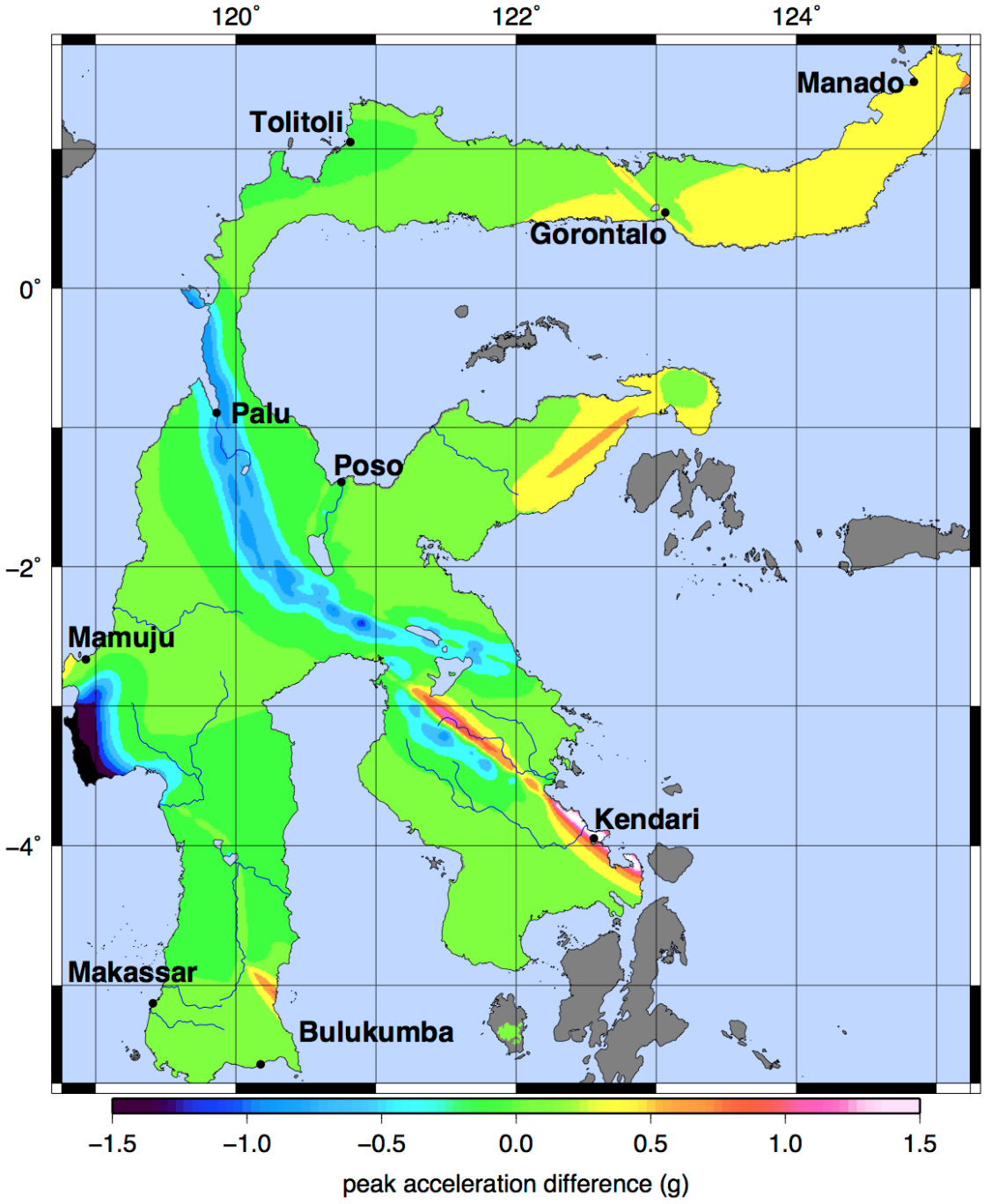

Figure 2.11: Peak response spectra (RSA) of 1.0 s for a 2500 year return period

2.6 Conclusions

This study conducts the first probabilistic seismic hazard assessment including the effects of site amplification for the island of Sulawesi in Indonesia. Most of the island, with the exception of South Sulawesi, is undergoing rapid deformation. This leads to high hazard in most regions (such that PGA $>$ 0.4g at 500 year return period including site effects) and extremely high hazard (like PGA $>$ 0.8 g at 500 year return period) along fast-slipping crustal scale faults such as the Palu-Koro-Matano Fault System and Lawanopo Fault. Active subduction and a complex array of active and inactive subducted slabs in the north drives very high hazard along the north arm of the island. Reported slip rates for active faults are balanced against background seismicity rates to avoid double counting of seismicity. In many cases, background rates exceed reported fault slip rates, highlighting the need for further geodetic and geological studies for better constraints. Site amplification is accounted for by using proxy methods. The conversion to intensity and classification of hazard zones would facilitate better application of hazard maps for spatial planning purposes. A high degree of uncertainty associated with these methods means there is a need for further, local scale studies to better characterize site effects. This is particularly important for population centres in Palu and Gorontalo, especially those sited in sedimentary basins created by active faults. These areas are exposed to both high seismicity rates and high amplification of ground motions. Building design in these areas should combine bedrock hazard results with locally measured site effects to determine the appropriate design criteria.

The next plan is to try to validate the amplification factor inferred from H/V using a geotechnical approach. Geotechnical investigation, such as NSPT and/or CPT, may be a promising method to validate the H/V method to achieve a more reliable amplification factor and, hence, produce a better seismic hazard map.

Acknowledgments
This work was supported by the Australia Agency for International Development and the Indonesian National Disaster Management Agency through the Australia-Indonesia Facility for Disaster Reduction. The authors are grateful to Masyhur Irsyam (Institut Teknologi Bandung) for sharing input parameters and results from the 2010 revision of the national seismic hazard maps. The authors acknowledge the hard work and fruitful discussions with the EQRM development team (Duncan Gray, Vanessa Newey, David Robinson, Geoscience Australia).

Chapter 3

Historical and Hypothetical Future Earthquakes Affecting Jakarta

Abstract: Jakarta has experienced no damaging earthquakes throughout the 20^{th} century, but historical accounts from the colonial era documented several earthquakes that devastated the city. Although the sources of these historical earthquakes are poorly known, a number of potential seismic sources are identified which enabled the simulations of ground motions. One of the parameters utilized in the simulation is the average shear-wave velocity at the upper 30 m of the soil, based on travel time from surface to the 30 m of depth (V_{S30}). Local geological condition is taken into account as one of the factors that contribute to the amplification of ground motions at the site. Using an empirical equation, the ground acceleration is converted to intensity scale. To compare the simulated and recorded intensities, the available macroseismic data in a number of cities in Indonesia were used. Results show that the shallow megathrust, the deep intraslab and the Baribis Thrust are active seismic sources that can be associated not just with historical damaging earthquakes, but also to potential earthquakes that may affect Jakarta significantly in the future.

3.1 Introduction

Jakarta is located at the north coast of West Java, about 250 km away from the Java subduction zone. For more than a century, the city has experienced explosive growth without a major damaging earthquake. However, in the past decade Jakartans felt strong ground shaking from the 9 August 2007 Indramayu and the 2 September 2009 Tasikmalaya events. These events were mostly felt by people working or living in the upper level of high storey buildings. The Mw 7.5 Indramayu event was a 280 km deep intraslab earthquake, while the Mw7.0 Tasikmalaya event is an intra-plate earthquake at 46 km depth, with epicenters were 80 and 180 km, respectively, from Jakarta. Even though no damage was reported for these events, the potential occurrence of larger and/or closer earthquakes poses a threat to the densely populated city of Jakarta.

During the the 17^{th} to 19^{th} centuries, on the other hand, at least 3 destructive earthquakes struck Jakarta. Although the sources of these earthquakes are poorly known, their impacts were well-documented by the Dutch colonial authorithy. These reports are valuable information for understanding the potential impacts of future earthquakes,

especially for use in urban planning. For this reason, we considered whether the recorded impacts could be modeled using synthetic simulations of possible earthquake scenarios. These simulations were conducted using the OpenQuake Engine - an open-source platform developed by the Global Earthquake Model (GEM) Foundation [*GEM*, 2014]. OpenQuake includes tools for earthquake modeling that enable the estimation of ground acceleration at any point of interest using earthquake source parameter and site class data as input. Modeling can be conducted both in probabilistic (Probabilistic Seismic Hazard Analysis–PSHA) and deterministic (Deterministic Seismic Hazard Analysis–DSHA) approaches. With the availability of recorded impacts and estimated ground motions, a comparative study can be done to determine which among the various likely earthquake scenarios produce simulation results that are comparable to the observed data.

For simplicity, the scale of the damage that recorded by *Nata & Witsen* [1700] and *Wichmann* [1918] [Translated by *Harris & Major* [2016]] is qualitatively converted to Modified Mercalli Intensity (MMI) scale. We model scenarios for each event to calculate the maximum acceleration in a gridded area using 2 km spacing. The estimated acceleration is converted to MMI and compared with the available historical data. Using this technique, the most likely source parameters and the degree of seismic hazard in Jakarta can be surmised.

3.2 Seismic Hazard of Jakarta

A number of studies have been carried out focusing on the seismic hazard of Jakarta. *Irsyam et al.* [2014] performed a seismic hazard assessment using both probabilistic and deterministic approaches, similar to the approach presented in Irsyam et al. (2010). For the probabilistic seismic hazard assessment (PSHA), an engineering basin depth (Vs$\geq$750 m/s) was inferred from seismic downhole measurements. Dutch cone penetration test (DCPT) and standard penetration test (SPT) measurements were utilized for characterizing the site condition. The deterministic part of the study estimated a maximum peak surface acceleration of about 0.24g if a Mw6.5 earthquake occurs within a 20 km radius of Jakarta. Probabilistic part of the study found that a peak surface acceleration between 0.2-0.4g has a 2% probability of exceedance in 50 years (2500 years of return period). It indicates a maximum amplification factor of 2.2 if a megathrust earthquake of Mw9.0 occurs.

Merati et al. [2000] used a modified version of EQRISK to implement a PSHA for Jakarta. The corresponding peak accelerations at bedrock for several spectral and return periods were calculated. Attenuation relationships developed by *Youngs et al.* [1997] for interface and intraslab events and *Boore et al.* [1997] for shallow crustal earthquakes were applied in this calculation. The model predicted that for a 500-year return period, the maximum peak ground acceleration (PGA) at bedrock reaches 179 gal. Furthermore, the maximum acceleration at 0.2s of spectral period were predicted to reach approximately 370 gal and 270 gal for the 500-year and 200-year return period, respectively, as depicted in Fig. 3.1.

Earthquake scenarios for the greater Jakarta area, which is inhabited by about 30 M people, are also available. Four earthquake scenario models utilize seismic sources including the Lembang Fault, Cimandiri Fault, megathrust and subducting slab using point, planar and complex earthquake source modeling in OpenQuake. Furthermore, fatality estimation was computed using InaSAFE which is a free access software [*InaSAFE*, 2007] for impact estimation developed by Indonesia's National Disaster Management Agency

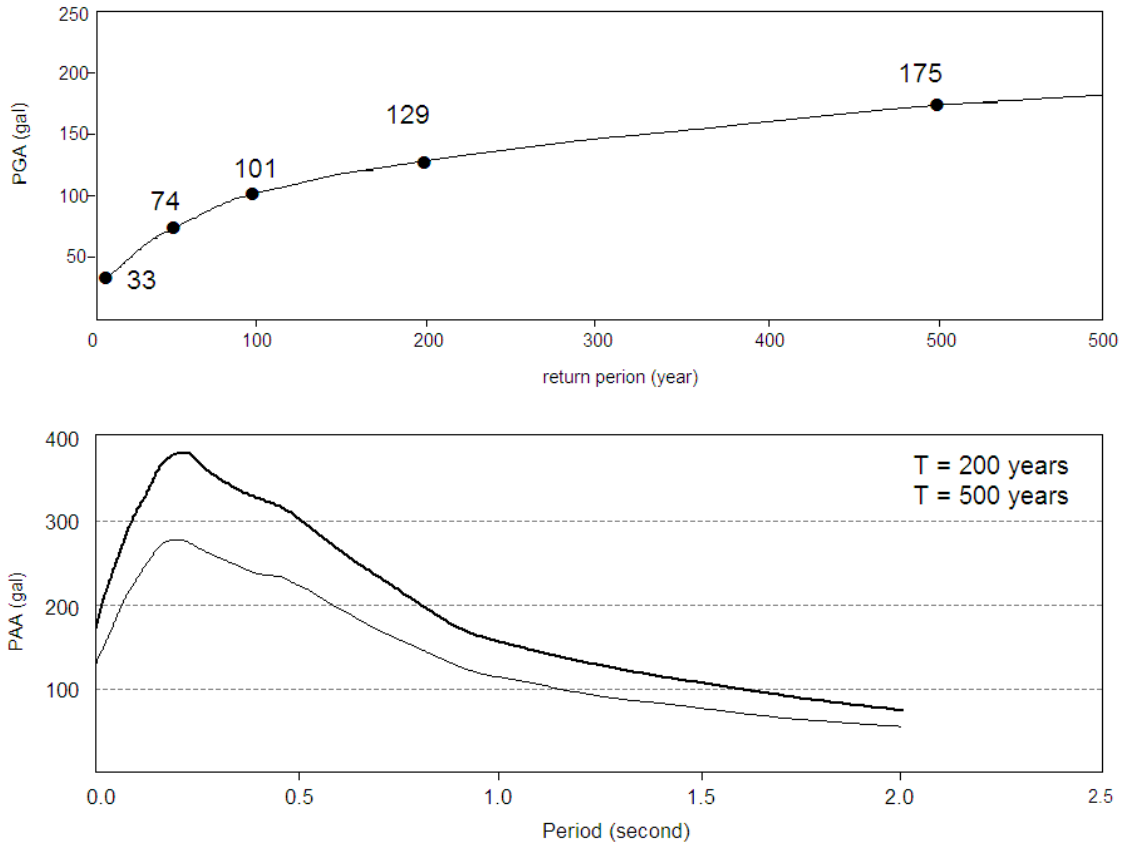

Figure 3.1: Peak ground acceleration (PGA) at bedrock of Jakarta for some return periods (top) and Peak spectral acceleration at bedrock of Jakarta for 200 and 500 years return period (bottom) *Merati et al.* [2000]
. The tick and thin lines are spectral acceleration for return period of 200 and 500 year.

(BNPB) and the Australian Government, through the Australia-Indonesia Facility for Disaster Reduction (AIFDR) and the World Bank-Global Facility for Disaster Reduction and Recovery (World Bank-GFDRR).

OpenQuake produces estimates of PGA and response spectral acceleration (RSA) at pre-defined periods. For comparison with the historical intensities, RSA at 1.0 sec is converted to MMI using empirical equation introduced by *Atkinson & Kaka* [2007], although the use of this empirical equation introduces uncertainties in the estimation. A number of parameters are used to model the historical earthquakes including GMPEs, slab structure [*Hayes et al.*, 2009], fault surface rupture length [*Wells & Coppersmith*, 1994] and site amplification estimated by geologic-topographic method of *Matsuoka et al.* [2006].

Several catalogues [e.g. *Wichmann* [1918, 1922]] documented the occurrence of large earthquakes and tsunami in the Indonesia. These documents emphasize that Jakarta may not be exempted from strong ground shaking. Wichmann recorded large earthquakes that hit Jakarta and the surrounding areas in 1699, 1780 and 1834 which thereby led to fatalities, buildings damage and landslides. We used these reports of large-scale damage to evaluate the intensity based on the MMI scale, and used these to identify possible fault sources for these events were identified based on the available knowledge of tectonics in Java and the seismic intensity distribution.

Very little information is available regarding active crustal faults that may be

the sources of the historical destructive earthquakes that impacted Jakarta. For seismic simulation purposes, a literature review of the tectonic setting in the vicinity of Jakarta and the identification of possible active faults that may significantly affect the city is essential. The Lembang Fault has been identified as active in several studies [e.g. *Afnimar et al.* [2015]; *Meilano et al.* [2012]; *Kertapati* [2006]] while Baribis fault, the closest active fault to Jakarta is presented in *Simandjuntak & Barber* [1996], *Martodjojo* [1984], *Bemmelen* [1949]. However, the Lembang fault is excluded from the scenarios considered here, since it produces maximum capable earthquake [*Afnimar et al.*, 2015; *Meilano et al.*, 2012] which is too small to significantly affect Jakarta.

Although the Java subduction zone is located further than 100 km from Jakarta, an earthquake scenario is simulated there since it can potentially produce a large magnitude, e.g. Mw 9.0, event. Megathrust surface rupture is estimeted using *Papazachos et al* [2004]:

$$\begin{aligned} logL &= 0.55M_w\text{–}2.19 \qquad \sigma = 0.18 \\ logW &= 0.31M_w\text{–}0.63 \\ logU &= 0.64M_w\text{–}2.56 \end{aligned} \tag{3.1}$$

where L, W, U and M_w are length, width, slip of fault and moment magnitude, respectively. Slab 1.0 [*Hayes et al.*, 2012] is used to to determine the geometry of fault rupture models for interface and intraslab earthquakes.

Crustal fault surface rupture length (SRL) is calculated using equation from *Wells & Coppersmith* [1994]:

$$M = a + b \times log(SRL) \tag{3.2}$$

where a and b are 5.16 and 1.12 for strike slip; 4.86 and 1.32 for normal fault; 5.0 and 1.22 for reverse fault.

In order to estimate ground shaking for scenario earthquakes, it is important to consider site amplification, which is often characeterised using the average shear wave velocity in the upper 30 meters of the soil profile, denoted V_{S30}. In the absence of in situ measurements of V_{S30}, it can be estimated using proxies such as slope-topography [*Wald & Allen*, 2007], which assumes areas of flat topography correspond to low velocity sediments while areas of high relief corespond to stiff soil or bedrock. In this study we estimated V_{S30} using the approach of *Matsuoka et al.* [2006] which incorporates a more complete set of geologic/geomorphic information. V_{S30} was estimated using an empirical function using coefficients for morphology (based on elevation, slope and distance from the site to the nearest pre-Tertiary or Tertiary mountain/hill) and geology (based on type and age of lithology) as predictor variables for site effects. Estimated values of V_{S30} are incorporated directly into GMPEs or classified into National Earthquake Hazard Reduction Program (NEHRP) site classes to be factored into the amplification in the estimation of ground motions (Fig. 3.2).

At present, a GMPE using strong motion data from the Indonesian region has not been derived yet. However, *Rudyanto* [2013], has shown that, amongst a wide set of available GMPEs, Zhao et al. (2006) match the strong-motion data recorded in Indonesia reasonably well. Hence we use this GMPE to estimate peak acceleration at each grid point for the earthquake generated at the subduction interface. GMPEs from *Atkinson & Boore* [2003], *Boore & Atkinson* [2008] are used to calculate peak acceleration for intraslab and

Table 3.1: List of parameters used for seismic hazard simulations

Scenario	Proposed sources	Mag	Rake/ Dip	Rupture	GMPE
1699A	Intraslab	8.0	-90°/45°	105.913°, -6.678°; 106.967°, -6.742°	*Zhao et al.* [2006]
1699B	Megathrust	8.0	90°/30°	105.913°, -6.678°; 106.967°, -6.742°	*Zhao et al.* [2006]
1780A	Baribis Thrust	7.0	90°/45°	106.530°, -6.340°; 106.840°, -6.390°	*Chiou & Youngs* [2008]
1780B	Crustal fault	7.0	0°/90°	106.530°, -6.340°; 106.840°, -6.390°	*Chiou & Youngs* [2008]
1780C	Intraslab	8.5	0°/90°	105.951°, -5.980°; 108.474°, -7.095°	*Zhao et al.* [2006]
1834A	Baribis Thrust	7.0	90°/45°	107.169°, -6.492°; 106.769°, -6.371°	*Chiou & Youngs* [2008]
1834B	Crustal fault	7.0	0°/90°	106.430°, -6.314°; 106.814°, -6.361°	*Chiou & Youngs* [2008]
1834C	Intraslab	7.7	-90°/45°	106.914°, -6.275°; 107.633°, -6.753°	*Zhao et al.* [2006]

crustal fault respectively, as also used in *Irsyam et al.* [2010, 2014]. The source parameters and used GMPEs are summarized in Table. 3.1.

The source parameters and GMPEs used in simulations are summarized in Table. 2.1. In this study, we convert pseudo-spectral acceleration (PSA) at 1 second period into the MMI intensity scale using the empirical relation introduced *Atkinson & Kaka* [2007]. All modelled MMI conversions are mapped at 2 km spatial grid size using these equations:

$$\begin{aligned} MMI &= C_1 + C_2\ log\ Y \qquad \text{for } log\ Y \leq 1.50 \\ MMI &= C_3 + C_4\ log\ Y \qquad \text{for } log\ Y \geq 1.50 \end{aligned} \tag{3.3}$$

where *C1, C2, C3,* and *C4* are 3.23, 1.18, 0.57, and 2.95, respectively while Y denotes peak acceleration at each point.

Having same intensity scale (MMI) between simulated and observed, we can compare these data to find scenarios that fit well with observed. The results pertaining to historical earthquake modeling are presented in the following subsections.

3.3 DSHA of the 5 January 1699 event

Historical data suggest that serious damage were experienced in Batavia (Jakarta), Buitenzorg (Bogor), Bantam (Banten) and the tip of southern Sumatra in Lampong (Lampung) during this event. These locations span more than 150 km from NW in Lampung to SE in Cisalak. Extensive damage over such a large area indicates that either a deep earthqauke of large magnitude located somewhere between Cisalak and Lampung, or a very large megathrust earthquake could be a candidate for this destructive event. Earthquakes with magnitude Mw8.0 have been simulated using a 120 km depth for intraslab (Scenario 1699A, Fig. 3.3**a**) and a M9.0 at 10 km depth for megathrust (Scenario 1699B, Fig. 3.3**b**)

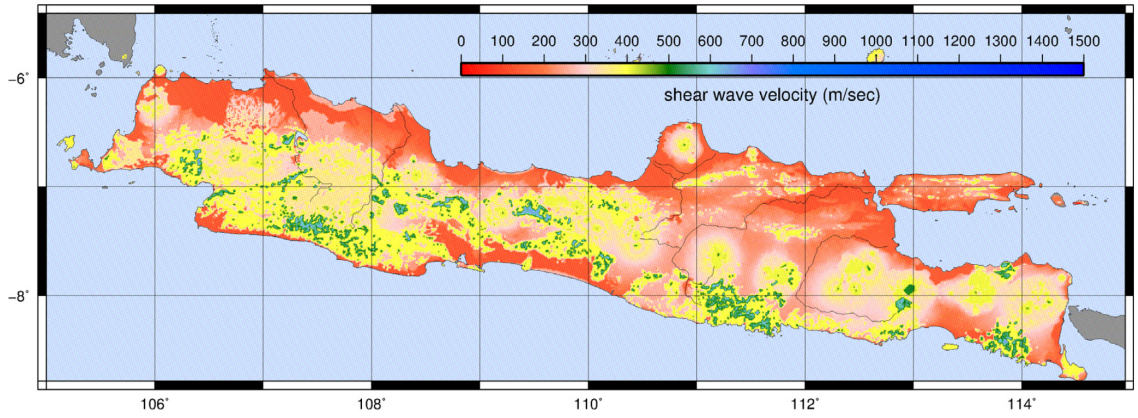

Figure 3.2: The V_{S30} map of Java created using *Matsuoka et al.* [2006] method. This map is used to scale ground motion estimates from the GMPEs at each site.

events. Consider to the distribution of observed intensity, a set of parameters, as listed in Table. 3.1, is created to simulate scenario modelings.

Scenario 1699A, the intraslab event resulted in a maximum MMI of VIII - IX in Jakarta, Bogor and Lampung where heavy damage was observed. This scenario also predict high intensity (MMI ≥VIII) along north coast of West Java as illustrated in Fig. 3.3**a**) where felt intensity or damage was not reported. Due to the lack of information, it is not possible to compare simulated and observed intensity along north coast of Java except in Banten and Jakarta. In Jakarta, simulated intensity is in accordance with observed intensity, however, in Banten, observed intensity was lower than the simulated. Furthermore, simulated intensity in Bogor is in range between VI to VII MMI, which is lower than observed intensity in Bogor (VIII MMI).

At the time of event, north coast of west Java, except seaport cities of Banten and Jakarta, was a *terra incognita*. This coastal area was growing fastly after the completion of Groote Postweg (Great Post Road, currently known as North Coast Road [Jalan Raya Pantura]) in the first decade of IX century. It suggest that although felt intensity or damage was not reported, it is possible that north coast of Java Island was suffered from high ground motion. The north cost of west Java is composed by Quaternary unconsolidated sediment which may amplify seismic waves. Similar to northcoast area, Bandung was growing rapidly since 1906, so that there was no felt intensity reported during the 1699 event, however, simulation suggest intensity of VIII MMI may hit Bandung.

Normal faulting is a common scenario for intraslab earthquakes. In the modeling for this scenario, the hanging wall was taken to be on northern side of the fault, which resulted in higher shaking there than on the foot wall on the southern side, along the southern mountain range. However, quite a large intensity (VII–VIII MMI) was estimated in mountainous area in the south of Bogor, near Sukabumi and Cianjur. These steepy areas are composed of loose pyroclastic materials such that the strong shaking (e.g. MMI VIII) may trigger landslides, consistent with the historical record.

Damage was reported over a wide area, from Bogor Regency where many landslides and significant damage were reported to Lampung in Sumatra. Although large intraslab earthquakes at 100 km depth are infrequent, they do occur and can be very destructive as, witnessed in Chile on 25 January 1939. The Ms7.8 Chilean earthquake, at 80-100 km depth, produced high intensity (e.g. MMI IX) over a wide area. Most of the

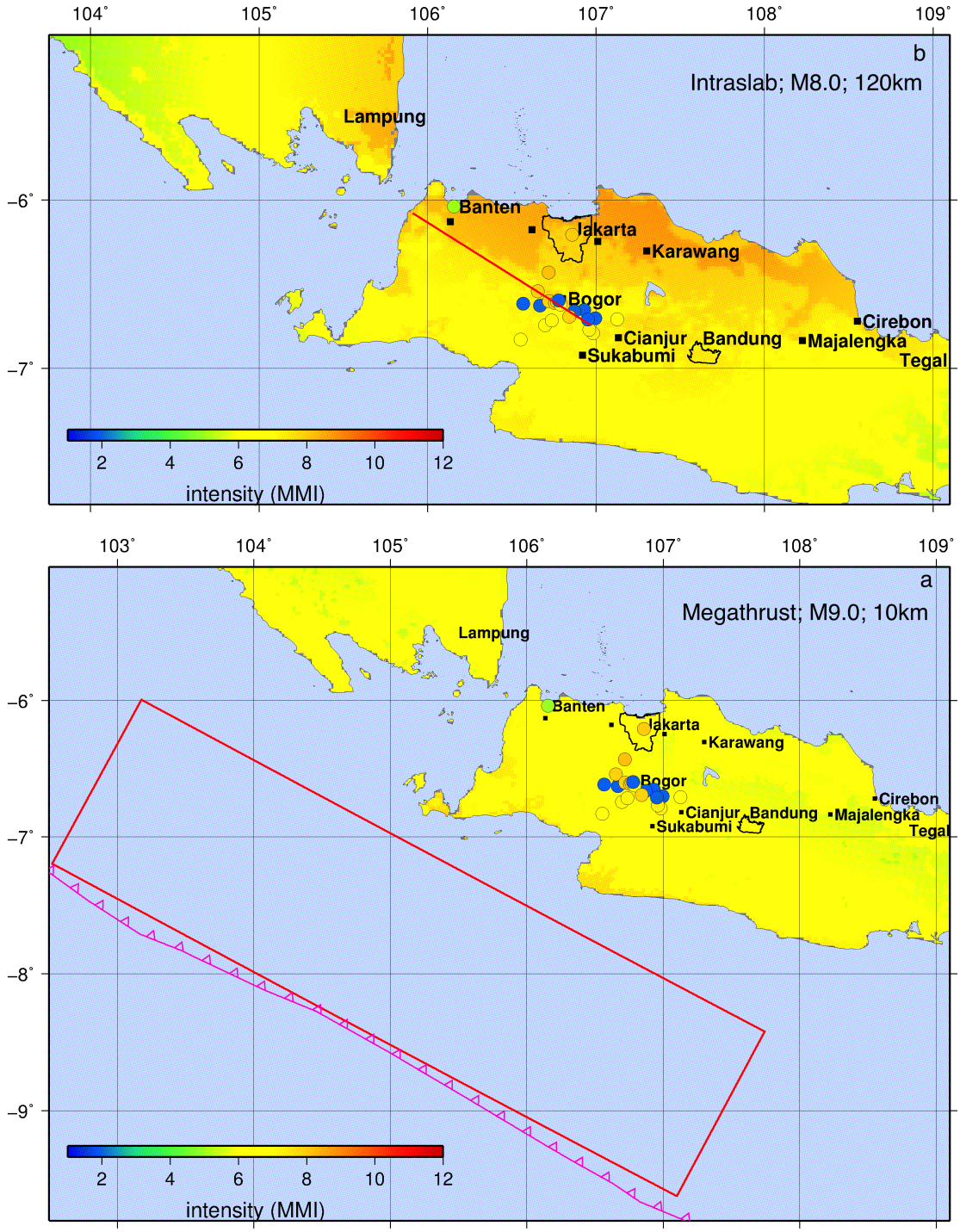

Figure 3.3: Intensity model of 5 January 1699 event resulted from scenarios intraslab (**a**) and megathrust (**b**). Black rectangles denote cities and colored circles denote estimated historical MMI. The blue dots are the low intensity records that reported from tea plantation. The pink-toothed-line and red-square are subduction and source model, respectively.

damage occurred within a 200 km radius, between Linares and Los Angeles [*Beck et al.*, 1988].

Scenario 1699B shown Fig. 3.3**b** resulted in intermediate intensity (e.g.MMI VI-VII) covering the western part of Java, except in the mountain ranges and south coast. In the mountain range, from west Bogor to south Cirebon up to the northern region of Cianjur (then Tjanjor or Tjiandjur), Bandung basin and Majalengka, the intensity varies from MMI V to MMI VII. Although areas affected in the mountain ranges are closer to the seismic source than the north coast, this area experienced less shaking. Compared to the north coast, which is composed of predominantly Holocene alluvium, the mountain ranges are composed of older undifferentiated volcanic materials which are stiffer than loose sediments of the Holocene. This stiffer soil implies a higher V_{S30} values on the mountain ranges in comparison to the north coast.

Low intensity was reported scattered in tea plantations around Bogor city. In those areas limited people were living. Bamboo and wood were the typical material to build houses.

In short, scenario 1699A, a scenario that simulated intraslab earthquake with magnitude M8.0 and epicenter depth of 120 km, predicts better intensity than scenario 1699B. The scenario modeling shows the effect of inclusion of V_{S30} into the ground motion calculation.

3.4 DSHA of the 22 January 1780 event

This event is considered as the largest earthquake to ever impact Jakarta (then Batavia). However, not much information is available to analyze this event [*Albini et al.*, 2013; *Musson*, 2012]. Ground shaking was felt over the whole of Java and SE Sumatra. It was felt most strongly in West Java as depicted in Fig. 3.4. Ground shaking caused 27 sheds and houses to collapse in Zandsee and Moorish gracht located in the present-day Central Jakarta where the Jakarta Cultural Centre is now standing. It was reported that 'a mighty bang' was heard from Mount Salak two minutes after the quake and Mount Gede 'smoked'. Meanwhile, Banten suffered from strong vibrations. A weak vibration was felt in Cirebon, and a seaquake was observed by the ship Willem Frederik, which was at the entrance to the Sunda Strait [*Wichmann*, 1918]. *Albini et al.* [2013] estimated the minimum magnitude could have been Mw8.5 or larger. Three scenarios are proposed for this event as described in the succeeding paragraphs.

Scenario 1780A in Fig. 3.4**a** represents a M7.0 event with a depth of 12km, located on the Baribis Thrust. This reverse fault is located on the northern part of Java and spans from Purwakarta Regency to Baribis Hills in Majalengka Regency [*Bemmelen*, 1949]. It has a dip angle of 31° to the south and a slip rate 1.5 mm/year [*Hutapea & Mangape*, 2009; *Simandjuntak & Barber*, 1996]. The Baribis-Kendeng Fault can be traced from the Sunda Strait eastwards across Java and through the Bali Basin into the Flores Thrust, north of Flores and may continue eastward up to the Wetar Thrust. This major Java back thrust is regarded as having been active since the Late Neogene [*Simandjuntak & Barber*, 1996]

The Baribis Fault is considered to be an active fault and is associated with a destructive earthquake in Majalengka Regency which occurred on 6 July 1990. This was a M5.5 earthquake with epicenter at 6.094°S and 108.12°E and focal depth of 14.2km. In the eastern part of this thrust, in the Anggarwati village, around 150 houses were damaged, 7 people were injured and 1 villager was killed [*Soehaimi*, 2011]. However, there has been

no record of a destructive earthquake in the western part of the fault, the portion that is close to Jakarta.

In the afternoon of January 22, 1780, a weak subterranean noise was heard, which was shortly followed by a rumbling resembling a heavy-laden lorry passing by. This small shaking was followed by larger shaking that destroyed and collapsed 27 sheds and houses in central Jakarta [*Wichmann*, 1918]. Unfortunately, less is known about the type of building collapsed¿ However, from this information, it suggested that earthquake intensity in Jakarta was in range III MMI (resembling a heavy-laden lorry passing by) to VIII MMI (building collapsed). This scenario 1780A resulted comparable intensity in south Jakarta (VII–IX MMI). *Wichmann* [1918] reported similar intensity was felt in Bogor meanwhile this scenario estimate VII – VIII is likely to happen in Bogor, Cianjur and surrounding area as shown in Fig. 3.4**a**

Wichmann [1918] also indicated that weak shaking was felt in east coast of Java, as well as in Cirebon (approximatelly II–III MMI) while much larger vibration was felt in Banten (estimated V–VI MMI). This scenario results good intensity estimation for Banten but highly overestimated in Cirebon. It was also reported by *Wichmann* [1918] that 'a mighty bang' was heard at Mt. Salak (south west of Bogor) Mt. Gede has smoked several tiems after the quake. However, it is difficult to assess whether the volcanic activities were reelated to earthquake or not.

Scenario 1780B in Fig. 3.4**b** is for a hypothetical crustal fault generating a M7.0 earthquake at a depth of 12km. Similar to Scenario1780A, Scenario 1780B also using GMPE proposed by *Chiou & Youngs* [2008] to calculate ground motion. Scenario 1780B results a good prediction of intensity in Jakarta and Bogor, slightly overestimated in Banten and and higher estimation in Cirebon. In general, Scenario 1780B produces similar ground motion distribution in comparison with Scenario 1780A. Boths scenarios produce good estimation of ground motion.

The intensities estimated for Jakarta, Bogor, Banten and Cirebon are MMI VIII, VI, IV and III respectively. Few recorded data were available to determine the intensity in Mount Gede and Mount Salak. Scenarios 1780A and 1780B resulted in a maximum intensity of MMI VIII in Jakarta, Bogor and Banten, which seem to be overestimates. These simulations also yielded similar intensity estimates in Cirebon, while historical accounts reported smaller intensity values.

Scenario 1780C in Fig. 3.4**c** refers to an intraslab M 8.0 earthquake at 160 km depth. It resulted in high intensity (VII–VIII MMI) along the north coast of West Java and part of Central Java (Tegal) which are composed of alluvium. Along the middle mountains-range, from Sunda Strait to Bogor, Cianjur, Bandung to the east, simulated MMI is about VI–VII MMI while in the southern mountains range, the simulated MMI is about IV MMI. Narrow band of VI–VII MMI is also appeared along south coast of west Java where alluvium is deposited.

As in Scenario 1780A and 1780B, this scenario also results good perdiction of MMI for Jakarta, Bogor and Banten. However, simulated MMI in Cirebon is far to high compare to intensity reported in *Wichmann* [1918]. In addition, medium level of intensity (VI-VII) is also spreading in most of the West Java Region where information regarding the effect of the earthquake is not available.

Scenario 1780A and Scenario 1780B resulted in good prediction of ground motions for Jakarta and Bogor. However for Tegal and Banten which are situated 200 km and 80 km away from Jakarta respectively, Scenario 1780B generated estimates higher than observed. Among these scenarios, Scenario 1780A yields the most reliable estimates.

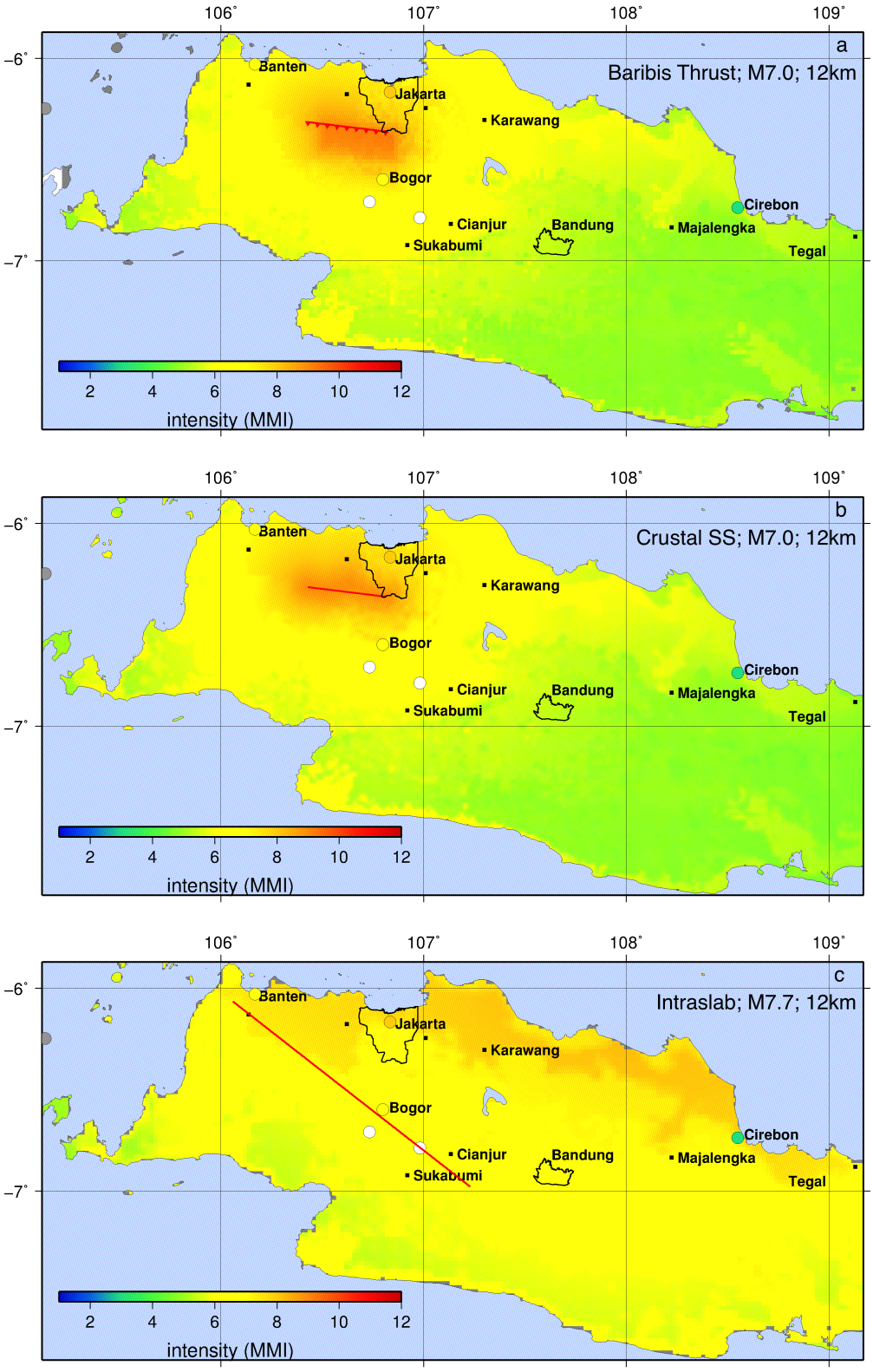

Figure 3.4: Intensity model of 22 January 1780 event resulted from scenarios Baribis thrust (**a**), strike-slip crustal fault (**b**) and intraslab (**c**). Middle mountains-range is lying on the central of West Java from Sunda Steet in the west to Bogor, Cianjur, Bandung and goes through to the east, is estimated to hit by ground motion with intensity about VI–VII. The green clolor in south Java is southern mountains-range where simulated MMI is about IV MMI. Black rectangles denote cities and colored circles denote estimated historical MMI, white circles denote cities where shaking was felt in unknown intensity.

Hence, the Baribis Fault (Scenario 1780A) is selected as the probable seismic source for the 1780 earthquake

3.5 DSHA of the 10 October 1834 event

A series of small tremors on the night of 10 October 1834 preceded the 'great concussion' earthquake in the early morning felt in Batavia (Jakarta), Banten, Krawang (Karawang), Bogor, and Preanger (Priangan) Residencies, and even as far as Tegal in Pekalongan Residency (Central Java) and Lampung. It was reported that shaking was extremely violent, quite long and accompanied by a strong subterranean roar. [*Musson*, 2012] stated that the minimum likely magnitude was Mw7.0.

Jakarta and Bogor were strongly affected (MMI VIII) by this event, as had been experienced in 1699, 135 years earlier. In addition, Cianjur was reported to have suffered from strong shaking (MMI VIII). There was no available report for Lampung whereas in Banten, a lower intensity (MMI V) was reported. The similarity in estimated intensities of the affected areas may indicate a similarity of hypocenter, but smaller earthquake magnitude compared to the 1699 event.

The Baribis Fault scenario (Scenario 1834A) in Fig. 3.5**a** with a M7.0 earthquake at 12 km depth fits the recorded MMI of the 1834 earthquake event, especially in the affected areas.

There were no reports of shaking but no damage from Banten and Tegal, with MMIs of IV and III, respectively, which are over-predicted by the simulation. Since the source depth is set at 12km, the earthquake shaking is mostly concentrated near the fault. Further from the source, the intensity decreases. It should also be noted that amplification effects due to soil properties may have occurred in places far from the source. It was reported that the most affected areas include Jakarta, Bogor, Cianjur and Tjiandjawar (Cihanjawar) where a number of palaces and regent houses partially collapsed and a mega-landslide occurred. A minimum intensity of MMI VIII can be inferred to have caused such damage. Simulated MMIs based on the Baribis scenario predicted intensities ranging from VIII and IX which agree well with reported intensity. However, the simulated intensity was over-predicted for Banten, Karawang and Tegal for the crustal earthquake using scenario B as shown in Fig. 3.5**a**.

The second scenario for the 1834 event (Scenario 1834B) was chosen to be the same as the Baribis fault Scenario 1834A but with the sense of movement changed to strike-slip (Fig. 3.5**b**). This simulation resulted in MMI VIII for Jakarta, Bogor and Cianjur, while MMI VII is simulated at Cihanjawar (a slightly lower intensity than the Baribis scenario). This scenario gives a better prediction for Tegal where the simulated intensity is MMI V while the reported intensity was MII IV.

Although both results from the Baribis Thrust and strike-slip fault models (1834A and 1834B, respectively) produced similar intensities as observed in historical events, Scenario 1834A fits better with historical data especially at sites with less damage like Banten and Karawang. The Mw 7.0 thrust earthquake (1834A) produced large ground shaking concentrated around Jakarta, Bogor and Cianjur, which matched the observed data much better.

The third scenario, as depicted in Fig. 3.5**c**, MMI VII to VIII was estimated for the north coast of West Java including Jakarta and Banten. The intensity in Jakarta, Bogor, Cihanjawar and Cianjur is slightly under predicted compared to the intensity inferred from historical data. On the other hand, the intensity in Banten and Karawang

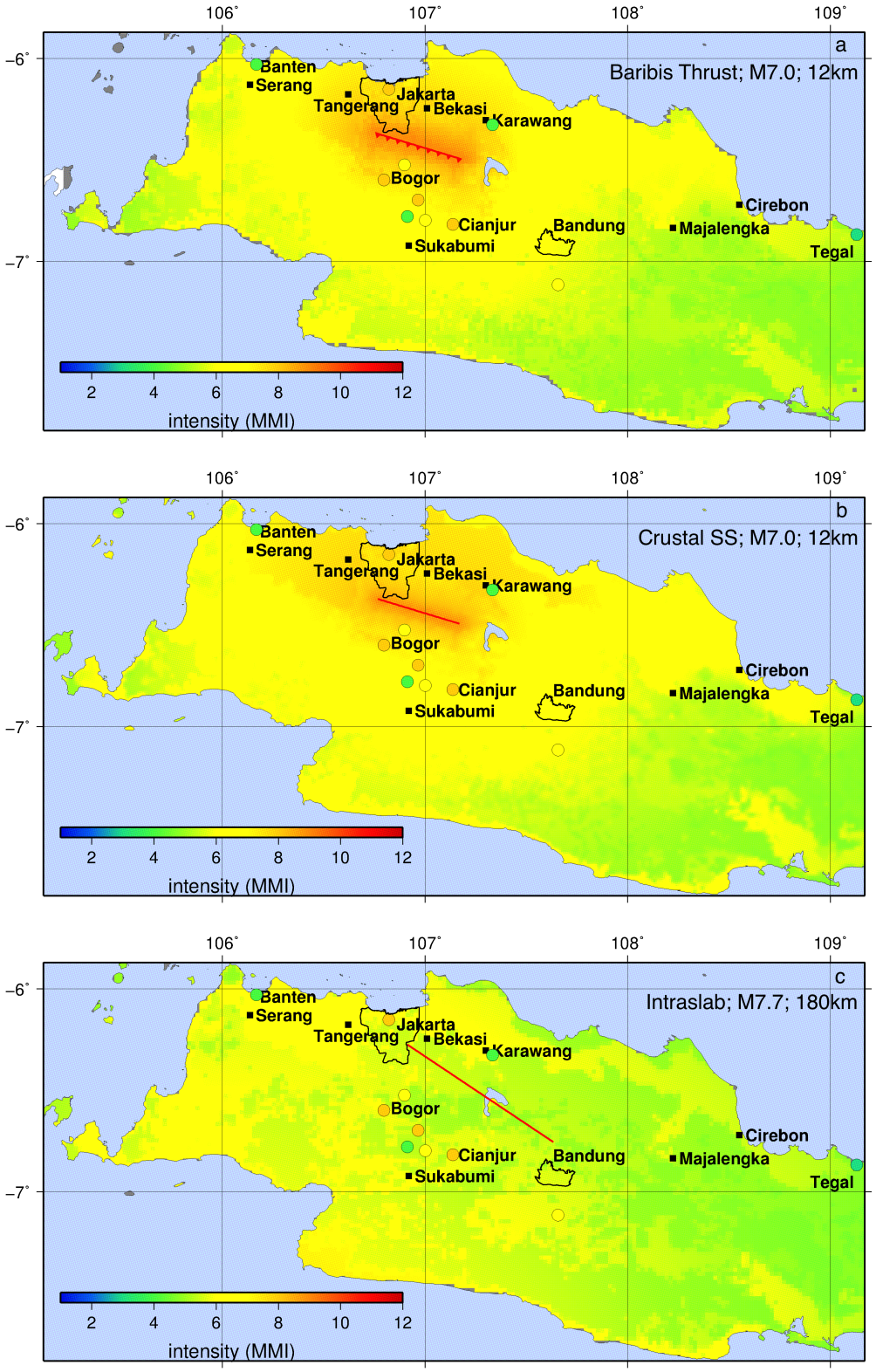

Figure 3.5: Intensity model of 5 October 1834 event resulted from scenarios Baribis thrust (*a*), strike-slip crustal fault (textitb) and intraslab (*c*). Black rectangles denote cities and colored circles denote estimated historical MMI.

is over predicted. In Tegal and Mt. Gede, simulated intensity was MMI VI, which is over predicted in comparison with the historical data. As the magnitude increases, the intensity increases by one level for the whole area except Bogor and Cianjur, which are mountainous areas.

Although both results from the Baribis Thrust and crustal fault models produced similar intensities as observed in historical events, scenario A fits better with historical data especially in cites with less damage like Banten and Karawang. The Mw7.0 thrust earthquake produced large ground shaking concentrated around Jakarta, Bogor and Cianjur, which matched the observed data much better.

The third scenario, 1834C, was a Mw 7.7 intraslab event at a depth of 180 km. As depicted in Fig. 3.5**c**, MMI VII to VIII was estimated for the north coast of West Java including Jakarta and Banten. The intensity in Jakarta, Bogor, Cihanjawar and Cianjur is slightly under predicted compared to the intensity inferred from historical data. On the other hand, the intensity in Banten and Karawang is over predicted. In Tegal and Mt. Gede, the simulated intensity was MMI VI, which is again over predicted in comparison with the historical data. As the magnitude increases, the intensity increases by one level for the whole area except Bogor and Cianjur, which are both mountainous areas

The ground shaking intensity in the Scenario 1834B ranges from MMI VII to VIII in the north coast of West Java including Jakarta and Banten. The intensity in Jakarta is slightly under predicted compared to the intensity defined from historical data. The same goes for Bogor, Cihanjawar and Cianjur. On the other hand, intensities in Banten and Karawang are over predicted. In Tegal and Gede Mountain, the simulated intensity was VI which is over predicted in comparison with historical data.

3.6 Conclusion

Investigations of three historical earthquakes were performed to better understand which sources of seismicity might pose a seismic hazard to Jakarta.

One of the historical events that significantly affected Java occurred on 5 January 1699. This event was felt over the whole of Java but was particularly intense in present-day Banten, Jakarta and West Java provinces, resulting in building collapse and fatalities. Modeled intensity results suggest that the event could have been generated by a Mw8.0 earthquake along the subducting slab at 160 km depth (Scenario 1699A).

Three scenarios were proposed for the 22 January 1780 earthquake. The event was felt across all of Java but was particularly intense in the western part. Results from an intraslab Mw8.0 earthquake at 160 km depth (Scenario 1780C) produced higher intensities than the observed. For the two alternative crustal fault scenarios (1780A and 1780B), both crustal earthquakes of Mw7.0, results closely matched the observations. The Baribis thrust scenario (1780A) fits the data slightly better, but an active but currently unknown fault (1780B) is also a possible source for this event.

Three scenarios were proposed for the 5 October 1834 earthquake. The earthquake was strongly felt along the northern coast of West Java with a maximum estimated intensity of MMI VIII in Jakarta, Bogor and Cianjur. The Baribis Thrust (Scenario 1834A) most likely is responsible for this earthquake, however we cannot rule out an intraslab event (Scenarion 1834C) as a potential source.

Chapter 4

Seismic Velocity Structure of the Jakarta Basin, Indonesia, using Trans-dimensional Bayesian Inversion of Horizontal-to-Vertical Spectral Ratios

Abstract: Characterizing the interior structure of the Jakarta Basin, Indonesia, is important for the improvement of seismic hazard assessment there. A dense portable seismic broadband network, comprising 96 stations, has been operated between October 2013 and February 2014 covering the city of Jakarta. The seismic network sampled broadband seismic noise mostly originating from ocean waves and anthropogenic activity. We used Horizontal-to-Vertical Spectral Ratio (HVSR) measurements of the ambient seismic noise to estimate fundamental-mode Rayleigh wave ellipticity curves, which were used to infer the seismic velocity structure of the Jakarta Basin. By mapping and modeling the spatial variation of low-frequency (0.124–0.249 Hz) HVSR peaks, this study reveals variations in the depth to the Miocene basement. These variations include a sudden change of basement depth from 500 to 1000 m along N-S profile through the center of the city, with an otherwise gentle increase in basin depth from south to north. Higher-frequency (2-4 Hz) HVSR peaks appear to reflect complicated structure in the top 100 m of the soil profile, possibly related to the sediment compaction and transitions among different sedimentary sequences. In order to map these velocity profiles of unknown complexity, we employ a Transdimensional Bayesian framework for the inversion of HVSR curves for 1D profiles of velocity and density beneath each station. Results show that very low-velocity sediments (<240 m/s) up to 100 m in depth cover the city in the northern to central part, where alluvial fan material is deposited. These low seismic velocities and the very thick sediments in the Jakarta Basin will potentially contribute to seismic amplification and basin resonance, especially during giant megathrust earthquakes or large earthquakes with epicenters close to Jakarta. Results have shown good correlation with previous ambient seismic noise tomography and microtremor studies. We use the 1D profiles to create a pseudo 3D model of the basin structure which can be used for earthquake hazard analyses of Jakarta, a megacity in which highly variable construction

practices may give rise to high vulnerability. The methodology discussed can be applied to any other populated city situated in a thick sedimentary basin.

4.1 Introduction

This study aims to develop a model for the basin structure of Jakarta, the capital city of Indonesia. Jakarta is one of the world's megacities, with at least 10 million inhabitants in Jakarta itself and over 30 million people living in the greater Jakarta area. Jakarta's average population density of about 14,000/km^2 indicates it is an area of high potential risk, and therefore it is important to carefully assess its seismic hazard. In terms of geotectonic and demographic conditions, Jakarta is similar to Mexico City, with both cities sitting on deep sedimentary basins and 250–350 km distant from the Java and Mexican Subduction zones, respectively. Therefore, it seems reasonable to expect that to first order the cities might experience similar impacts from a major subduction zone earthquake.

The 1985 Mw 8.1 Michoacán earthquake occurred at the Mexican subduction zone more than 300 km away from Mexico City. Despite the relatively large distance, this event resulted in about 10,000 deaths and extensive damage of more than 2000 structures [*Esteva*, 1988; *Padilla y Sanchez*, 1989]. Poorly consolidated lake sediments and the geometry of the Mexico City Valley acted to amplify and increase the duration of shaking, the combined effect of which had a critical influence the extent of damage [*Furumura & Kennett*, 1998; *Kawase & Aki*, 1989; *Padilla y Sanchez*, 1989].

At any given site, the dynamic soil properties and basin geometry are the principal components that account for site amplification and prolonged duration of ground motion. Understanding the seismic shear velocity profile is important for reliable forecasts of ground response for earthquake scenarios and seismic hazard evaluation. In Europe, America and Japan, models for sedimentary basins are available such as the Mygdonian Basin in Greece [*Manakou et al.*, 2010], the Lower Rhine Embayment in Germany [*Ewald et al.*, 2006], the Santiago de Chile Basin in Chile [*Pilz et al.*, 2010], the Osaka Basin in Japan [*Kagawa et al.*, 2004; *Iwaki & Iwata*, 2011], the Tagus Basin in Portugal [*Borges et al.*, 2016], the Mexico Valley Basin in Central Mexico [*Cruz-Atienza et al.*, 2016] and the Po Plain in Northern Italy [*Berbellini et al.*, 2017]. For the case of the Jakarta Basin, however, very few geophysical studies are available (see e.g. *Saygin et al.* [2016, 2017]; *Ridwan et al.* [2016]; *Ridwan* [2016]). Furthermore, only a few measured boreholes have reached the geological bedrock deemed as the Pliocene-Pleistocene boundary *Delinom et al.* [2009].

Jakarta's sedimentary basin is undergoing rapid subsidence, with a maximum rate of about 26 cm per year, mainly due to groundwater extraction [*Ng et al.*, 2012; *Abidin et al.*, 2011]. From this fact alone it can be deduced that Jakarta Basin is filled with highly saturated poorly consolidated sediments which can accommodate a huge volume of groundwater. This suggests that, in addition to increasing the intensity and duration of seismic wave motion, Jakarta Basin may also be prone to liquefaction if it were to experience earthquake-generated strong ground motion.

Hence, in order to ascertain the extent to which future earthquakes may affect the megacity of Jakarta, it is vital to develop a robust model for the geometry and physical properties of the Jakarta Basin. Since the basin is a densely populated urban area, passive seismic methods are the most viable approach to determining basin structure. Amongst passive seismic methods, spatial auto-correlation (SPAC, see e.g. *Aki* [1957]; *Okada* [2003]; *Asten* [2006]), ambient seismic noise tomography (ANT, see e.g. *Shapiro & Campillo*

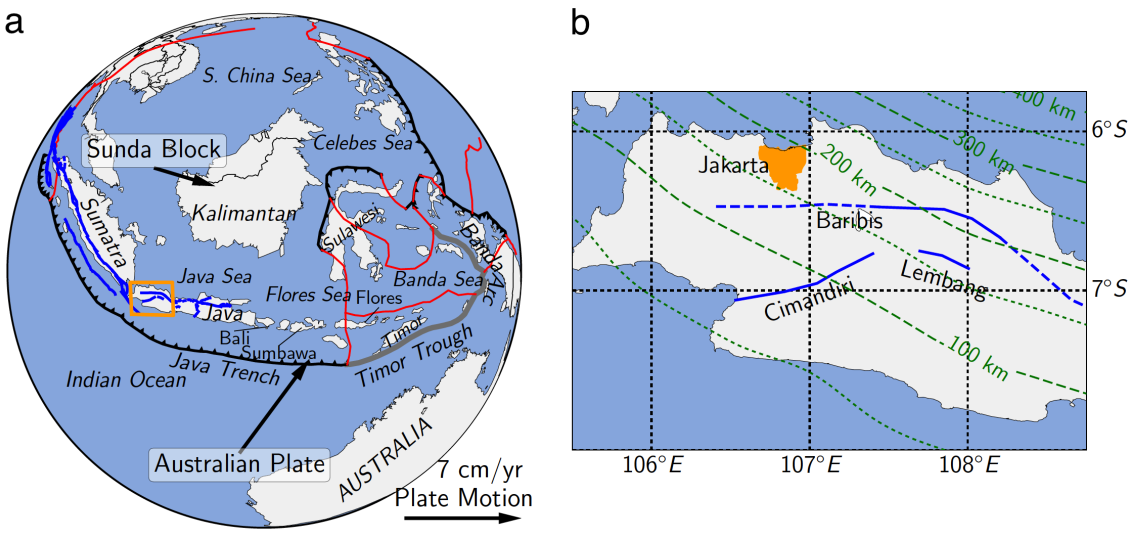

Figure 4.1: (**a**) Simplified tectonic setting of the Indonesian region and (**b**) western Java, detail of inset area indicated in (**a**). The subduction boundary is shown as toothed curve while the study area is the orange shaded area in (**b**). Motion of the Australian and Eurasian Plates are indicatd by back arrows, with relative movement at the Java Trench resolving to nearly normal convergnece at a rate of 7 cm per year. Major faults are indicated by blue lines, while black toothed, red and green dashed lines denoted subduction, microcontinent boundaries, and Benioff counturs, respectively. The blue dashed-line is the continuation of the Baribis fault to the west and east as described in *Simandjuntak & Barber* [1996].

[2004]; *Shapiro et al.* [2005]) and horizontal-to-vertical spectral ratio (HVSR, see below) are the most common techniques applied in urban areas. While SPAC and ANT utilize inter-station cross correlation of ambient seismic noise as estimates of surface wave dispersion curves, HVSR makes use of single-station horizontal-to-vertical spectral ratios as estimates of the Rayleigh wave ellipticity. In this study, a Transdimensional Bayesian approach is applied for the ellipticity curve inversion to obtain 1D velocity profiles at each station. Subsequently, a 3D basin model is constructed by interpolating these 1D profiles.

4.2 Geotectonic Setting and Historical Earthquakes

Two major tectonic components comprise the Indonesian archipelago: the Sundaland or Sunda block in the west and microblocks in the east. The former is composed of Java, Sumatra, Kalimantan, Sulawesi and Nusa Tenggara Islands. Jakarta is located on northwest Java as highlighted in Fig. 5.2. Estimates of the northward motion of Australia with respect to Java range from 67 mm/yr *Simons et al.* [1997] to 70 mm/yr *Hall* [2009], with direction almost normal to the Java Trench. This megathrust plate boundary located approximately 250 km south of Jakarta and the subducting slab beneath Java pose a high seismic hazard that may seriously affect the city when large earthquakes occur. In addition, crustal faults including the Cimandiri, Lembang and Baribis Faults, located within the vicinity of Jakarta, also contribute to the high hazard level in the city.

Using borehole and geohydrological data, *Lubis et al.* [2008] described Jakarta Basin as separated from Depok in the south by normal faults, and underlain by geological bedrock composed of Tertiary rock. The depth of the bedrock near Depok was estimated

at 50 m, undergoing an abrupt change 3 km from the basin's southern rim, up to a depth of 250 m. The basin depth gradually deepens from that point to central Jakarta to a depth of at least 350 m, and the basin floor was thought to flatten from central Jakarta to Jakarta Bay in the north. However, a recent ambient seismic noise tomography study suggested a basin depth of more than 1000 m *Saygin et al.* [2016] while a microtremor array study estimated a maximum depth to engineering bedrock (where shear-wave velocity V_S $\geq$900 m/s) of 725 m *Ridwan et al.* [2016]; *Ridwan* [2016].

The surface geology of Jakarta is composed of Quaternary sedimentary units like alluvium, alluvial fan and beach ridge deposits *Turkandi et al.* [1992]. Alluvium is exposed from the coastline to 6 km southward in the city center, which covers 35% of Jakarta. Further southward, the surface geology is dominated by alluvial fan deposits with a patch of Tertiary volcanic material deposited in the west. The alluvial fan sediments are deposited from elevated areas in the south of Jakarta, piling up at the center with up to 300 m thickness. These Plio-Pleistocene sediments, mostly composed of clayey-sand, unconformably overlie the Miocene formations which are cropping out and encircling the basin in the west, south and east. These uplifted Tertiary formations are known as the Tangerang High in the west, Depok High in the south and Rengasdengklok High in the east *Delinom* [2008].

Throughout Jakarta's history, at least three large earthquakes have devastated the city. The 1699 earthquake caused 28 casualties *Reid* [2012] and triggered a number of landslides within the vicinity of Bogor *Nata & Witsen* [1700], a city located about 50 km south of Jakarta. The largest earthquake to impact the city had a magnitude of Mw 8.5 and occurred on 22^{nd} of January, 1780 *Albini et al.* [2013]. Ground shaking caused 27 sheds and houses to collapse in Zandsee and Moorish *gracht* (canal), located in present-day Central Jakarta where Jakarta Cultural Centre is now standing [*Wichmann* [1918] translated by *Harris & Major* [2016]]. Half a century later, on 10 October 1834, a Mw 7.0 earthquake was associated with seismic intensity considered to be the highest to strike the region *Musson* [2012]. With 30 M people inhabiting Greater Jakarta, the fatality count could be very high should any of these historical events re-occur today *Nguyen et al.* [2015].

4.3 HVSR Measurements

Microtremor survey methods to evaluate shear-wave velocity profile are gaining in popularity because of their applicability in urban areas. These methods are non-invasive, utilizing continuous energy produced by both natural phenomena and human activity. *Kanai* [1957] observed that the amplitude-frequency relation of earthquake motion exhibited peaks whose period depended on "each kind of ground" - short period (0.1–0.4 s) on hard ground and longer period (0.4–0.8 s) on softer ground - and noted that the same peak periods were observed in ambient seismic noise (microtremors). *Aki* [1957], using microtremors recorded at night (18–22 PM), also observed that dispersion was site dependent, and appeared to be characteristic of the underlying medium. Although the HVSR method was first applied for seismic microzonation by *Nogoshi & Igarashi* [1971], *Nakamura* [1989] is more widely cited for his promotion of the method and for proposing that the fundamental resonance frequency be defined as the peak of the HVSR curve, defined as:

$$HVSR(\omega) = \frac{\sqrt{H_{EW}(\omega) \times H_{NS}(\omega)}}{V(\omega)} \tag{4.1}$$

where $H_{EW}(\omega)$ and $H_{NS}(\omega)$ denote Fourier amplitude spectra in east-west and north-south directions, respectively, while $V(\omega)$ is the Fourier amplitude spectrum for the vertical component. The two horizontal components are combined using the geometric average, then divided by $V(\omega)$ to obtain the measured HVSR curve [*Harutoonian et al.*, 2013].

Since this early work, the HVSR technique has been widely used to characterize site response in seismic microzonation studies. The method as proposed by *Nakamura* [1989] equated both the HVSR peak amplitude and period with those of the S-wave transfer function. Subsequent studies found that, while the period of the HVSR peak coincides with the resonant period of S-waves in the sediment column, the amplitude of the peak often does not match that of the S-wave transfer function *Lunedei & Albarello* [2010]; *Bonilla et al.* [1997]; *Lachet & Bard* [1994]; *Lermo & Chavez-Garcia* [1993]. Several studies have used HVSR to measure this resonant period in the range 0.1–2.0 s to infer site class *Ghofrani & Atkinson* [2014]; *Zhao et al.* [2006] and to explain the spatial patterns of earthquake damage *Gosar* [2010]. HVSR measurements of resonant period have also been used to infer depth of sediments when velocity is known from e.g. surface wave dispersion *D'Amico et al.* [2008]; *Ibst-von Seht & Wohlenberg* [1999] or average velocity when depth is known from geophysical surveys *Bodin et al.* [2001].

Other studies have confirmed the original result of *Nogoshi & Igarashi* [1971] that, although the peak in the HVSR curve coincides with the S-wave resonant period, the HVSR curve itself is closely related to the ellipticity of Rayleigh waves *Konno & Ohmachi* [1998]; *Arai & Tokimatsu* [2000]. This is true not only when the ambient seismic noise was confirmed to be dominated by Rayleigh waves *Scherbaum et al.* [2003], but also in numerical studies that used full wavefield modeling of the ambient seismic noise *Field & Jacob* [1993]; *Lachet & Bard* [1994]; *Lunedei & Albarello* [2010]. This has led to a number of studies that used the relationship between HVSR and Rayleigh wave ellipticity to invert for S-wave velocity profiles *Fäh et al.* [2003]; *Scherbaum et al.* [2003]; *Arai & Tokimatsu* [2004]; *Parolai et al.* [2005], and this is the approach we adopt in this study.

The Jakarta Basin is thought to have a relatively long resonant period, with the results of *Saygin et al.* [2016]indicating an average S-wave velocity of 500 m/s extending to an average depth of 500 m. This suggests an S-wave resonant period of about $4 \times h/V_S = 4$ s, with even longer periods possible in the deepest part of the basin beneath northern Jakarta. Although most of the aforementioned studies have involved S-wave resonant peak periods in the range of 0.1 to 1.0 s, typically associated with S-wave velocity structure at 100 m depth or less, a few involved situations similar to the Jakarta Basin. *Yamanaka et al.* [1994]used HVSR measurements with peak periods of 2–8 s to infer basin depths in the Kanto Plain of 1550 m. *Bodin et al.* [2001] used HVSR measurements with peaks in the range 2–5 s to infer average basin velocities of 600-1000 m/s in the Mississippi Embayment, for which previous studies had established a maximum depth of about 1000 m.

In order to make HVSR measurements covering long resonant periods, passive seismic measurements have been carried out using 3-component Trillium Compact sensors, with sensitivity to velocity flat in the frequency range 0.05-100 Hz. These sensors recorded background noise at 96 sites distributed over the Jakarta Basin (Fig. 4.2**a**). Ambient seismic noise was recorded for at least 1 month at each site, and processed according to the details given below.

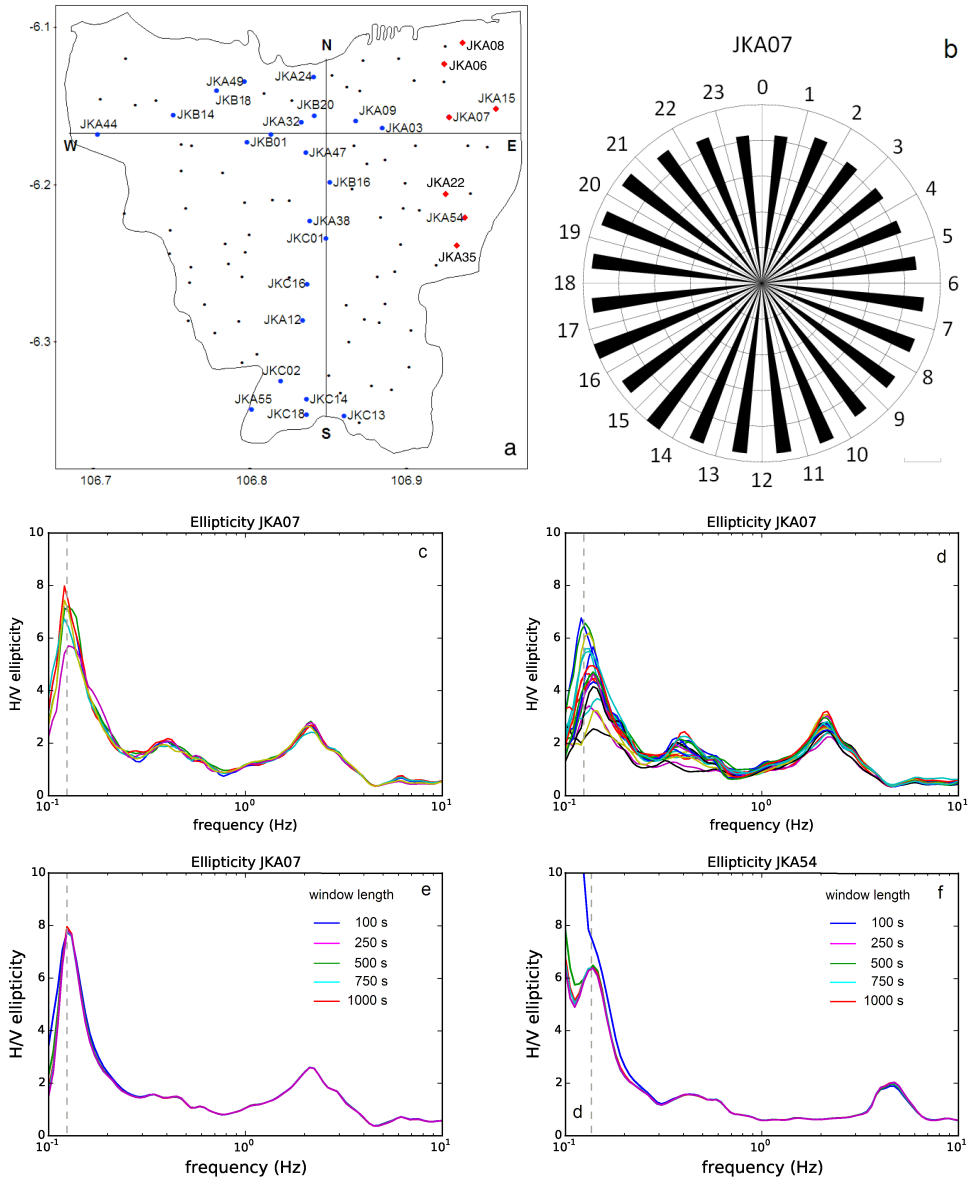

Figure 4.2: (**a**) Distribution of stations indicated as black dots while blue dots indicate stations mentioned in the text and red diamonds are stations which profiles are shown in Fig. S4 in Supplementary Material. The horizontal (WE) and vertical (SN) lines indicate the transect lines used in Fig. 4.5. (**b**) The variation in peak frequency over 24 hours, the longer the bar, the higher the peak frequency (in range 0.0 to 0.145 Hz), and numbers 0–23 indicate hours. (**c**, **d**) Comparison between elipticity curves recorded at quiet (10 pm–4 am) and busy (4 am - 10 pm) times, respectively, at JKA07. Dashed-line indicates average peak frequency computed from quiet times in a week. Each color represents the time of measurement. (**e**, **f**) For most cases, in order to measure reliable HVSR curves at about 0.1 Hz, a window-length of 100 s as suggested by SESAME is enough. However, for a few cases, window-lengths of 750 s or longer are needed. Color represents window-length used in the analyses.

4.3.1 Assumptions

Foremost among our assumptions is that the HVSR curves we estimate are determined by the ellipticity of the fundamental mode Rayleigh wave. It is important to note that in general the ambient seismic noise wave field consists of body waves (P and S) and surface waves (Rayleigh and Love) (e.g. [*Bonnefoy-Claudet et al.*, 2006]). Indeed, the original explanation of the HVSR method as proposed by *Nakamura* [1989] was that it is determined solely by the SH-wave resonance. However, subsequent studies showed that the HVSR curve is closely linked with Rayleigh wave ellipticity (e.g. *Lermo & Chavez-Garcia* [1994]; *Lachet & Bard* [1994]; *Fäh et al.* [2001, 2003]). Failing to account for other, non-Rayliegh wave components of the ambient seismic noise can lead to an overestimation of the Rayleigh wave ellipticity [*Poggi et al.*, 2012; *Hobiger et al.*, 2013]. Following the conclusions of the comprehensive review of the nature of the seismic ambient seismic noise wavefield by *Bonnefoy-Claudet et al.* [2006], our assumption that the ambient seismic noise wavefield is dominated by the fundamental mode Rayleigh wave is supported by the proximity of the ocean, both the Java Sea to the north and the Indian Ocean to the south. This suggests that the dominant sources of seismic noise will be associated with Rayleigh waves excited by ocean swell [*Yamanaka et al.*, 1993; *Longuet-Higgins*, 1950]. The long period, 5-7 s, of the main peak in our HSVR curves (see below), and even the higher frequency peaks at 2-4 Hz are likely associated with this natural source of Rayleigh-wave energy, especially since we used measurements made at night and verified their stability.

Our assumption that the fundamental mode is dominant is supported by the ANT study of *Saygin et al.* [2016]), who used this same dataset and noted that possible higher order Rayleigh wave modes arriving before the dominant fundamental mode had a much lower signal to noise ratio. While several studies that use HVSR to invert for V_S profiles have obtained satisfactory results using only the fundamental mode Rayleigh wave [*Yamanaka et al.*, 1994; *Konno & Ohmachi*, 1998; *Scherbaum et al.*, 2003], other studies have found that higher modes can make an important contribution to the HVSR curve, particularly when low-velocity zones are present [*Arai & Tokimatsu*, 2004; *Parolai et al.*, 2005; *Savage et al.*, 2013; *Rivet et al.*, 2015]. The emergent higher mode Rayleigh waves are usually related to peaks above the S-wave resonance frequency, hence the secondary and later peaks should be treated carefully because they may be contaminated with higher mode energy [*Asten et al.*, 2004].

Finally, we note that we assume the velocity structure beneath the station can be approximated by a set of horizontal layers, each uniform in seismic velocities and density. Previous studies (see, e.g. *Ridwan et al.* [2016]; *Saygin et al.* [2016, 2017], although these studies themselves assumed a locally 1D approximation) suggested that the seismic velocity structure in the Jakarta Basin is slowly varying, except for a possible sharp increase in depth from about 300 to 500 m in central Jakarta along the South-North profile (see Fig. 13.1 of *Saygin et al.* [2016]). The influence of 3D structure on HVSR curves has been studied by *Uebayashi et al.* [2012a,b] for Osaka Basin and *Guéguen* [2007] for the Grenoble Basin, who have noted that the 3D structure can lead to peaks in HVSR curves that are broader than those predicted from the 1D velocity profile beneath the station, and can also shift the peak HVSR frequencies by 10-20% or more. Thus, care should be taken in interpreting our HVSR curves both at the edges of the Jakarta Basin and in at the putative sharp increase in depth near central Jakarta.

4.3.2 Data

Prior to the seismometer deployment whose data are used here, the only previous seismographic study covering the Jakarta Basin was that of *Ridwan et al.* [2016] and *Ridwan* [2016], who used short-period sensors to estimate surface wave dispersion curves in the frequency range 0.2-3.0 Hz using the SPAC method [*Aki*, 1957]. The considerable depth to basement (>700 m) and the low velocities of the sediments comprising the basin (≈500 m/s) found by *Ridwan et al.* [2016] and *Ridwan* [2016] suggested that the seismic records from broadband seismometers may be more useful in modeling its interior geometry. To this end, 52 3-component, broadband sensors were deployed at various sites throughout Jakarta from October 2013 to January 2014 [*Saygin et al.*, 2016]. In order to cover the basin at an average inter-station spacing of about 2 km, 26 seismometers were re-deployed successively at 44 locations every three months. In total, 96 seismic stations were installed, with seismic ambient seismic noise recorded over intervals ranging from 1 to 3 months.

The data from this broadband experiment was used in an ambient seismic noise tomography (ANT) study to image the shear-wave velocity structure of the Jakarta Basin [*Saygin et al.*, 2016], as well as in a study of P-wave reflectivity from autocorrelation of seismic noise [*Saygin et al.*, 2017]. However, both of these studies have limiting resolving power for the basement: the long wavelengths of the ANT study precluded imaging of sharp discontinuities, and the P-wave reflectivity P-wave reflectivity method lacked an advanced modeling framework. In this study, these same ambient seismic noise recordings are used to compute HVSR curves, and an inversion is applied to these curves to obtain a velocity profile at each station.

Since both the ANT study of *Saygin et al.* [2016] and the SPAC study of *Ridwan et al.* [2016] suggest that slow shear-wave velocities extend to a basin depth of 500-700 m or more, it was important for the data processing to resolve the HVSR at periods of 5 s or longer. While HVSR studies typically use a time window of around 100 s duration (see e.g. *SESAME* [2004]), we tried to ensure stability of our long-period H/V curves by using time windows of 1000 s duration (see Fig. 4.2**a**–**f**). We note that *Langston & Horton* [2004] suggested a 600 s window to retrieve fundamental frequencies near 0.1 Hz in the Mississippi Embayment. We used the Geopsy software [*GEOPSY*, 2006] to compute the HVSR curves in the frequency range from 0.1 to 10 Hz as shown in Fig. 4.2. In general, the observed peak frequencies and amplitudes at each station changed slightly with time, but using measurements at quiet times (i.e. from 10 pm to 4 am, see Fig. 4.2) resulted in very stable curves, for peak frequency as well as amplitude. For most stations, a 100-second time series window resulted in reliable HVSR curves. However, for stations JKA54 and JKA42, a window-length of 750 s or higher was needed. Therefore, for consistency, a 1000 s window-length was applied for all stations.

Raw spectra often show narrow modulations and spikes that lead to extreme values of HVSR. To mitigate this effect, the smoothing operator proposed by *Konno & Ohmachi* [1998] was introduced. Also, the ratio between the average level of signal amplitude over a short period of time (STA) and long term average (LTA) is used as a parameter to exclude transient signals. The STA and LTA are set to 1 s and 30 s, respectively, and only windows with STA/LTA ratio between 0.2 and 2.5 were used for the HVSR computation.

4.4 HVSR Curves

HVSR curves show peaks for certain dominant periods that are diagnostic of the impedance contrasts in the underlying velocity structure. Peaks in the HVSR curve are typically associated with zeros in the vertical component Rayleigh wave, at frequencies where the sense of motion switches from prograde to retrograde or vice versa, and the Rayleigh wave is horizontally polarized (see e.g. *Konno & Ohmachi* [1998]; *Berbellini et al.* [2016]). Such peaks typically coincide with the fundamental resonant frequency f_0 of S-waves in the sedimentary column, given by period $f_0 = {}^1/_4\ V_S/h$, where h is the depth to to a strong impedance contrast and V_S is the shear velocity of basin sediments.

In this study, we found that the HVSR curves were typically characterized by two peaks, one a low-frequency peak in the range 0.1-0.3 Hz which we denote f_0^l and a high-frequency peak above 1 Hz, which we denote f_0^h. We found that our observations could be broadly classified into four groups: **(1)** the absence of any peak (i.e. a flat HVSR curve, or no peak with amplitude > 2) which may reflect the absence of a strong impedance contrast due to gradual compaction of the rock during self-loading, as observed at site JKC13 (Fig. 4.3**a**); **(2)** a sharp and high peak at a f_0^l, followed by another sharp and quite high peak at f_0^h between 1 and 2 Hz, as observed at site JKA49 (Fig. 4.3**b**) recorded in the northern basin where the Holocene alluvium overlies older alluvial sand; **(3)** a sharp and high peak at a f_0^l, followed by a second peak at f_0^h higher than 2 Hz (Fig. 4.3**c**), observed in stations near alluvial fan deposits or along an alluvium boundary where river channel deposits slice through alluvial fan, or where beach ridges are deposited over alluvium; and **(4)** a single peak at f_0^l, as observed at alluvial fan sites such as JKC01 as shown in Fig. 4.3**d**.

Types 2-3 are all characterized by sharp f_0^l peaks, while Type 4 includes both sharp and broad f_0^l peaks. We distinguish between these sharp and broad f_0^l peaks in the following section. Overall, most of the stations having lowest f_0^l (0.12-0.13 Hz) are located in areas predominantly composed by recent alluvium, however, a less clear correlation between f_0^l and surface geology is shown in Fig. 4.3**e**.

4.4.1 Sharp f_0^l peaks

Almost all the stations recorded sharp HVSR peaks in the frequency range 0.1-0.2 Hz, except for the southernmost stations. These sharp f_0^l peaks suggest a strong and deep impedance contrast. A high and narrow peak indicates a strong and sharp impedance contrast [*Gosar*, 2010]. The greater the magnitude and sharpness of the contrast in lithology, the higher and sharper the peak in the HVSR curve is expected to be [*Tarabusi & Caputo*, 2016].

While observed f_0^l range from 0.124 to 0.249 Hz, the frequencies of the f_0^h peaks range between 1 and 6 Hz or are absent. Generally, the stations in the south have f_0^l peaks that are lower and broader, and centered at higher frequencies than the f_0^l peaks for stations in the north. The broad peak amplitude may reflect the irregular structure of the basin floor, the stratigraphic complexity at depth or the unconformity between younger volcanic and older marine formations. At JKC18 where the Plio-Pleistocene volcanic rocks and alluvial fan are underlain by Tertiary marine formations, a broad HVSR curve was recorded.

In the north, the absence of Pleistocene volcanic rocks should result in a significant impedance contrast between the Tertiary basement and overlying soft sediment. Near

the surface, the broad variability of f_0^h indicates a corresponding variability of surficial sediment thickness. This also suggests variability in short-period amplification level. On the other hand, the absence of an HVSR peak as shown in Fig. 4.3**a** may be related to a shallow stratigraphic horizon, or compaction that is gradual with depth and results in weak basement impedance contrast (it might also be due to bedrock outcrop, but little or no such outcrop exists in our study area). This implies that little or no amplification will occur [*Castellaro & Mulargia*, 2009a,b].

Cipta et al. [2018] have used 2D waveform modeling along a NS cross-section of the Jakarta Basin model developed here to show that very large amplification of ground motion (up to 1500% PGV) can occur for a large scenario earthquake on the Java Trench, with the thicker sediments in the north experiencing the largest amplification. However, the wedged shape of the basin edge as it shallows to the south also plays an important role in amplifying seismic waves (up to 1200% PGV), particularly for the intraslab earthquake scenario considered by *Cipta et al.* [2018]. For both the megathrust and intralsab scenarios, the spectral amplifications were most prominent in the period range 5-7 s, similar to that of the observed f_0^l HVSR peaks.

4.4.2 Broad f_0^l peaks

Lower amplitude and broader peak could reflect a weaker contrast or a more gradual discontinuity. A high variability of surface lithology may also cause a lower peak amplitude. A broad peak is also indicative of irregularity of subsurface structure *Uebayashi* [2003] and a broad asymmetric peak indicates variability in rock formation *Gosar* [2010].

Broad HVSR peaks at f_0^l as observed at stations JKA55 and JKC02 (Fig. 4.4) may be related to steeply dipping bedrock underlying shallow sediments [*Özalaybey et al.*, 2011] or variability of bedrock formation [*Uebayashi*, 2003; *Bonnefoy-Claudet et al.*, 2009; *Gosar*, 2010]. Broad HVSR peaks may also correspond to meaningful 2D or 3D variation in the bedrock-sediment interface. In such a situation, diffracted waves including body and surface waves, including Love and higher order Rayleigh waves may be present, so that our intrepretation of the HVSR curves in terms of fundamental mode Rayleigh waves in a 1D structure may not be reliable [*Bonnefoy-Claudet et al.*, 2009]. In any case, the study of such small-scale 3D structure is beyond our scope.

Broad HVSR peaks at f_0^l are recorded at the southernmost stations where the bedrock depth is expected to be shallow. The slightly bumpy topography decorated by low hills reflects the variation of underlying bedrock structure. In accordance to its proximity to the stream heads, this area is relatively closer to the basin rim, and as a consequence the bedrock depth is shallow. This geographic condition may lead to the emergence of broad f_0^l peaks at stations JKA55 and JKC02, as shown in Fig. 4.4. Similarly, broad HVSR curves are observed at stations in elevated areas in southwest Izmit Bay basin where the basin depth is about 200 m based on a gravimetric study [*Özalaybey et al.*, 2011].

4.5 HVSR peak frequencies and amplitudes

The HVSR technique is able to furnish estimates of the frequencies f_0^l and the corresponding HVSR peak amplitudes at each site. Both of these can potentially be used as proxies to map basement depth, and in Fig. 4.5**a** and **b** we have mapped the interpolated values of f_0^l and peak amplitudes, respectively. These both suggest a pattern of deepening basement from south to north that is very similar to the results of *Saygin et al.* [2016]. It

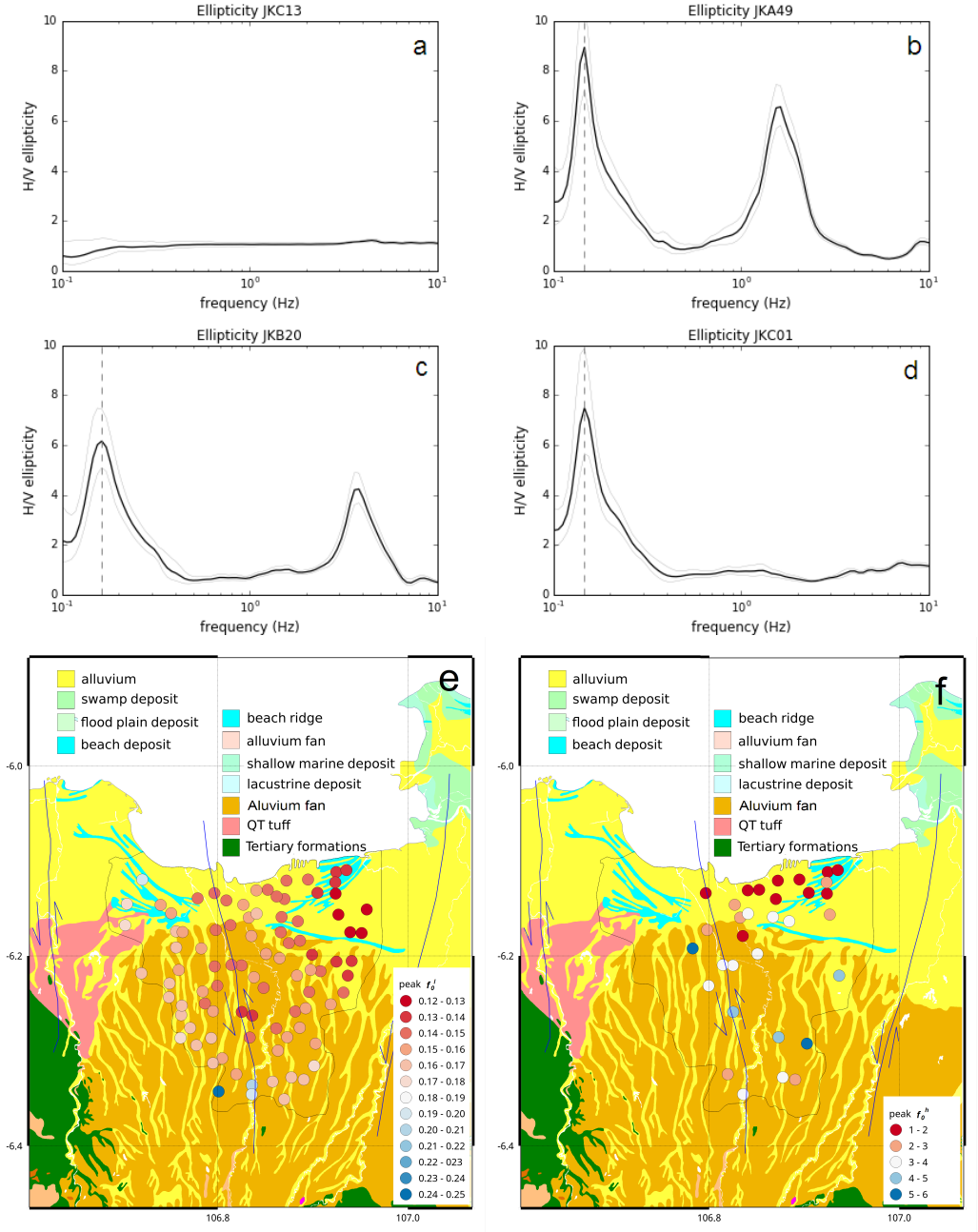

Figure 4.3: Ellipticity curves measured in Jakarta: (**a**) flat, (**b**) sharp peak at low frequency (<0.25 Hz) and another at a frequency between 1-2 Hz, (**c**) peak at low frequency (<0.25 Hz) and at frequency above 2 Hz and (**d**) peak only at low frequency (<0.25 Hz). Variability of the second peak (or absence of this high-frequency HVSR peak) roughly reflects surface geology. Fig. 4.3**e** and **f** show the distribution of low (f_0^l) and high-frequency (f_0^h) peaks, respectively, plotted on a geological map. Thin blue lines indicate Cisadane, Ciliwung and Kali Bekasi faults as mentioned by *Moechtar* [2015] and *Putra et al.* [2016]. Location of stations is shown in Fig. 4.2**a**.

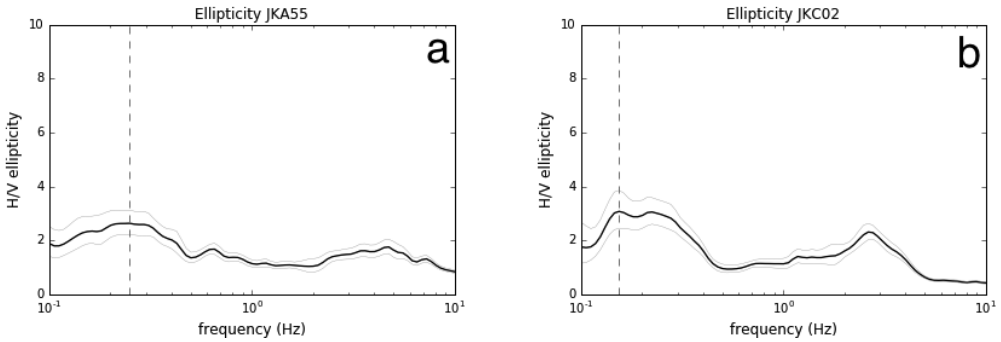

Figure 4.4: Curves showing broad peaks at f_0^l at stations JKA55 and JKC02, both located in the southernmost of the city where basin depth is shallow. Location of stations is shown in Fig. 4.2**a**.

is important to note, the simple kriging method is used to interpolate datasets and produce those maps. The kriging method considers the distance and the degree of variation between known data points when estimating values in unknown areas. However, at the data points themselves it may produce values that are slightly different from the observed data.

Maps of f_0^l and corresponding peak amplitudes (Fig. 4.5**a**, **b**, respectively) show two areas that exhibit both pronounced lows in peak frequency f_0^l and high peak amplitude: (**1**) the deepest part of the basin located in the northeast; and (**2**) the high peak amplitude passage crossing the city from the northwest to the southeast. The former coincides with high rates of subsidence [*Abidin et al.*, 2011] while the latter may reflect a fault or anticline axis.

Supplementary to f_0^l, higher-frequency peaks at f_0^h emerge at 33 stations. Stations that exhibit f_0^h peaks are distributed mostly in northern Jakarta where thin marine and terrestrial sediments overlie the stiffer and older alluvium. Recently deposited and intercalated marine and terrestrial sediments may form a relatively thin sediment layer which may be responsible for the f_0^h in the frequency ranges 1–2 Hz (Fig. 4.2**f**). We surmise that the high amplitude of these f_0^h peaks indicates a high impedance contrast between relatively young sediments and underlying stiffer alluvium in Fig. 4.3**b**–**f**, and Fig. 4.6**a**–**d**.

Higher-frequency (f_0^h) peaks also emerge at stations in the SN cross section indicated in Fig. 4.2**a** where alluvial fan deposits dominate the surface geology. In these stations, f_0^h appears at higher frequency (4–6 Hz) than those that emerge at northern stations. We speculate that self-compaction and near-surface weathering are the cause of the emergence of higher-frequency f_0^h peaks. Low amplitude (less than or equal to 3) at f_0^h (4–6 Hz) implies this geological phenomenon, where thin degraded alluvial fan is overlying the firmer soil (Fig. 4.4**b**, Fig. 4.3**f**, 4.6**a**–**d**).

In Fig. 4.6**a**–**b**, two-dimensional transects have been constructed which show the correlation of f_0^l and f_0^h HVSR peaks between adjacent stations, and illustrate how they vary in SN and WE directions. A sudden decrease of f_0^l is clearly visible in the south-north (SN) transect. In particular, f_0^l decreases from 0.223 Hz (JKC02) to 0.146 Hz (JKA12), indicating an abrupt change in basin depth over a distance of only 2.6 km. At the northernmost stations (e.g. JKA24), f_0^l has increased slightly to 0.154 Hz, over a distance from JKA12 of around 14.6 km. This suggests an abrupt increase in basement depth northward between JKC02 and JKA12, the basement then flattening up to the

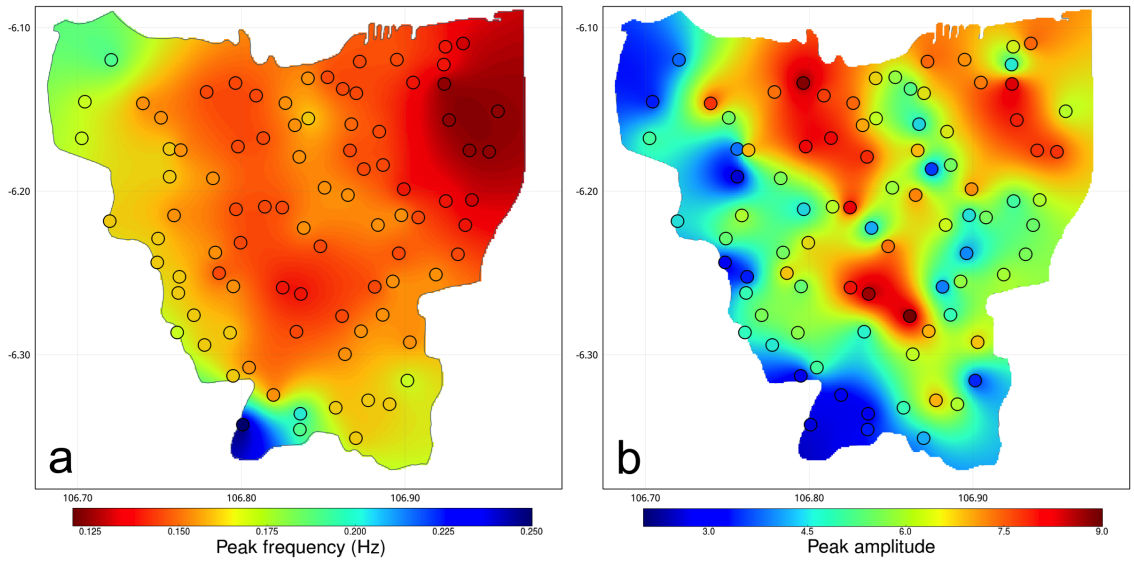

Figure 4.5: (**a**) Map of interpolated f_0^l frequencies, showing two prominent low-frequency areas (colored red) in the northeast corner and along a northwest-southeast passage. Colored circles indicate stations at which the corresponding peak frequencies were observed. (**b**) Map of interpolated f_0^l amplitudes, with colored circles indicting the stations where the corresponding amplitudes were observed.

central part of Jakarta and becoming slightly shallower to the north.

The West-East (WE) transect shows a complexity of near-surface layering, as reflected by the f_0^h peaks. Sites JKA44 and JKB14, located near and on Plio-Pleistocene tuff deposits, respectively, do not show clear f_0^h (Fig. 4.6**c**–**d**). The absence of f_0^h peaks suggest there are no strong impedance contrasts in the near-surface layering. Further to the east, as the surface geology changes from tuff to alluvial fan and alluvium with locally intercalated beach deposits, the f_0^h peaks are more pronounced. These f_0^h peaks appear at a frequency of 4 Hz except for stations JKA32 and JKA07 where they appear near 2 Hz. In addition, a smooth decrease of f_0^l is shown in the WE transect. The f_0^l at the westernmost station decreases towards the center, fluctuates and then decreases eastward. This pattern indicates a shallower basement in the west, undulating in the center and deeper in the east (Fig. 4.6**c**–**d**).

The peak frequency data from 93 stations covering Jakarta have indicated significantly low f_0^l in the northeast corner of the city, high f_0^l in the west and south and fluctuating values of f_0^l at the center. A low f_0^l patch along the NW-SE portion of central Jakarta is sandwiched within the 3 narrow patches of high f_0^l in the west, south and east. This gully-like feature is situated at high peak HVSR, with surrounding low peak HVSR within the vicinity. In general, the low f_0^l values in Jakarta corresponds to high peak HVSR and vice versa as depicted in Fig. 4.5.

4.6 Inversion of HVSR curve

Quantitative estimates of depth profiles of elastic properties such as shear-wave velocity V_S can be obtained through HSVR curve inversion, wherein it is typically assumed that the shape is determined by the Rayleigh-wave ellipticity. However, the nonlinear dependence of the HVSR curve on the depth profile of elastic parameters makes the inversion challenging.

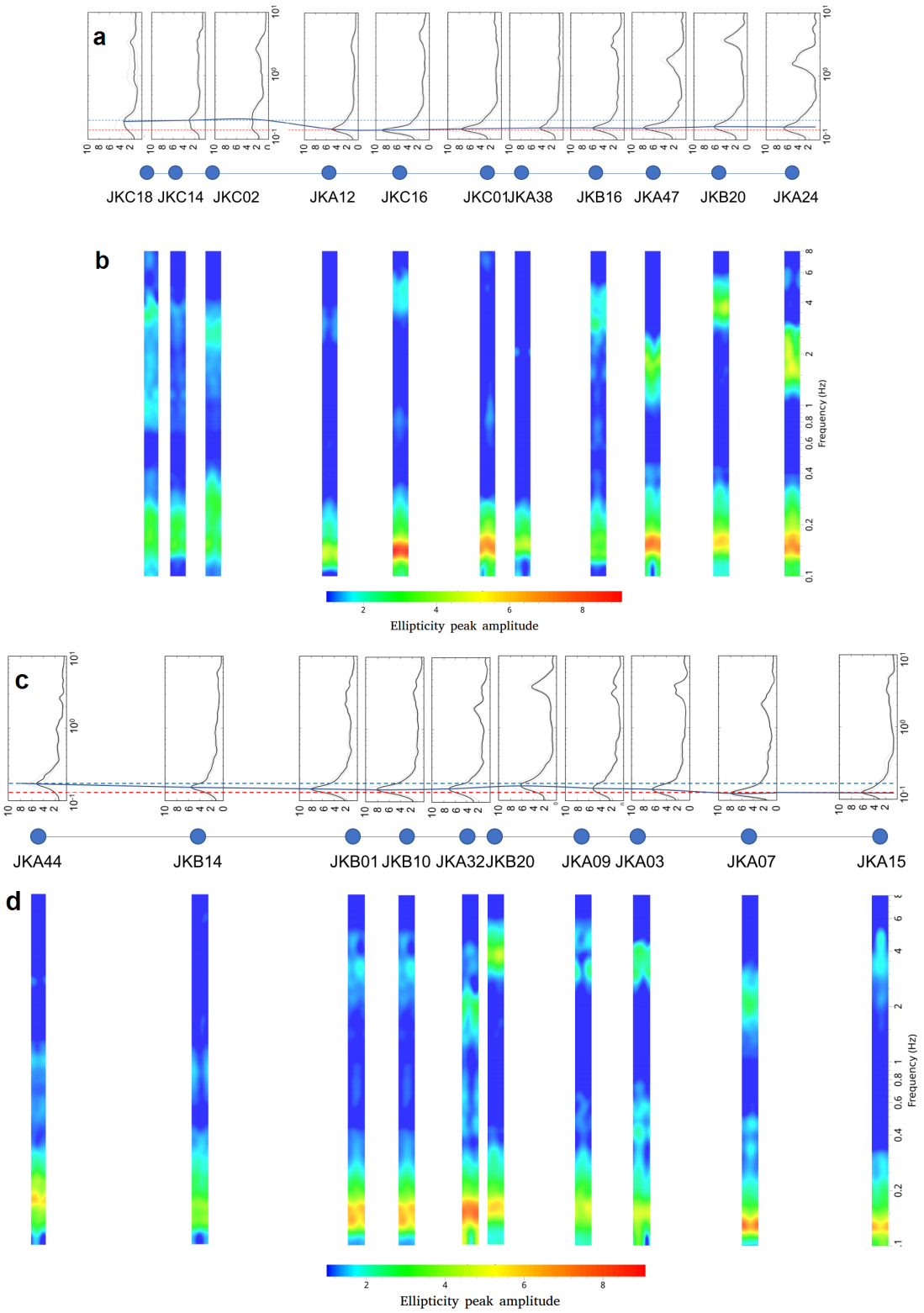

Figure 4.6: Comparison of HVSR spectra along the SN (**a-b**) and WE (**c-d**) transects indicated in Fig. 4.2**a**. The SN transect (**a-b**) shows that the frequency f_0^l of the low-frequency HVSR peak abruptly decreases at JKA12, then gradually increases at JKA47. This graph also illustrates the effect of the impedance contrast at shallower depth on the high-frequency peak amplitude in the ellipticity curve. The WE transect (**c-d**) shows highest f_0^l at the western end, lowest f_0^l at the eastern end, and variable f_0^l in the middle. Blue and red dashed lines are the highest and lowest peak frequencies (peak f_0^l), respectively, at corresponding cross-sections. The green solid lines show lineation of peak frequency and blue dots are stations indicated in Fig. 4.2**a**. The X-axis is the relative location of stations in the SN **(b)** and WE **(d)** directions, as indicated by blue dots in **a** and **c**.

Scherbaum et al. [2003] used a simple model in which V_S having a power-law dependence on depth overlies a half-space to invert HVSR curves for model parameters using a grid search. *Arai & Tokimatsu* [2004] developed a nonlinear least squares approach in inverting HVSR curves using multi-model Rayleigh wave ellipticity to resolve V_S profiles including low velocity zones. More recently sampling methods, with a fixed number of layers, are becoming widely used [*Fäh et al.*, 2003; *Wathelet et al.*, 2004; *Parolai et al.*, 2005; *Hobiger et al.*, 2013]. All of these methods use simplifying assumptions on the model, e.g. power-law depth dependence [*Scherbaum et al.*, 2003], fixed number of layers [*Fäh et al.*, 2003; *Parolai et al.*, 2005; *Hobiger et al.*, 2013], fixed V_P and/or density [*Scherbaum et al.*, 2003], restricted Poisson's ratio [*Hobiger et al.*, 2013] or fixed bedrock velocity [*Parolai et al.*, 2005].

A priori constraints on the complexity of velocity profiles in the Jakarta Basin present a problem, because we don't know how complicated they might be. The surface geology is dominated by poorly consolidated, water-saturated sediments with a basement at hundreds of meters depth. Thus, we expect the velocity profile to be complicated in the topmost 100 m of the profile, where water saturation will lead to a high Poisson's ratio that will decrease rapidly with depth along with an increase in seismic velocity due to compaction. Deeper than 100 m, there may be intervening layers of marine Pliocene and Quaternary sand and deltaic sediments until the basement is reached at several hundred meters depth or more. We would like to find the simplest model that can fit the data, but we do not know what minimum complexity is required, nor what the uncertainty is in our HVSR curves.

Bayesian inversion provides a framework to combine information on model parameters we have before making an observation with a probabilistic expression of data information to obtain an *a posteriori* probability density function (PDF) for the model parameters. To define the posterior distribution, Bayes' theorem [*Bayes*, 1763; *Sivia & Skilling*, 2006] is used, which is expressed as:

$$\text{posterior} = \frac{\text{likelihood} \times \text{prior}}{\text{evidence}}$$

More specifically, if we consider a model space consisting of a fixed number k of horizontal layers, each having a uniform distribution of S-wave velocity V_S^k, ratio of P- to S-wave velocity $(V_P/V_S)^k$, and density ρ^k, Bayes' theorem can be expressed for a data vector $\mathbf{d}$ and model vector $\mathbf{m}_k$ as:

$$P(\mathbf{m}_k|\mathbf{d}) = \frac{P(\mathbf{d}|\mathbf{m}_k)P(\mathbf{m}_k)}{\int_{\mathcal{M}} P(\mathbf{d}|\mathbf{m'}_k)d\mathbf{m'}_k} \tag{4.2}$$

where $P(\mathbf{m}_k|\mathbf{d})$ is the conditional probability of the model given the data (the "posterior"), $P(\mathbf{d}|\mathbf{m}_k)$ is the conditional probability of the data given the model (the "likelihood"), $P(\mathbf{m}_k)$ is the *a prior* probability of the model (the "prior"), and $\int_{\mathcal{M}} P(\mathbf{d}|\mathbf{m'}_k)d\mathbf{m'}_k$ is the probability of the data (the "evidence"). We note that in Bayesian inversion the evidence integral is typically regarded as a normalization constant and ignored, and the numerator of the posterior PDF can be explored using a Markov chain [*Mosegaard & Tarantola.*, 1995], which would sample over the space of models with k uniform layers. While it might be possible to perform multiple inversions for different values of k, and test the hypothesis that a model with k' layers is more plausible than one with k layers using the ratio of evidence values (Bayes' Factor), in practice computation of the evidence integral $\int_{\mathcal{M}} P(\mathbf{d}|\mathbf{m'}_k)d\mathbf{m'}_k$ is very time consuming, and this would not address the problem of

assessing how our lack of knowledge of an appropriate value for k contributes to model uncertainty.

Green [1995] showed that Bayes' rule can be written for a Bayesian hierarchical model to include a hyperparameter k:

$$P(k, \mathbf{m}_k|\mathbf{d}) = \frac{P(k)P(\mathbf{d}|k, \mathbf{m}_k)P(\mathbf{m}_k|k)}{\sum_{k' \in \mathcal{K}'} \int_{\mathcal{M}} P(k')P(\mathbf{d}|k', \mathbf{m}'_{k'})d\mathbf{m}'_{k'}} \tag{4.3}$$

where k can be interpreted as indexing possible choices of models, in our case models with different numbers of layers. As with Eq. (4.2), the denominator Eq. (4.3) can be regarded as a normalizing constant and ignored, and the posterior $P(k, \mathbf{m}_k|\mathbf{d})$ can be explored by using a Markov chain Monte Carlo approach to sample the numerator, as described in *Malinverno* [2002]; *Sambridge et al.* [2006]; *Dettmer et al.* [2010], and elsewhere. This "Trans-dimensional" approach allows a group of model parametrizations, in our case models with varying number of layers, to be considered simultaneously for analysis. Because all models are considered in the analysis, the Trans-dimensional approach allows us to account for how limited knowledge about the number of layers affects the parameter and uncertainty estimates based on the posterior. Inferences obtained in this manner avoid the inherent biases involved in selecting a single fixed number of layers and are hence more realistic and reflective of the state of knowledge about model parameters.

We invert our HVSR curves for depth profiles of elastic parameters using Trans-dimensional Bayesian inversion *Malinverno* [2002]; *Sambridge et al.* [2006]; *Dettmer et al.* [2010]. Since this statistical sampling method requires very rapid forward computations, we make use of the highly optimized forward computations of *Wathelet et al.* [2004], which parameterize the velocity structure as a stack of homogeneous layers overlying a half-space. We invert for the number of layers k as well as for V_S, V_P/V_S, ρ and thickness h in each layer. In addition, we use a hierarchical approach [e.g. *Bodin et al.* [2012]; *Dettmer et al.* [2012]] to estimate the noise (i.e., the value of σ) as part of the inversion.

Following *Dettmer et al.* [2012]'s Eq. 6, we use the likelihood function:

$$\begin{aligned} P(\mathbf{d}|k, \mathbf{m}_k) = & \frac{1}{(2\pi)^{N/2}|\mathbf{C}_d|^{1/2}} \times \\ & \exp\left(-\frac{1}{2}(\mathbf{d} - \mathbf{d}(k, \mathbf{m}_k))^T \mathbf{C}_d^{-1}(\mathbf{d} - \mathbf{d}(k, \mathbf{m}_k))\right) \end{aligned} \tag{4.4}$$

where $\mathbf{C}_d = \sigma^2 * \mathbf{I}$, with $\mathbf{I}$ the identity matrix and σ the noise standard deviation (the magnitude of the noise), and the data vector $\mathbf{d} = [HVSR(\omega_0), HVSR(\omega_1), ..., HVSR(\omega_n)]$. The modelled data vector $\mathbf{d}(k, \mathbf{m}_k)$ is the value of $HVSR$ calculated at frequencies $\omega_0, \omega_1, ..., \omega_n$ for the model having number of layers k and model vector $\mathbf{m}_k$ consisting of the layer parameters h^i, V_S^i, $(V_P/V_S)^i$, and ρ^i, where $i = 1, ..., k$. These layer parameters, as well as the number of layers k and the standard deviation σ, are unknowns in the inversion.

As described in more detail by *Dettmer et al.* [2012], this Trans-dimensional approach to model selection lets the data infer its own noise magnitude and model complexity. Although it involves no regularization such as model smoothing, *Malinverno* [2002] has shown that Bayesian model selection tends to "parsimony" in the sense that models with more complexity than is required to fit the data tend to be assigned low posteriori probability.

Besides the advantages of applying Trans-dimensional Bayesian approach, inher-

ent disadvantages are also embodied in this method. Trans-dimensional Bayesian does not tell us how to select the prior, since the results are heavily influenced by prior, less correct prior will lead to misleading results. In addition, it comes with expensive computational cost.

4.6.1 Synthetic tests

The importance of model selection with trans-D models on uncertainty quantification is illustrated with a simulation example in Fig. 4.7 and 4.8. Data were simulated for a 10-layer model which is representative of the expected complexity in the Jakarta Basin. In addition, Gaussian-distributed random noise with $\sigma = 0.07$ was added to the HVSR curve. In the true model, velocity rapidly increases with depth in the top 100 m due to compaction, after which there is little variation until a basement is reached at 900-m depth (white curve in Fig. 4.7**c**). This structure results in two peaks in the fundamental-mode Rayleigh wave ellipticity spectrum at 3.0 and 0.16 Hz, corresponding to the velocity increase in the top 100 m and the 900-m basin depth, respectively. Three inversions were carried out: (1) Figure 4.7 shows the results for trans-D inversion, where the number of layers in the model is treated as unknown. The prior for the number of layers was set as uniform between 3 and 20 layers. (2) Figure 4.8, shows results for an inversion were the number of layers was fixed at 3, which would generally be accepted as a reasonable choice and represents an under-parametrized inversion. (3) Figure 4.9 shows results for an inversion were the number of layers was fixed at 20, which represents an over-parametrized inversion and is expected to cause spurious, unconstrained structure. In both cases eight Markov chains were run in parallel and more than 100,000 posterior samples were recorded. The total number of steps was much larger, since only every 100^{th} step was recorded and half the initial steps were discarded as "burn-in". The prior was uniform and is given by the plot boundaries in Fig. 4.7. The bounds are wide so that data information predominantly constrains the solution. Convergence for these inversions was judged based on examining the chain history for all 8 chains. Since the chains are independent but sample the parameters in highly similar manner, convergence is likely.

The trans-D results in Fig. 4.7 show excellent agreement with the true model. Importantly, uncertainty estimates appear reasonable and increase substantially with depth, which is commonly observed for diffusive wave fields, such as Rayleigh waves. The data also appear to provide only limited information about selecting the number of layers for this site which results in substantial uncertainty in k and models with 7 to 15 layers all fit the data acceptably well. However, the posterior also shows clearly that the V_S marginal profile is parsimonious in that it captures an appropriate level of complexity without introducing spurious layers. The trans-D result also provides an excellent data fit and the noise standard deviation estimated by the inversion is close to the true value with some uncertainty from 0.06 to 0.10.

In the 3-layer case (Fig. 4.8), an apparently reasonable and well-constrained model is obtained. However, the estimated posterior bears little resemblance to the true model and uncertainties are estimated to be low and increase only slightly with depth. In addition, the estimated noise standard deviation is 4 times larger than the true value, a known issue for inversions with under-parametrized models [*Dettmer et al.*, 2009]. The large noise standard deviation is also reflected in the poor data fit.

In the 20-layer case (Fig. 4.9), the data fit is excellent and the noise standard deviation is estimated close to the true value. Such good data fits commonly boost con-

fidence in the inversion results. However, the posterior estimate does not represent the true model well. Rather, the results are plagued by very large uncertainties and erroneous, unconstrained structure. In conclusion, the trans-D results are far superior and this parametrization is appropriate for HVSR data. Importantly, the ability of HVSR curve inversion to resolve multiple V_S layers is encouraging for our application. The resolution of V_P/V_S and ρ is poor and we include these parameters in the inversion as nuisance parameters but will not interpret them further.

4.6.2 Inversion of Jakarta's HVSR curves

Out of the 96 stations with data, 93 stations were deemed useful in mapping the geometry of the Jakarta Basin. The trans-D inversion is applied to HVSR curves from these stations to obtain estimates of V_S profiles in this deep basin with an irregular bedrock-sediment interface. The HVSR curves are assumed to be a representation of fundamental-mode Rayleigh wave ellipticity over the frequency band of 0.1 to 10 Hz.

To assign the prior, we choose upper and lower limits for parameter values (k and V_S), based on existing geological knowledge (thickness and age of rock formations), boreholes, and hydrogeological investigations (depth and thickness of aquifers). The hydrogeological study of *Delinom et al.* [2009] found that underneath the Jakarta Basin, there are 3 groundwater aquifers at depths of 0–40 m, 40–140 m and 140-250 m, respectively. This may indicate that there are at least 3 distinguishable layers in the top 250 m of soil. The series of volcanic products and by-products, such as alluvial fans, that were deposited after the Plio-Pleistocene thrusting [*Kloosterman*, 1989], marked the early Quaternary sedimentation and likely have different density from underlying Late Miocene formations. In addition, an interface due to the Oligocene-Miocene tectonic period [*Turkandi et al.*, 1992] is expected. Therefore, we set a uniform prior on k between 3 and 20 layers, ensuring that the expected structure fits well within this prior specification. The prior for interfaces to occur is chosen to be uniform from 0 to 3000-m depth. The prior on V_S is chosen uniform between 100 and 4000 m/s to include a wide variety of sediment and rock types. Both density and V_P/V_S are treated as unknown nuisance parameters in the inversion. For density, the prior is set uniform between 1.5 and 4.0. Finally, the V_P/V_S prior is set uniform from $\sqrt{2}$ to 8, to include the potential of poorly consolidated, highly water-saturated sediments.

Figure 4.10 shows an example of inverted V_S profiles and observed and computed HVSR curves for station JKB18. Log likelihood, optimum number of layers and standard deviation are also presented. Figure 4.11 shows V_S results and HVSR curves for stations JKB20 and JKA12. The slim colored bands indicate the posterior probability (normalized at each depth level) and show that the prior information was substantially updated with data information which resulted in a narrow range of acceptable velocity-depth profiles. The data fits for these stations are also shown and show good fits to both the low- and high-frequency HVSR peaks.

The inversion procedure was repeated for the remaining 93 stations in identical manner. The maximum *a posteriori* V_S profiles from each station were then gridded with linear interpolation in 3D-space. Since all models featured an abrupt change in V_S from a value of 700-900 to 1500-2100 m/s at some depth that we interpret as basement, an iso-surface at V_S 1500 m/s was used to construct a basin depth model. On average, the depth of this iso-surface ranges from 700 to 900 m, although some western and eastern parts of the Jakarta Basin are significantly deeper than 1250 m, while more shallow basement

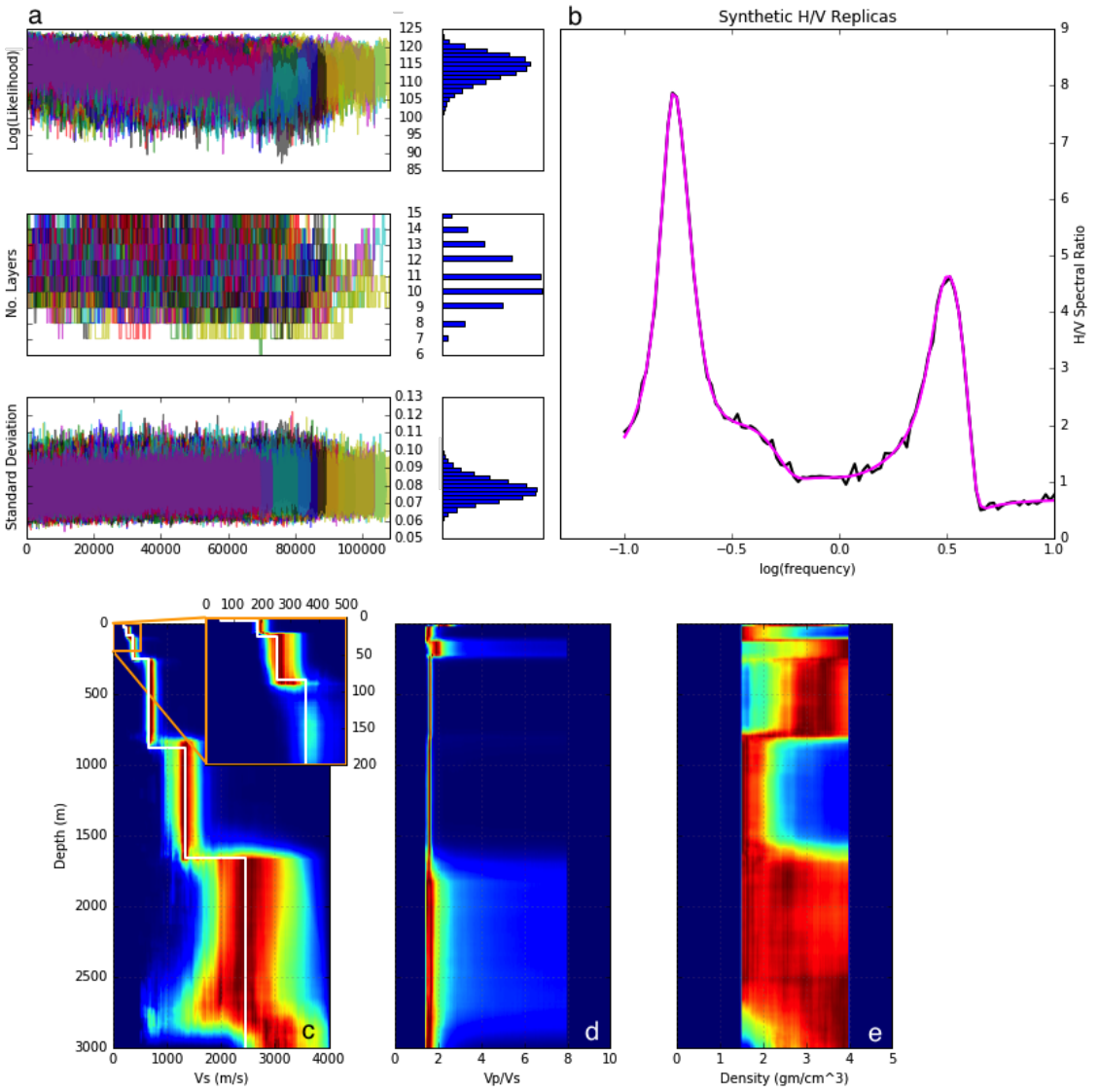

Figure 4.7: Results of a synthetic trans-dimensional inversion in which random noise with standard deviation of 0.07 has been added to forward calculations of an HVSR curve calculated using a 10-layer model (white curve). The top left panels (a), indicate log likelihood (top), number of layers (middle) and standard deviaton (bottom), for individual steps of the Markov Chain used to sample the posterior PDF. Each of the eight parallel Markov Chains is assigned a distinct color, so it can be seen that each chain is sampling a consistent distribution. (only every 100^{th} step in each chain was saved, and half the initial steps were discarded as "burn-in", leaving about 70,00-100,00 steps in each chain which are displayed). In (b), the synthetic data used as the observed (black curve) HVSR is displayed along with the HVSR curve for the model associated with the maximum sampled posterior PDF (magenta curve). The lower panels display histograms of the sampled models for V_S, V_P/V_S and density ρ in (c), (d), and (e), respectively. The inset of (c) shows detail for the shallowmost 200 m of the V_S profile. The white curve indicates the V_S used to produce the synthetic HVSR curve.

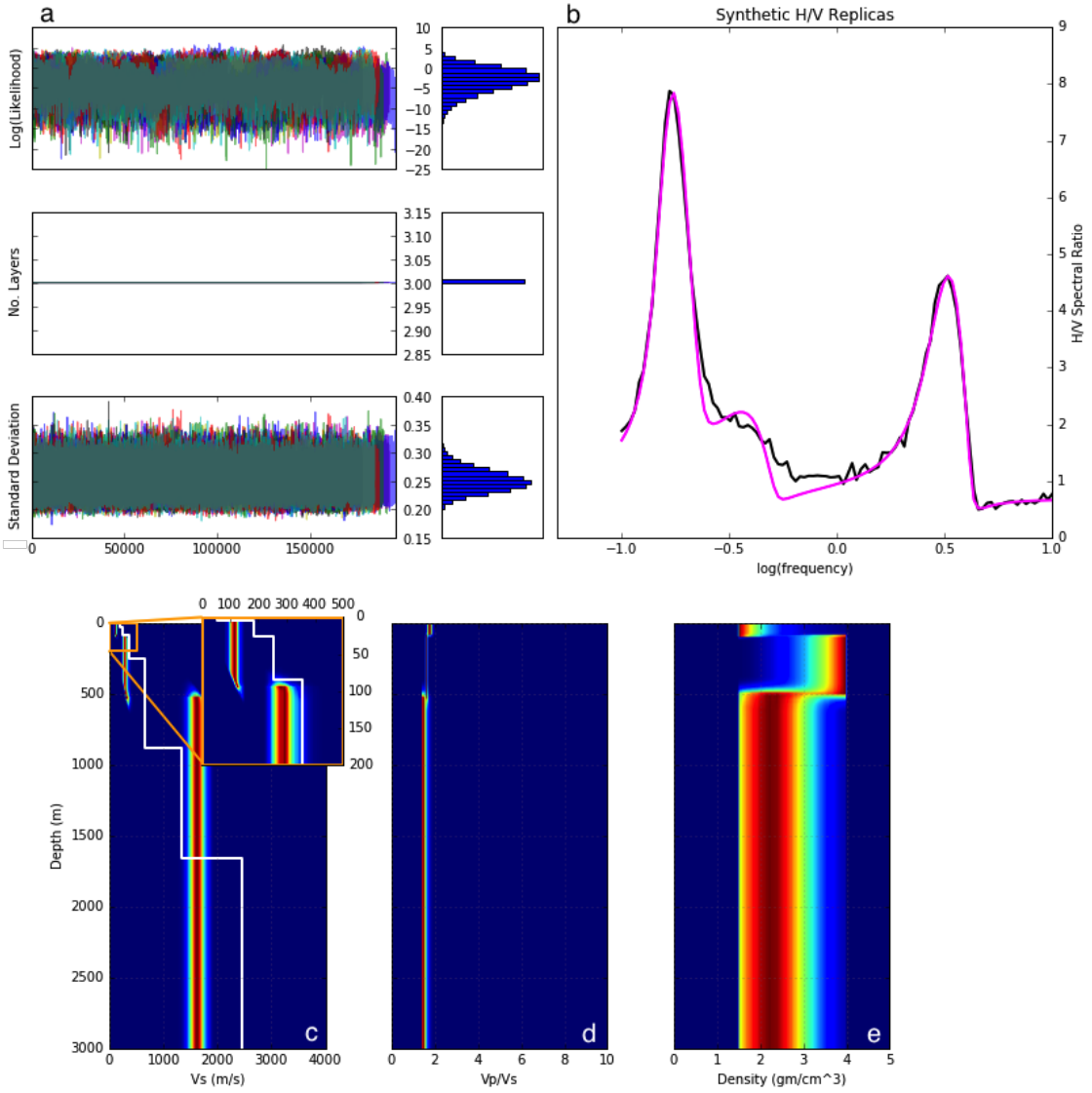

Figure 4.8: As for Fig. 4.7, but the number of layers in the inversion is fixed to three. This results in velocity profile far from the initial model and the inversion cannot recover the ellipticity curve, hence the noise level is overestimated (∼0.27 compared with the true value of 0.07).

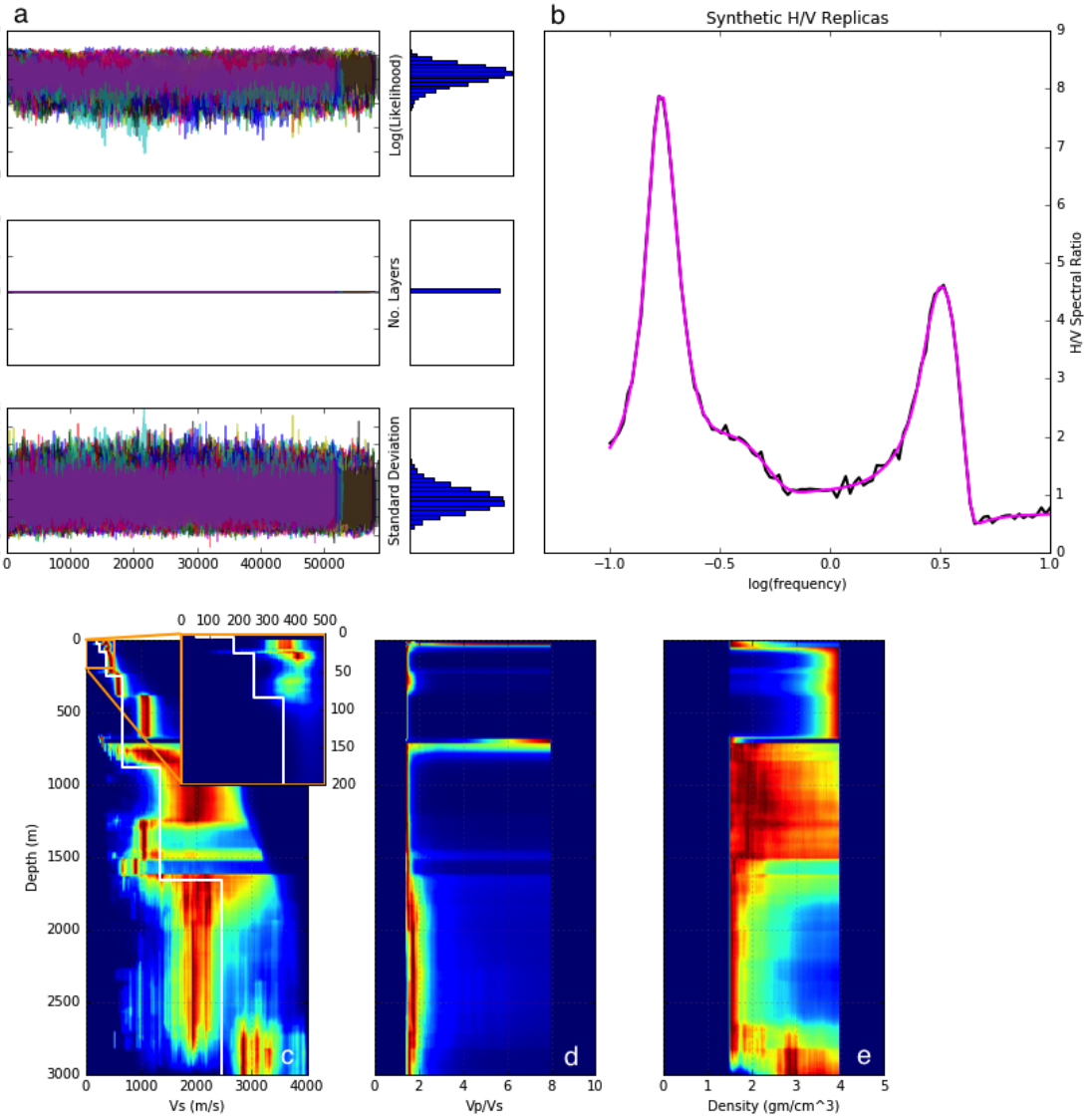

Figure 4.9: As for Fig. 4.7, but in contrast to the 3-layer model of Fig. 4.8, a 20-layer model recovers the ellipticity curve well. However the estimated velocity profile is much more complicated than the true one. The white curve indicates the velocity model used to produce the synthetic HVSR curve.

depths of ∼300 m or less are estimated in the south. In general, the southern part of the basin is shallower than the northern part.

A South-North (SN) transect of basin structure constructed by interpolating inversion results along the line indicated in Fig. 4.2**a** shows the variation in basement geometry (Fig. 4.14**a**). A zone of very low velocity (300 m/s or less) dominates the top ∼100 m, while the shear-wave velocity above the basement is less than 900 m/s, abruptly increasing to 1500-2100 m/s in the basement. Taking this as the basement-sediment boundary, in the the southern half of the city it is significantly shallower than the northern, with an abrupt increase in depth at around 6.24°S as depicted in Fig. 4.14**a**. These velocity profiles are in good agreement with the distribution of low-frequency HVSR peaks. The stations in the south, including JKC18, JKC14 and JKC02 recorded higher f_0^l (0.191–0.224 Hz), while the central stations, such as JKA12, JKC16 and JKC01, recorded significantly lower f_0^l (0.138–0.146 Hz), The northern stations, including JKA38, JKB16, JKA47, JKB20 and JKA24, recorded higher f_0^l (0.154 Hz) compared to the stations at the center, as shown in the same figure.

A shallow basin depth in the south has also been inferred from the surface geological data. At the head of the alluvial fan, the deposits are thinner with coarser grain-size components. Further from the head, along the gentle slope, thicker and finer grain-size sediments were deposited. This may explain the basement depth reaching a maximum depth in central Jakarta. The accumulation of younger marine sediments overlies the alluvial fan on the northern part of the city, which together with the alluvial fan and Pliocene-Pleistocene tuff fill the basin up to a thickness of 1300 m. The tectonic high known as Thousand Islands High in the north of the bay of Jakarta limits the sedimentation rates along the coastal plain. Consequently, sediment deposits are gradually thinning northward. Prograde depositions, both from the south and north, caused thick sedimentation in the center while thinning southward and northward as indicated in the basin depth map in Fig. 5.3.

4.7 Shallow-depth velocity profile

We have tested the ability of our HVSR inversions to recover details of shallow (<100 m) structure by comparing our HVSR-derived V_S profiles with those obtained by *Ridwan* [2016]. Of the 9 sites studied by *Ridwan et al.* [2017] at which both spatial autocorrelation of surface waves (SPAC) and Standard Penetration Tests (SPT, Fig. 4.13) were used to infer V_S profiles for the shallowmost 40 m of the soil profile, 7 (SKPR, PLGD, CLCG, ROTN, MLKS, RADJ and BMKG) are close (within 0.2 to 1.0 km) to 8 sites at which HVSR estimates of VS profiles have been made in this study. As shown in Fig. 4.13, the three methods resulted in comparable shallow velocity profiles at these sites. These comparisons indicate that a simple measurement like HVSR is able to produce reliable velocity profiles even within the top 40 m of the soil profile. However, due to the limited number of SPAC-NSPT-HVSR co-located stations, comparison among these three methods could not be made for whole city.

4.8 Discussion

Our study has shown that the Jakarta Basin, a Miocene basin filled with Pliocene-Holocene sediments, has thickness ranging from 300 m up to 1350 m. It is located approximately

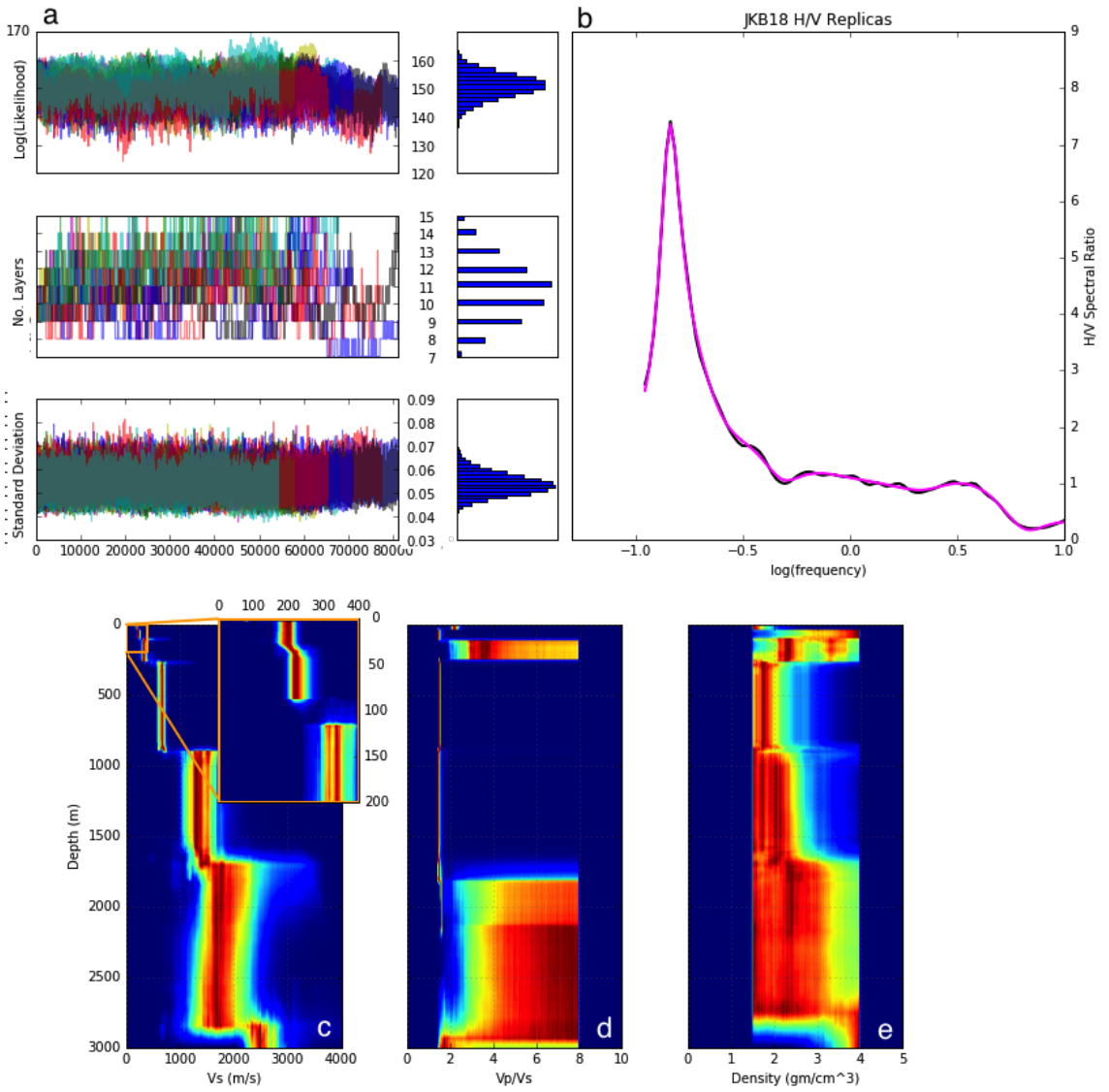

Figure 4.10: Transdimensional inversion that allows the data to determine the number of layers. The 11-layer model can recover the ellipticity curve well and shows a strong impedance contrast at a depth of about 950 m that may indicate basement depth. The location of JKB 18 is shown in (Fig. 4.2**a**).

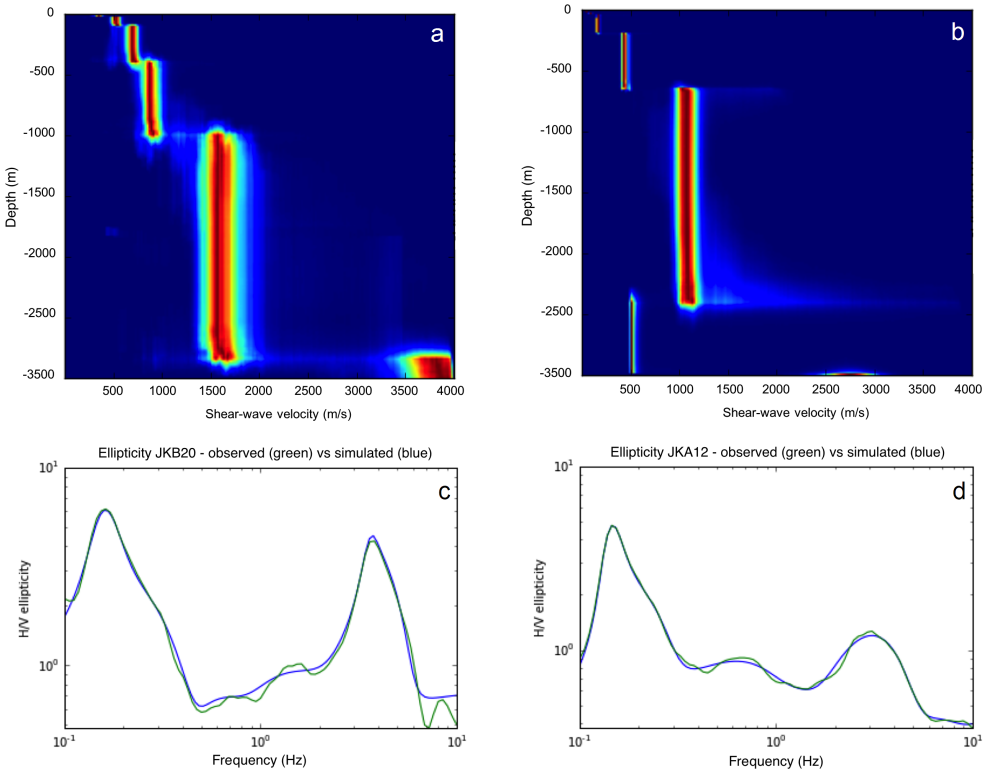

Figure 4.11: Inverted velocity profile at stations JKB20 (**a**) and JKA12 (**b**), the relatively thin colored bands near surface and broader in the deeper part indicate standar deviation broader as depth increasing, as expected. The very thin bar at depth more than 2300 m indicate that inversion can not resolve the data well (**b**). Computed ellipticity curves (green) at stations JKB20 (**c**) and JKA12 (**d**) fit observed ellipticity curves (blue) well.

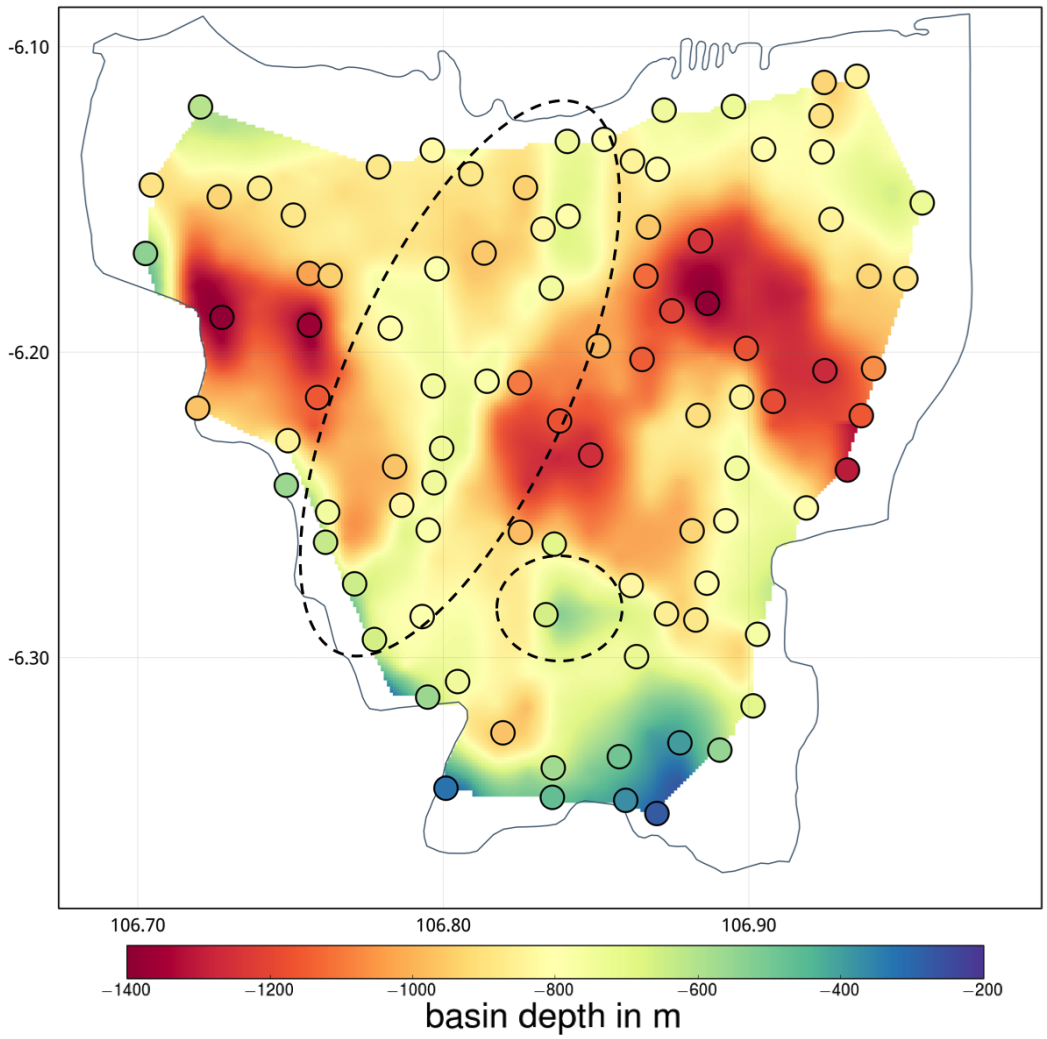

Figure 4.12: Considering velocity=1500 m/s as the basement, we can map the geometry of the basin. The basin depth ranges from 300 m in the southeast to more than 1300 m in the west and east. Colored Circle is actual data point resulted from inversion of HVSR, while areas surrounded by deeper bedrock-depth is indicated by black dashed-lines.

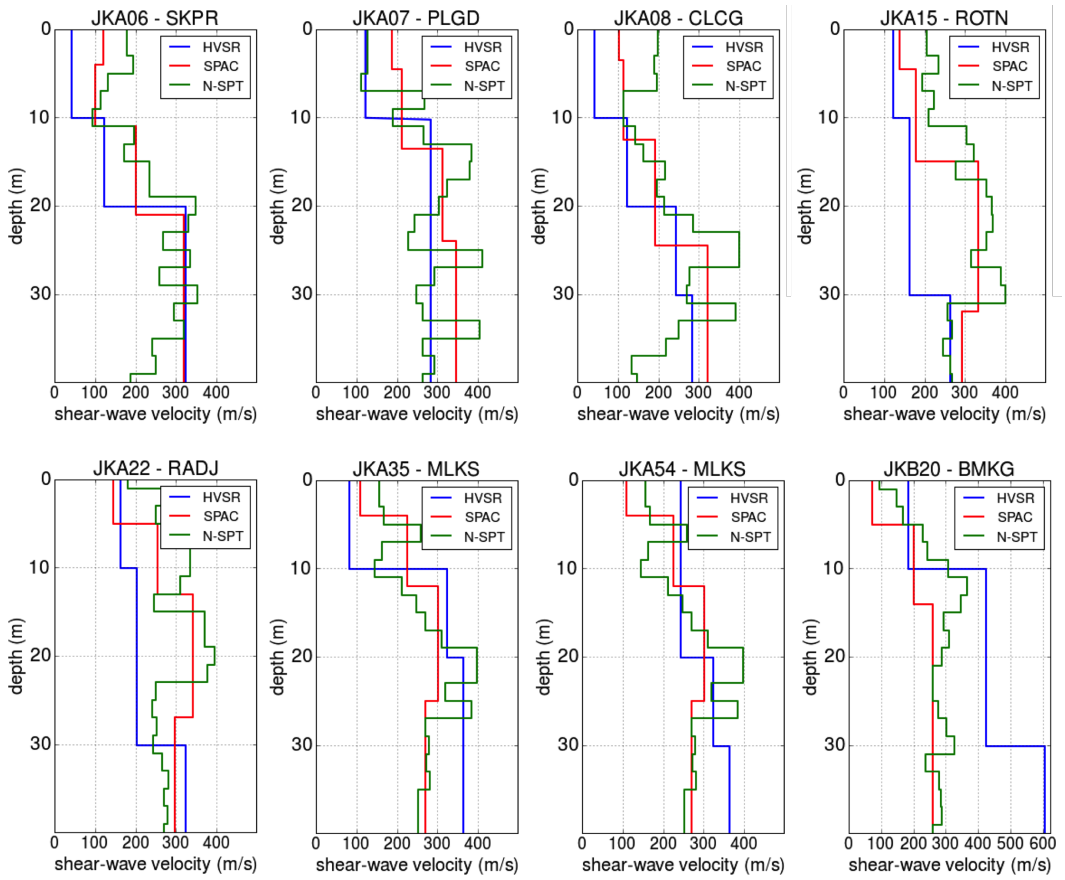

Figure 4.13: Shear-wave velocity profiles to the depth of 40 m obtained from HVSR, NSPT and SPAC techniques. Location of stations is presented in Fig. 4.2**a**

200 km from the Java subduction zone. The similarity in geology and tectonics suggests that Jakarta may experience significant building damage analogous to Mexico City if a high-magnitude subduction-zone or intraslab earthquake occurs. Further complicating the situation for Jakarta are 69 tall buildings (40+ storeys) that are currently in use, ranking Jakarta as 14th among the cities with the greatest number of buildings of at least 150 m height [*CTBUH*, 2017; *Emporis*, 2017]. Such high-rise buildings are prone to high shaking at 3 s or longer periods as was observed in Mexico City during the Michoacán Earthquake [*Flores-Estrella et al.*, 2007; *Padilla y Sanchez*, 1989].

Previous studies in the basins of southern California [*Magistrale et al.*, 2000] and the Lower Rhine Embayment [*Ewald et al.*, 2006] showed the importance of 3D basin geometry in modeling the characteristic basin propagation of seismic waves. Data from the 3D simulations of wave propagation are available including wave front focusing due to low velocity zones or edge-diffracted waves [*Ewald et al.*, 2006], basin resonance [*Castellaro et al.*, 2014], and local-scale multi-scattering and prolonged ground-motion [*Olsen et al.*, 2006; *Furumura & Hayakawa*, 2007; *Denolle et al.*, 2014,b; *Cruz-Atienza et al.*, 2016; *Viens et al.*, 2016]. Interesting research of *Roten et al.* [2014] found that non-cohessive shallow low-velocity sediments of Los Angeles Basin may may reduce seismic shaking generated by San Andreas Fault. Accordingly, a rigorous quantification of seismic properties and geometry of the Jakarta Basin is a prerequisite to generating a robust seismic hazard map for the city.

Given the basin model presented in Fig. 5.3, it is clear that there are some regions flanked by deeper depressions. A ridge-like structure (light-green: shallower depth), extending from the central-north coast to the southwest, is sandwiched by two deeper bedrock regions (yellow–red) on its northwest and southeast sides (dashed-lines). The southern basin is shallower but also exhibits significant topography, including a shallow "bump" in the basement that is surrounded by deeper sediment. In the case of the Lower Rhine Embayment, prolonged shaking is recorded in an area situated between 2 deep depressions. The dependence of seismic wave amplitude on basin depth was also observed in the Lower Rhine Embayment [*Ewald et al.*, 2006]. In Jakarta, this phenomena may occur in the northwest and northeast where the basin is very deep.

Profiling of velocity structure, sediment thickness and basin topography can also be accomplished via the joint inversion of HVSR and the surface wave dispersion curves, where the latter can be generated using auto-correlation [*Claprood et al.*, 2012] or multi-channel analysis [*Gorstein & Ezersky*, 2015; *Pandey et al.*, 2016]. As shown in Fig. 4.14**a**, our direct inversion of the ellipticity curve resulted in a velocity profile that is comparable with the results obtained using ambient seismic noise tomography (ANT) conducted by *Saygin et al.* [2016]. The advantage of ANT is its treatment of lateral variability, while in our HVSR analysis we have assumed locally 1D structure. However, the vertical resolution of our results is higher than the results presented by *Saygin et al.* [2016].

4.9 Conclusion

We have shown that the Horizontal-to-Vertical Spectral Ratio (HVSR) of seismic ambient seismic noise in the Jakarta Basin can be used to make robust estimates of the HVSR peak periods, which has been shown to coincide with the S-wave resonant period in many studies [*Lermo & Chavez-Garcia*, 1993; *Lachet & Bard*, 1994; *Bonilla et al.*, 1997; *Lunedei & Albarello*, 2010]. In Jakarta, these peak periods are in the range 4–8 s, with generally shorter periods in the south and longer periods in the north, in agreement with previous

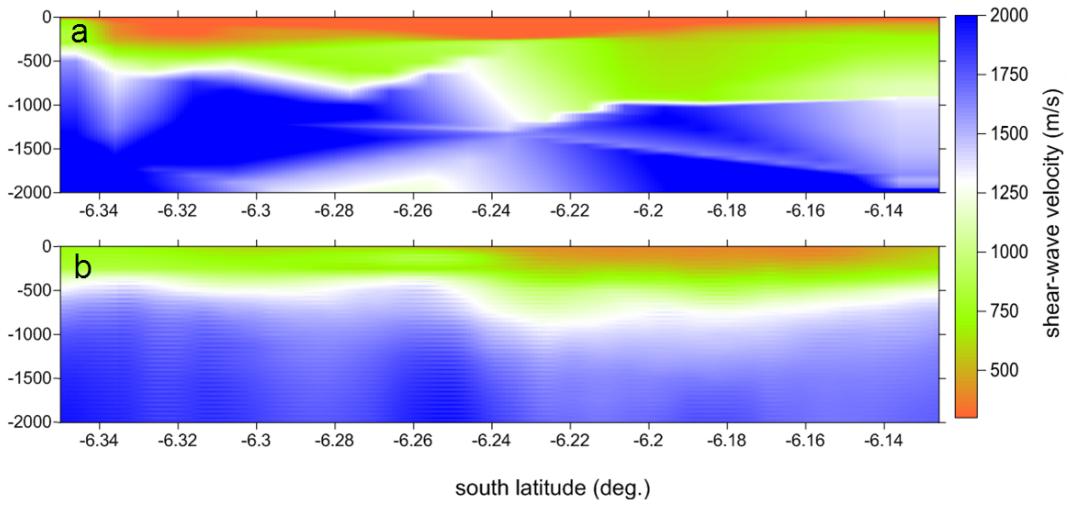

Figure 4.14: A drastic velocity change is apparent as velocity reaches about 1100 m/s. We consider this boundary to be the basement (white strip). Considering this white stripe as basement, it can be concluded that in southern Jakarta the sediment thickness reach 700 m and the thickest sediment accumulated in the center of Jakarta. A normal fault-like structure delimits the thinner sediment in the south from the thicker sediment in the north. Comparison between (**a**) HVSR and (**b**) ANT, in general, both methods resulted similar patterns, with the southern half of the city having significantly shallower basement than the northern half. An abrupt topographic change in basement depth is appears in the center of the cross-section. ANT and HVSR results were gridded using the simple krigging interpolation method. The location of the cross-section line (and its S-N direction) and measurement points are presented in Fig. 4.2**a**.

studies suggesting very low velocities extending to a basement at several hundred meters depth that deepens northward [*Saygin et al.*, 2016; *Ridwan et al.*, 2016; *Ridwan*, 2016]. S-wave resonant periods in this range are potentially a concern for very tall (40–80 storey) buildings, which are prevalent in Jakarta currently and whose number is expected to increase in the next decade.

Assuming the HVSR curve measured from ambient seismic noise in the Jakarta Basin is dominated by the fundamental mode Rayleigh wave, and is therefore an expression of its ellipticity [*Arai & Tokimatsu*, 2004; *Scherbaum et al.*, 2003; *Lachet & Bard*, 1994] we have also inverted this curve to estimate the S-wave velocity structure of the basin. In order to resolve both shallow velocity structure due to compaction of unconsolidated sediments as well as the deep basin architecture, we used Transdimesnional Bayesian inference, which not only allows the complexity of the model (in our case the number of layers) to adapt to fit the data, but also accounts for uncertainty in the model due to the unknown number of layers. At the same time the "Bayesian parsimony" feature of Bayesian model selection [*Malinverno*, 2002] assigns low *a posteriori* probabilities to models whose complexity is not required by the data. The dense seismic network we deployed in the Jakarta Basin enabled the mapping of basement topography, whose depth varies within the range 300-1400 m in a pattern similar to that obtained in previous studies using Ambient Noise Tomography [*Saygin et al.*, 2016] and SPAC [*Ridwan et al.*, 2016], respectively.

Previous studies using HVSR to infer basin structure have noted limitations of the type of HVSR analysis presented here. Several have noted the importance of using higher-order Rayleigh modes in fitting observed HVSR curves, particularly when

low velocity zones may present [*Arai & Tokimatsu*, 2004; *Asten et al.*, 2004; *Parolai et al.*, 2005; *Poggi et al.*, 2012; *Rivet et al.*, 2015]. Others have discussed the importance of also taking into account Love and body wave energy when interpreting the HVSR curve [*Arai & Tokimatsu*, 2004; *Sánchez-Sesma et al.*, 2011; *Salinas et al.*, 2014], as well as the importance of jointly inverting HVSR data with other datasets such as surface-wave dispersion curves to avoid some of the strong trade-offs in thickness vs. velocity model layers [*Scherbaum et al.*, 2003; *Parolai et al.*, 2005; *Hobiger et al.*, 2013]. Finally,*Guéguen* [2007] have discussed the difficulty in applying HVSR to basins with small aspect ratio. We agree that all of these are potential shortcomings of the approach we have taken in the present study, and for this reason regard our model of the Jakarta Basin as preliminary pending further investigation of these limitations. However, we believe that we have shown that the Transdimesnional Bayesian approach to inversion of HVSR data is an effective approach to this highly nonlinear inverse problem that is worthy of further study, especially in deep sedimentary basins like Jakarta.

Acknowledgement

Computations were performed on the Terrawulf cluster, a computational facility supported through AuScope and the Australian Geophysical Observing System (AGOS). We used geopsy software to compute HVSR curve, the source code can be downloaded from (http://www.geopsy.org/). Most of the figures are drawn using Generic Mapping Tools (Wessel & Smith 1998), python and QGIS (QGIS Development Team). We also thank Laurence Davies for crucial advice on the use of the *Wathelet*[2005] code for HVSR computation. We wish to express our gratitudes to Muriel Naguit for comments that helped improve the manuscript. We also thank the reviewers, who provided comments that greatly improved the paper. This work was partially supported by Australian Department of Foreign Affairs and Trades Grant 91982 and Australian Research Council (ARC) Linkage Grant LP110100525. I was supported by a scholarship from the Indonesian Ministry of Energy and Mineral Resources (MAK 020.01.01.1881.002.001.012 A.521219).

Chapter 5

Basin Resonance and Seismic Hazard in Jakarta, Indonesia

Abstract: We use earthquake ground motion modelling via Ground Motion Prediction Equations (GMPEs) and numerical simulation of seismic waves to consider the effects of site amplification and basin resonance in Jakarta, the capital city of Indonesia. While spectral accelerations at short periods are sensitive to near-surface conditions (i.e., V_{S30}, average shear-wave velocity at topmost 30 m of soil), our results suggest that, for basins as deep as Jakarta's, available GMPEs cannot be relied on to accurately estimate the effect of basin depth on ground motions at long periods (>3 s). Amplitudes at such long periods are influenced by trapping of seismic waves in the basin, resulting in longer duration of strong ground motion, and interference between incoming and reflected waves as well as focusing at basin edges may amplify seismic waves. In order to simulate such phenomena in detail, a basin model derived from a previous study is used as a computational domain for deterministic earthquake scenario modeling in a 2-dimensional cross-section. A M_w 9.0 megathrust, a M_w 6.5 crustal thrust and a M_w 7.0 intraslab earthquake are chosen as scenario events that pose credible threats to Jakarta, and the interactions with the basin of seismic waves generated by these events were simulated. The highest long-period PGVs amplifications are recorded at sites near the middle of the basin and near its southern edge, with maximum amplifications of PGV in the horizontal component of 726% for the crustal, 1500% for the megathrust and 1125% for the deep intraslab earthquake scenario, respectively. Amplification here is the ratio of ground motion in the soil to bedrock. We find that the levels of response spectral acceleration fall below those of the 2012 Indonesian building Codes's design response spectra for short periods (¡1 s), but closely approach or may even exceed these levels for longer periods.

5.1 Introduction

A number of methods are used to parameterize basin geometry for ground motion studies. These methods can be simply divided into 2 main approaches. The first approach uses basin depth as a function of a certain reference shear-wave velocity (Z) and the second approach is source-site specific. Recent Ground Motion Prediction Equations (GMPEs) describe basin depth as the depth to where shear-wave velocity reaches 1.0 km/s, denoted $Z_{1.0}$ (e.g. *Chiou & Youngs* [2008, 2014]), while *Campbell & Bozorgnia* [2014] uses $Z_{2.5}$,

which corresponds to the depth to a shear-wave velocity of 2.5 km/s to parametrize basin depth. The latter is thought to be a better description of basin depth [*Marafi et al.*, 2017]. In this study, the GMPEs from [*Chiou & Youngs*, 2008, 2014] and *Campbell & Bozorgnia* [2014] are used to compute ground motions triggered by a crustal earthquake while for the megathrust *Abrahamson et al.* [2016] and *Ghofrani & Atkinson* [2014] are used, and for intraslab events *Abrahamson et al.* [2016] and *García et al.* [2005], respectively, are used. In this chapter, these GMPEs are referred as CY2008, CY2014, CB2014, AEA2015, GA2014, AEA2015S and GEA2005, respectively.

The HVSR analysis of the previous chapter provides the model for the geometry of the Jakarta Basin that we use in this chapter to simulate more realistic seismic wave propagation. Long period ground motion modeling was carried out by means of 2D deterministic wave propagation with the SPECFEM2D software (*http://geodynamics.org/cig/software/specfem2d/*; *Komatitsch & Vilotte* [1998]), which uses the spectral element method. These simulations are conducted to evaluate the effect of Jakarta basin structure on long period ($\geq$4s) ground-shaking in the city of Jakarta. Scenario modeling includes a megathrust, a medium-depth intraslab and shallow crustal earthquakes. The main objective of this chapter is to analyse the effect of the deep sedimentary basin on amplification of long period ground motion spectra in the city of Jakarta. Long duration ground shaking is expected to build up due to seismic wave entrapment inside the basin [*Graves*, 1998] and the conversion of incident shear waves at the basin edge and/or walls [*Bard & Bouchon*, 1985].

The deep Jakarta basin is filled with alluvial fan and alluvium deposited continuously during the early Quaternary to the present day. Rapid subsidence of Jakarta soil due to water extraction – up to 26 cm per year [*Ng et al.*, 2012; *Abidin et al.*, 2011] shows the high extent of water saturation of sediment fill. Underneath these Quaternary sediments lie volcaniclastic deposits of Pliocene-Pleistocene age that are mainly composed of tuff and locally tuffaceous breccia, lava and lahar. Volcanic material has ben shown to strongly amplify seismic ground motion – as high as 50 times compared to bedrock sites – in Mexico City during the event of 1985 Michoacán Earthquake [*Cruz-Atienza et al.*, 2016]. In Jakarta, a combination of volcanic, alluvial fan and alluvium deposits as thick as 300-1400 m overlie Tertiary bedrock. By numerical modelling of multiple earthquake scenarios, we can assess the variability of ground motion and amplification effects caused by the combination of basin geometry and soft sediment with the different scenarios. Amplification here is described as the ratio of ground motion in the soil and bedrock.

The final basin model is established by using a paleo-topographic approach to identify the basin edges and extend the basin model derived from the HVSR method. This final basin model will be used in the computational domain for the SPECFEM2D code (*http://geodynamics.org/cig/software/specfem2d/*; *Komatitsch & Vilotte* [1998]). is a powerful software package for 2-dimensional modelling of seismic wave propagation at local or regional scales. It facilitates simulations of acoustic, elastic, anelastic and poroelastic seismic wave propagation. The spectral element method used by SPECFEM2D combines the flexibility of the finite element method (FEM) with the high accuracy of high-order basis functions. A diagonal mass matrix can be obtained due to the combination of discretisation and integration, which will greatly simplify the algorithm and reduce computing time. In this study, waves originating from a megathrust event (M_w 9.0) propagate from 1002 source points through 5-layer domain model. The other scenarios, a shallow M_w 6.5 crustal and a medium-depth M_w 7.0 intraslab earthquake, use a smaller number of source points and elements..

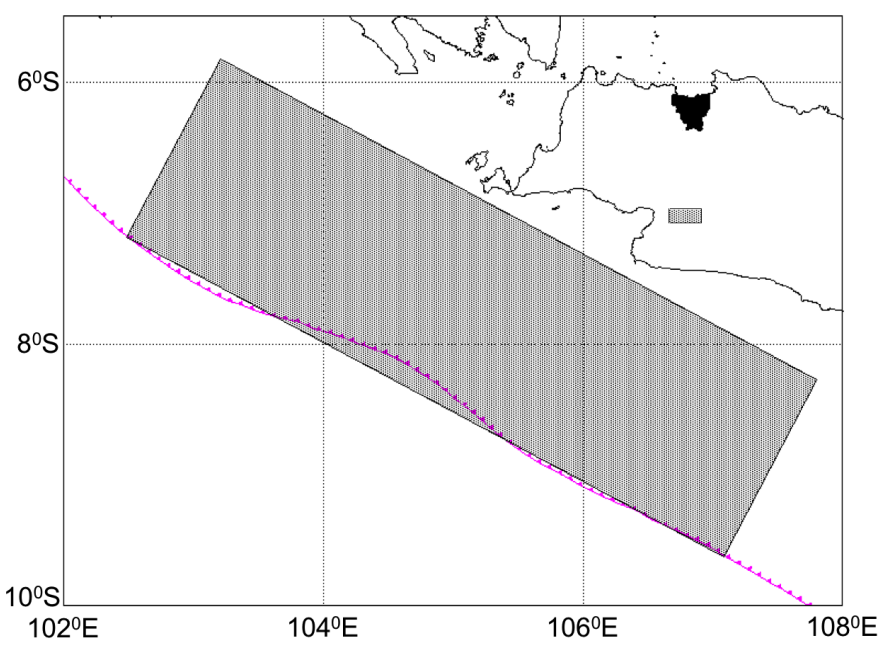

Figure 5.1: Location of Jakarta and earthquake scenarios used in the seismic waveform simulations. The black polygon, large grey rectangle, small grey rectangle and pink toothed line indicate Jakarta city, megathrust, crustal fault sources and Java Trench, respectively. Intraslab scenario source is located beneath Jakarta city with strike 90∘.

5.2 Tectonic Setting of Jakarta and Surroundings

Java island, where Jakarta is located, is part of the Sunda Arc that extends from the Andaman Sea in the northwest to the Banda Sea in the east. The Australian Plate is moving northward at a rate of 67 [*Simons et al.*, 1997] to 70 [*Hall*, 2009] mm/year and subducting beneath the Eurasian Plate. *Pusgen* [2017] estimated that the Sunda Strait and West-Central Java segments of the Sunda Subduction Zone can accommodate earthquakes as large as a M_w 8.7. These are the closest segments to Jakarta and located about 250 km from the city to the south. In the last decade, the West-Central segment produced 2 destructive earthquakes, namely the M_w 7.6 Pangandaran (2006) and the M_w 7.0 Tasikmalaya (2009) Earthquakes [*Pusgen*, 2017].

The tectonics and seismicity of Jakarta and adjacent areas is highly influenced by the the convergence of the Australian Plate toward the Eurasian Plate (Figure 5.2). Apart from producing megathrust earthquakes, the northward motion of the Australian Plate is also responsible for earthquake activity on shallow crustal faults, some of which are located near Jakarta such as the Cimandiri, Lembang and Baribis Faults. The Cimandiri Fault shows a dominant strike-slip movement with rake angle less than 15° and dip larger than 70° [Dardji et al., 1994]. The same author also observed high-angle reverse movement, and argued that permutation between strike-slip and dip-slip systems may happen over relatively short intervals along the strike of an active fault. Despite a disagreement regarding sense of movement, Dardji et al. [1994], Abidin et al. [2009], Supartoyo et al, [2013], Marliyani & Arrowsmith [2014] and Handayani et al [2017], using paleostress, GPS, morphometry, geomorphology and audio-magnetotelluric methods, respectively, conclude that the Cimandiri Fault is active and its segmentation limits the maximum magnitude of potential earthquakes.

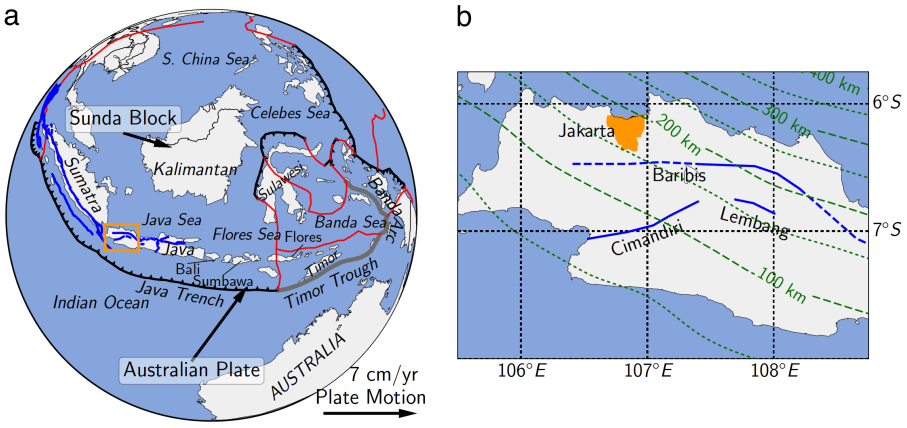

Figure 5.2: (**a**) Simplified tectonic setting of the Indonesian region and (**b**) western Java, with more detail of the inset area indicated in (**a**). The study area is the orange shaded area in (**b**). Motion of the Australian Plate at a rate of 7 cm a year toward the Eurasian Plate is indicated by a black arrow. Major faults are indicated by blue lines, while black toothed, red and green dashed lines denoted subduction, microcontinent boundaries, and Benioff countours, respectively. The blue dashed-line indicates the continuation of the Baribis fault to the west and east as mentioned in *Simandjuntak & Barber* [1996].

The 24 km length of the Lembang Fault with a slip rate of 2.0 mm/year is thought capable of producing a M_w 6.8 earthquake [*Pusgen*, 2017]. An earlier study by *Meilano et al.* [2012] indicates a larger slip-rate (6 mm/year) with fault locking at 3–15 km and this study also observed shallow creep at rate of 6 mm/year. During 2009–2015, there were 4 earthquakes recorded along the Lembang Fault, three of which showed left-lateral faulting, and an earthquake located at the eastern edge of the fault showed oblique slip with a normal-dominant movement [*Pusgen*, 2017].

The Baribis or Baribis-Kendeng Fault has been proposed as a major thrust and fold structure extending all the way across Java from the Sunda Strait in the west to beyond East Java in the east, and it is suggested that some segments are still active [*Simandjuntak & Barber*, 1996]. The strike-slip Cimandiri and Citanduy Faults cut across the Baribis-Kendeng Thrust near the border of West-Central Java and therefore it is not clear whether this is one single structure or is divided into the Baribis Thrust in the west and the Kendeng Thrust in the east. Koulali et al. [2017] suggest that the Baribis Thrust is accommodating convergence between Java and the Sunda Block at about 5 mm/year, while *Pusgen* [2017] show the the Baribis-Kendeng Thrust as a highly segmented system of faults starting from Subang in the west (north of the Lembang Fault) to Surabaya in the east. Each segment can accommodate earthquakes in the magnitude range M_w 6.0–M_w 6.5.

5.3 The Jakarta Basin

A model of the seismic velocity structure of the Jakarta Basin was constructed by *Cipta et al.* [2018] using analysis of Horizontal-to-Vertical Spectral Ratios (HVSR) of ambient seismic noise (Figure 5.3), but this model does not extend to the basin edges. The sediment deposits along the city border are thick, from about 200 m in the south, to 800 m in the west and more than 1000 m in the east. Because the model does not include the basin edges,

it is necessary to extend the model beyond Jakarta itself to estimated plausible margins of the basin, which are presumed to be the axes of low angle folds that will appear as topographic highs. For this purpose, geological data namely, the lateral distribution of lithology, drainage pattern and topographic information was utilized. A simple method to reconstruct the paleo-topography called the arc-method is used (for detail see e.g., *Allmendinger* [2017]). By comparing geological data and sediment thickness as presented in Figure 5.3, it is a reasonable guess to interpret the basement of the basin as the upper Parigi formation deposited in the Late Miocene. To construct a paleotopography, i.e., a topography before the more recent Cibuluh formation was deposited, we need to plot the strike and dip of the Parigi formation layering in a 2D cross-section.

The topographic map shows that Jakarta in particular and the north coast of West Java in general is an area of gentle slope (slope 1–10 %). The morphology and surface lithology of this area is well illustrated in its drainage pattern, an excellent example of a dendritic drainage pattern characteristic of gentle topography with homogeneous lithology. Careful analysis of the drainage pattern discloses the faint topographic highs to the west and east of the city. Most of the tributaries of the Cisadane River (1 In Figure 5.4) flow only from the west, while further to the west the Cimanceuri River (4 in Figure 5.4) flows from the south, veers westward then flows northward. These two rivers encircle a topographic high that can be identified with the western rim of the Jakarta basin. The geological map shows that near the Cimanceuri River (4 In Figure 5.4) the lithology is changing from aluvial fan Qav to QT tuff (north) and Oligocene-Miocene formations (south). This changing lithology confirms the hypothesis that the Cimanceuri River lies at the western rim of the Jakarta basin, in the slightly elevated land that is known as the Tangerang High as indicated in Fig. 5.5.

The Kali Bekasi River (3 in Figure 5.4) to the east of the city receives water intake mostly from the east, and further to the east the Citarum River (5 in Figure 5.4) flows from the south, turns to the east and circles back to the west, eventually flowing into the Kali Bekasi River and the Java Sea. This drainage pattern is indicative of a topographic high just east of the Kali Bekasi River, known as the Rengasdengklok High as indicated in Fig. 5.5.

The Kali Bekasi River also marks the boundary between two alluvial fan bodies, alluvial fan Qav to the west of the Kali Bekasi River, and alluvial fan Qav/Qos to the east of the river. The changing lithology and topographic high to the east suggest that the eastern rim of the basin is situated around the Kali Bekasi River.

Oil prospecting studies using the seismic reflection method have succesfully recognized five principal oil reservoir groups within the North West-Java Basin. These oil caps are (1) Eocene–Oligocene fractured volcanics (Jatibarang Volcanics), (2) Oligocene–Lower Miocene deltaic sandstones (Talang Akar Formation), (3) Lower Miocene reefs (Baturaja Formation), (4) Lower–Middle Miocene sandstones (Upper Cibulakan Formation), and **(5)** Middle-Upper Miocene carbonates (Parigi Limestones and Upper Cibulakan Formation) (*Kingston* [1988]). On the top of these reservoirs, the Parigi, Cibuluh and Quaternary formations were deposited successively, with a hiatus due to decreasing sea level separating these formations (Fig. 5.5). From these data, it can be inferred that the Jakarta Basin, also known as the Ciputat Basin, is part of the North West-Java Basin in which the basement is composed of carbonates of the the upper Parigi formation deposited in the Middle-Upper Miocene (Fig. 5.5)

The HVSR method imaged the velocity model within Jakarta Basin from surface to basement. However, the actual basin is larger than the available model. Therefore, to

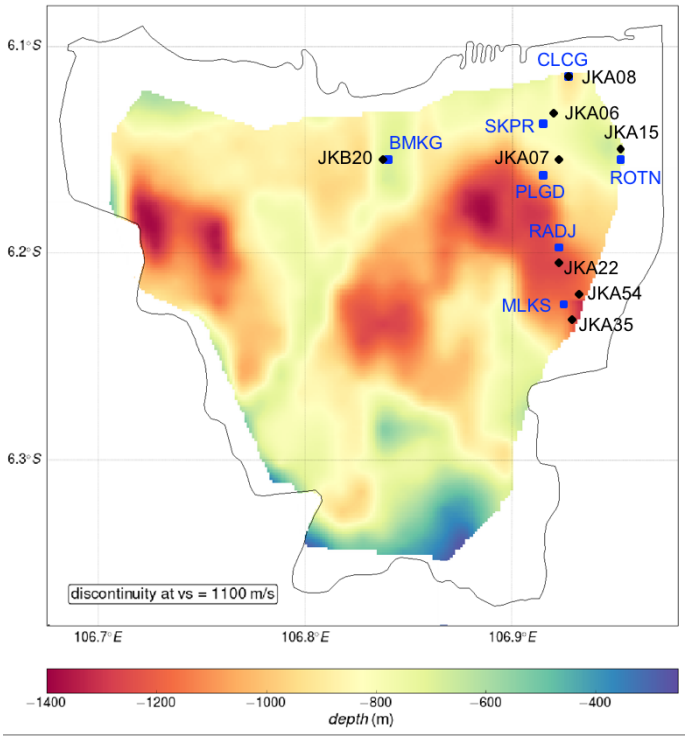

Figure 5.3: The bedrock-depth is defined as medium having shear-wave velocity $V_S = 1300$ m/s, hence the geometry of the basin is defined. The labelled black diamonds and blue squares are HVSR and SPAC co-located stations. The black rectangle is station where ground motion is calculated from SPECFEM2D simulation.

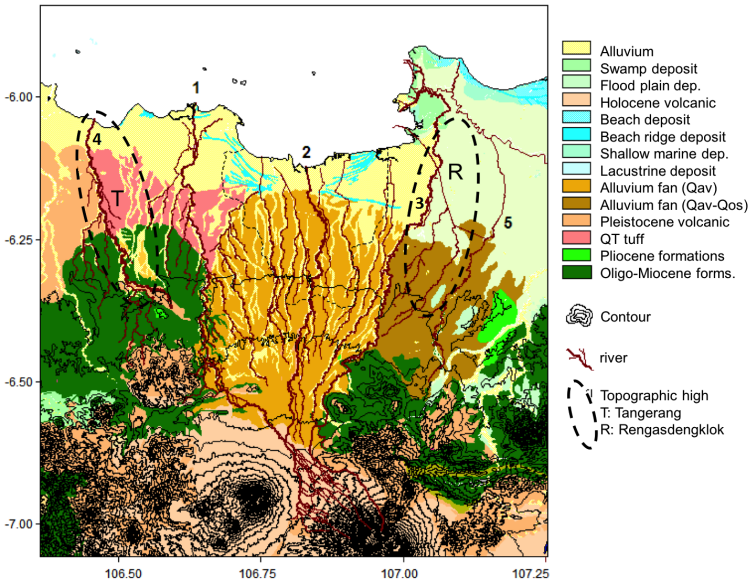

Figure 5.4: Contour lines and drainage patterns overlaid on a map of surface geology show the funnel-shaped basin, bounded by the Cisadane (1) and Kali Bekasi (3) Rivers in the west and east, respectively. Mountains from which the Cisadane (1), Ciliwung (2) and Kali Bekasi (3) Rivers sprout form the narrow base of a funnel-shaped topographic low with Jakarta Bay at its mouth. The Cimanceuri River is labeled as (4). The SN Line is the cross-section used in the numerical simulation. Tangerang and Rengasdengklok Highs are indicated by dashed lines, labeled T and R, respectively.

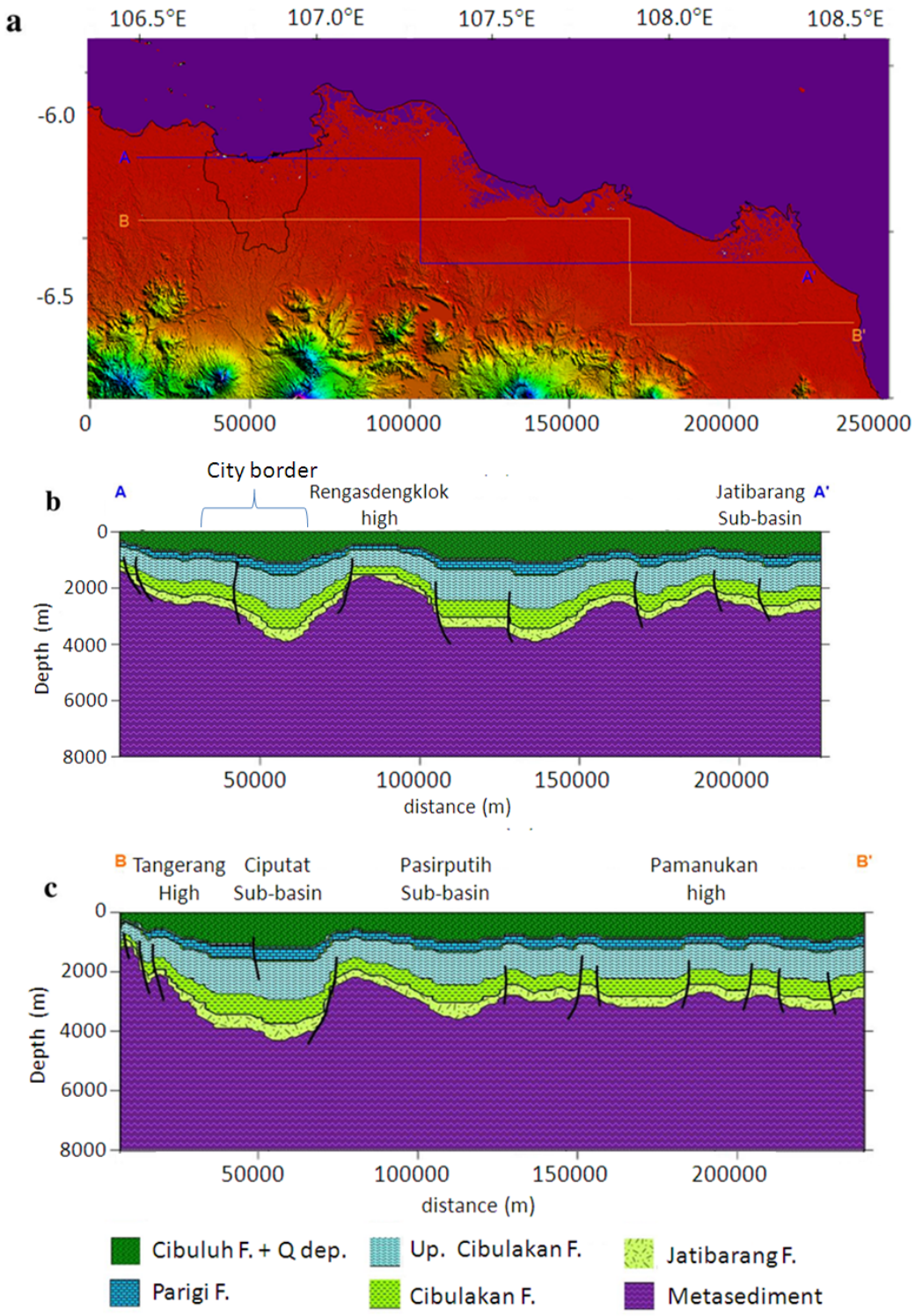

Figure 5.5: Jakarta basin is basically formed by a half-graben in the west and a graben (Ciputat sub-basin) in the east. Jakarta basin is contolled by normal-oblique faults on both sides, formed by the Tangerang high in the west and Rengasdengklok high in the east, and a normal fault that separates the Ciputat sub-basin and west sub-basin. Figure **(a)** depicts the location of Jakarta (thin black line) within West Java, figures **(b)** and **(c)** illustrate lithostratigraphy along A-A' and B-B' indicated in **(a)**. Figures are modified from *Putra et al.* [2016] and *Kingston* [1988]

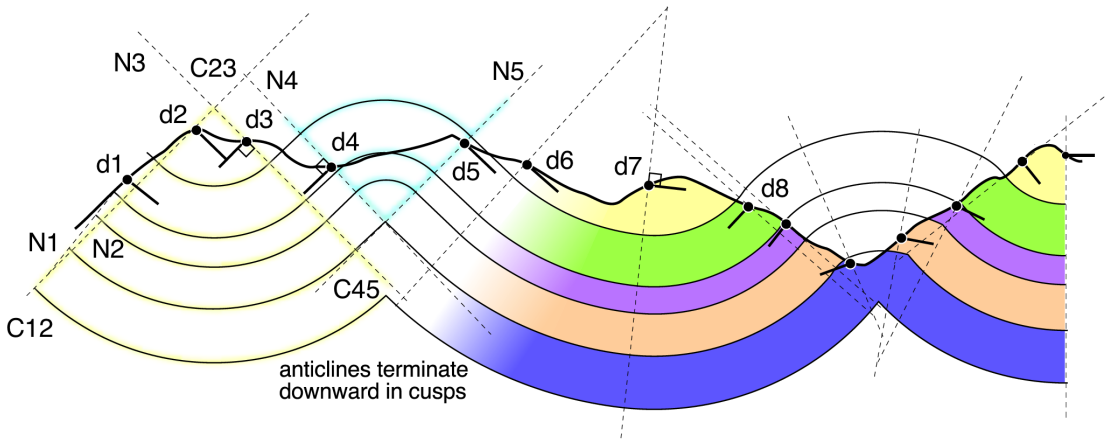

Figure 5.6: Fold reconstruction using arc method (also known as Busk method, published by H.G. Busk in 1929). Numbered line is dip representation, an auxiliary line (green) drawn perpendicular to dip, from intersection of adjacent auxiliary lines (center of arc, denoted as C), an arc (black lines) is drawn from point of measurement toward neighbor auxiliary line (i.e from point d1 to N2 using C12 as center of the arc). The colored strips represent rock layering.

create a full basin model a simple method called the Busk method or better known as the arc method is used. By comparing geological data (Fig. 5.5) and sediment thickness as presented in Fig. 5.3, it is a reasonable guess to interpret that the basement of the basin as the upper Parigi formation deposited in the Late Miocene. To construct a paleotopography, i.e. a topography before the Cibuluh formation was deposited, we need to plot the strike and dip of the Parigi formation layering in a 2D cross-section plot, as is illustrated schematically in Fig. 5.6. We draw dashed-line N1 perpendicular to d1 and dashed-line N2 perpendicular to d2, and let these 2 lines meet at C12. Using a compass, draw lines from N1 to N2, by applying this method to all plotted dips, so that a paleo-fold and paleo-basin can be reconstructed as seen in [*Allmendinger*, 2017]. The final basin model, which is the composite of the HVSR-derived model (covering the city) and that derived using the arc method (covering outside the city to the basin's rim) is presented in Figure 5.7.

5.4 Ground Motion Prediction Equations (GMPEs)

A GMPE is a generic term for a mathematical relationship between a statistical estimate of expected ground motion, and earthquake magnitude and some measure of distance to the earthquake fault rupture. GMPEs can supply a probability density function of ground motion values for a given earthquake scenario. These equations provide probabilistic descriptions of the level of ground shaking as a function of the earthquake parameters, accounting for path and site effects. Some Next Generation Attenuation (NGA) functions take into account independent estimator variables such as earthquake magnitude (f_{mag}), geometric attenuation (f_{dis}), style of faulting(f_{flt}), hanging-wall geometry (f_{hng}), shallow site response (f_{site}), basin response (f_{sed}), hypocentral depth (f_{hyp}), rupture dip (f_{dip}), and (apparent) anelastic attenuation (f_{atn}) (*Campbell & Bozorgnia* [2013]). They model a ground motion parameter Y, which could represent Peak Ground Acceleration (PGA), Peak Ground Velocity (PGV) or spectral acceleration (SA) at specific periods as:

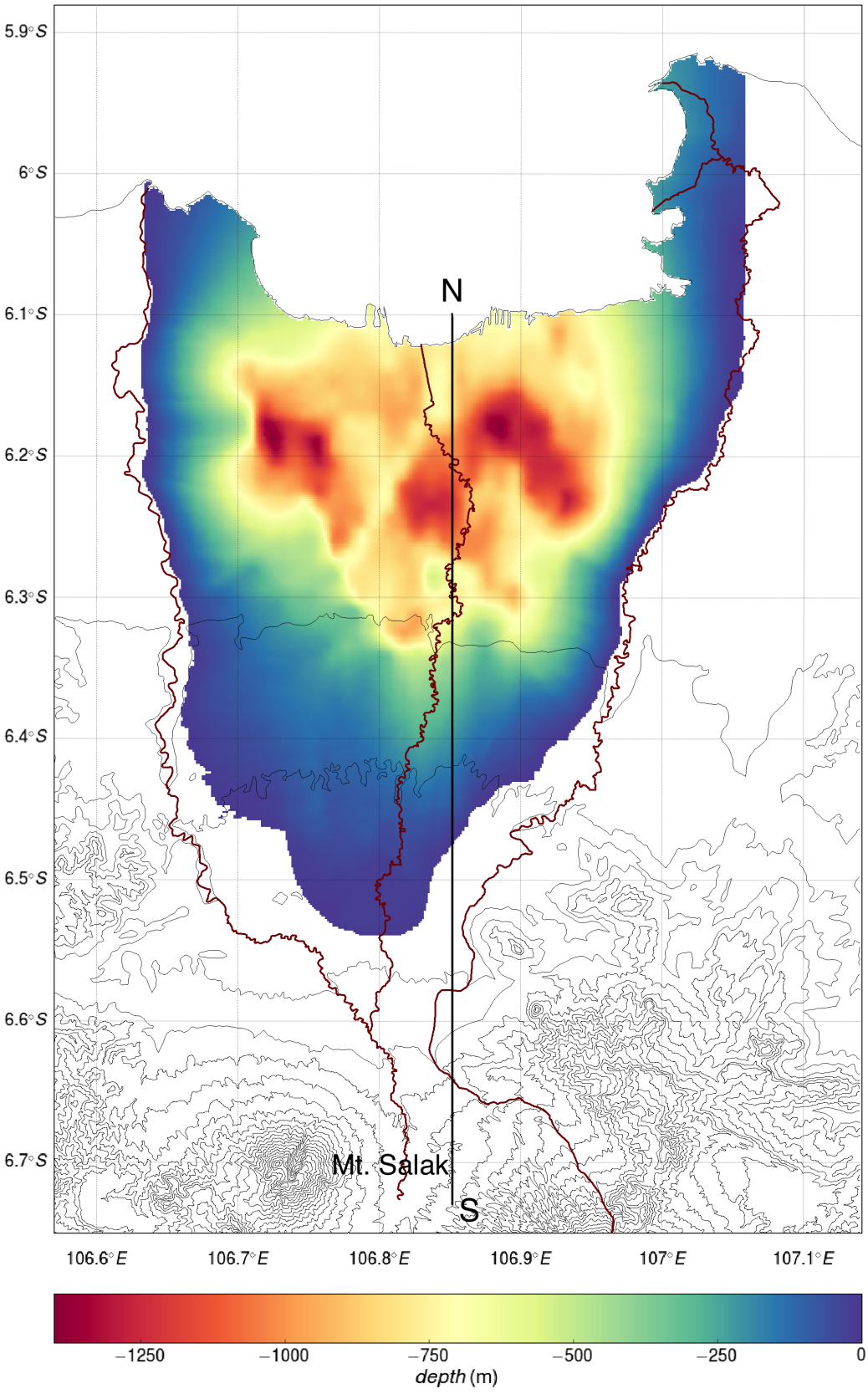

Figure 5.7: The extended basin model presented here merges the basin model derived from the HVSR technique that covered only the city of Jakarta with the result of the arc (Busk) method that considered geological data to estimate the basin edges.

$$lnY = f_{mag} + f_{dis} + f_{flt} + f_{hng} + f_{site} + f_{sed} + f_{hyp} + f_{dip} + f_{atn} \tag{5.1}$$

Out of these parameters, we are interested in investigating the f_{sed} parameter, which is intended to parametrize basin depth. The preliminary ground motion simulations are readily performed as the selected NGA GMPEs (CY2014 and CB2014) are incorporated in OpenQuake, a software platform developed by the Global Earthquake Model (GEM) Foundation for seismic hazard and risk calculations [*Pagani et al*, 2004].

The three GMPEs mentioned above require site parameters that use V_{S30} as a proxy for near-surface geology (soil) classification, and $Z_{1.0}$ or $Z_{2.5}$ to describe basin depth ($Z_{1.0}$ is the depth to a V_S of 1 km/s, while $Z_{2.5}$ is depth to 2.5 km/s). Here, V_{S30} is described as the average shear wave velocity in the topmost 30 m of soil, based on travel time from surface to the 30 m of depth. Using data from Japan and California, *Chiou & Youngs* [2014] provide empirical equations relating V_{S30} and $Z_{1.0}$ and *Campbell & Bozorgnia* [2013] provide empirical equations to estimate $Z_{2.5}$. To asses whether the velocity structure of the Jakarta Basin covers a similar parameter range to those in California and Japan that are used for these GMPEs, we plotted the empirical equations of *Chiou & Youngs* [2014] for $Z_{1.0}$ as a function of V_{S30} against data from the *Cipta et al.* [2018] model for the Jakarta Basin, where $Z_{1.0}$ is taken directly from the model and V_{S30} is either taken from the *Cipta et al.* [2018] model or the NSPT data of *Ridwan et al.* [2016].

Regardless of which estimate of V_{S30} is used, Figure 5.8a shows that $Z_{1.0}$ estimated for the Jakarta Basin are always much greater than the $Z_{1.0}$ calculated from the *Chiou & Youngs* [2014] empirical relations, either for California or Japan. Figure 5.8b shows amplification of PSA as a function of period for $V_{S30} = 100$ m/s, typical of the Jakarta Basin, and values of $Z_{1.0}$ ranging from 100 to 1500 m. The amplification curve for $Z_{1.0} = 100$ m exhibits a pronounced peak at period 0.8 s, and this peak broadens and its period increases to 1.5 s and 2.0–2.5 s for $Z_{1.0} = 500$ and 1000 m, respectively, but changes little in amplitude or period range for $Z_{1.0} = 1500$ m. A typical HVSR curve for the Jakarta Basin, on the other hand, exhibits a pronounced peak at around 6 s (some curves such as this one also exhibit a secondary peak at shorter periods, see *Cipta et al.* [2018]. While the HVSR curve does not necessarily represent the amplification of seismic waves, its peak period is widely regarded as coinciding with that of S-wave amplification [*Nakamura*, 1989], it has been used to explain spatial patterns of earthquake damage [*Gosar*, 2010], and it agrees with the fundamental period of S-wave resonant oscillation calculated form the Jakarta Basin velocity models of both *Cipta et al.* [2018] and *Saygin et al.* [2016]. Thus, the basin parameters calculated for the Jakarta Basin model of *Cipta et al.* [2018], appear to lie outside the range of values used for the development of the deep sediment corrections of CY2014, and the period dependence of CY2014 predictions for PSA using these corrections do not agree with the characteristics of ground motion implied by observed HVSR curves. Therefore, Therefore, we are skeptical that the deep sediment corrections of CY2014 will correctly account for seismic resonance in the Jakarta Basin.

In addition to soil characterization, NGA GMPEs also require $Z_{1.0}$ or $Z_{2.5}$ to describe basin depth. Using data from Japan and California, *Chiou & Youngs* [2014] provides empirical equations relating V_S30 and $Z_{1.0}$ and *Campbell & Bozorgnia* [2013] provide empirical equations to estimate $Z_{2.5}$ as follow:

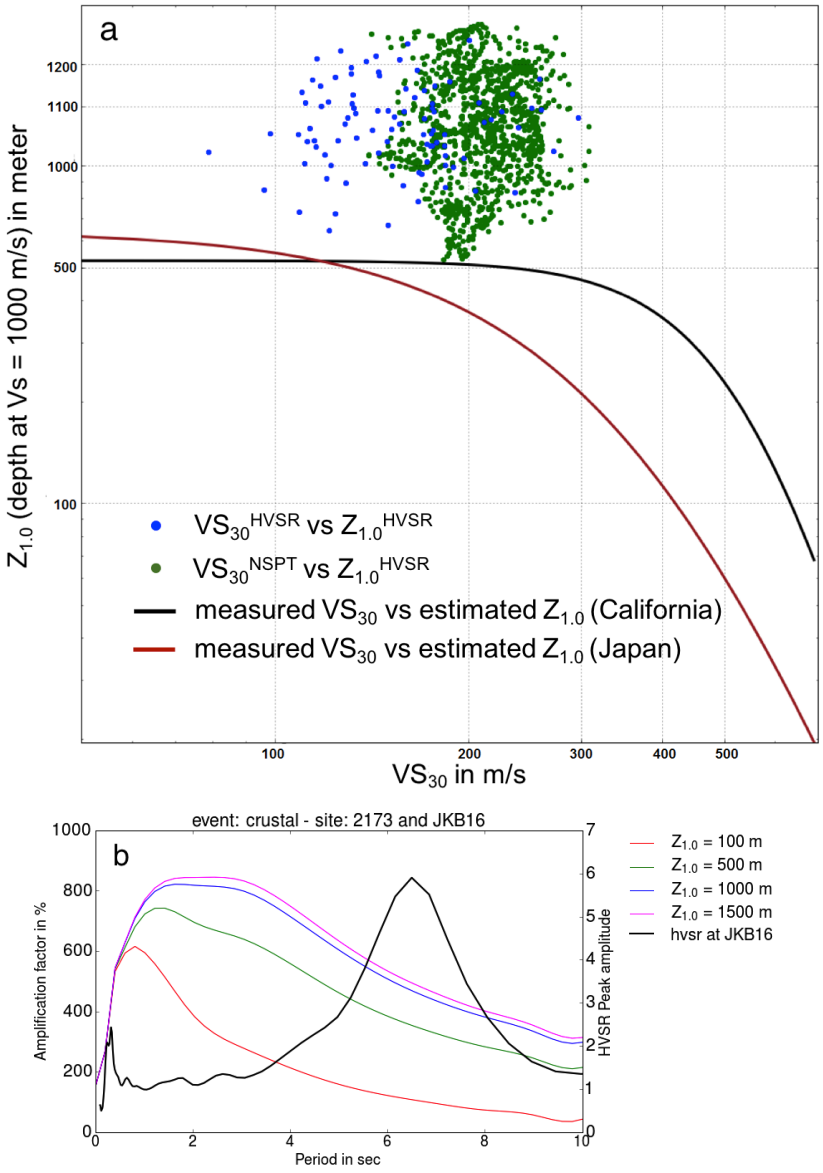

Figure 5.8: The behaviour of the deep sediment terms in the CY2014 GMPE compared with parameters for the Jakarta Basin. (**a**) Plot of V_{S30} against $Z_{1.0}$ and curves showing estimated $Z_{1.0}$ as a function of measured and computed V_{S30} derived by *Chiou & Youngs* [2014] from data taken in California (black line) and Japan (brown line). The blue and green dots are plots of $Z_{1.0}$from the *Cipta et al.* [2018] model for the Jakarta Basin plotted against V_{S30} taken from the same model and from the NSPT data of *Ridwan et al.* [2016], respectively. (**b**) Amplification of pseudo-spectral acceleration as a function of period calculated for different values of $Z_{1.0}$, compared with a typical HVSR curve for the Jakarta Basin measured by *Cipta et al.* [2018]. Locations of S2176 and JKB16 are showing in Figure 5.3.

$$ln(Z_{1.0}) = \frac{-7.15}{4}\, ln\left(\frac{(V_S30)^4 + 571^4}{1360^4 + 571^4}\right) \quad [California\ dataset] \tag{5.2}$$

$$ln(Z_{1.0}) = \frac{-5.23}{4}\, ln\left(\frac{(V_S30)^4 + 412^4}{1360^4 + 412^4}\right) \quad [Japan\ dataset] \tag{5.3}$$

$$ln(Z_{2.5}) = 7.089 - 1.144 ln V_S30 \quad [California\ dataset] \tag{5.4}$$

$$ln(Z_{2.5}) = 5.359 - 1.102 ln V_S30 \quad [Japan\ dataset] \tag{5.5}$$

$$ln(Z_{2.5}) = 6.510 - 1.181 ln V_S30 \quad [California\ and\ Japan\ datasets] \tag{5.6}$$

However, these empirical relationship are not suitable for Jakarta. When we calculate $Z_{1.0}$ directly from our HVSR-derived velocity profiles and plot these against the corresponding V_S30 derived from either NSPT or HVSR, the result is as indicated by the green and blue dot, respectively, in Fig. 5.8. The $Z_{1.0}$ calculated from the Jakarta dataset is always far above the curves from the [*Chiou & Youngs*, 2014] formulae, presumably because the Jakarta Basin is much deeper than basins in California and Japan. In this study we use $Z_{1.0}$ and $Z_{2.5}$ obtain from our HVSR study when we calculate ground motions using the NGA GMPEs.

5.5 Numerical Simulation of Seismic Waves

Earthquake-generated ground shaking depends not only on the earthquake source parameters, but also on the medium in which seismic waves propagate, especially near surface and basin structure. In this study, seismic waves generated by synthetic ruptures on a crustal fault, the Java Megathrust, and an intraslab fault are simulated using SPECFEM2D. This software uses the Spectral Element Method (SEM), which combines the flexibility of the finite element method (FEM) with the accuracy of high-order (trigonometric) element basis functions. SEM is very effective at achieving high accuracy even for realistic earth models, and is therefore applicable for a wide range of applications in seismology [*Komatitsch & Vilotte*, 1998]. This approach to scenario ground modelling is similar to that used by *Molnar et al.* [2014] and *Molnar et al.* [2014b] to study seismic wave interaction with 3D structure of the Georgia Basin, British Columbia, Canada.

The seismic characteristics of the Jakarta Basin as obtained from the HVSR analysis will be represented in our 2D domain as a SN cross section over which the earthquake simulation takes place. To avoid extremely small elements, the sediment inside the basin is taken to be a homogeneous medium overlying bedrock, which is part of a 3-layer lithosphere, with maximum domain area as large as 445 km in length by 150 km in depth (Figure 5.10). The shear-wave velocity both in the sediment-filled basin and bedrock are taken as averages from the corresponding depths of the HVSR model. Crustal P-wave velocity (V_P) outside the basin is taken to be 1.8 times V_S as indicated in *Cipta et al.* [2018].

The surface geology in the area of interest, from older to younger deposits, is composed of Tertiary marine formations, Pliocene-Pleistocene volcanic rocks, alluvial fan and recent alluvium. Alluvial fan deposits are the main component filling the basin, overlaying the Tertiary-Quaternary volcanic rocks that are presumed to act as basement.

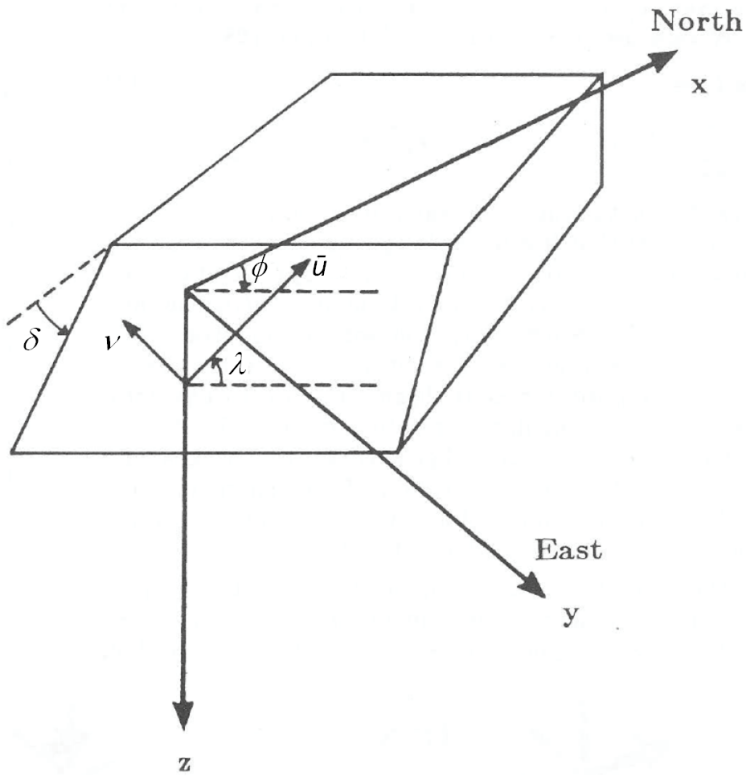

Figure 5.9: Fault orientation in Cartesian coordinate system. The origin is in the epicenter O, strike angle ϕ is measured clockwise from the north, dip angle δ is measured from horizontal down and rake or slip angle λ is measured anticlockwise from horizontal. The $\bar{u}$ and ν are slip vector and fault normal and λ denotes rake angle [*Aki & Richard*, 1980]

It is also possible that Miocene marine deposits play a role as bedrock, especially in the northern part of the basin. Heterogeneities both in vertical and horizontal directions make it difficult to set the elastic properties of the basin, particularly since the very low V_S(¡100 m/s) near the surface will require extremely small elements to model accurately. Instead of describing the detailed spatial variation of basin velocities, V_S is set to the average velocity in the basin resulting from inversion of HVSR ellipticity curves, 582m/s. Compressional-wave velocity (V_P) in the basin is set to 3–4 times V_S under the assumption that as a groundwater basin, the sediments filling Jakarta Basin are highly saturated, as also indicated by HVSR inversion that shows high ($\sim$ 4) V_P/V_S [*Cipta et al.*, 2018].

5.5.1 2D fault in Cartesian coordinate system

We assumed each earthquake rupture area as a planar surface along which seismic energy is radiated by an propagating elastic dislocation. The fault geometry is described as the orientation (strike ϕ, dip δ) and the direction of rake or slip direction (λ) along the plane. Alternatively, the fault plane can be characterised by direction of motion or slip vector $\bar{u}$ andand fault normal vector ν (see Fig. 5.9).

The moment M_0 of a shear dislocation is $\mu A\bar{u}$, where μ is rigidity in the source region, A is the area of rupture and $\bar{u}$ is the average dislocation. The Cartesian components

of the moment tensor **M** are:

$$
\begin{aligned}
M_x x &= -M_0\ (sin\ \delta\ cos\ \lambda\ sin\ 2\phi_s\ +\ sin\ 2\lambda\ sin\ \lambda\ sin^2\ \phi_s) \\
M_{xy} &= \ M_0\ (sin\ \delta\ cos\ \lambda\ cos\ 2\phi_s\ +\ \frac{1}{2}\ sin2\ \delta sin\ \lambda\ sin2\ \phi_s) = M_{yx} \\
M_{xz} &= -M_0\ (cos\ \delta\ cos\ \phi\ cos\ \phi_s\ +\ cos2\delta sin\lambda\ sin\ \phi_s) = M_{zx} \\
M_{yy} &= \ M_0\ (sin\ \delta\ cos\ \lambda\ sin2\ \phi_s\ -\ sin2\delta\ sin\ \lambda\ cos^2\ \phi_s) \\
M_{yz} &= -M_0\ (cos\ \delta\ cos\ \lambda\ sin\ \phi_s\ -\ sin2\ \delta\ sin\ \lambda\ cos\ \phi_s) = M_{zy} \\
M_{zz} &= M_0\ sin2\ \delta\ sin\ \lambda
\end{aligned}
\tag{5.7}
$$

where θ, δ and λ are strike, dip and rake angles respectively.

The simulation will be performed in a 2D domain oriented in the SN direction, or the xz plane of Fig. 5.9, and the strike of megathrust, intraslab and crustal fault will be perpendicular to this plane with θ = -90∘ or 90∘ for the megathrust and crustal fault, respectively, and $\lambda = 90°$, so that (5.7) can be written as:

$$
\begin{aligned}
M_{xx} &= -M_0\ sin(2\delta) \\
M_{xy} &= 0 = M_{yx} \\
M_{xz} &= M_0\ cos(2\delta) = M_{zx} \\
M_{yy} &= 0 \\
M_{zz} &= M_0\ sin(2\delta)
\end{aligned}
\tag{5.8}
$$

And we need consider only the three moment tensor elements Mxz, Mzz, Mxx=-Mzz in our 2D simulation.

5.5.2 Domain area and source parameters

The seismic characteristics of the Jakarta Basin as obtained from the HVSR analysis will be represented in our 2D domain as a SN cross section over which the earthquake simulation takes place. To avoid extremely small elements, the sediment inside the basin is taken to be a homogeneous medium overlying bedrock, which is part of a 3-layer lithosphere, with maximum domain area as large as 445 km in length by 150 km in depth (Figure 5.10). The shear-wave velocity both in the sediment-filled basin and bedrock are taken as averages from the corresponding depths of the HVSR model. Crustal P-wave velocity (V_P) outside the basin is taken to be 1.8 times V_S as indicated in *Cipta et al.* [2018].

The surface geology in the area of interest, from older to younger deposits, is composed of Tertiary marine formations, Pliocene-Pleistocene volcanic rocks, alluvial fan and recent alluvium. Alluvial fan deposits are the main component filling the basin, overlaying the Tertiary-Quaternary volcanic rocks that are presumed to act as basement. It is also possible that Miocene marine deposits play a role as bedrock, especially in the northern part of the basin. Heterogeneities both in vertical and horizontal directions make it difficult to set the elastic properties of the basin, particularly since the very low V_S(¡100 m/s) near the surface will require extremely small elements to model accurately. Instead of describing the detailed spatial variation of basin velocities, V_S is set to the

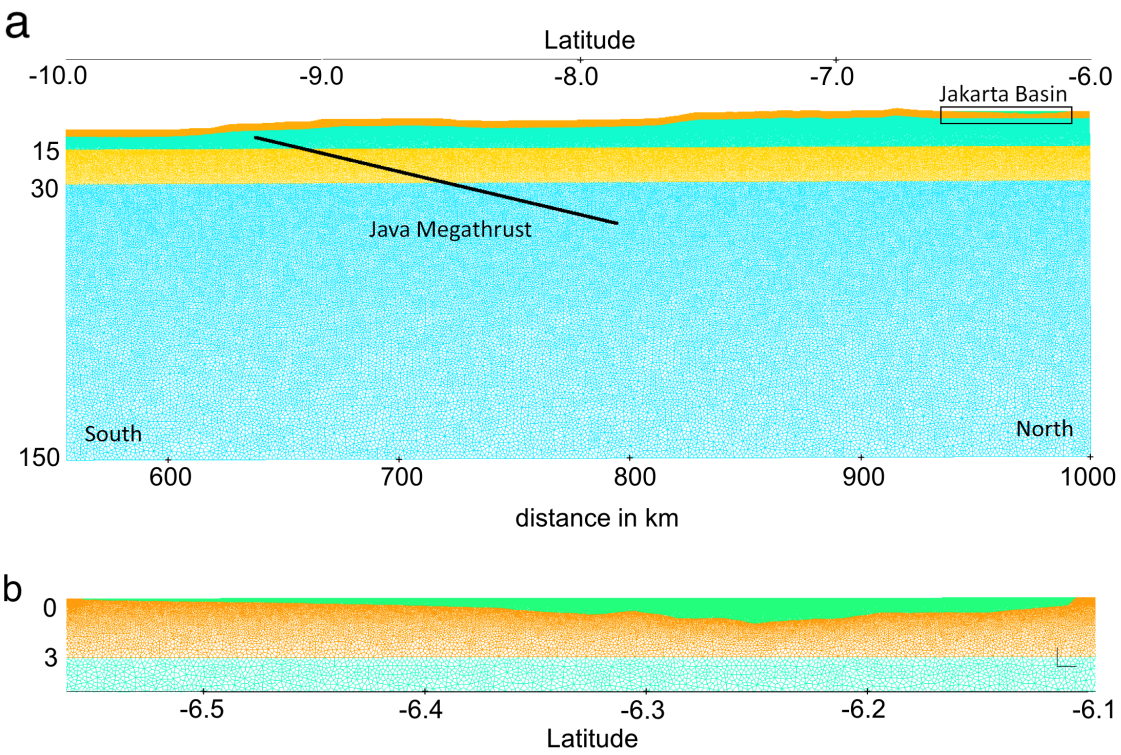

Figure 5.10: (**a**) The SPECFEM2D computational domain consists of a 5-layered medium, with the surface topography extracted from SRTM and the basin geometry resulting from the HVSR inversion. The vertical axis is depth (km) and horizontal is latitude in km and degree. The thick black line represents an inclined set of 1002 point sources along the subduction zone megathrust, and the area of the rectangle basin inset shown in (**b**) is indicated. For the crustal fault and deep intraslab scenarios, different dimensions of domain areas are used but the mesh-sizes for the first 4 top layers are the same.

average velocity in the basin resulting from inversion of HVSR ellipticity curves, 582m/s. Compressional-wave velocity (V_P) in the basin is set to 3–4 times V_S under the assumption that as a groundwater basin, the sediments filling Jakarta Basin are highly saturated, as also indicated by HVSR inversion that shows high (~ 4) V_P/V_S (*Cipta et al.* [2018]).

The total length of the computational domain for the megathrust event extends from 6° to 10° south latitude, the maximum depth is 150 km and highest elevation is 1.5 km. The topographic surface is extracted from the Shuttle Radar Topography Mission DEM (SRTM Digital Elevation Model, freely downloaded from: `https://dds.cr.usgs.gov/srtm/version2_1/SRTM3/Eurasia/`). The domain area accommodates source locations and is divided into 5 zones including the basin, a 3-layer crust and the mantle. Irregular quadrangle meshes are generated to fill the domain area, the coarsest (maximum gridsize: 2000 m) meshes filling the lower layer while the finest meshes are arranged in the basin (maximum gridsize: 12.5 m). The very small mesh size in the basin, together with the large computational domain that includes the megathrust, results in a very large mesh size, of 800,000 elements. This large mesh size is the main reason that calculations in this study were limited to 2-D, as a 3-D mesh at this resolution would have resulted in very long computation time. The topographic surface is set to be a free surface while the other sides are set to be absorbent surfaces to avoid waves reflecting back into the domain area (see Figure 5.10).

While seismic attenuation in sedimentary basins like Jakarta can be high, we found that the viscoelastic calculations of SPECFEM2D for our large computational mesh were prohibitive (even the elastic calculations using 28 CPUs required a wall time of 18 hours; viscoelastic calculations took much longer). To our knowledge no studies of seismic attenuation or seismic quality factor for the Jakarta region have been undertaken, but in order to test the influence of attenuation we use Qp = 44 and Qs = 25, taken from a study conducted *Hauksson et al.* [1987] in the Los Angeles Basin. Tests using these values for Qp and Qs in the basin indicated that viscoelasticity had a small effect for periods ¿ 1 s. Therefore, in the simulations described here we neglected attenuation in the basin for reasons of computational efficiency. All parameters for simulations are presented in Table 5.1.

Table 5.1: Domain parameters used in simulation

layer	rho ($kg.m^{-3}$)	V_P (ms^{-1})	V_S (m^{-1})	Q_{Kappa}	Q_{mu}	max depth (m)
Basin	1200	1600	582	44	25	1385
Layer 2	2200	4100	2300	283	150	3000
Layer 3	2900	5100	2800	450	450	13,467
Layer 4	3200	6500	3200	500	500	15,000
Layer 5	3800	8000	4000	600	700	120,000

* Parameter values were tested but not used in the simulations presented here.

In this study, we assume that seismic waves are generated outside the basin, in the Java subduction zone for the megathrust scenario, in the shallow crust to the south of the basin for the crustal earthquake scenario, and in the mantle for the intralsab scenario. Seismic waves propagate from the source through a 5-layer mantle + crustal model to the surface, as indicated in Table 5.1 On the surface, both inside and outside the basin, seismic waves will be recorded at stations located at 2 km spacing along a south-north cross-section. In order to account for 3-D geometrical spreading and attenuation in the crust and upper mantle outside 2-D elastic simulation, we scaled the computational results by matching the long-period (1–10 s) spectra of seismograms recorded just outside the basin with results from suitable GMPEs for the appropriate magnitude and distance. For the megathrust scenario, we scaled the seismograms by matching spectra with results of the AEA2014 GMPE, for the crustal source we used CY2014, and for the intraslab earthquake scenario we matched spectra to AEA2014S. Earthquake source parameters used in the megathrust, crustal and intraslab scenarios are indicated (Table 5.2).

Table 5.2: Source parameters used in simulation of seismic waves propagation

Magnitude	M_w9.0 (Megathrust)	M_w6.5 (crustal)	M_w7.0 (slab)
Total energy released (Nm)	1.259e+21	7.079e+18	3.981e+19
dip	30°	45°	45°
rupture depth (km)	10-50	2-14	180-204
no. of point sources	1002	120	120

In order to compare characteristic of seismic waves in the basin and on bedrock, we simulate seismic waves propagation to bedrock by changing all the parameters in the basin into parameters of the underlying medium, so that parameters in the basin are the

same as the parameters in layer 2.

5.6 Results

5.6.1 GMPE Modeling Results

GMPE simulations have been performed for the three earthquake scenarios described above and results for the crustal earthquake scenario are displayed in Figure 5.11. Figure 5.11a–c show amplification of PGV, PGA and PSA(5 s) which vary between 200–500, 70–180 and 200–700%, respectively (note that we describe amplification following [*Pilz et al.*, 2011], as described below in Section 5.7, where 0% corresponds to hard rock ground motion). The absolute values of these quantities are shown in Figure 5.11e–g, where it can be seen that PGV, PGA and PSA(5 s) have values of about 6 cm/s, 5% g and 0.6–0.8% g near the southern edge of the basin, about 60 km from the earthquake source. As distance from the earthquake increases in the center and northern part of the basin, the absolute level of ground motion (Figure 5.11e–f steadily decreases with increasing distance from the earthquakes. The amplification (Figure 5.11a–c), on the other hand, increases in the north of the basin, closely following the pattern of V_{S30} decrease indicated in Figure 5.11d.

For the amplification at PSA (5.0 s), which is close to the apparent resonance peak in most of the HVSR measured by *Cipta et al.* [2018], it might be expected that variation in basin geometry would have a significant influence on the long period ground motion, but there is very little correlation with the pattern of basin depth variations (Figure 5.11h). We believe this is reflective of the "saturation" in peak ground motion period depicted in Figure 5.8a as $Z_{1.0}$ reaches the value 1000 m that is typical of most of the Jakarta Basin. For this reason, it seems clear that caution should be used when trying to use the deep sediment terms of CY2014, and presumably othe GMPEs with deep sediment correction developed using similar datasets, to describe basins elsewhere, to estimate earthquake ground motion in the Jakarta Basin.

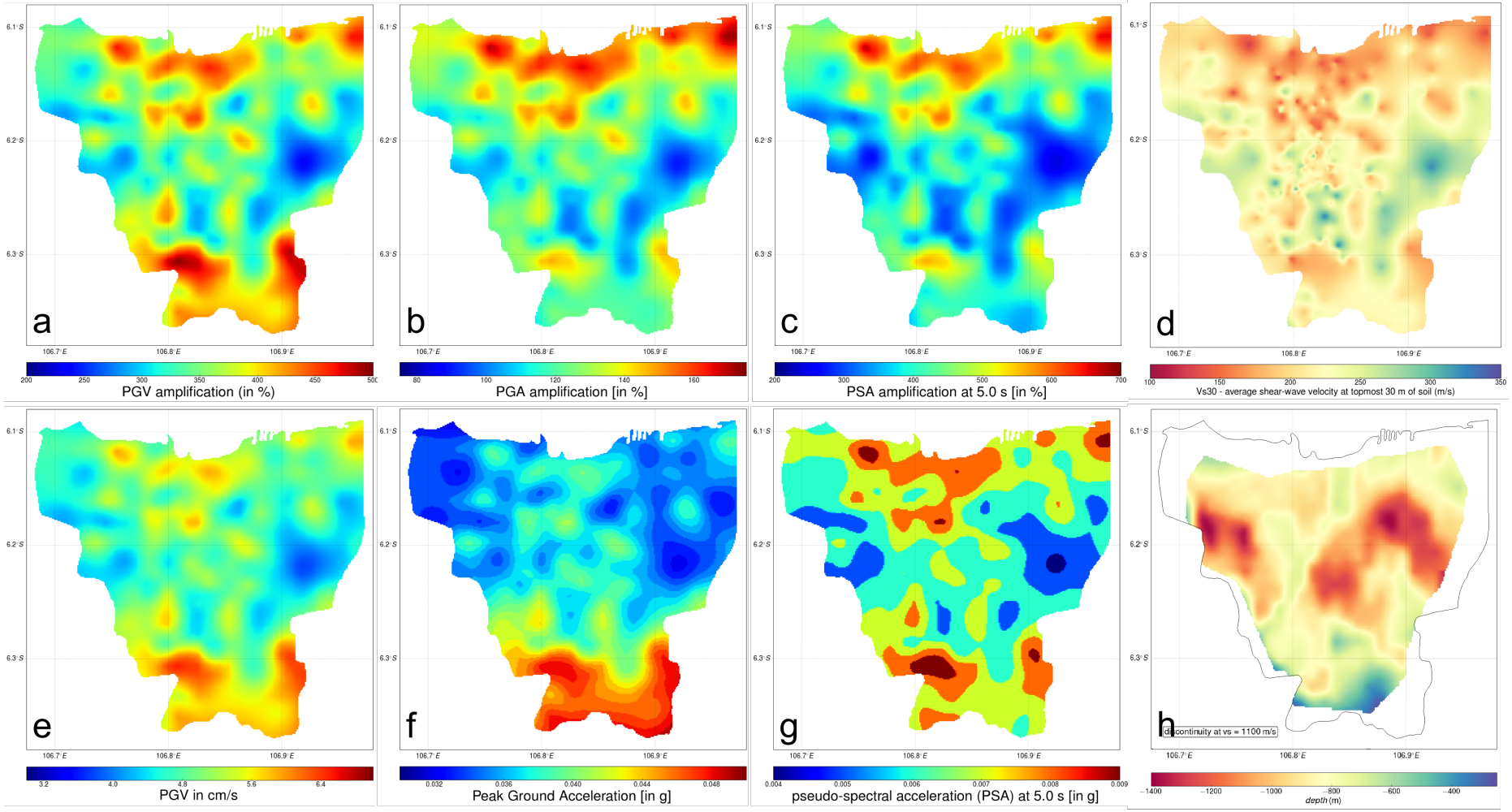

Figure 5.11: Results of GMPE modeling using CY2014 for the crustal earthquake scenario, and comparison with Jakarta Basin V_{S30} and basin depth. (**a**–**c**) PGA, PGV and PSA 5.0 s, respectively calculated for the crustal earthquake scenario using CY2014 with the deep sediment correction $Z_{1.0}$ derived from the Jakarta Basin model of *Cipta et al.* [2018]. (**d**) V_{S30} derived form NSPT data of *Ridwan et al.* [2016]. (**e**–**g**) PGA, PGV and 5.0 s PSA amplification obtained by dividing the results in (**a**–**c**), respectively, by the corresponding calculations for hard rock. (**h**) A map of the Jakarta Basin depth from *Cipta et al.* [2018], from which the $Z_{1.0}$ values for the deep sediment correction of CY2014 were taken.

5.6.2 Numerical Simulation Results

The crustal and megathrust events are situated south of Jakarta at distances 85 km and 200 km and with magnitudes M_w 6.5 and M_w 9.0, respectively. The megathrust is dipping north while the crustal fault is dipping south. The third scenario simulates propagation of seismic waves originating from a medium-depth intraslab earthquake located at the depth of the subducting slab at 180–204 km (fault width = 34 km) directly beneath the city. This fault is dipping south and the earthquake has magnitude M_w 7.0.

Snapshots from the crustal fault scenario are presented in Figure 5.12. After 10 s, the P-wave is showing up in the lower left corner of the topmost panel and at 12 s, both P-wave (dark) and S-wave (vermilion) are observed approaching the basin. At 50 s, seismic waves, both body and surface waves, have entered and are trapped inside the basin. Surface waves are modulated inside the basin and at 90 s, while body waves are attenuated and have faded away outside the basin, surface waves are still reverberating in the basin.

Seismograms (horizontal component) resulting from these three scenarios are presented in Figure 5.13a–c. Two types of seismograms are plotted: (1) those calculated using the elastic parameters indicated in Table 5.1, colored blue in Figure 5.13 and referred to here as 'basin seismograms', and those calculated using an identical computational mesh but with the basin elastic parameters replaced by those of the basement (i.e., the Basin parameters in Table 5.1 are replaced by those of Layer 2), colored orange in Figure 5.13 and referred to here as 'bedrock seismograms'. The three record sections in Figure 5.13a–c clearly show that seismic waves propagating through the soft sediment inside the basin are amplified to different degrees. Outside the basin the orange colored curves (bedrock seismograms) match the blue curves (basin seismograms) perfectly, meaning that outside the basin, no amplification is observed. On the other hand, inside the basin, basin seismograms have much higher amplitudes and prolonged durations in comparison to bedrock seismograms. It is interesting to note that the basin-bedrock seismogram ratio is not uniform, and basin depth is not the only factor contributing to the amplification. Basin geometry and direction of incoming waves also appear to influence the degree of amplification.

For the crustal earthquake scenario, Figure 5.13a, seismic waves propagating toward the north edge of the basin are reflected back into the basin and recorded at 200 s at the southernmost station (S2117) and at progressively earlier times at more northerly stations. However, at S2157 to S2176, reflected waves are not clearly seen because they interfere with seismic waves propagate northward, producing high amplitude seismograms at 50–60 s (Figure 5.18). The megathrust earthquake also exhibits reflected waves that are clearly observed at S2130 to S2169, again with reflected waves recorded earlier in the north than in the south (Figure 5.13b).

In contrast to the other two scenarios, the intraslab earthquake scenario shows reflected waves from both south and north edges. Near the south edge, high amplitude seismic waves are observed at stations S2130-2135 at times 50–100 s. These high amplitudes are generated from interaction between incoming and reflected waves as well as trapping at the basin's edge. As time goes by, waves reflected by the northern edge of the basin are recorded after 100 s in the southern stations and recorded earlier in the central and northern stations.

Seismograms in Figure 5.14**a,b** record incoming P- and S-waves at 20 s and 36 s, respectively, for the crustal fault scenario. For the basin seismograms in Figure 5.14**c,d**, the direct S-wave is followed by a series of reverberations comprised of S-wave

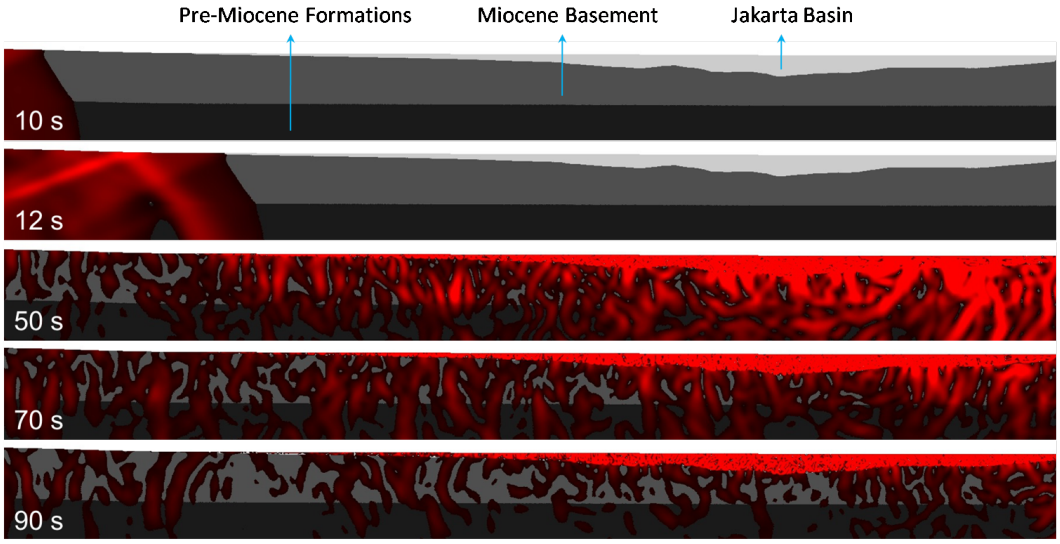

Figure 5.12: Snapshots of wave propagation, showing waves approaching (10 and 12 s, top two panels) and reverberating inside (50, 70 qnd 90 s, bottom three panels) the basin. The modeled M_w 6.5 earthquake is taken to have ruptured a southward dipping, shallow crustal thrust fault 85 km south of the city center. The Jakarta Basin is the light gray colored area, overlying the dark grey medium, clearly shown in the top two pictures capturing snapshots at 10 and 12 s, respectively.

and Rayleigh wave energy, that builds up over the following 15 s, with the highest vertical component amplitude achieved 10 s after the direct S-wave arrival. It is observed that S-wave/Rayleigh wave coda that builds up at about 37 s is still observed after more than 150 s. The bedrock seismograms (Figure 5.14**e,f**) are dominated by the direct S-wave and have a very weak coda after only a few seconds.The long duration (>120 s) and very high amplitude of basin seismic waves after 40 s is likely due to the constructive interference between seismic body waves and surface waves.

The intraslab scenario produces similar results, at the same station, with surface waves observed after 55 s and still trapped inside the basin after 240 s. In the case of the megathrust event, the Rayleigh wave arrives about 25 s after the P-waves recorded in the seismograms. The interference of reverberating surface waves leads to very high amplitudes, compared to the crustal and intraslab scenario. Entrapment of seismic waves inside the basin prolongs the duration of seismic waves, with high amplitude seismic waves still observed 10 minutes after the earthquake. Interference between seismic body waves and secondary surface waves was recognized as a main cause of building collapse in Kobe during the 1995 Great Hanshin Earthquake (*Zhao et al.* [2010]).

The three scenarios indicate that the larger the magnitude, the longer the seismic waves were observed inside the basin. The "red" (i.e., long-period dominant) spectra of frequency content generated by the larger rupture area may be responsible for the very long duration of long period ground motions generated by the megathrust scenario (Fig. 5.12). Together with the maximum amplitude and duration of seismic waves, frequency content is also a very important factor that is responsible for building damage. According to *Shoji et al.* [2004], duration is more event-dependent than site-dependent while the site-dependency for a given total power is greater than the event-dependency.

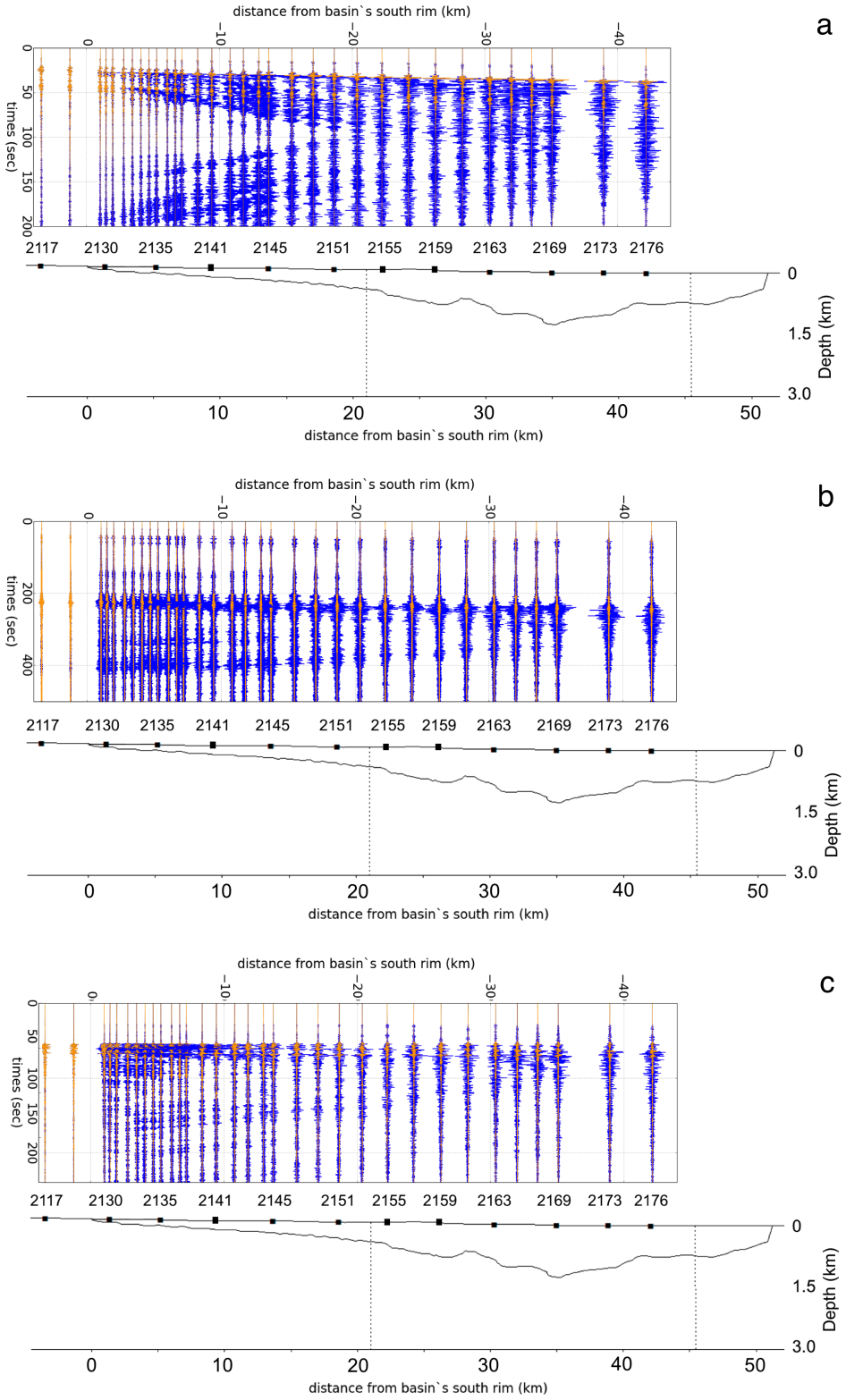

Figure 5.13: Bedrock seismograms (orange traces) are plotted over basin seismograms (blue traces) for (**a**) crustal, (**b**) megathrust and (**c**) intraslab events, respectively. Labelled points indicate location of stations corresponding to the seismograms plotted directly above the points. In the area between dotted lines (21–41 km from the basin's rim) the basin structure is inferred from *Cipta et al.* [2018], while the extension of the basin is estimated from geological data. The basinal area in this figure is the same as the basinal area in Figure 5.12.

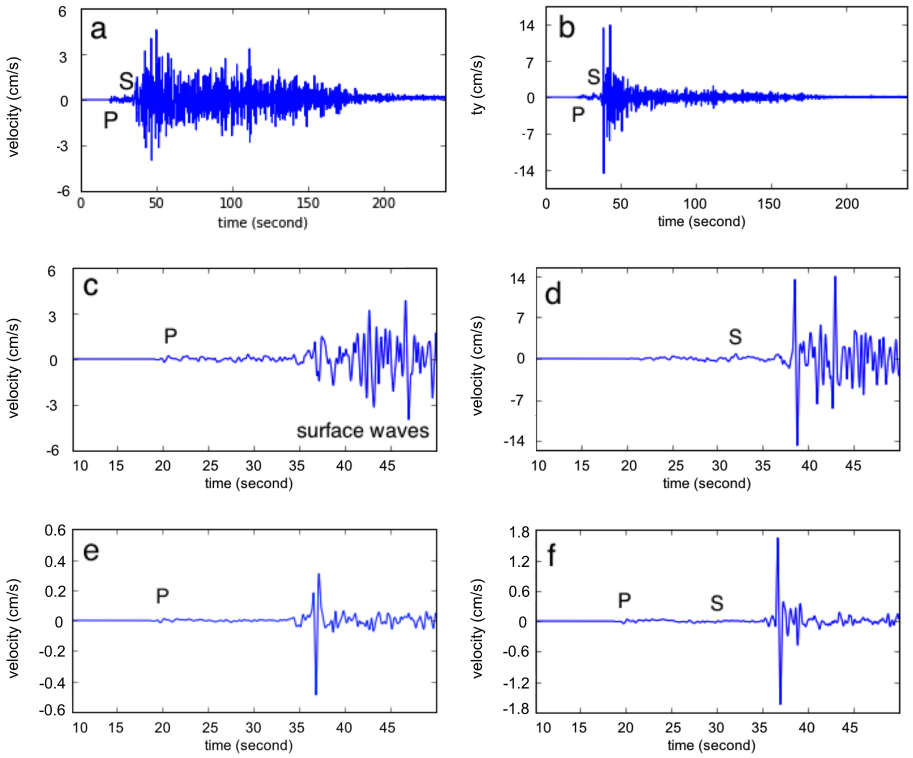

Figure 5.14: Seismograms at stations S2169, both for vertical (**a**) and horizontal (**b**) components, showing P-, S- and surface waves generated from the crustal fault scenario. Figure (**c**,**d**): the same seismograms at time 10–50 second, showing the arrival of direct S followed by Rayleigh surface waves at about 37 s. Similar to (**c**,**d**), (**e**,**f**) are seismograms recorded at bedrock sites.

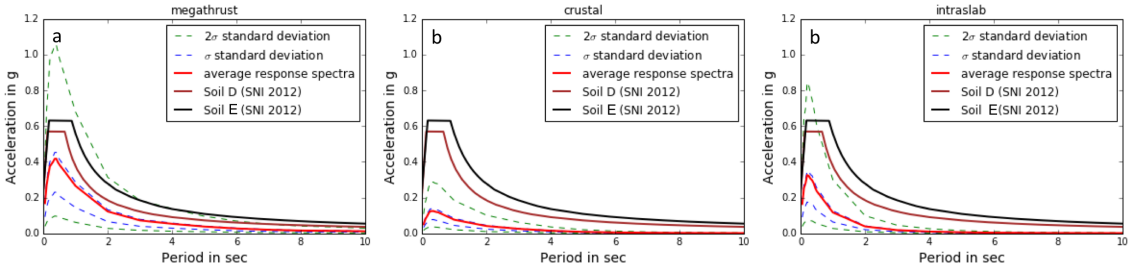

Figure 5.15: Design response spectra used for the 2012 Indonesian Building Code for soil sites (classes D and E are brown and black curves, respectively) in Jakarta, compared with average, 1- and 2-σ (solid red, blue dashed and green dashed, respectively) results for simulated response spectra (SRS) calculated in the Jakarta Basin for the (**a**) megathrust (GMPE:AEA2015); (**b**) crustal (GMPE: CY2014) and (**c**) intraslab (GMPE:AEA2015S)earthquake scenarios. Each curve represents the results of calculations at all sites for which V_{S30} and $Z_{1.0}$, have been estimated, as well as 1000 ground motion realizations that have sampled the aleatory variability in the respective GMPEs.

5.7 Discussion

5.7.1 GMPE-Seismic Hazard

Using GMPE modelling, pseudo-spectral acceleration (PSA) for each spectral period can be computed, and it's variability can be accounted for by sampling the aleatory variability in the GMPEs as well as computing ground motion over the range of site response information (V_{S30}, $Z_{1.0}$, and $Z_{2.5}$) available for the Jakarta Basin. Results for average and 1- and 2-σ simulated response spectra (SRS) for the three earthquake scenarios considered are shown in Figure 5.15, where they are compared with the design response spectra for Jakarta. At short periods (< 1 s), the average and 1-σ simulated response spectra (SRS) curves lie well below the design spectra for all three scenarios, but the 2-σ curves exceed the design spectra for the megathrust and intraslab scenarios. However, since GMPE simulations do not fully take the effects of basin geometry into account, longer period PSA may be underestimated, and hence we need to be careful in interpreting the curves presented in Figure 5.15. For this reason, let us compare design seismic response and SRS at the shorter periods (< 1 s) only, and note that shorter period response spectra correspond to the natural resonance of most residential buildings (which, however, are not generally required to conform to the Indonesian building code)

The current building code (2012 Indonesia's National Standard–SNI 1726-2012) adopted the updated seismic map of *Irsyam et al.* [2011] that estimated ground motions for a 2% probability of exceedance in 50 years (2500 years return period) as the maximum considered earthquake (MCE) level. Figure 5.15 shows that the current seismic building code in Indonesia that takes into account D and E soil classes performs well against the PSA estimated from GMPEs for the crustal earthquake scenario, but has significant probability of being exceeded (at the 2-σ level) for the megathrust and intraslab earthquakes. In this figure, the thick black and magenta curves represent designed ground motion produced by the MCE in a 2500 years return period for D- and E-type soils, respectively.

5.7.2 Numerical Simulations–Peak Ground Velocity (PGV)

The Mw 6.5 crustal fault scenario generates a maximum peak ground velocity of 13.45 cm/s and the maximum PGV amplification is about 726%. Figure 5.16a shows that amplification is not uniform throughout the basin, while in S2147 basin depth gives small effect to peak velocity, in other stations basin geometry amplify peak velocity significantly. Most striking is the amplification observed at S2169 at the deepest part of the basin (Figures 5.16 and 5.17a–c. Amplification here is describe in a manner similar to that used by *Pilz et al.* [2011] in calculating estimated PGV amplification in Santiago Basin, Chile: we subtract the PGV values for the bedrock seismograms from the value for the basin seismograms, and divide this by the PGV value for the bedrock seismograms (multiplying by 100 to convert to percentage amplification).

Different characteristic of simulated PGV and amplification are produced by megathrust earthquake scenario. PGV and amplification tent to incerase as the basin gets deeper. Prominent high PGV and amplification are simulated at stations S2153 and S2173. Simulated PGV at these stations are 149.67 cm/s and 153.37 cm/s while amplifications are 1269% and 1504%, respectively (Figures 5.16a and 5.18a–c). While these ground motion levels may seem very high, we note that the M_w 9.0 Tohoku Earthquake resulted in 50 cm/s pseudo-velocity response at 7 s period observed in the Osaka Basin at 770 km distance, along with 2.7 m peak-to-peak roof displacements at one high-rise building (*Sato et al.* [2012] and *Tsai et al* [2017], respectively). The M_w 8.0 Michoacan earthquake resulted in an observed PGV of 40 cm/s at 350 km distance (*Singh & Ordaz* [1993]). In light of these observed basin effects observed at much greater distance and smaller magnitud, our simulated result of ≈150 cm/s for a M_w 9.0 earthquake at 250 km distance from Jakarta Basin does not seem unreasonable.

The intraslab earthquake scenario results in very large amplification, especially at S2131 (1134%), so that the estimated PGV in that station (17.24 cm/s) is significantly higher than the other stations. The source of the intraslab scenario is very deep and directly beneath the city, so that rupture-to-station distance is the same for all stations, hence the variation of amplification with respect to rupture distance can be neglected. Therefore, large amplification at this station is most probably due to focusing of seismic waves by the basin edge, while trapping of seismic waves inside the basin may also affect amplification at this station. High amplification is also recorded at S2165, where particulary thick basin fill is responsible for large amplification (Figures 5.16a and 5.19a–c). Recorded PGVs (cm/s) and amplification (%) for all three scenarios are presented in Table 5.3. Minor amplification or deamplification recorded at stations S2117 and S2124 that are located outside the basin may come from simulation noise.

5.7.3 Numerical Simulation-Response Spectral Acceleration

The megathrust scenario generated the highest peak ground velocity and amplification in the basin, especially at station S2173. In this section, we will look at the response spectral acceleration that is widely used to characterise ground motion in civil engineering, then compare the design building code against spectral acceleration resulting from SPEFEM2D modeling. At station S2169 and S2173, simulated horizontal acceleration at period 1 s are about 0.45 g, which is higher than the design response spectra used by the building code. At periods about 1 s very high accelerations are observed (Figure 5.20a,c), however, these results may be inaccurate since neither near surface attenuation κ nor crustal and basin frequency-dependent attenuations for V_P and V_S (Qp and Qs) for Jakarta region are

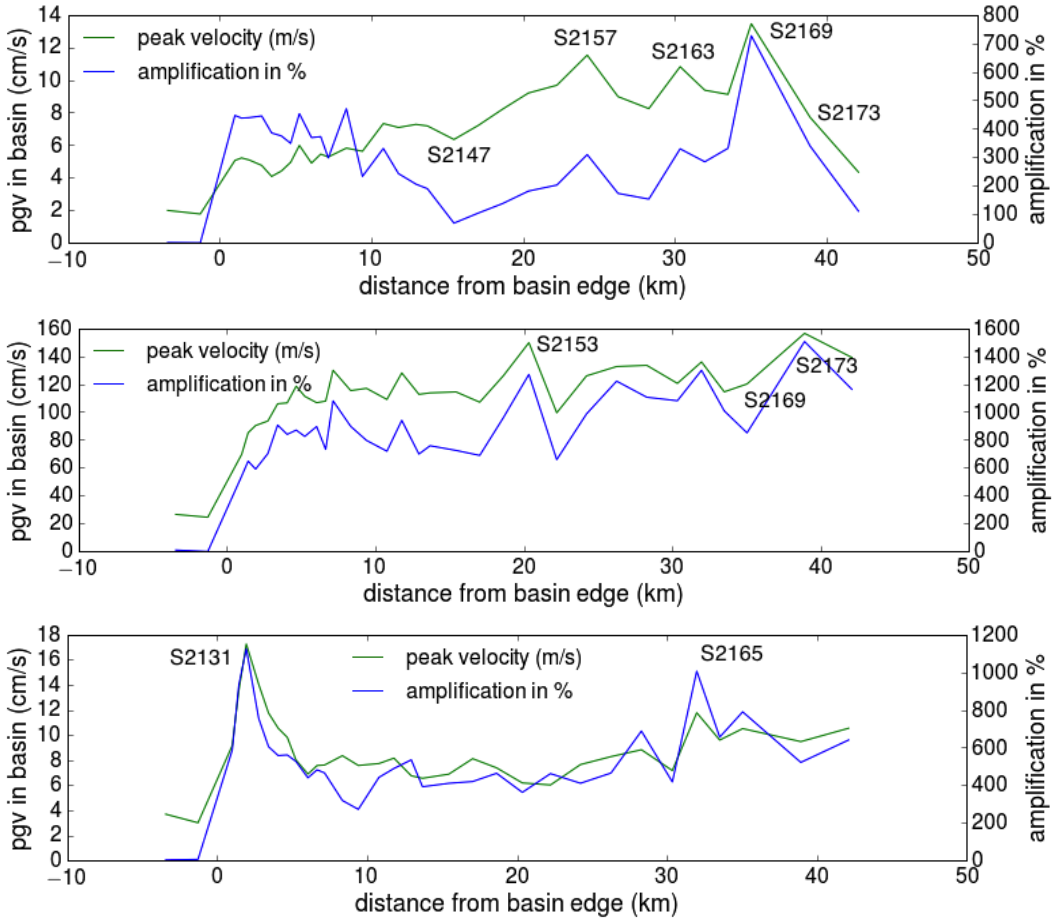

Figure 5.16: Peak velocity at stations plotted as a function of distance from the basin edge, generated for (**a**) crustal fault, (**b**) megathrust, and (**c**) intraslab scenarios. Blue and green curves represent peak velocity in the basin stations and amplification (in %), respectively. Selected station names are indicated by labelled dots.

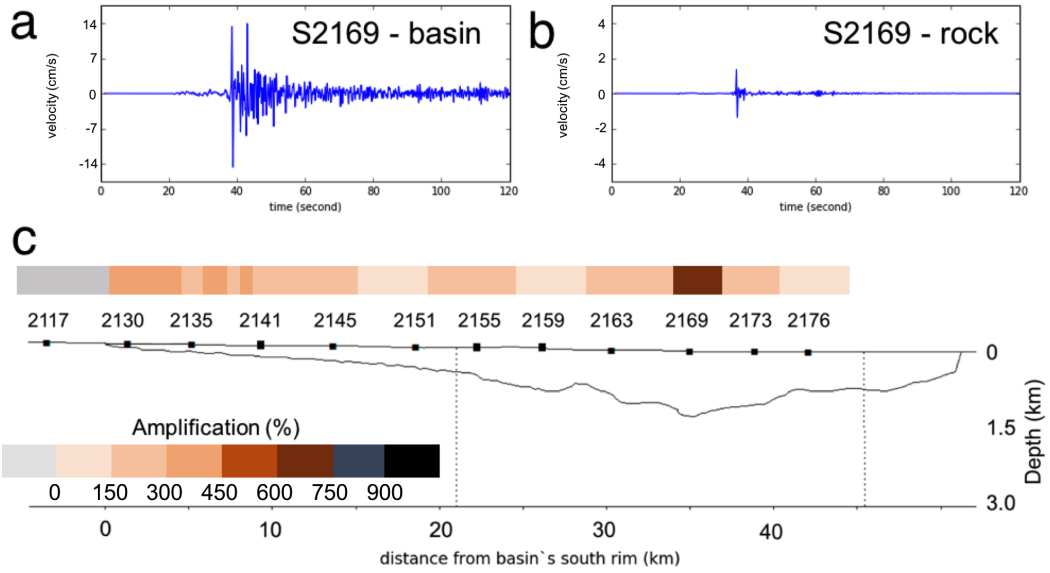

Figure 5.17: Amplification for the crustal (**a**–**c**) earthquake scenario, Figure (**a**,**b**) show velocity seismogram at stations S2169 for basin and bedrock sites respectively, and Figure (**c**) shows PGV amplification at each station along the S-N cross-section for the crustal fault scenario. The cross-section is located at the longitude 108.84335° and seismograms are the horizontal component.

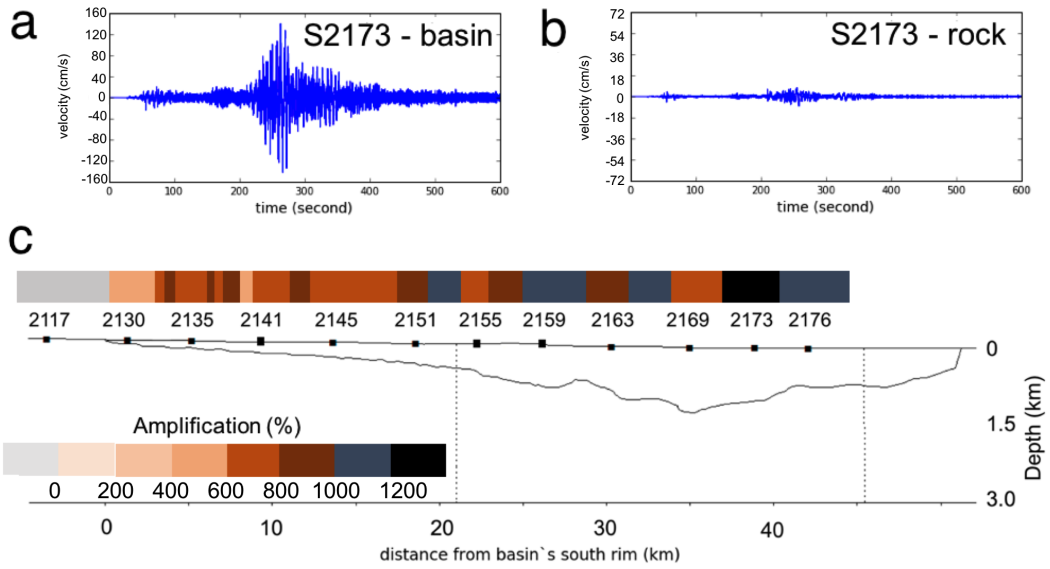

Figure 5.18: Similar to Figure 5.17**a**–**c**, these figures depicting seismograms at **(a)** basin and **(c)** rock sites (S2173) and **(c)** PGV amplification for the megathrust earthquake scenario.

Table 5.3: PGVs and Amplification in % resulted from 3 scenarios.

Station Station	**PGV-C (cm/s)**	**Ampli-C (%)**	**PGV-M (cm/s)**	**Ampli-M (%)**	**PGV-S (cm/s)**	**Ampli-S (%)**
S2117	1.98	1	26.44	8	3.68	2
S2124	1.77	0	24.39	−2	3	5
S2129	5.05	447	69.49	539	9.15	586
S2130	5.21	437	85.07	646	13.52	930
S2131	5.08	439	90.2	589	17.24	1125
S2132	4.75	445	93.46	701	14.03	754
S2133	4.07	385	105.82	906	11.74	604
S2134	4.4	375	106.43	838	10.54	557
S2135	4.94	349	118.45	869	9.8	560
S2136	5.98	453	111.16	824	8	525
S2137	4.89	369	106.6	895	6.88	439
S2138	5.44	372	107.74	731	7.56	481
S2139	5.27	297	129.84	1079	7.6	465
S2140	5.81	470	115.27	896	8.34	318
S2141	5.62	233	116.89	795	7.56	271
S2142	7.32	331	108.93	718	7.72	441
S2143	7.08	242	127.94	939	8.15	488
S2144	7.27	205	112.59	697	6.74	534
S2145	7.17	190	113.63	757	6.54	391
S2147	6.34	69	114.33	723	6.87	409
S2149	7.2	104	106.95	688	8.11	419
S2151	8.19	137	125.93	959	7.37	463
S2153	9.19	181	149.67	1269	6.17	361
S2155	9.67	202	99.34	657	6.01	461
S2157	11.52	309	125.83	985	7.64	410
S2159	8.97	173	132.54	1221	8.27	464
S2161	8.23	153	133.4	1105	8.82	687
S2163	10.81	330	120.44	1080	7.16	417
S2165	9.36	284	135.84	1298	11.77	1005
S2167	9.11	331	114.37	1007	9.59	655
S2169	13.45	726	120.02	849	10.5	789
S2173	7.7	339	156.37	1505	9.47	521
S2176	4.34	111	139.01	1162	10.53	640

Note: PGV-C, PGV-M, PGV-S, Ampli-C, Ampli-M, Ampli-S are peak ground velocity (PGV) and amplification (Amp) generated from crustal fault, megathrust and intraslab.

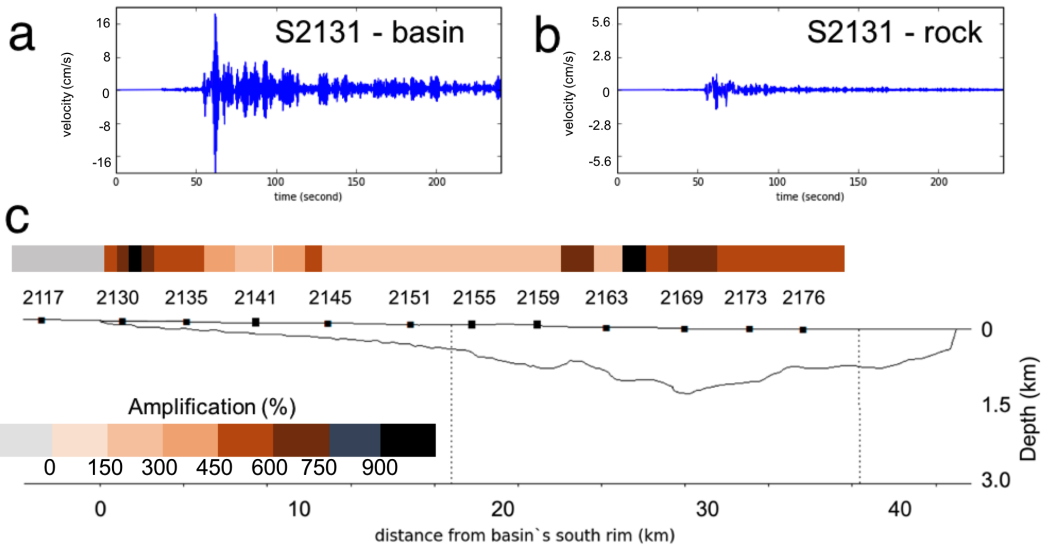

Figure 5.19: Similar to Figures 5.17 and 5.18, but for medium-depth intraslab earthquake scenario. Figure (**a**,**b**) are basin and bedrock seismograms (at S2131, located about 500 m north of S2130) and Figure (**c**) shows PGV amplification along the S-N cross-section.

available.

Since long period (>3 s) ground motions are much less sensitive to κ, Qp and Qs, it seems reasonable to consider how these compare to the design response spectra. At S2169, for all frequencies, mean ground motion predicted from GMPE fall below both the 2012-SNI [*Irsyam et al.*, 2011] in Figure 5.15 and the 2002-SNI proposed by *Puskim* [2011] (see also *Sukamta & Alexander* [2012]) design response spectra (Figure 5.20a–d). On the other hand, ground motion predictions on soil inferred from the SPECFEM2D modeling are much higher than design response spectra of 2002-SNI (since 2012-SNI provides response spectra from PGA to PSA 4 s, we compare PSA 4–10 s with 2002- SNI). Figure 5.20a–d shows that ground motion on bedrock is lower than 2002-SNI and 2012-SNI, therefore we believe that basin depth and surface condition is of great importance for magnifying seismic motion, as shown in Figures 5.16b and 5.18a–c amplification factor can reach 1200% for megathrust events. This amplification factor should be considered.

For the intraslab earthquake scenario, basin edge effects can be particularly pronounced as observed in Figure 5.13c. Amplification of short period ground motions, particularly at periods of about 1.0 s, result in very high acceleration (>1 g) at S2131 (5.21). At this point, the PGV amplification is 1125% (Figure 5.19 and Table 5.3), but this high frequency content may not be realistic due to the lack of consideration of attenuation effects as discussed above. On the other hand, large amplification at S2165 in the deepest part of the basin as can be seen in Figures 5.16c and 5.21 is experienced by ground motion at period >4. The spectral amplification at this point is as high as 424%. There is interesting characteristic of amplification at S2131 and S2165, while PSA ¿4 s at S2131 fall below the 2002-SNI design response spectra (Figure **b**) at S2165 the scenario response spectra at about 5.5 s is much higher the design response spectra (Figure b). An acceleration of about 0.2 g and amplification of 335% (for period of 5.5 s) are estimated by the simulation (Figure 5.21).

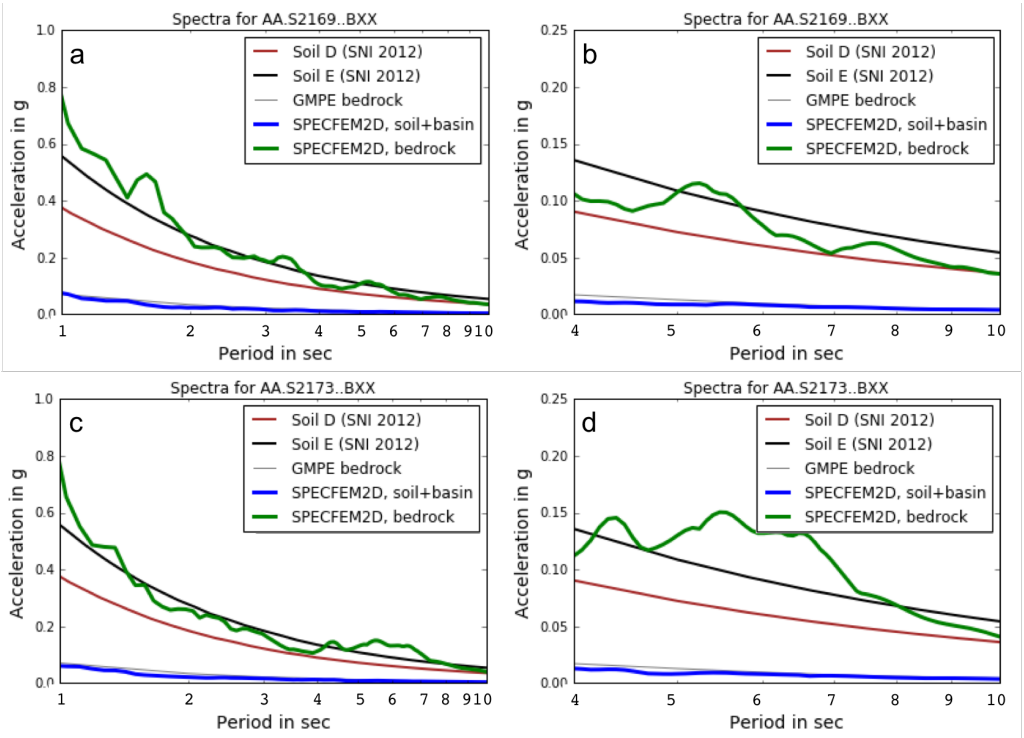

Figure 5.20: Computed acceleration response spectra for the megathrust earthquake scenario, plotted with the PSA using the AEA2015 GMPE and the Jakarta Building Code's design response spectra (for D-type soil, thick-black curve) at stations (**a**) S2169 and (**c**) S2173. (**b**,**d**) are zoomed images of (**a**,**c**), respectively for the period band 4–10 s. Location of stations are indicated in Figures 5.18 and 5.19.

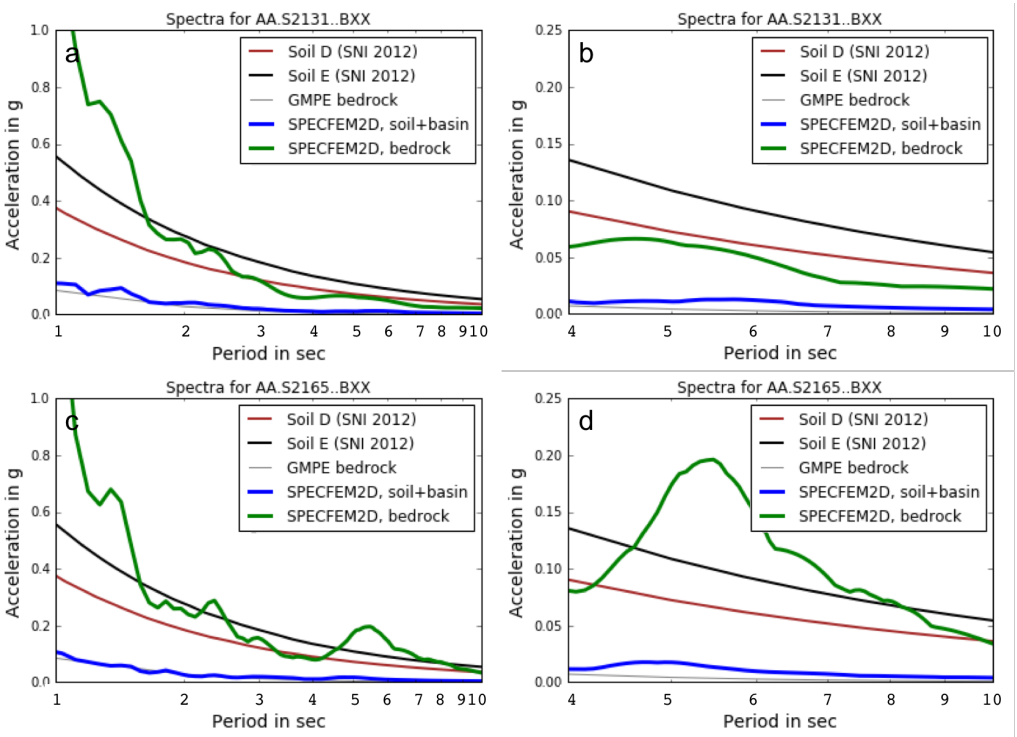

Figure 5.21: Computed acceleration response spectra for the intraslab earthquake scenario, plotted with the PSA using the AEA2015S GMPE and the Jakarta Building Code's design response spectra (for D-type soil, thick-black curve) at stations S2131 (**a**) and S2165 (**c**). (**b**,**d**) are zoomed images of (**a**,**c**), respectively, for the period band 4–10 s. Locations of S2165 are indicated in Figure 5.16 while S2131 is 500 m north of S2130 in the same figures. Note, that the Y-axes have different scales.

5.8 Conclusion

We have shown that GMPE modeling predicts significant influence of near-surface geology, represented by V_{S30}, on short-period (<1 s) seismic waves. However, for a very deep basin filled with soft sediment, available GMPEs are not capable of capturing the effects of basin geometry on seismic waves, at least for basins the Jakarta Basin. Consequently, more realistic approaches should be used to estimate ground motions. SPECFEM2D was chosen to simulate earthquake scenario ground motions, and the results show how soft sediment filling a deep basin amplifies seismic waves, generating high ground motion on the basin surface.

The amplification of ground motion due to basin geometry and depth varies from site to site, and depends upon depth of the basin, distance from the source, distance from the basin edge and also magnitude of the earthquake. While the megathrust scenario showed a close correspondence between PGV and spectral amplification, the crustal fault and especially intraslab scenarios showed a more complex relationship. These latter scenarios show large amplification in the south and north parts of basin and low amplification in the central part. The largest PGV are observed at the north stations, where the basin is very deep (>1000 m), in the crustal fault and megathrust scenarios. In contrast, the intraslab scenario triggered the highest long period PGVs near the basin edge.

The crustal fault scenario produced high spectral amplitudes at frequencies in the range 0.4–0.6 Hz, while the megathrust event generated high ground motions at frequencies of about 0.2 Hz and 0.5 Hz (5.20). Pronounced high ground motions at frequencies about 0.2 Hz are generated by the deep intraslab scenario (5.21). The high spectral amplitudes in the period range of 1.6–10 s are approximately in accordance with natural periods of 16–100 story buildings, therefore, basin resonance may be a more important consideration for high-rise buildings construction than previously realised.

Megathrust earthquakes may trigger high spectral accelerations in Jakarta. Especially at a period of 1 s, the simulated acceleration is higher than the design spectra of the building code. At some stations (e.g., S2173), acceleration at about period 5 s is also a bit higher than the building code's design spectra. This high acceleration and long duration of seismic waves inside the basin, as shown in Figure 5.18, should be of concern, because these factors can be responsible for building collapse. The high spectral accelerations (0.07–0.08 g) at periods between 5–7 s are estimated from the megathrust scenario, but high spectral acceleration (0.06 g) at a period of about 5.5 s is also estimated due to the intraslab earthquake scenario.

While results in this study should be regarded as preliminary in that they neglect the effects of attenuation inside the basin and do not account for 3-D wave propagation, overall they show the greatly enhanced seismic hazard in Jakarta due to its deep basin structure. When this is combined with Jakarta's proximity to earthquake sources (megathrust and active faults) and destructive earthquakes that have devastated Jakarta centuries ago, the risk of catastrophic damage should one of these large historical events occur today seems very real.

Chapter 6

Summary and Future Works

Undertaking reliable, scenario-based hazard modeling is important for better understanding the risk involved in a densely populated city like Jakarta tha lies in a seismically active region like Indonesia. The core elements at risk are human lives and economic loss, which are both critically dependent on building damage. Jakarta is a rapidly growing city in a country experiencing rapid economic development, and high-rise buildings will be a popular choice for residential accommodation for the foreseeable future. Fostering resilience against earthquakes therefore necessitates proper evaluation of high-rise building performance.

6.1 Summary

Despite many recent advances in the science of earthquakes and technology for earthquake monitoring, the time and location of the next big earthquake cannot be predicted with any precision. Even though the major plate boundaries were known and a number of active fault zones were mapped, unpredicted earthquake behavior continues to surprise us. One example is the 2011 Northeast Japan Earthquake, whose magnitude was much larger than scientists had expected, despite the massive investment in cutting-edge earthquake science and monitoring technology following the 1995 Kobe earthquake. Another is the Pidie Jaya, Indonesia Earthquake on December 7, 2016, which occurred on a previously unknown fault. Despite this confirmation of how poor our ability is to predict what types of earthquakes will occur at any time and place, this uncertainty should not impede our attempts to understand earthquakes and the hazard they pose, in an attempt to develop mitigation measures to lessen their potential impacts. This research endeavoured to provide a better understanding of seismic hazard in Jakarta and elsewhere, particularly by improving our understanding of the influence of local geology on seismic waves, so that the potential levels of future ground motion can be reliably estimated and appropriate measures taken to minimize impacts.

6.1.1 Historical Earthquakes Impacting the Jakarta Area

In this thesis, an investigation of the three historical earthquakes known to have devastated Jakarta (then Batavia) during the colonial era was undertaken to better understand which sources of seismicity might pose a threat to modern-day Jakarta. The three historical earthquakes known to have devastated Batavia, and which were generally felt and sometimes caused damage throughout western Java, occurred on 5 January 1699, 22 January 1780 and 5 October 1834. Analysis of the felt reports from historical archives with respect to the possible sources of seismicity in Java suggest that the 1699 event was a

Mw 8 intraslab earthquake (Scenario 1699A of Chapter 2) while the 1780 and 1834 events could have been Mw 7 crustal earthquakes on the Baribis Fault (Scenarios 1780A and 1834A, respectively, of Chapter 2).

The analysis of historical events in Chapter 2 thus suggests that the main earthquake threats to Jakarta are from intraslab earthquakes and earthquakes on the Baribis Fault south of the city. Such events were accordingly chosen for the scenario earthquake modeling undertaken in Chapter 5. However, given the fact that the Mw 9.0 11 March, 2011 Northeast Japan Earthquake was far greater than any in Japan's historical experience, it seemed remiss not to consider giant earthquakes on the Java Subduction Zone megathrust as a potential earthquake threat to Jakarta. For this reason the scenario modeling of Chapter 5 also includes a Mw 9 megathrust earthquake, even though there is no historical record of any such earthquake impacting Jakarta (such an event was considered and rejected as a candidate for the 1699 earthquake, because it did not match the seismic intensity pattern inferred from historical accounts).

6.1.2 PSHA with Site Response: Sulawesi Case Study

The first Probabilistic Seismic Hazard Analysis (PSHA) incorporating the effects of site amplification for the island of Sulawesi in Indonesia has been conducted. Most of the island, with the exception of South Sulawesi, is undergoing rapid deformation. This leads to high hazard in most regions (such that PGA $>$ 0.4 g at 500 year return period when site effects are included) and extremely high hazard (e.g., PGA $>$ 0.8 g at 500 year return period) along fast-slipping crustal faults such as the Palu-Koro-Matano Fault System and Lawanopo Fault. These high hazard levels are alarming when it is considered that among the 4 largest population centers on Sulawesi, Makassar (pop. 1.47M), Manado (pop. 0.70M), Palu (pop. 0.34M) and Kendari (pop. 0.32M), Palu and Kendari lie astride the Palu Koro and Lawanopo Fault, respectively. This means a total urban population of over 0.66M have a 10% chance of experiencing PGAs greater than 0.8 g (and 2.5g RSA at 0.2 s period) in the next 50 years. An even greater number of people in Manado have a 10% chance of experiencing PGAs greater than 0.5 g (and 1.5g RSA at 0.2 s period) in the next 50 years. Building design in these areas should combine bedrock hazard results with locally measured site effects to determine appropriate design criteria.

The contribution of site effects to the hazard level on a regional scale was accounted for by integrating the parameter VS30 into the seismic hazard calculation. This seismic hazard study for Sulawesi confirmed that site condition represented by VS30 is of great importance in quantifying the potential damage due to seismic ground shaking. VS30 can be estimated in a number of different ways, and three ways were considered here: The first Probabilistic Seismic Hazard Analysis (PSHA) incorporating the effects of site amplification for the island of Sulawesi in Indonesia has been conducted. Most of the island, with the exception of South Sulawesi, is undergoing rapid deformation. This leads to high hazard in most regions (such that PGA ¿ 0.4 g at 500 year return period when site effects are included) and extremely high hazard (e.g., PGA $>$ 0.8 g at 500 year return period) along fast-slipping crustal faults such as the Palu-Koro-Matano Fault System and Lawanopo Fault. These high hazard levels are alarming when it is considered that among the 4 largest population centers on Sulawesi, Makassar (pop. 1.47M), Manado (pop. 0.70M), Palu (pop. 0.34M) and Kendari (pop. 0.32M), Palu and Kendari lie astride the Palu Koro and Lawanopo Fault, respectively. This means a total urban population of over 0.66M have a 10% chance of experiencing PGAs greater than 0.8 g (and 2.5g RSA

at 0.2 s period) in the next 50 years. An even greater number of people in Manado have a 10% chance of experiencing PGAs greater than 0.5 g (and 1.5g RSA at 0.2 s period) in the next 50 years. Building design in these areas should combine bedrock hazard results with locally measured site effects to determine appropriate design criteria.

The V_S30 can be estimated in a number of different ways, and three ways were considered here: (1) using topography as a proxy for V_S30 (flat topography suggests soft soil, steep topography hard rock, see [*Wald & Allen*, 2007]); using topography combined with surface geology and other geomorphic indicators, as a proxy for V_S30, as proposed by [*Matsuoka et al.*, 2006], and; (3) in situ measurement using the HVSR technique. The first two proxy methods are much more cheap and easy to apply than the in situ HVSR method, but they are probably less accurate. Assuming HVSR yields a more accurate estimate of V_S30, we compared the two proxy methods to the HVSR estiamtes of V_S30 and found that the proxy methods yield systematically higher estimates than the HVSR measurements. Even though both proxy methods appear biased to high V_S30 values, we found that *Matsuoka et al.* [2006] resulted in the correct choice of the National Earthquake Hazard Reduction Program (NHRP) site class often used in PSHA more frequently than was the case for the *Wald & Allen* [2007] approach, so we used *Matsuoka et al.* [2006] in the definition of surface seismic hazard for Sulawesi.

However, given the apparently poor performance of even the *Matsuoka et al.* [2006] method for estimating Vs30, we stress the need for site specific and city scale seismic hazard analyses to use in situ measurements of V_S30 whenever possible. Such in situ measurements can be made using HVSR, Multichannel Analysis of Surface Waves (MASW), Standard Penetrometer Tests (NSPT), or Vertical Seismic Profiling (VSP).

6.1.3 HVSR Analysis for Jakarta Basin Structure

We have shown that the Horizontal-to-Vertical Spectral Ratio (HVSR) of seismic ambient seismic noise in the Jakarta Basin can be used to make robust estimates of the HVSR peak periods, which has been shown to coincide with the S-wave resonant period in many studies. In Jakarta, these peak periods are in the range 4–8s, with generally shorter periods in the south and longer periods in the north, in agreement with previous studies suggesting very low velocities (<200 m/s) extending to 100-150 meters depth [*Ridwan et al.*, 2016; *Ridwan*, 2016]. Our results show that the average S-wave velocity for whole basin, from surface to the basement is appear to be 852 m/s. S-wave resonant periods in this range are potentially a concern for very tall (40–80 storey) buildings, which are prevalent in Jakarta currently and whose number is expected to increase in the next decade.

We have also inverted the HVSR curves obtained in Jakarta to estimate the S-wave velocity structure of the basin. In order to resolve the deep basin architecture, we used Trans-dimesional Bayesian inference, which not only allows the number of layers to adapt to fit the data, but also accounts for uncertainty in the model due to the unknown number of layers. While the shallow velocity structure due to compaction of unconsolidated sediments can be constrained well as long as the inversion fitted the higher frequency peak. The dense seismic network we deployed in the Jakarta Basin enabled the mapping of basement topography, whose depth varies within the range 300-1400 m in a pattern similar to that obtained in previous studies using Ambient Noise Tomography and SPAC (*Saygin et al.* [2016] and *Ridwan et al.* [2016], respectively.)

6.1.4 Earthquake Scenario Ground Motions for Jakarta

Modern Ground Motion Prediction Equations (GMPEs) generally include site parameters such as V_S30 to account for site amplification effects. However, as suggestd by *Huang et al.* [2009] study of the Taipei Basin, it seems likely that V_S30 is only useful for parameterizing site class for ground motions at periods less than 1 second. Recent GMPEs, known as New Generation Attenuation (NGA) models. attempt to account for deep basin effects using parameters such as Z1.0, the depth to V_S=1.0 km/s. We find that, because these GMPEs were developed using data from California and Japan, they do not appear to be suitable for the much deeper basin depths encountered in Jakarta.

Instead of using GMPEs, more realistic approaches should be used to estimate ground motions, such as the earthquake scenario simulations we presented in Chapter 5. These simulations using SPECFEM2D showed how the deep basin filled with low Vs sediment amplifies seismic waves, leading to high amplitude ground motion of long duration in the Jakarta Basin. Our results for scenario modeling suggest that in some cases the long period (1-10 s) response spectral ground motion can reach or exceed the design spectrum used in the current Building Code for Jakarta.

6.2 Future Work

HVSR is proven to be a reliable technique to determine deep basin geometry and this method has high reproducibility and applicability. However, as noted in Chapter 4 our approach suffers from a number of limitations. Foremost among these is the assumption that the HVSR curve is dominated by the fundamental mode Rayleigh wave. This assumption should be checked through 3-components analysis of the ambient noise data, and the possible existence of Love waves or higher-mode Rayleigh waves should be accounted for. In order to better constrain Vs30 estimates and avoid trade-offs between Vs and layer thicknesses, HVSR curves should be jointly inverted with surface wave dispersion data.

If these limitations can be overcome, the HVSR method should be applied to other sedimentary basins in Indonesia, such as the Bandung Basin. Bandung Basin is a giant intra-montane basin surrounded by volcanic highlands in the north, south and east while in the west karst is dominant. This basin covers an approximately 2300 km2 water catchment area, make the basin one of the largest watersheds in Java [*Abidin et al.*, 2013]. Bandung Basin is mostly filled with intercalation of lacustrine and volcanic deposits [*Dam*, 1997]. This condition, to some extent, is similar to the Jakarta Basin. Its proximity to the Lembang Fault, which has a measured geodetic slip rate of 6 mm/year [*Meilano et al.*, 2012], confirms an earthquake threat that may impact Bandung in the future. Investigating the structure of the Bandung basin, where the second largest metropolitan area in Indonesia lies, is an important challenge for the future.

Earthquake scenario modeling that incorporates basin geometry, although it has here been undertaken only for a 2D SN cross-section, hints at potential ground motions that may severely affect Jakarta. There are two approaches to map the effect of deep basin on seismic waves propagating to Jakarta city. The first method is perform 2D ground motion simulation for parallel cross-sections, spaced 1 km each other, either in SN or WE direction. By rotating the strike of the fault in the anti-clockwise direction by the same amount as the azimuth of the site with respect to the epicenter, the ground motion in yz-axis can be calculated. The result will be a 2.5D ground motion model [*Narayan*, 2001, 2003]. This method consume computational time 12-15% more than required for 2D

modeling [*Narayan*, 1999]. The second method is conduct 3D simulataion that consume much longer computational time and creating 3D domain model.

However, our current modelling approach ignores: intrinsic attenuation (Q) along the path from source to receiver, as well as in the basin itself; 3D spreading and scattering effects and; variation of VS in the basin, both laterally and as a function of depth. Although modeling of these effects is computationally expensive, it has been achieved in recent studies [*Molnar et al.*, 2014; *Furumura & Chen*, 2005]. Given adequate computational resources, there is no reason why similar simulations could not be undertaken for the Jakarta Basin in the near future, and this fully 3D approach would be the best way to reliably model ground motions in the Jakarta Basin.

Finally, a new approach to the estimation of earthquake ground motion in sedimentary basins avoids the need to estimate seismic velocity structure as an intermediate step, by utilising both phase and amplitude information in the ambient noise Green's functions [*Denolle et al.*, 2013, 2014b; *Viens et al.*, 2016]. This Virtual Earthquake Approach (VEA) has been used to characterize basin amplification effects in the Los Angeles [*Denolle et al.*, 2013], Kanto *Viens et al.* [2017] and Nobi [*Viens et al.*, 2015] Basins. The study by (Viens et al., 2015) also showed that combined offshore-onshore noise recordings can be used to accurately simulate the long-period ground motions generated by an offshore subduction zone earthquake. All of these studies have noted that the VEA is most successful in the 4-10 s period range, so the 5-6 second resonant period of the Jakarta Basin makes it an excellent candidate for the application of this technique.

This research shows that in the Jakarta's seismic future has potential for catastrophic events, given Jakarta's location on a thick, low Vs sedimentary basin, its proximity to earthquake sources (megathrust and active faults), the historic occurrence of destructive earthquakes that devastated Jakarta centuries ago, and the prevalence of non-engineered masonry construction. It should be our concern to translate these results into simple, powerful messages that are easily to understood by policy makers and the public.

Bibliography

Abidin, H.Z.; Andreas, H.; Kato, T.; Ito, T.; Meilano, I.; Kimata, F.; Natawidjaja, D.; Harjono, H. Crustal deformation studies in Java (Indonesia) using GPS. *J. Earthq. Tsunami* **2009**, *3*, 77–88

Abidin, H. Z., H. Andreas, I. Gumilar, Y. Fukuda, Y. E. Pohan and T. Deguchi. (2011). Land subsidence of Jakarta (Indonesia) and its relation with urban development. *Nat. Hazards* **18**, 232–242

Abidin, H. Z., I. Gumilar, H. Andreas, D. Murdohardono, and Y. Fukuda. (2013). On causes and impacts of land subsidence in Bandung Basin, Indonesia. *Environmental Earth Sciences* **68(6)**, 1545–1553

Abrahamson, N. A. (2011). Is VS30 an effective parameter for site characterization? In *the 4th IASPEI/IAEE International Symposium: Effects of Surface Geology on Seismic Motion* University of California, Santa Barbara, 23–26 August 2011, http://esg4.eri.ucsb.edu/sites/esg4.eri.ucsb.edu/files/Abrahamson%20ESG4%20Vs30.pdf (last accessed September 2017).

Abrahamson, N. A., N. Gregor and K. Addo (2016). BC Hydro Ground Motion Prediction Equations for Subduction Earthquakes. *Earthquake Spectra* **32(1)**, 23–44

Abrahamson, N. A., W. J. Silva and R. Kamai (2014). Summary of the ASK14 Ground Motion Relation for Active Crustal Regions. *Earthquake Spectra* **30(3)**, 1025–1055

Afnimar, E. Yulianto, and Rasmid. (2015). Geological and tectonic implications obtained from first seismic activity investigation around Lembang fault. *Geoscience Letters* **2(1)**, n/a–n/a

Agostini, L., J. Boaga, Galgaro, A., and A. Ninfo (2015). HVSR technique in near-surface thermal-basin characterization: the example of the Caldiero district (North-East Italy). *Environ Earth Sci* **74**, 1199–1210

Aki, K. and P. G. Richards (1980). *Quantitative Seismology, Vol. I*, W. H. Freeeman and Company, San Francisco

Aki, K. (1965). Maximum likelihood estimate of b in the formula logN= a-bM and its confidence limits. *Bull. of the ERI* **43**, 237–239 東京大学地震研究所

Aki, K. (1957). Space and time spectra of stationary stochastic waves, with special reference to microtremors. *Bull. of the ERI* **35**, 415–456

Allmendinger, R. W. (2017). *Modern Structural Practice: A structural geology laboratory manual for the 21st Century v.1.7.0 ©2015-2017.* http://www.geo.cornell.edu/geology/faculty/RWA/structure-lab-manual/

Anderson, J. G., Y. Lee, Y. Zeng, and S. Day (1996). Control of Strong Motion by Upper 30 Meters. *Bull. Seism. Soc. Am.* **86(6)**, 1749–1759.

Albini, P., R. M. W. Musson, A. A. Gomez Capera, M. Locati, A. Rovida, M. Stucchi, and D. Viganó. (2013). *Global Historical Earthquake Archive and Catalogue (1000-1903)*. Pavia, Italy

Arai, H. and K. Tokimatsu (2004). S-Wave Velocity Profiling by Inversion of Microtremor H/V Spectrum. *Bull. Seism. Soc. Am.* **94(1)**, 53–63

Arai, H. and K. Tokimatsu (2000). Effects of Rayleigh and Love Waves on Microtremor H/V Spectra. Proceeding: *the 12_{th} WCEE* Auckland, New Zealand

Arnold, C., B. Bolt, D. Dreger, E. Elsesser, R. Eisner, W. Holmes, G. McGavin, and C. Theodoropoulos (2006). *Risk Management Series: Designing for Earthquakes, A Manual for Architects* Earthquake Engineering Research Institute (EERI) of Oakland, California, FEMA/DHS

Arya, A. S., T. Boen and Y. Ishiyama (2013). Guidelines for Earthquake Resistant Non-Engineered Construction. *UNESCO*

Asten, M. W. and D. M. Boore (2005). Comparison of Shear-Velocity Profiles of Unconsolidated Sediments near the Coyote Borehole (CCOC) Measured With Fourteen Invasive and Non Invasive Methods. *USGS Open-File Report* 2005-1169

Asten, M. W. (2006). On bias and noise in passive seismic data from finite circular array data processed using SPAC methods. *Geophysics* **7(6)**, V153–V162

Asten, M. W., T. Dhu, and N. Lam (2004). Optimised array design for microtremor array studies applied to site classification—Observations, results and future use, Proceedings: *the 13^{th} WCEE*, Vancouver, Paper 2903

Atkinson, G. M. and D. M. Boore (2003). Empirical Ground-Motion Relations for Subduction-ZoneEarthquakes and Their Application to Cascadia and Other Regions. *Bull. Seism. Soc. Am.* **93(4)**, 1703–1729.

Atkinson, G. M. and SL. I. Kaka (2007). Relationships between Felt Intensity and Instrumental Ground Motion in the Central United States and California. *Bull. Seism. Soc. Am.* **97(2)**, 497-510

Bala, A., A. Aldea, D. Hannich, D. Ehret, and V. Raileanu (2009). Methods to assess the Site Effects Based on in situ Measurements in Bucharest City, Romania. *J. Romanian Reports in Physics* **61(2)**, 335–346

Bard, P. Y. (1999). Microtremor Measurements: A tool for site effect estimation? *The effects of Surface Geology on Seismic Motion*, Irikura, Kudo, Okada and Sasatani (eds), 1251-1279

Bard, P. Y. and M. Bouchon (1985). The two-dimensional resonance of sediment-filled valleys *Bull. Seism. Soc. Am.*, **75(2)**, 519–541

Bayes,T. (1763). Bayes. An Essay Towards Solving a Problem in the Doctrine of Chances (ed. C. Davis). *Royal Society of London.*

Beck, S., S. Barrientos, E. Kausel, and M. Reyes (1988). Source characteristics of historic earthquakes along the central Chile subduction zone. *J. South American Earth Sciences* 11(2), 115–129

Berbellini, A., A. Morelli, and A.M.G. Ferreira (2016). Ellipticity of Rayleigh waves in basin and hard-rock sites in Northern Italy. *Geophys. J. Int.* **11(2)**, 115–129 **206**, 305–407.

Berbellini, A., A. Morelli, and A.M.G. Ferreira (2017). Crustal structure of northern Italy from the ellipticity of Rayleigh waves. *Physics of the Earth and Planetary Interiors.* **265**, 1–14

Beroya, M.A.A. and A. Aydin (2010). A new approach to liquefaction hazard zonation: Application to Laoag City, Northern Philippines. *Soil Dyn Earthq. Eng.*. **30**, 1338–1351

Bonilla, L. F., J. H. Steidl, G. T. Lindley, A. G. Tumarkin, and R. J. Archuleta (1997). Site amplification in the San Fernando Valley, California: Variability of site-effect estimation using the S-wave, coda, and H/V methods. *Bull. Seism. Soc. Am.* **87(3)**, 710–730

Bemmelen, R.W. van (1949). *The Geology of Indonesia and Adjacent Archipelagoes Vol. IA*, Martinus Nijhoff. The Hague

BNPB (Indonesian National Disaster Management Agency - Badan Nasional PenganggulanganBencana) (2010). Disaster Data and Information Indonesia (Data dan Informasi Bencana Indonesia). http://dibi.bnpb.go.id

BIG–Badan Informasi Geospasial [Geospatial Information Agency] (2015). http://www.bakosurtanal.go.id/berita-surta/show/indonesia-memiliki-13-466-pulau-yang-terdaftar-dan-berkoordinat, accessed June 2017

Bock, Y., L. Prawirodirdjo, J. F. Genrich, C. W. Stevens, R. McCaffrey, C. Subarya, S. S. O. Puntodewo, and E. Calais (2003). Crustal motion in Indonesia from Global Positioning System measurements. *J. Geophys. Res.* **108(B8)**, n/a–n/a

Bodin, T., M. Sambridge, H. Tkalčic, P. Arroucau, K. Gallagher, and N. Rawlinson (2012). Transdimensional inversion of receiver functions and surface wave dispersion. *J. Geophys. Res.: Solid Earth* **117(B2)**, 2156–2202

Bodin, T. and M. Sambridge (2009). Seismic tomography with the reversible jump algorithm. *Geophys. J. Int.* **178(3)**, 1141–1436

Bodin, P., K. Smith, S. Horton, and H. Hwang (2001). Microtremor observation of deep sediment resonance in metropolitan Mamphis, Tennessee. *Eng. Geology* **62**, 159–168

Bonnefoy-Claudet, S., S. Baize, L. F. Bonilla, C. Berge-Thierry, C. Pasten, J. Campos, P. Volant, and R. Verdugo (2009). Site effect evaluation in the basin of Santiago de Chile using ambient noise measurements. *Geophys. J. Int.* **176(3)**, 925–937

Bonnefoy-Claudet, S., A. Köhler, C. Cornou, M. Wathelet, and P.-Y. Bard (2008) Effects of Love Waves on Microtremor H/V Ratio. *Bull. Seism. Soc. Am.* **98(1)**, 925–937

Bonnefoy-Claudet, S., F. Cotton, and P.-Y. Bard (2006) The nature of noise wavefield and its applications for site effects studies. A literature review. *Earth-Science Reviews* **79**, 205–227

Boore D.M., W. B. Joyner and T. E. Fumal (1997). Equations for estimating horizontal response spectra and peak acceleration from western North American earthquakes: A summary of recent work (with 2005 Erratum) *Seismol. Res. Lett.* **68**, 128–153

Boore, D. M., and G. M. Atkinson (2008). Ground-motion prediction equations for the average horizontal component of PGA, PGV, and 5%-Damped PSA at spectral periods between 0.01s and 10.0s *Earthquake Spectra* **24(1)**, 99–138

Borcherdt, R. D. (1994). Estimates of site-dependent response spectra for design (methodology and justification). *Earthquake Spectra* **10(4)**, 617–653

Borges, J. F. , H. G. Silva, R. J. G. Torres, B. Caldeira, M. Bezzeghoud, J. A. Furtado, J. Carvalho (2016). Inversion of ambient seismic noise HVSR to evaluate velocity and structural models of the Lower Tagus Basin, Portugal. *J. Seismol.* **20**, 875–887

BPS (Indonesian Central Agency for Statistics - Badan Pusat Statistik) (2010). Population Census of Indonesia (SensusPenduduk 2010). www.sp2010.bps.go.id

BSSC - Building Seismic Safety Council (2003). NEHRP Recommended Provisions for seismic Regulations for New buildings and other Structures. *Part1: Provisions, FEMA* 368, Washington, D.C.

Calderón-Macías, C., and B. Luke (2007). Improved parameterisation to invert Rayleigh-wave data for shallow profiles containing stiff inclusions. *Geophysics* **72(1)**, U1–U10

Campbell K. W. and Y. Bozorgnia (2014). NGA-West2 Ground Motion Model for the Average Horizontal Components of PGA, PGV, and 5% Damped Linear Acceleration Response Spectra. *Earthquake Spectra* **30(3)**, 1087–1115

Campbell, K.W., and Y. Bozorgnia (2013). NGA-West2 Campbell-Bozorgnia Ground Motion Model for the Horizontal Components of PGA, PGV, and 5%-Damped Elastic Pseudo-Acceleration Response Spectra for Periods Ranging from 0.01 to 10 sec. *PEER*, Report No. **2013/06**

Campbell, K.W., and Y. Bozorgnia (2008). Ground motion model for the geometric mean horizontalcomponent of PGA, PGV, PGD and 5% damped linear elastic response spectra for periods ranging from 0.01 to 10.0 s. *Earthquake Spectra* **24(1)**, 139–171

Castellaro, S. and F. Mulargia (2009). Estimates of Vs30 Based on Constrained H/V Ratio Measurements Alone, in: Mucciarelli, M., M. Herak, and J. Cassidy (eds), *Increasing Seismic Safety by Combining Engineering Technologies and Seismological Data* pp. 85–97, Dordrecht: Springer Netherlands.

Castellaro, S. and F. Mulargia (2009). VS30 Estimates Using Constrained H/V Measurements. *Bull. Seism. Soc. Am.* **99(2A)**, 761–773.

Castellaro, S., L. A. Padrón and F. Mulargia (2014). The different response of apparently identical structures: a far-field lesson from the Mirandola the 20^{th} May 2012 earthquake. *Bull. of Earthq. Eng.* **12(5)**, 2481–2493

Chen, K. C., J. M. Chiu and Y. T. Yang (1994). Qp-Qs Relations in the Sedimentary Basin of the Upper Mississippi Embayment Using Converted Phases. *Bull. Seism. Soc. Am.* **84(6)**, 1861–1868

Chimoto, K., H. Yamanaka, S. Tsuno, H. Miyake, and N. Yamada (2016). Estimation of shallow S-wave velocity structure using microtremor array exploration at temporary strong motion observation stations for aftershocks of the 2016 Kumamoto earthquake. *Earth, Planets and Space* **68**, 206

Chiou, B., and R. Youngs (2008). An NGA model for the average horizontal component of peakground motion and response spectra. *Earthquake Spectra* **24(1)**, 173–215

Chiou, B., and R. Youngs (2014). Update of the Chiou and Youngs NGA Model for the Average Horizontal Component of Peak Ground Motion and Response Spectra. *Earthquake Spectra* **30(3)**, 1117–1153

Cipta A., R. Robiana, J. Griffin, N. Horspool, S. Hidayati and P. Cummins (2016). A Probabilistic Seismic Hazard Assessment for Sulawesi, Indonesia. In: Cummins, P. R. & Meilano, I. (eds) *Geohazards in Indonesia: Earth Science for Disaster Risk Reduction* Geol. Soc., London, Special Publications **441**, The Geol. Soc. of London

Cipta, A., P. Cummins, M. Irsyam, and S. Hidayati, 2018. Basin Resonance and Seismic Hazard in Jakarta, Indonesia. *Geosciences* **8(4)**, 128.

Claprood, M., M. W. Asten and J. Kristek (2012). Combining HVSR microtremor observations with the SPAC method for site resonance study of the Tamar Valley in Launceston (Tasmania, Australia). *Geophys. J. Int.* **191(2)**, 765–780

Clements, B., R. Hall, H.R. Smyth and M.A., Cottam (2009). Thrusting of the Volcanic Arc: a New Structurel Model for Java. *Petroleum Geosci.* **15**, 159–174

Council on Tall Buildings and Urban Habitat (CTBUH) (2017). The Skyscrapper center: The Global Tall Building Database of CTBUH. http://www.skyscrapercenter.com/index.php/city/jakarta, accessed on August 2, 2017

Cranswick E., K. King, D. Carver, D. Worley, and R. A. Williams (1990). Site response across downtown Santa Cruz, California. *Geophys. Res. Lett.* **17(1)**, 1793–1796

Cruz-Atienza, V. M., J. Tago, J. D. Sanabria-Gómez, E. Chaljub, V. Etienne, J. Virieux, and L. Quintanar (2016). Long Duration of Ground Motion in the Paradigmatic Valley of Mexico. *Nature* **6(38807)**

Dam, M.A.C. (1997). *The Late Quaternary Evolution of the Bandung Basin, West Java Indonesia*, Geological Research and Development Center, Bandung

Dardji, N., T. Villemin, J.P. Ramnoux. Paleostresses and strike-slip movement: The Cimandiri Fault Zone, West Java, Indonesia. *J. Southeast Asian Stud.* **1994**, *9*, 3–11

Delinom, M.R. (2008). Groundwater management issues in the Greater Jakarta Area, Indonesia. *Proceedings of International Workshop on Integrated Watershed Management for Sustainable Water Use in a Humid Tropical Region* 8(2), JSPS-DGHE Joint Research Project, Tsukuba October 2007, Bull. TERC, Univ. of Tsukuba

Delinom, M. R., H. Z. Abidin, M. Taniguchi, D. Suherman, R. F. Lubis, and E. Yulianto. (2009). The contribution of human activities to subsurface environment degradation in Greater Jakarta Area, Indonesia. *Science of the Total Environment* **407**, 3129–3141

DeMets, C., R. G. Gordon, and D. F. Argus (2010). Geologically current plate motions. *Geophys. J. Int.* **181**, 1–80

Denolle, M. A., E. M. Dunham, G. A. Prieto, and G. C. Beroza (2013). Ground motion prediction of realistic earthquake sources using the ambient seismic field. *J. Geophys. Res.* **118**, 2102–2118

Denolle, M. A., H. Miyake, S. Nakagawa, N. Hirata, and G. C. Beroza (2014). Long-period seismic amplification in the Kanto Basin from the ambient seismic field. *Geophys. Res. Lett.* **41(7)**, 2319–2325

Denolle, M. A., E. M. Dunham, G. A. Prieto, and G. C. Beroza (2014). Strong Ground Motion Prediction Using Virtual Earthquakes. *Science* **343(6169)**, 399–403

Dettmer, J. , S. Molnar, G. Steineger, S. E. Dosso, and J. F. Cassidy (2012). Trans-dimensional inversion of microtremor array dispersion data with hierarchical autoregressive error models *Geophys. J. Int.* **188(2)**, 719–734

Dettmer, J. , S. E. Dosso, and C. W. Holland. (2010). Trans-dimensional geoacoustic inversion. *J. acoust. Soc. Am.* **128(6)**, 3393–3405

Dettmer, J. , S. E. Dosso, and C. W. Holland. (2010). Bayesian evidence computation for model selection in non-linear geoacoustic inference problems. *J. acoust. Soc. Am.* **128(6)**, 3406–3415

Dettmer, J. , S. E. Dosso, and C. W. Holland. (2009). Model selection and Bayesian inference for high-resolution seabed reflection inversion. *J. acoust. Soc. Am.* **125**, 706–716

Dettmer, J. , S. E. Dosso, and C. W. Holland. (2007). Uncertainty estimation in seismo-acoustic reflection travel-time inversion. *J. acoust. Soc. Am.* **122**, 161–176

Di Giulio G., S. Marzorati, F. Bergamaschi, P. Bordoni, F. Cara, E. D'Alema, C. Ladina, M. Massa, and the L'Aquila Experiment Team (2011). Local variability of the ground shaking during the 2009 L'Aquila earthquake (April 6, 2009—Mw 6.3): the case study of Onna and Monticchio villages. *Bull Earthq. Eng.* **9**, 783–807

Dixit, J., D. M. Dewaikar, and R. S. Jangid (2012). Free Field Surface Motion at Different Site Types due to Near-Fault Ground Motions. *ISRN Geophysics* Article ID **8210517**

Dosso, S. E. (2002). Quantifying uncertainties in geoacoustic inversion I: A fast Gibbs sampler approach. *J. acoust. Soc. Am.* **111**, 2166–2177

Dosso, S. E., P. L. Nielsen and M. J. Wilmut (2006). Data error covariance in matched-field geoacoustic inversion. *J. acoust. Soc. Am.* **119**, 208–219

D'Amico, V. M. Picozzi, F. Baliva, and D. Albarello. (2008). Ambient Noise Measurements for Preliminary Site-Effects Characterization in the Urban Area of Florence, Italy. *Bull. Seism. Soc. Am.* **98(3)**, 1373–1388

EERI (2009). Learning from Earthquakes: The Mw 7.6 Western Sumatra Earthquake of September 30, 2009. *EERI Special Report* December 2009

Emporis GmbH (2017). https://www.emporis.com/city/100259/jakarta-indonesia, accessed on August 2, 2017

Ewald, M., Heiner Igel, K.-G. Hinzen, and F. Scherbaum. (2006). Basin-related effects on ground motion for earthquake scenarios in the Lower Rhine Embayment. *Geophys. J. Int.* **166(1)**, 197–212

Esteva, L. (1988). Mexico earthquake of September 19, 1985—Consequences, lessons, and impact on research and practice. *Earthquake Spectra* **4(3)**, 413–426

Fäh, D., F. Kind, and D. Giardini. (2003). Inversion of local S-wave velocity structures from average H/V ratios, and their use for the estimation of site-effects. *J. Seismology* **7(4)**, 449–467

Fäh, D., F. Kind, and D. Giardini. (2001). A theoretical investigation of average H/V ratios. *Geophys. J. Int.* **145(2)**, 355–549

Fauzi, A., M. Irsyam, and U. J. Fauzi (2014). Empirical Correlation of Shear Wave Velocity and N-SPT Value for Jakarta. *Int. J. GEOMATE* **7(1)**, 980–984

FEMA - Federal Emergency Management Agency (2003). NEHRP (National Earthquake and Hazards Reduction Program) recommended provisions for seismic regulations for new buildings and other structures. *BSSC* Washington D.C.

Fergany, E. and K. Omar (2017). Liquefaction potential of Nile delta, Egypt. *NRIAG J. Astro. Geophys.* **6**, 60–67

Field, E. and K. Jacob (1993). The theoretical response of sedimentary layers to ambient seismic noise. *Geophys. Res. Lett.* **20(24)**, 2925–2928

Flores-Estrella, H., S. Yussim and C. Lomnitz (2007). Seismic response of the Mexico City Basin: A review of twenty years of research. *Nat. Hazards* **40**, 357–372

Foti, S., C. Comina, D. Boiero and L. V. Socco (2009). Non-uniqueness in surface-wave inversion and consequences on seismic site analyses. *Soil Dyn. Eq. Eng.* **29(6)**, 982–993

Furumura, T. and B. L. N. Kennett (1998). On the nature of regional seismic phases III. The influence of crustal heterogeneity on the wave-field for subduction earthquakes: the 1985 Michoacán and 1995 Copala, Guerrero, Mexico earthquakes. *Geophys. J. Int.* **135(3)**, 1060–1084

Furumura, T. and L. Chen (2005). Parallel simulation of strong ground motions during recent and historical damaging earthquakes in Tokyo, Japan. *Parallel Computing* **31(2)**, 149–165

Furumura, T. and T. hayakawa, 2007. Anomalous propagation of long-period ground motions recorded in Tokyo during the 23 October 2004 Mw 6.6 Niigata-ken Chuetsu, Japan. *Bull. Seism. Soc. Am.*. **97(3)**, 863–880

Galgaro, A., J. Boaga, and M. Rocca (2014). HVSR technique as tool for thermal-basin characterization: a field example in N-E Italy. *Environ Earth Sci* **71**, 4433–444

Galetzka, J., D. Melgar, J. F. Genrich, J. Geng, S. Owen, E. O. Lindsey, X. Xu, Y. Bock, J.-P. Avouac, L. B. Adhikari, B. N. Upreti, B. Pratt-Sitaula, T. N. Bhattarai, B. P. Sitaula, A. Moore, K. W. Hudnut, W. Szeliga, J. Normandeau, M. Fend, M. Flouzat, L. Bollinger, P. Shrestha, B. Koirala, U. Gautam, M. Bhatterai, R. Gupta, T. Kandel, C. Timsina, S. N. Sapkota, S. Rajaure, N. Maharjan (2015). Slip pulse and resonance of the Kathmandu basin during the 2015 Gorkha earthquake, Nepal. *Science* **349(6252)**, 1091–1095

García, D., S. K. Singh, M. Herraíz, M. Ordaz, and J. F. Pacheco (2005). Inslab Earthquakes of Central Mexico: Peak Ground-Motion Parameters and Response Spectra. *Bull. Seism. Soc. Am.* **95(6)**, 2272–2282

García-Jerez, A., F. Luzón, M. Navarro, and J. A. Peréz-Ruiz (2006). Characterization of the Sedimentary Cover of the Zafarraya Basin, Southern Spain, by Means of Ambient Noise. *Bull. Seism. Soc. Am.* **96(3)**, 957–967

Geological Agency of Indonesia (Badan Geologi) (2009). Laporan Singkat Gerakan Tanah Cikangkareng, 2 September 2009. *unpublished report*

GEM Foundation (2014). Openquake source code. https://www.globalquakemodel.org/

GEOPSY TEAM (2006). Geopsy source code. http://www.geopsy.org/download.php

Ghofrani, H. and G. M. Atkinson (2014). Site condition evaluation using horizontal-to-vertical response spectral ratios of earthquakes in the NGA-West 2 and Japanese databases. *Soil Dyn. Eq. Eng.* **67**, 30–43

Ghasemi, H., M. Zare, Y. Fukushima and K. Koketsu (2009). An empirical spectral ground-motion model for Iran. *J. Seismology* **13(4)**, 499–515

Gorstein, M. and M. Ezersky (2015). Combination of HVSR and MASW Methods to Obtain Shear Wave Velocity Model of Subsurface in Israel. *nternational J. Geohazards and Environment* **1(1)**, 20–41

Gosar, A. (2010). Site effects and soil-structure resonance study in the Kobarid basin (NW Slovenia) using microtremors. *Nat. Hazards Earth Syst. Sci.* **10**, 761–772

Gouveia, W. P. and J. A. Scales (1998). Bayesian seismic waveform inversion: Parameter estimation and uncertainty analysis. *J. Geophys. Res.: Solid Earth* **03(B2)**, 2759–2779

Graves, R. W., A. Pitarka, and P. Sommerville (1998). Ground-motion amplification in the Santa Monica area: Effects of shallow basin-edge structure. *Bull. Seism. Soc. Am.* **88(5)**, 1224–1242

Green, P. J., 1995. Reversible jump Markov chain Monte Carlo computation and Bayesian model determination. *Biometrika*. **82**, 711–732

Guéguen, P., C. Cornou, S. Garambois, and J. Banton (2007). On the Limitation of the H/V Spectral Ratio Using Seismic Noise as an Exploration Tool: Application to the Grenoble Valley (France), a Small Apex Ratio Basin. *Pure Appl. Geophys* **164(1)**, 115–134

Guillier, B. , C. Cornou, J. Kristek, P. Moczo, S. Bonnefoy-Claudet, P.-Y. Bard, and D. Fah (2006). Simulation of seismic ambient vibrations: does the H/V provide quantitative information in 2D-3D structures?. *Int. Symp. on the Effects of Surface Geology on Seismic Motion* Grenoble, France, paper **185**

Gulick, S. P., J. A. Austin Jr., L. C. McNeill, N. L. Bangs, K. M. Martin, T. J. Henstock, J. M. Bull, S. Dean, Y. S. Djajadihardja, and H. Permana (2011). Updip rupture of the 2004 Sumatra earthquake extended by thick indurated sediments. *Nature Geoscience* **4(7)**, 453–456

Hall, R., B. Clements, H. R. Smyth, and M. A. Cottam (2007). A New Interpretation of Java's Structure. Proceedings: 31^{st} *Annual Convention and Exihibition of IPA* **PA-07-G-035**

Hall, R. (2009). Indonesia, Geology. *Royal Holoway University of London.* searg.rhul.ac.uk/pubs/hall_2009_Indonesia%20Islands.pdf

Han, X., K. Megawati, and H. Yamanaka (2012). Shear-Wave Velocity Structure underneath the City of Padang, Indonesia. Proceedings: *the* 15^{th} *WCEEA* Lisboa.

Handayani, L.; Maryati, Kamtono, M.; Mukti, M.; Sudrajat, Y. Audio-Magnetotelluric Modeling of Cimandiri Fault Zone at Cibeber, Cianjur. *Indones. J. Geosci.* **2017**, *4*, 39–47.

Hall, R. (2011). Australia–SE Asia collision: plate tectonics and crustal flow. *Geological Society of London* **355(1)**, 75–109

Hanks, T. C. and A. G. Brady (1991). The Loma Prieta earthquake, ground motion, and damage in Oakland, Treasure Island, and San Francisco. *Bull. Seism. Soc. Am.* **81(5)**, 2019–2047

Hanks, T. C. and H. Kanamori (1979). A moment magnitude scale. *J. Geophys. Res.* **84(B5)**, 2348–2350

Harris, R. and J. Major (2016) Waves of destruction in the East Indies: the Wichmann catalogue of earthquakes and tsunami in the Indonesian region from 1538 to 1877. In: Cummins, P. R. & Meilano, I. (eds) *Geohazards in Indonesia: Earth Science for Disaster Risk Reduction* Geol. Soc., London, Special Publications **441**, The Geol. Soc. of London

Hasancebi, N. and R. Ulusay (2006). Empirical correlations between shear wave velocity and penetration resistance for ground shaking assessments. *Bull. of Eng. Geol. and the Envi.* **66(2)**, 203–213

Hauksson, A., T. L. Teng, and T. L Henyey (1987). Results from a 1500 m Deep, Three-level Downhole Seismometer Array: Site Response, Low Q values and f_{max}. *Bull. Seism. Soc. Am.* **7(6)**, 1883–1904

Harutoonian, P., C. J. Leo, K. Tokeshi, T. Doanh, S. Castellaro, J. J. Zou, D. S. Liyanapathirana, H. Wong (2013). Investigation of dynamically compacted ground by HVSR-based approach. *Soil Dyn. and Earthq. Eng.* **46**, 20–29

Harutoonian, P. (2012). *Geotechnical Characterisation of Compacted Ground by Passive Ambient Vibration Techniques.* Dissertation at Univ. of Western Sydney, Sydney, Australia

Haskell, N. A. (1953). The dispersion of surfacewaves on multilayered media. *Bull. Seism. Soc. Am.* **43**, 17–34

Haris, R. and J. Major (2016). Waves of destruction in the East Indies: the Wichmann catalogue of earthquakes and tsunami in the Indonesian region from 1538 to 1877. In: Cummins, P. R. & Meilano, I. (eds) *Geohazards in Indonesia: Earth Science for Disaster Risk Reduction* Geol. Soc., London, Special Publications **441**, The Geol. Soc. of London

Hayes, G. P., D. J. Wald, and R. L. Johnson (2012). Slab1.0: A three-dimensional model of global subduction zone geometries. *JGI* **117(B1)**, n/a–n/a

Hayes, G. P., D. J. Wald, and K. Keranen (2009). Advancing techniques to constrain the geometry of the seismic rupture plane on subduction interfaces a priori: Higher-order functional fits. *Geochemistry Geophysics Geosystems* **10(9)**, n/a–n/a

Hobiger, M., C. Cornou, M. Wathelet, G. Di Giulio, B. Knapmeyer-Endrun, F. Renalier, P.-Y. Bard, A. Savvaidis, S. Hailemikael, Bihan N. Le, M. Ohrnberger, and N. Theodoulidis (2013). Ground structure imaging by inversions of Rayleigh wave ellipticity: sensitivity analysis and application to European strong-motion sites. *Geophys. J. Int.* **192(1)**, 207–229

Huang, W-H., J-H. Wang, H-H. Hsieh, and K-L. Wen (1979). High frequency site amplification evaluated from Borehole data in the Taipei Basin. *J. Seismology* **13(4)**, 601–6011

Husen, S., and J. L. Hardebeck (2010). Earthquake location accuracy. *Community Online Resource for Statistical Seismicity Analysis, doi:10.5078/corssa-55815573* Available at http://www.corssa.org

Hutapea, B. M. and I. Mangape (2009). Analisis Hazard Gempa dan Usulan Ground Motion pada Batuan Dasar untuk Kota Jakarta . *Jurnal Teknik Sipil* **16(3)**, 121–132

Ibs-von Seht, M. and J. Wohlenberg (1999). Microtremors measurements used to map thickness of soft soil sediments. *Bull. Seism. Soc. Am.* **89**, 250–259

Indonesian National Board for Disaster Management (BNPB), Australian Government and the World Bank (GFDRR) (2007). InaSAFE source code. http://inasafe.org/

Irsyam, M., W. Sengara, F. Aldiamar, S. Widiyantoro, W. Triyoso, D. H. Natawidjaja, E. Kertapati, I. Meilano, Suharjono, M. Asrurifak, and M. Ridwan (2010). Development of Seismic Hazard Maps for Indonesia for Revision of Seismic Hazard Map in **SNI 03-1726–2002**

Irsyam, M.; Sengara, W.; Aldiamar, F.; Widiyantoro, S.; Triyoso, W.; Hilman, D.; Kertapati, E.; Meilano, I.; Suhardjono, S.; Asrurifak, M.; et al. *Development of Seismic Hazard Maps of Indonesia for Revision of Seismic Hazard Map in SNI 03-1726-2002*; Research Report: Indonesian Ministry of Public Works, Jakarta, Indonesia, 2011.

Irsyam, M., D. Hutabarat, M. Asrurifak, I. Imran, S. Widiyantoro, Hendriyawan, I. Sadisun, B. Hutapea, T. Afriansyah, H. Pindratno, A. Firmanti, M. Ridwan, S. W. Haridjono, and R. Pandhu (2014). Development of seismic risk microzonation maps of Jakarta city. Proceedings: *Geotechnics for Catastrophic Flooding Events*, August 2014

Iwaki, A. and T. Iwata (2011). Estimation of three-dimensional boundary shape of the Osaka sedimentary basin by waveform inversion. *Geophys. J. Int.* **186(3)**, 1255–1278

Kagawa, T., B. Zhao, K. Miyakoshi, and K. Irikura (2004). Modeling of 3D Basin Structures for Seismic Wave Simulations Based on Available Information on the Target Area: Case Study of the Osaka Basin, Japan. *Bull. Seism. Soc. Am.* **94(4)**, 1353–1368

Kanai, K(1957). Semi-empirical formula for the seismic characteristics of the ground. *Bull. of the ERI* **35**, 309–325

Kanai, K. and T. Tanaka (1954). Measurement of the microtremor I. *Bull. of the ERI* **32**, 199–209

Kawase, H. and K. Aki (1989). A study on the response of a soft basin for incident S, P, and Rayleigh waves with special reference to the long duration observed in Mexico City. *Bull. Seism. Soc. Am.* **79(5)**, 1361–1382

Kawase, H. (1996). The cause of the damage belt in Kobe: "The basin-edge effect," constructive interference of the direct S-wave with the basin induced diffracted Rayleigh waves. *Seism. Res. Lett.* **67(5)**, 25–34

Kawase, H. and Y. Hayashi (1996). Strong motion simulation in Chuo, Kobe, during the Hyogoken-nanbu Earthquake of 1995 based on the inverted bedrock motion. *J. Struct. Construct. Eng.* **480**, 67–76

Kemendagri - Ministry of Internal Affair (2015). http://www.kemendagri.go.id/pages/profil-daerah/p accessed June 2017

Kertapati, E. and R. P. Koesoemadinata (1992). Aftershock studies of the February 10, 1982, Sukabumi earthquake, West Java, Indonesia *Bull. of the IISEE*, **20**, 91–101

Kertapati, E. (2006). *Aktifitas Gempa Bumi di Indonesia, Persfektif Regional pada Karekteristik Gempa Bumi Merusak*, Badan Geologi, Bandung

Kingston, J. (1988). Undiscovered petroleum resources of Indonesia. Open-File Report: *USGS* **88-379**

KKP–Kementerian Kelautan dan Perikanan [Ministry of Marine and Fisheries] (2017). https://jpp.go.id/humaniora/sosial-budaya/301315-kkp-akan-mendaftarkan-14-572-pulau-ke-pbb, accessed June 2017

Kloosterman, F. H. (1989). *Groundwater flow systems in the Northern Coastal Lowlands of West- and Central Java, Indonesia.*. Dissertation at Vrije University, Amsterdam, the Netherland.

Koller, M. G., JL. Chatelain, B. Guillier, A. M. Duval, K. Atakan, C. Lacave, P.-Y. Bard and participants (2004). Practical user guidelines and software for the implementation of the H/V ratio technique: measuring conditions, processing method and results interpretation. Proceedings: *the 13th WCEE*, paper no. **3132**, Vancouver, B. C. Canada, 1–6 August 2004

Komatitsch, D. and J. P. Vilotte (1998). The spectral element method: an efficient tool to simulate the seismic response of 2D and 3D geological structure. *Bull. Seism. Soc. Am.* **88(2)**, 368–392

Komatitsch, D. and J. Tromp (1999). Introduction to the spectral element method for three-dimensional seismic wave propagation. *Geophys. J. Int.* **139(3)**, 806–822

Komatitsch, D., Q. Liu, J. Tromp, P. Süss, C. Stidham, and J. H. Shaw (2004). Simulations of ground motion in the Los Angeles basin based upon the spectral-element method. *Bull. Seism. Soc. Am.* **94(1)**, 187–206

Konno, K. and T. Ohmachi (1998). Ground-Motion Characteristics Estimated from Spectral Ratio between Horizontal and Vertical Components of Microtremor. *Bull. Seism. Soc. Am.* **88(1)**, 228–241

Koulali, A.; McClusky, S.; Susilo, S.; Leonard, Y.; Cummins, P.; Tregoning, P.; Meilano, I.; Efendi, J.; Wijanartob, A.B. The kinematics of crustal deformation in Java from GPS observations: Implications for fault slip partitioning. *Earth Planet. Sci. Lett.* **2017**, *458*, 69–79.

Kramer, S. L. (1996). Geotechnical earthquake engineering. In: *Prentice-Hall international series in civil engineering and engineering mechanics*

Lachet, C. and P.Y. Bard (1994). Numerical and Theoretical Investigations on the Possibilities and Limitations of Nakamura's Technique. *J. Physics of the Earth* **42(5)**, 377–397

Lachet, C. and P.Y. Bard (1995). Theoretical investigations on the Nakamura's technique. Proceedings: *the 3^{rd} international conference on recent advanced in Geotechnical Earthquake Engineering and Soil Dyn.*, 2–7 Apr 1995, St. Louis (Missouri), vol. **II**

Langston, C. A. and S. P. Horton (2004). Three-Dimensional Seismic-Velocity Model for the Unconsolidated Mississippi Embayment Sediments from H/V Ambient Noise Measurements. *Bull. Seism. Soc. Am.* **104(5)**, 2349–2358

Lee, W. L. and M. D.Trifunac (2010). Should average shear-wave velocity in the top 30 m of soil be used to describe seismic amplification? *Soil Dyn. and Earthq. Eng.* 30, 1250–1258

Lee, W. L. (1987). *Influence of soil and geologic site conditions on Fourier spectrum amplitudes of recorded strong motion accelerations.*, Civil Engineering Technical Report Series - Strong Motion Group Contributions **CE 87-04**, USC, L.A.

Lee, C.-T. and B.-R. Tsai (2008). Mapping Vs30 in Taiwan. *Terr. Atmos. Ocean. Sci.* **19(6)** 671–682

Lermo, J. and J. Chavez-Garcia (1993). Site Effect Evaluation Using Spectral Ratios with Only One Station. *Bull. Seism. Soc. Am.* **83(5)**, 1574–1594

Lermo, J. and J. Chavez-Garcia (1994). Are microtremors useful in the site response evaluation? *Bull. Seism. Soc. Am.* **84(5)**, 1350–1364

Longuet-Higgins, M. S. (1950). A Theory of the Origin of Microseisms. *Philosophical Transactions of the Royal Society of London. Series A, Mathematical and Physical Sciences* **243(857)**, 1–35

Lontsi (1950). Full microtremor H/V(z, f) inversion for shallow subsurface characterization. *Geophys. J. Int* **202**, 298–312

Lubis, R. F., Y. Sakura and R. Delinom (2008).Groundwater recharge and discharge processes in the Jakarta groundwater basin, Indonesia. *Hydrogeology Journal* **16**, 927–938

Lunedei, E. and D. Albarello (2010). Theoretical HVSR curves from full wavefield modelling of ambient vibrations in a weakly dissipative layered Earth. *Geophys. J. Int.* **181(2)**, 1093–1108

McCaffrey, R. and R. Sutardjo (1982). Reconnaissance microearthquake survey of Sulawesi, Indonesia. *Geophys. Res. Lett.* **9(8)**, 793–796

Magistrale, M., S. Day, R. W. Clayton, and R. Graves (2000). The SCEC Southern California Reference Three-Dimensional Seismic Velocity Model Version 2. *Bull. Seism. Soc. Am.* **90(6B)**, S65–S76

Malinverno, A. (2002). Parsimonious Bayesian Markov chain Monte Carlo inversion in a nonlinear geophysical problem. *Geophys. J. Int.* **151(3)**, 675–688

Manakou, M. V., D. G. Raptakis, F. J. Chávez-Garcıía, P. I. Apostolidis, and K. D. Pitilakis. (2010). 3D soil structure of the Mygdonian basin for site response analysis. *Soil Dyn. Eq. Eng.* **30(11)**, 1198–1211

Marafi, M. A., M. O. Eberhard, and J. W. Berman (2017).Effects of the Yufutsu Basin on Structural Response during Subduction Earthquakes. Proceeding at *the 16thWCEE 2017)* No. **2629**

Marliyani G.I.; Arrowsmith, R. Tectonic Geomorphology of the Hanging Wall Blocks of the Cimandiri Fault Zone, West Java, Indonesia. In Proceeding of the American Geophysical Union Fall Meeting, T41C-4650, San Francisco, CA, USA, 15 December 2014

Martodjojo (1984) Evolusi Cekungan Bogor (The Evolution of Bogor Basin). Dissertation in *Bandung Institute of Technology*, unpublished

Matsuoka, M., K. Wakamatsu, K. Fujimoto S. and Midorikawa (2006). Average shear-wave velocity mapping using Japan engineering geomorphologic classification map. *JSCE* **23(1)**, 57–68

Mavko, G., T. Mukerji and J. Dvorkin (2009). *Rock Physics Handbook - Tools for Seismic Analysis in Porous Media*. Cambridge Univ. Press

R. McCaffrey(2009). The Tectonic Framework of the Sumatran Subduction Zone. *Annu. Rev. Earth. Planet. Sci.* **37**, 3.1–3.22

Meilano, I., H. Z. Abidin, H. Andreas, I. Gumilar, D. Sarsito, R. Hanifa, Rino, H. Harjono, T. Kato, F. Kimata, and Y. Fukuda (2012). Slip Rate Estimation of the Lembang Fault West Java from Geodetic Observation. *JDR* **7(1)**, 12–18

Merati, W., M. Irsyam, J. Firmansyah, W. Wangsadinata and A. Surachman (2000). Development of Synthetic Ground Motions-Bedrock of Jakarta. Proceedings: *the 12th WCEE* Auckland, New Zealand

Molnar, S., S. E. Doso and J. F. Cassidy (2010). Bayesian inversion of microtremor array dispersion data in southwestern British Columbia. *Geophys. J. Int.* **183(2)**, 923–940

Molnar, S., J. F. Cassidy, K. B. Olsen, S. E. Dosso, and J. He (2014). Earthquake ground motion and 3D Georgia basin amplification in SW British Columbia: Deep Juan de Fuca plate scenario earthquakes. *Bull. Seism. Soc. Am.* **104**, 301–320

Molnar, S., J. F. Cassidy, K. B. Olsen, S. E. Dosso, and J. He (2014b). Earthquake ground motion and 3D Georgia basin amplification in SW British Columbia: Shallow blind-thrust scenario earthquakes. *Bull. Seism. Soc. Am.* **104**, 321–335

Mosegaard, K. & A. Tarantola, 195. Monte Carlo sampling of solutions to inverse problems. *J. Geophys. Res.*. **100(B7)**, 12 431–12 447

Motosaka, M. and M. Nagano (1996). Analysis of Ground-Motion Amplification Characteristics in Kobe City Considering a Deep Irregular Underground Structure–Interpretation of Heavily Damaged Belt Zone during the 1995. Hyogo-ken. *J. Phys. Earth* **44**, 577–590

Mucciarelli, M. and M. R. Gallipoli (2004). The HVSR Technique from Microtremor to Strong Motion: Empirical and Statistical Considerations. *the 13th WCEE*, Vancouver, B.C., Canada

Moechtar, H. (2015) Cekungan-Cekungan Kuarter Jakarta (Quaternary Basins of Jakarta). Weekly seminar in *Badan Geologi [Geological Agency of Indonesia]*, unpublished

Musson, R. M. W. (2012). A provisional catalogue of historical earthquakes in Indonesia. *British Geological Survey*

Nakamura, Y. (1989). A method for dynamic characteristics estimation of subsurface using microtremor on the ground surface. *Quarterly Report of RTRI* **30(1)**, 25–33

Narayan, J. P. (1999). Site-specific strong ground motion prediction using 2.5-D modelling. *Geophys. J. Int.* **146(2)**, 269–281

Narayan, J. P. (2001). 2.5-dimensional crosshole acoustic response: a variable density approach. *Geophys. J. Int.* **139(3)**, 879–887

Narayan, J. P. (2003). 2.5D Simulation of basin-edge effects on the ground motion characteristics. *Proc. Indian Acad. Sci. (Earth Planet. Sci.)* **112(3)**, 463–469

Nakamura, Y. (1997). Seismic Vulnerability Indices for Ground and Structures using Microtremor. Proceeding: *World Congress on Railway Research*, Florence, Nov. 1997

Nata, T. P. and B. Witsen (100). A Relation of the Bad Condition of the Mountains about the Tungarouse and Batavian Rivers, Having Their Source from Thence, Occasioned by the Earthquake between the 4th and 5th of January, 1699. Drawn up from the Account Given by the Tommagon Porbo Nata, (Who Hath Been There) and Sent to the Burgermaster Witsen, Who Communicated It to the R. Society, of Which He is a Member. *Philosophical Transactions* **22(260-276)**, 595–598

Natawidjaja, D.H. and W. Triyoso (2007). The Sumatran Fault Zone - From Source to Hazard. *J. Earthquake and Tsunami* **1(1)**, 21–47

Nath, S. K., K. K. S. Thingbaijam, M. D. Adhikari, A. Nayak, N. Devaraj, S. K. Ghosh, and A. K. Mahajan (2013). Topographic gradient based site characterization in India

complemented by strong ground-motion spectral attributes. *Soil Dyn. and Earthq. Eng.* **55**, 233–246

Newcomb, K. R. and W. R. McCann (1997). Seismic history and seismotectonics of the Sunda Arc. *J. Geophys. Res.* **92(B1)**, 421–439

Ng, A. H.-M., L. Ge, X. Li, H. Z. Abidin, H. Andreas, and K. Zhang. (2012). Mapping land subsidence in Jakarta, Indonesia using persistent scatterer interferometry (PSI) technique with ALOS PALSAR. *Int. J. Appl. Earth Obs. and Geoinfo.* **18**, 232–242

Nguyen, N., J. Griffin, A. Cipta, and P. Cummins (2015). Indonesia's Historical Earthquakes Modelled examples for improving the national hazard map. *Geoscience Australia* Record **2015/23**, Canberra

Nichols, G. (2009). *Sedimentology and Stratigraphy* 2^{nd} edition, Wiley-Blackwell. Chichester, West Sussex, UK

Nogoshi, M. and T. Igarashi (1971). On the amplitude characteristics of ambient noise (Part 2). *J. Seis. Soc. Japan* **24**, 26–40

Ohta, Y. and N. Goto (1978). Empirical shear wave velocity equations in terms of characteristic soil indexes. *Erthq. Eng. and Struc. Dyn.* **6**, 167–187

Okada, H. (2003). The Microtremors Survey Method. *AGU, Geophysical Monograph* **12**

Okal, E. A., S. H. Kirby (2001). Energy-to-moment ratios for damaging intraslab earthquakes: preliminary results on a few case studies. *USGS* Open-File Report **2002-328**

Olsen, K. B., S. M. Day, J. B. Minster, Y. Cui, A. Chourasia, M. Faerman, R. Moore, P. Maechling, and T. Jordan., 2006. Strong shaking in Los Angeles expected from southern San Andreas earthquake. *Geophys Res. Lett.* **33**

Orhan, A., M. Tosun, and H. Tosun (2013). Preliminary hazard assessment and site characterization of Meselik campus area, Eskisehir-Turkey. *Nat Hazards Earth Syst Sci* **13**, 75–84

Ottemöller, L., P. Voss and J. Havskov (2011). Seisan earthquake analysis software for Windows, Solaris, Linux and Macosx. Univ. of Bergen, Bergen

Özalaybey, S., E. Zor, S. Ergintav and M. C. Tepirdamaz (2011). Investigation of 3-D basin structures in the Ízmit Bay area (Turkey) by single-station microtremor and gravimetric methods. *Geophys. J. Int.* **186(2)**, 883–894.

Padilla y Sanchez, R. J. (1989). Geology and tectonics of the basin of Mexico and their relationship with the damage caused by the earthquakes of September 1985. *Int. J. Mining and Geol. Eng.* **7(1)**, 17–28

Pagani, M.; Monelli, D.; Weatheril, G.; Danciu, L.; Crowley, H.; Silva, V.; Henshaw, P.; Butler, L.; Nastasi, M.; Panzeri, L.; et al. (2014). OpenQuake Engine: An Open Hazard (and Risk) Software for the Global Earthquake Model. *Seismol. Res. Lett.* **2011**, *85*, 692–702.

Pandey, B., R. S. Jakka, A. Kumar and H. Mittal (2016). Site Characterization of Strong-Motion Recording Stations of Delhi Using Joint Inversion of Phase Velocity Dispersion and H/V Curve. *Bull. Seism. Soc. Am.* **106(3)**, 1254–1266

Panzera, F., S. D'Amico, A. Lotteri, P. Galea, and G. Lombardo (2012). Seismic site response of unstable steep slope using noise measurements: the case study of Xemxija Bay area, Malta. *Nat. Hazards Earth Syst. Sci.* **12**, 3421–3431

Papazachos B. C., E. M. Scordilis, D.G. Panagiotopoulos, C.B. Papazachos, and G.F. Karakaisis (2004). Global relations between seismic fault parameters and moment Magnitude of Earthquakes *Bull. Geol. Soc. Greece***XXXVI**, 1482–1489, Proceedings of the 10th International Congress, Thessaloniki, April 2004

Parolai, S. M. Picozzi, M. Richwalski and C. Milkereit (2005). Joint inversion of phase velocity dispersion and H/V ratio curves from seismic noise recordings using a genetic algorithm, considering higher modes. *Geophys. Res. Lett.* **32(1)**, n/a–n/a

Pazzi, V., L. Tanteri, G. Bicocchi, M. D'Ambrosio, A. Caselli, R. Fanti (2017). H/V measurements as an effective tool for the reliable detection of landslide slip surfaces: Case studies of Castagnola (La Spezia, Italy) and Roccalbegna (Grosseto, Italy). *Physics and Chemistry of the Earth* **98**, 136–153

Pelinovsky, E., D. Yuliadi, G. Prasetya and R. Hidayat (1997). The 1996 Sulawesi Tsunami. *Nat. Hazards* **16**, 29–38

Peltzer, G., F. Crampé, S. Hensley, and P. Rosen (2001). Transient strain accumulation and fault interaction in the Eastern California Shear Zone. *Geology* **29(11)**, 975–978

Pilz, M., S. Parolai, M. Picozzi, R. Wang, F. Leyton, J. Campos and J. Zschau (2010). Shear wave velocity model of the Santiago de Chile basin derived from ambient noise measurements: a comparison of proxies for seismic site conditions and amplification. *Geophys. J. Int.* **182(1)**, 355–367

Pilz, M., S. Parolai, M. Stupazzini, R. Paoluci, and J. Zschau (2011). Modelling basin effects on earthquake ground motion in the Santiago de Chile basin by a spectral element code. *Geophys. J. Int.* **187(2)**, 929–945

Pilz, M., S. Parolai, D. Bindi, A. Saponaro, and U. Abdybachaev (2013). Combining Seismic Noise Techniques for Landslide Characterization. *Pure Appl. Geophys.* **171(8)**, 1729–1745

Pitarka, A., K. Irikura, T. Iwata, and T. Kagawa (1996). Basin Structure Effects in the Kobe Area Inferred from the Modeling of Ground Motions from Two Aftershocks of the January 17, 1995, Hyogo-ken Nanbu Earthquake. *J. Phys. Earth* **4**, 563–576

Poggi, V., D. Fah, J. Burjanek, and D. Giardini (2012). The use of Rayleigh-wave ellipticity for site-specific hazard assessment and microzonation: application to the city of Lucerne, Switzerland. *Geophys. J. Int.* **188(3)**, 1154–1172

Prabowo, U.N., Marjiyono, and Sismanto (2016). Mapping the fissure potential zones based on microtremor measurement in Denpasar City, Bali. *IOP Conf. Ser.:Earth Environ.* **29**

Pramatadie, A. M., H. Yamanaka, K. Chimoto, Afnimar, K. Koketsu, M. Sakaue, H. Miyake, I. W. Sengara, and I. A. Sadisun (2016). Microtremor exploration for shallow S-wave velocity structure in Bandung basin, Indonesia. *Exploration Geophysics* **48(4)**, 401–412

Pusat Studi Gempa Nasional (National Center for Earthquake Studies). *Peta Sumber dan Bahaya Gempa Indoensia Tahun 2017*; Pusat Litbang Perumahan dan Pemukiman PU: Bandung, Indonesia, 2017

Pusat Litbang Perumahan dan Pemukiman PU. 2011. Available online: `http://puskim.pu.go.id/Aplikasi/desain_spektra_indonesia_2011/` (accessed on 20 November 2017).

Puspita, S. D., R. Hall and C. F. Elders (2005). Structural styles of the offshore West Sulawesi fold belt, North Makassar Straits, Indonesia. In: *Proceedings: the 30th Annual Convention Indonesian Petroleum Association* 519–542

Putra, S. D. H., Suryantini, and W. Srigutomo (2016). Thermal modeling and heat flow density interpretation of the onshore Northwest Java Basin, Indonesia. *Geothermal Energy* **4(12)**, n/a–n/a

Reid, A. (2012). Historical Evidence for Past Tsunamis in the Java Subduction Zone. *Asia Research Institute, Working paper series* **178**

Renalier, F., D. Jongmans, M. Wathelet, C. Cornou, B. Endrun, M. Ohrnberger and A. Savvaidis (2009). Influence of parameterisation on inversion of surface wave dispersion curves and definition of a strategy of inversion. *EGU General Assembly, Geophys. Res. Abstract* **11**, EGU 2009-7799

Rial, J. A., N. G. Saltzman and L. Hui (1992). Earthquake-induced resonance in Sedimentary Basin. *American Scientist* **80(6)**, 566–57

Ridwan, M., S. Widiyantoro, M. Irsyam, Afnimar and H. Yamanaka (2016). Development of an engineering bedrock map beneath Jakarta based on microtremor array measurements. *Geol. Soc., London, Special Publications* 7(1), 44

Ridwan, M. (2016). Study of Ground Subsurface in Jakarta by Using Microtremor Array Method: Identification of Engineering Bedrock Depth and Site Class. Dissertation: *Institut Teknologi Bandung*

Ridwan, M., S. Widiyantoro, M. Irsyam, P. Cummins, and Afnimar, 2017. Site characterisation at Jakarta city by using microtremor array and their comparison with NSPT data. in preparation

Rivet, D., M. Campillo, F. Sanchez-Sesma, N. Shapiro and S. K. Singh (2015). Identification of surface wave higher modes using a methodology based on seismic noise and coda waves. *Geophys. J. Int.* **203(2)**, 856–868

Ristek, Humas (1990). Gempa yang Mengintai Jakarta. *Info Iptek* November 22, 2010. http://www.ristek.go.id/?module=News% 20News& id=7356 ,accessed on March 29, 2015

Research Institute for Human Settlements (2012). Techincal Report: *Pekerjaan Pemboran Dalam dan Pengujian Tanah*

Research Institute for Human Settlements (2013). Techincal Report: *Pekerjaan Pemboran Dalam dan Pengujian Tanah*

Robinson, D., V. Newey, and D. Gray (2006), EQRM source code https://code.google.com/archive/p/eqrm/source/default/source

Rosenblueth, E. and E. Ovando (1991). Geotechnical Lessons Learned from Mexico and Other Recent Earthquakes. Proceeding: *2nd International Conferences on Recent Advances in Geotechnical Earthq. Eng. and Soil Dyn.* **11**

Roten, D., K. B. Olsen, S. M. Day, Y. Cui, and D. Fäh, 2014. Expected seismic shaking in Los Angeles reduced by San Andreas fault zone plasticity *Geophys. Res. Lett.*. **8**, 2769–2777

Rudyanto, A. (2013). Development of Strong-motion Database For Sumatra-Java Region. Masters Thesis, Australian National Univ., Canberra

Rusnardi, R. and J. Kiyono (2001). Estimation of Earthquake Ground Motion in Padang, Indonesia *Int. J. GEOMATE* **1(8)**, 71–77

Salinas, V., F. Luzón, A. García-Jerez, F. J. Sánchez-Sesma, H. Kawase, S. Matsushima, M. Suarez, A. Cuellar, and M. Campillo (2014). Using Diffuse Field Theory to Interpret the H/V Spectral Ratio from Earthquake Records in Cibeles Seismic Station, Mexico City. *Bull. Seism. Soc. Am.* **104(2)**, 995–1001

Sambridge, M. . Gallagher, A. Jackson, and P. Rickwood (2006). Trans-dimensional inverse problems, model comparison and the evidence. *Geophys. J. Int.* **167(2)**, 528–542

Sambridge, M. and Mosegaard (2002). Monte Carlo methods in geophysical Inverse problems. *Rev. Geophys* **40(3)**, 1–29

Sánchez-Sesma, F. J., M. Rodríguez, U. Iturrarán-Viveros, F. Luzón, M. Campillo, L. Margerin, A. García-Jerez, M. Suarez, M. A. Santoyo and A. Rodriguez-Castellanos (2011). A theory for microtremor H/V spectral ratio: application for a layered mediu. *Geophys. J. Int.* **186(1)**, 221–225

Sarsito, D.A, H. Z. Abidin, B. Sapiie, W. Triyoso, I. Meilano and W. J. F. Simons (2011). Geometric and kinematic modelling of Sulawesi - East Kalimantan zone based on GNSS-GPS and global gravitation data. Presented at: *XXV IUGG General Assembly Earth on the Edge: Science for a Sustainable Planet*, JG06JS06S4, Melbourne, Australia, 27 June–8 July 2011

Sato, T, Y. Nakamura, and J. Saita (2004). Evaluation of the Amplification Characteristic of Subsurface Using Microtreomor and Strong Motion –the Studies at Mexico City –. Proceedings: *the 13th WCEE*, Vancouver, B.C. Canada

Sato, K.; Asano, K; Iwata, T. Long-period ground motion characteristics of the Osaka Sedimentary Basin during the 2011 Great Tohoku Earthquake. In Proceedings of the Fifteenth World Conference on Earthquake Engineering, Lisabon, Portugal, 24–28 September 2012

Savage, M. K., F.-C. Lin, and J. Townend (2013). Ambient noise crosscorrelation observations of fundamental and higher-mode Rayleigh wave propagation governed by basement resonance. *Geophys. Res. Lett.* **40(14)**, 3556–3561

Saygin, E., P. R. Cummins, A. Cipta, R. Hawkins, R. Pandhu, J. Murjaya, Masturyono, M. Irsyam, S. Widiyantoro, and B. L. N. Kennett (2016). Imaging architecture of the Jakarta Basin, Indonesia with transdimensional inversion of seismic noise. *Geophys. J. Int.* **204(2)**, 918–931

Saygin, E., P. R. Cummins, D. Lumley (2017). Retrieval of the P wave reflectivity response from autocorrelation of seismic noise: Jakarta Basin, Indonesia. *Geophys. Res. Lett.* **44(2)**, 792–799

Scales, J. A. and R. Snieder (1997). To Bayes or not to Bayes? *Geophysics* **62(4)**, 1045–1046

Schevenels, M., G. Lombaert, G. Degrande and S. François (1997). A probabilitistic assessment of resolution in the SASW test and its impact on the prediction of ground vibrations. *Geophys. J. Int.* **172(1)**, 262–275

Schwartz, D. P., and K. J. Coppersmith (1984). Fault behavior and characteristic earthquakes: Examples from the Wasatch and San Andreas Fault Zones. *J. Geophys. Res.* **89(B7)**, 5681–5698

Schwartz, G. (1978). Estimating the dimension of a model. *Ann. Stat.* **6**, 461–464

Scherbaum, F., K.-G. Hinzen, and M. Ohrnberger (2003). Determination of shallow shear wave velocity profiles in the Cologne, Germany area using ambient vibrations. *Geophys. J. Int.* **152(3)**, 597–612

Seed, H. B. , C. Ugas and J. Lysmer (1976). Site-dependent spectra for earthquake-resistant design. *Bull. Seism. Soc. Am.* **66(1)**, 221–243

Seno, T., and M. Yoshida (2004). Where and why do large shallow intraslab earthquakes occur?. *Physics of the Earth and Planetary Interiors* **4**, 183–206

SESAME Team (2004). Guidelines for the implementation of the H/V spectral ratio technique on ambient vibrations; measurements, processing, and interpretation. *WP12 European Commission - Research General Directorate* Project No. EVG1-CT-2000-00026 SESAME, Report Number **D23.12**

Shapiro, N.M., M. Campillo, L. Stehly, and M. H. Ritzwoller (2005). High-resolution surface-wave tomography from ambient seismic noise. *Science* **307(5715)**, 1615–1618

Shapiro, N.M. and M. Campillo (2004). Emergence of broadband Rayleigh waves from correlations of the ambient seismic noise. *Geophys. Res. Lett.* **31(7)**, n/a–n/a

Shearer, P. M. and J. A. Orcutt (1987). Surface and near-surface effects on seismic waves theory and borehole seismometer results. *Bull. Seism. Soc. Am.* **77(1)**, 1168–1196

Shoji, Y., K. Tanii, and M. Kamiyama (2004). The Duration and Amplitude Characteristics of Earthquake Ground Motions with Emphasis on Local Site Efects. Conference Paper No. 436. *the 13_{th}WCEE* Vancouver, B.C., Canada

Shooshpasha, I. A. Hasanzadeh, and A. Taghavi (2013). Prediction of the Axial Bearing Capacity of Piles by SPT-based and Numerical Design Methods. *Int. J. GEOMATE* **4(2)**, 560–564

Sidarto (2008) Dinamika Sesar Citarik. *Jurnal Sumberdaya Geologi* **XVIII(3)**, 149–162

Silver, E. A. and J. C. Moore (1978). The Molucca sea collision zone, Indonesia. *J. Geophys. Res.* **83(B4)**, 1681–1691

Silver, E. A., R. McCaffrey and R. B. Smith (1983). Collision, rotation, and the initiation of subduction in the evolution of Sulawesi, Indonesia. *J. Geophys. Res.* **88(B11)**, 9407-9418.

Silver, E. A., R. McCaffrey, Y. Joyodiwiryo, and S. Stevens (1983). Ophiolite emplacement by collision between the Sula Platform and the Sulawesi island arc, Indonesia. *J. Geophys. Res.* **88(B11)**, 9419–9435

Simandjuntak, T. O. (1986). Sedimentology and tectonics of the collision complex in the east arm of Sulawesi. PhD Thesis: *University of London* **106(1)**, 185–201

Simandjuntak, T. O. and A. J. Barber (1996). Contrasting tectonic styles in the Neogene orogenic belts of Indonesia. *Geol. Soc., London, Special Publications* **106(1)**, 185–201

Simandjuntak, T. O (1993). Neogene tectonics and orogenesis of Indonesia. In: Teh, G. H. (ed.) Proceedings of the Symposium on Tectonic Framework and Energy Resources of the Western Margin of the Pacific Basin *Geol. Soc. of Malaysia Bull.* **33**, 43–64, Geol. Soc. of Malaysia

Simons, W. J. F. , A. Socquet, C. Vigny, B. A. C. Ambrosius, S. H. Abu, C. Promthong, C. Subarya, D. A. Sarsito, S. Matheussen, P. Morgan, and W. Spakman (1997). A decade of GPS in Southeast Asia: resolving Sundaland motion and boundaries. *J. Geophys. Res.* **112(B6)**, n/a–n/a

Singh, S.K.; Ordaz, M. On the origin of long coda observed in the lake-bed strong-motion records of Mexico City. *Bull. Seismol. Soc. Am.* **1993**, *83*, 1298–1306

Singh, A. P., A. Shukla, M. R. Kumar, and M. G. Thakkar (2017).Characterizing Surface Geology, Liquefaction Potential, and Maximum Intensity in the Kachchh Seismic Zone, Western India through Microtremor Analysis. *Bull. Seism. Soc. Am.* **107(3)**, n/a–n/a

Sivia, D. and Skilling, J., 2006. *Data Analysis: A Bayesian Tutorial*, Oxford University Press, Oxford, UK.

Socco, L. V. and D. Boiero (2008). Improved Monte Carlo inversion of surface wave data. *Geophys. Prospect.* 112(B6) 56(3), 357–371

Socquet, A., W. Simons, C. Vigny, R. McCaffrey, C. Subarya, D. Sarsito, B. Ambrosius and W. Spakman (2006). Microblock rotations and fault coupling in SE Asia triple junction (Sulawesi, Indonesia) from GPS and earthquake slip vector data. *J. Geophys. Res.* **111(B8)**, n/a–n/a

Soehaimi, A. (2011) *Seismotektonik Jawa Barat dan Mikrozonasi Potensi Bencana Gempa Bumi DKI Jakarta* Geological Agency, Bandung

Soetardjo, M. Untung, E. P. Arnold, R. Soetadi, S. Ismail, and E. K. Kertapati (1985) in E. P. Arnold (ed.) *Series on Seismology Vol V: Indonesia* Southeast Asia Association of Seismology and Earthq. Eng.

Sukamta, and N. Alexander (2012). State of Practice of Performance-Based Seismic Design in Indoensia. *I. J. High-Rise Building* **1(3)**, 211–220

Supartoyo, I.A.; Sadisun, E.; Suparka, A. Cimandiri Fault Activity at Sukabumi Area, West Java, Indonesia (Based on Morphometry Analysis). In Proceeding of the ISEGA I, Bandung, Indonesia, 13 October 2013.

Supartoyo *Geomorfologi Tektonik Sesar Cimandiri Daerah Sukabumi dan Sekitarnya, Provinsi Jawa Barat*, PhD dissertation at Institut Teknologi Bandung. Bandung

Spencer, J. E. (2011). Gently dipping normal faults identified with Space Shuttle radar topography data in central Sulawesi, Indonesia, and some implications for fault mechanics. *Earth and Planetary Science Letters* **308(3-4)**, 267–276

Stewart, J. P., Y. Choi and R. W. Graves (2005). Empirical Characterization of Site Conditions on Strong Ground Motion *PEER* Report No. **2005/01**

Supartoyo and Surono (2008). Katalog Gempabumi Merusak di Indonesia Tahun 1629-2007. Badan Geologi, Bandung

Tarabusi, G. and R. Caputo (2016). The use of HVSR measurements for investigating buried tectonic structures: the Mirandola anticline, Northern Italy, as a case study. *IJEaS* **106(1)**, 341–353

Thomson, W. T. (1950). Transmission of elastic waves through a stratified solid medium. *J. Appl. Phys.* **21**, 89–93

Trifunac, M. D. (1987). *Influence of soil and geologic site conditions on Fourier spectrum amplitudes of recorded strong motion accelerations.*, Civil Engineering Technical Report Series - Strong Motion Group Contributions **CE 87-06**, USC, L.A.

Tsai, V.C.; Bowden, D.C.; Kanamori, H. Explaining extreme ground motion in Osaka basin during the 2011 Tohoku earthquake. *Geophys. Res. Lett.* **2017**, *44*, 7239–7244

Turkandi, T., D. A. Agustiyanto and M. M. Purbo-Hadiwidjojo (1992). Geologic Map of Jakarta and Kepulauan Seribu Quadrangles, Jawa. *GRDC*, Bandung, Indonesia

UBC (2003). *International Conference of Building Officials. Uniform Building Code*, Willier, California

Uebayashi, H. (2003). Extrapolation of Irregular Subsurface Structures Using the Horizontal-to-Vertical Spectral Ratio of Long-Period Microtremors. *Bull. Seism. Soc. Am.* **93(2)**, 570–582

Uebayashi, H., H. Kawabe and K. Kamae (2012). Temporal Variation and Reproduction of Microseism H/V Spectral Features in the Osaka Sedimentary Basin with an Irregular-Shaped Interface. *Proceedings: the 15th WCEE*, Lisboa, 2012.

Uebayashi, H., H. Kawabe and K. Kamae (2012). Reproduction of microseism H/V spectral features using a three-dimensional complex topographical model of the sediment-bedrock interface in the Osaka sedimentary basin. *Geophys. J. Int.* **189(2)**, 1060–1074

Viens, L., H. Miyake, and K. Koketsu (2015). Long-period ground motion simulation of a subduction earthquake using the offshore-onshore ambient seismic field. *Geophys. Res. Lett.* **42(13)**, 5282–5289

Viens, L., H. Miyake, and K. Koketsu (2016). Simulations of long-period ground motions from a large earthquake using finite rupture modeling and the ambient seismic field. *J. Geophys. Res.* **121**, 8774–8791

Viens L., M. Denolle, H. Miyake S. Sakai and S Nakagawa (2017). Retrieving impulse response function amplitudes from the ambient seismic field *Geophys. J. Int.* **1(1)**, 210–222

Wald, D. J., and T. I. Allen (2007). Topographic slope as a proxy for seismic site conditions and amplification. *Bull. Seism. Soc. Am.* **97**, 1379–1395

Walter, T. R., R. Wang, B.-G. Luehr, J. Wassermann, Y. Behr, S. Parolai, A. Anggraini, E. Günther, M. Sobiesiak, H. Grosser, H.-U. Wetzel, C. Milkereit, P. J. K. Sri Brotopuspito, P. Harjadi, J. Zschau (2008). The 26 May 2006 magnitude 6.4 Yogyakarta earthquake south of Mt. Merapi volcano: Did lahar deposits amplify ground shaking and thus lead to the disaster?. Research Letter: *Geochemistry, Geophysics, Geosystems* **9(5)**, n/a–n/a

Wang, K., and Y. Hu (2006). Accretionary prisms in subduction earthquake cycles: The theory of dynamic Coulomb wedge. *J. Geophys. Res.* **111(B6)**, n/a–n/a

Wang, W. J., K. F. Ma, F. Mothereau, and D. Eberhart-Phillips (2009). Three-dimensional Qp- and Qs-tomography beneath Taiwan orogenic belt: implications for tectonic and thermal structure *Geophys. J. Int.* **180(2)**, 891–910

Wthelet, M., D. Jongmans, and M. Ohrenberger (2004). Surface-wave inversion using a direct search algorithm and its application to ambient vibration measurements. *Near Surface Geophys* **2**, 211–221

Wathelet, M. (2005). Array recordings of ambient vibrations: surface-wave inversion. PhD thesis: Univ. de Liége, Liége, Belgium

Wathelet, M. (2006). http://www.geopsy.org/documentation/geopsy/

Wardhani, P.W.K., B. T. Sumbodo, W. Suryanto, and Novianto (2013). Site Effect Investigation using Spectral Ratio Method in Muara Labuh Geothermal Field, Indonesia. Proceeding: *11_{th} SEGJ International Symposium*, Yokohama, Japan, 18-21 November 2013.

Watkinson, I. M., R. Hall and F. Ferdian (2011). Tectonic re-interpretation of the Banggai-Sula-Molucca Sea margin, Indonesia. *Geol. Soc., London* Special Publications, **355(1)**, 203–224

Wells, D. L. and K. J. Coppersmith (1994) New empirical relationships among magnitude, rupture length, rupture width, rupture area, and surface displacement. *Bull. Seism. Soc. Am.* **84(4)**, 974-1002

Wichmann, A. (1918) *Die Erdbeben des Indischen Archipels bis zum Jahre 1857* Verhandelingen Der Koninklijke Akademie van Wetenschappen Te Amsterdam, 20, 193.

Wichmann, A. (1922) *Die Erdbeben Indischen Archipels von 1858 bis 1877* Verhandelingen Der Koninklijke Akademie van Wetenschappen Te Amsterdam, 22, 209.

Wiegel, R. L. (1970) *Earthquake Engineering* 518 pp, Prentice-Hall, Englewood Cliffs, N. J., 22, 209

Widiyantoro, S. and R. van der Hilst (1996) Structure and Evolution of Lithosperic Slab Beneath the Sunda Arc, Indonesia. *Science* **271(5255)**, 1566–1570

Xia, J. R. D. Miller, and C. B. Park (1999) Estimation of near-surface shearwave velocity by inversion of Rayleigh wave. *Geophysics* **64**, 691–700

Xia, J. R. D. Miller, C. B. Park, J. A. Hunter and J. B. Hariis (2000) Comparing shear-wave velocity profiles from MASW with borehole measurements in unconsolidated sediments, Fraser River delta, B.C., Canada. *J. Environ. Eng. Geophys.* **5**, 1–13

Xia, J. R. D. Miller, X. Yixian L. Yinhe, C. Chao, L. Jiangping, J. Ivanov and C. Zheng (2009) High-frequency Rayleigh-wave method. *J. Earth. Sci.* **20(3)**, 563–579

Yamanaka, H., M. Dravinski and H. Kagami (1993) Continuous Measurements of Microtremors on Sediments and Basements in Los Angeles, California. *Bull. Seism. Soc. Am.* **83(5)**, 1595–1609

Yamanaka, H., M. Takemura, H. Ishida and M. Niva (1994) Characteristics of long-period microtremors and their applicability in exploration of deep sedimentary layers. *Bull. Seism. Soc. Am.* **84(6)**, 1831–1841

Youngs, R. R. and K. J. Coppersmith (1985). Implications of fault slip rates and earthquake recurrence models to probabilistic seismic hazard estimates. *Bull. Seism. Soc. Am.* **75(4)**, 939–964

Youngs, R. R., S. J. Chiou, W. J. Silva and J. R. Humphrey (1997). Strong ground motion attenuation relationships for subduction zone earthquakes. *Seis. Res. Lett.* **68(1)**, 58–73

Zhao, J. X., J. Zhang, A. Asano, Y. Ohno, T. Oouchi, T. Takahashi, H. Ogawa, K. Irikura, H. K. Thio, and P. G. Somerville (2006). Attenuation Relations of Strong Motion in Japan using site classification based on predominant period. *Bull. Seism. Soc. Am.* **96(3)**, 898–913

Zeid, N.A., E. Corradini, S. Bignardi, V. Nizzo, and G. Santarato (2017). The Passive Seismic Technique 'HVSR' as a Reconnaissance Tool for Mapping Paleo-soils: The Case of the Pilastri Archaeological Site, Northern Italy . *Archaeol. Prospect.* **9999**, n/a–n/a

Zhao, J. X., K. Irikura, J. Zhang, Y. Fukushima, P. G. Somerville, A. Asano, Y. Ohno, T. Oouchi, T. Takahashi, and H. Ogawa (2006). An Empirical Site-Classification Method for Strong-Motion Stations in Japan Using H/V Response Spectral Ratio. *Bull. Seism. Soc. Am.* **96(3)**, 914–925

Zhao, Z., Z. Zhao and J. Xu (2010). Interference between seismic body wave and secondary surface wave resulting in the peak collapse ratios of buildings. *J. Appl. Geophysics* **72(1)**, 1–9.

Zhao, J. X. (2011). Comparison between VS30 and site period as site parameters in ground-motion prediction equations for response spectra. In: *IAEE International Symposium: Effects of Surface Geology on Seismic Motion* 23–26

Zhao, J. X. and H. Xu (2011). Comparison between VS30 and site period as site parameters in ground-motion prediction equations for response spectra. In: *IAEE International Symposium: Effects of Surface Geology on Seismic Motion* 23–26